

Preferential alignment of anisotropic transition dipole moments in organic and perovskite thin films

Dissertation

zur Erlangung des akademischen Grades

Dr. rer. nat.

eingereicht an der

Mathematisch-Naturwissenschaftlich-Technischen Fakultät

der Universität Augsburg

von

Thomas Morgenstern

Augsburg, Mai 2019



1. Gutachter: Prof. Dr. Wolfgang Brütting
 2. Gutachter: Prof. Dr. Hubert Krenner
 3. Gutachter: Prof. Dr. Kristiaan Neyts
- Datum der mündlichen Prüfung: 18.07.2019

Contents

1. Introduction	1
I. Basics - From dipole radiation to thin film devices	3
2. Dipole radiation in thin film microcavities	5
2.1. Dipolar light emission in dielectric media	7
2.1.1. Maxwell's equations for light emission	7
2.1.2. Plane waves and their interaction with media	8
2.1.3. Dipole radiation	8
2.2. Thin film microcavities	9
2.2.1. Refraction at planar interfaces	9
2.2.2. Stacked layered media	10
2.3. Classical dipoles within one-dimensional microcavities	10
2.3.1. Purcell effect	11
2.3.2. Mode coupling	14
3. Photophysical properties of excitonic light emission	17
3.1. Generation of excitons in thin films	18
3.2. Radiative decay of excitonic states	18
3.3. Diffusion of excited states in thin films	20
3.4. Decay rates of excitons in fluorescent and phosphorescent systems	22
4. Anisotropy in thin film media	25
4.1. Birefringence	25
4.2. Anisotropy of emissive transitions	26
5. Light emission from thin film optoelectronic devices	33
5.1. Electrical operation	35
5.2. Optical mode distribution	36
5.3. Color tuning of thin film devices	39
5.4. Effects of preferential alignment on device performance	42

II. Methods - Extracting molecular properties to quantify thin film anisotropy	51
6. Computational methods	53
6.1. Calculation of molecular properties	53
6.2. Amorphous molecular ensembles	56
6.2.1. Molecular dynamics simulations	56
6.3. Predicting optical device properties	60
7. Experimental methods	63
7.1. Optical spectroscopy	63
7.1.1. Spectroscopy of visible light	63
7.1.2. Polarization anisotropy	70
7.1.3. Time resolved spectroscopy	71
7.1.4. Determination of the radiation pattern and orientation parameters	74
7.2. Electrical characterization	85
7.2.1. Extracting interfacial sheet charge density from impedance measurements	85
7.2.2. Determination of the preferential alignment of PDMs	88
III. Results - Understanding and predicting optical anisotropy in amorphous thin films	91
8. Anisotropy of small fluorescent molecules	93
8.1. Alignment mechanisms of small polar dyes	94
8.1.1. Dipolar interactions Coumarin6 and DCM	96
8.1.2. Preferential alignment of polar dyes in diluted guest host systems	107
8.2. Fluorescence anisotropy in organic guest-host systems	112
9. Preferential alignment of organometallic Ir-complexes	115
9.1. Photophysics of phosphorescent Ir-complexes	118
9.2. Preferential alignment of heteroleptic Ir-complexes	121
9.2.1. Pinpointing the molecular orientation	121
9.2.2. Understanding and predicting the alignment mechanisms	144
9.3. Orientation mechanisms of homoleptic C-C complexes	149
9.3.1. Photophysical properties of sky-blue Ir-complexes	150
9.3.2. Preferential alignment of homoleptic C-C complexes	157

9.3.3. Confirming the isotropic nature of Ir(ppy) ₃	162
10. Tunable anisotropic light emission in lead-halide perovskite nanocrystals	167
10.1. Carrier dynamics in CsPbBr ₃ nanocrystals	169
10.1.1. Light emission from lead-halide perovskites	169
10.1.2. Quantum confining the excited state in perovskite nanocrystals	171
10.2. Manipulating the emissive transition dipole moment of LHP nanocrystals	173
10.2.1. Anisotropic emission from self-organized LHP nanocubes .	173
10.2.2. Tunability of the anisotropic properties of LHP nanocubes	176
10.2.3. LHP TDM in quantum confined NCs	180
10.2.4. Superior optical properties of LHP nanoplatelets	183
10.3. Performance limit of perovskite LEDs	186
IV. Summary and Outlook	193
V. Appendix	215

Preface

This thesis aims to provide insight into selected topics regarding the preferential alignment of emissive transition dipole moments. While an introduction is given into the background of the emissive materials and theoretical descriptions, the reader is advised to be familiar with basic concepts of organic semiconductors, their emissive properties and basic concepts of organic light emitting diodes, such as given by [1, 2]. Further basic knowledge of wave-optics [3] as well as computational chemistry is recommendable, e.g., given by [4].

Within this work, the concepts of earlier theses of the author are used. Most notably, the optical simulations of organic semiconductors as discussed in [5, 6]. Further, it includes parts of the work of the students Philippe Linsmayr, Markus Schmid, Felix Höhnle and Thomas Gimpel. The computational and experimental methods used within this thesis, partially rely on preceding research by Bert Scholz, Jörg Frischeisen, Christian Mayr, Tobias Schmid, Nils Reinke, and Stefan Nowy. For a detailed insight into this research, the reader is advised to [7].

Note that the selected topics within this thesis do not aim to give a complete picture of preferential alignment in organic and hybrid thin films but focus on the detailed description of the work performed and published by the author. For a broader coverage of alignment mechanisms, the reader is referred to [8].

The results presented in the chapters of this work include the support of the organic semiconductors group at the University of Augsburg as well as collaboration partners at the University of Southern California, the University of Berkeley, the Molecular Foundry at the Lawrence Berkeley National Laboratory and the Technical University of Braunschweig. Details of the persons involved throughout the chapters are given in the appendix.

The descriptions within this thesis use several abbreviations for common effects and molecules. While the terms generally are introduced within the chapters, molecular abbreviations are not introduced explicitly. Instead, the chemical expressions for the molecules can be found in the appendix.

1. Introduction

Applications for thin film optoelectronics are commercially established and widely used in different technologies. Especially organic and hybrid organic-inorganic semiconducting materials are the state-of-the-art technology for smartphone and television displays. Despite the first discovery of organic semiconductors as lighting technology more than 22 years ago [9], new processes within the complex thin films regularly arise [8, 10, 11]. Due to its importance for light emitting applications, this thesis will focus on the excitonic emission of photons from amorphous and hybrid thin films, such as organic semiconducting guest-host systems.

The process of light generation in thin films is a well-understood mechanism and high-end computations even allow for the inclusion of relativistic effects on a single particle level. However, due to the highly integrated application in light emitting devices, structural information about the involved thin films is of crucial importance. Especially the anisotropy behavior of the emissive transition dipole moments within the light generating entities is a key factor for the efficiency of the devices. However, as these quantities are hidden by the low dye concentrations and the amorphous nature of the thin films, substantial effort has to be taken to identify the significant processes limiting the performance of device applications.

The following sections will introduce the reader to the basic principles of light generation in organic and hybrid thin films. Therein, the properties of the photon generation will be generalized in different quantities such as the emissive transition dipole moment, radiative and nonradiative exciton decay rates and other excitonic processes. Describing the quantum mechanical effects of the complex amorphous system from these quantities enables the description of the light emission process from a classical perspective. This approach based on Maxwell's equations allows for an easily accessible understanding of the visible light emission from a thin film while maintaining the complex properties of the system. Based on these considerations, the author describes selected topics of organic thin films and their application to light emitting devices. Further, special focus is set to the anisotropic properties of amorphous thin films and their quantification.

From a methodical perspective, several approaches can be taken to quantify amorphous thin films. While experimental efforts include precise measurements of the thin film radiation pattern as well as polarization and transient phenomena, none of those experiments can contribute to an understanding of the system

without computational input. Most notably, even if one were to obtain the complete structural information of a non-crystalline organic thin film, the pure amount of data would be overwhelming and impossible to interpret without a computerized approach. Hence, the utilization of several computational methods, such as density functional theory, molecular dynamics and extensive optical calculations is a mandatory set of tools for the understanding of anisotropic properties in thin films.

The third part of this thesis will focus on selected topics regarding the anisotropy in amorphous and hybrid thin films. In particular, the first two chapters will describe the molecular preferential alignment in organic fluorescent and phosphorescent thin films. The aforementioned organic films are subject to great disorder. Hence, it is even more surprising that many organic systems exhibit some anisotropy despite their naturally amorphous structure. While some effects are more straightforward to access, such as dipolar interaction or preferred orientation of rod-like molecules, the second chapter will set the topic to organometallic Ir-complexes. These molecules exhibit numerous different anisotropic effects despite their bulky structure. Hence, the unintuitive behavior of this class of materials requires extensive investigations to understand their amorphous properties.

The final chapter of the anisotropic properties of thin films is dedicated to the most remarkable effect observed throughout this thesis. The preferential alignment of the emissive transition dipole within cubic nanocrystals is unexpected due to the symmetric structure of the emissive species. However, theoretical approaches confirm the observed properties. Further, the research was extended to quantum confined nanocrystals. Within the experiments, the author was able to conclude a significant effect on the emissive transitions within the thin films. Additionally, the findings were used to unravel the performance limit of perovskite light emitting diodes, revealing a vast potential for their application in display and lighting technologies.

Part I.

Basics - From dipole radiation to thin film devices

What I am going to tell you about is what we teach our physics students in the third or fourth year of graduate school... It is my task to convince you not to turn away because you don't understand it. You see my physics students don't understand it... That is because I don't understand it. Nobody does.

Richard P. Feynman

2. Dipole radiation in thin film microcavities

The generation of photons within the visible spectrum is one of the main goals of many opto-electronic thin film applications. Due to the dimensions of the thin films, usually being within a few nm to microns [9, 12], and many timescales, residing in the nanosecond or microsecond regime [13, 14], the optics of thin films can mostly be described within the framework of Maxwell's equations and interference of the dipole radiation [1, 15].

Further, the emission of photons can be described by treating the transition dipole moment (TDM) of the emissive species as a classical oscillating dipole. Therein it is important to take into account that a microcavity traps the oscillating dipole in-between [1]. Hence, the emission of photons is not only influenced by the properties of the dipole but also its interference with the surrounding films [1, 15, 16].

The general model that allows for the description of these systems is shown in fig. 2.1. This one-dimensional layout can describe the necessary properties of all planar thin film devices. Important key factors of this system include the wavelength of the emitted photons being within the range of the system thickness, ensuring proper conditions leading to microcavity effects. Further, the media are isotropic and infinitely extended within the $x - y$ plane as depicted in fig. 2.1 [1]. Note that this system is not limited to visible applications but was first used to describe the propagation of long wave radio communication with the earth's atmosphere by Sommerfeld in 1909 [7, 17].

The following sections will introduce theoretical considerations in the description of dipole radiation within thin film microcavities. At first, Maxwell's equations will be used to derive the electric field of an oscillating dipole within a thin film microcavity. Additional descriptions will investigate the properties of thin-film microcavities, including stacked films. Finally, the Purcell effect will be introduced to investigate mode coupling of the electromagnetic waves within thin film structures describing optoelectronic applications. Note that the following paragraphs are based on earlier work as cited and do not reflect the entirety of theory necessary for all details of the thin film systems but only selected topics.

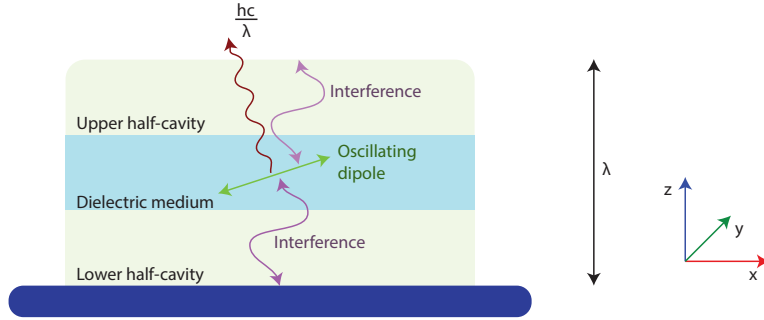


Figure 2.1.: Simplified model system for the emission of electromagnetic waves from dipole radiation within a one-dimensional microcavity. The oscillating TDM and thus the emitted photons themselves are affected by the interference with the surrounding microcavity. One crucial prerequisite for this system is the wavelength of the emitted photons being comparable to the thickness of the thin films, ensuring interference of the electromagnetic waves [1, 15]. Note that the coordinate system given on the right-hand side of the picture is valid throughout this work keeping the z-axis parallel to the surface normal of the microcavities and the x-axis the propagation direction of modes with the cavity (being equivalent to the y-axis or any other in-plane direction).

2.1. Dipolar light emission in dielectric media

To achieve the goal of describing excitonic light emission within thin film optoelectronic devices, this section will focus on the properties of a TDM within a dielectric medium. This oscillating dipole is subject to Maxwell's equations and thus can be adequately described by those. Further it is important to understand the propagation of basic plane waves in thin films and their interaction with surrounding media [3, 7].

2.1.1. Maxwell's equations for light emission

The classical behavior of electromagnetic waves and their interaction with media can be completely described via Maxwell's equations using the charge density ρ as well as the current \vec{j} [3]:

$$\vec{\nabla} \cdot \vec{D} = \frac{\rho}{\epsilon_0} \quad (2.1)$$

$$\vec{\nabla} \cdot \vec{B} = 0 \quad (2.2)$$

$$\vec{\nabla} \times \vec{E} = -\frac{\partial \vec{B}}{\partial t} \quad (2.3)$$

$$\vec{\nabla} \times \vec{H} = \mu_0 \vec{j} + \mu_0 \varepsilon_0 \frac{\partial \vec{D}}{\partial t} \quad (2.4)$$

Therein \vec{E} and \vec{B} describe the electric and magnetic field, whereas \vec{D} and \vec{H} indicate the displacement field and the magnetizing field. The latter are affected by material properties via the dielectric constant ε and the magnetic permeability μ [3]:

$$\vec{D} = \varepsilon \vec{E} = \varepsilon_0 \vec{E} + \vec{P} \quad (2.5)$$

$$\vec{H} = \frac{1}{\mu} \vec{B}. \quad (2.6)$$

Throughout this thesis the magnetic properties of the materials will not be investigated and thus, the magnetic permeability will be assumed as unity. The dielectric constant ε takes the polarizability \vec{P} of the surrounding medium into account [3]. This quantity generally depends on both the frequency of the electromagnetic wave, as well as the direction of propagation. Hence it has to be treated as a tensor [3]. In the context of this work, ε will be limited to uniaxial media, leaving the expression as follows:

$$\varepsilon = \begin{pmatrix} \varepsilon_{xy} & 0 & 0 \\ 0 & \varepsilon_{xy} & 0 \\ 0 & 0 & \varepsilon_z \end{pmatrix}. \quad (2.7)$$

2.1.2. Plane waves and their interaction with media

In order to describe the propagation of electromagnetic waves within materials, the electric field \vec{E} is assumed as a monochromatic wave expressed via [3]:

$$\vec{E} = \vec{E}_0 \exp(i(\vec{k} \cdot \vec{x} - \omega \cdot t)). \quad (2.8)$$

In this expression the real part describes the propagation in time (t) and space (\vec{x}) of an electromagnetic wave within a dielectric medium for a given amplitude \vec{E}_0 . Note that the electric field is always perpendicular to the direction of propagation given by the wavevector \vec{k} . Thus, electromagnetic waves are always transversal. Further, the frequency and thereby the wavelength is given by ω . With this expression for the electromagnetic wave, Maxwell's equations can be rewritten into a plane-wave equation [3]:

$$\vec{k} \times (\vec{k} \times \vec{E}) + \omega^2 \mu \varepsilon \vec{E} = 0 \Leftrightarrow \bar{M} \vec{E} = 0. \quad (2.9)$$

The relationship between the wavevector \vec{k} and the frequency of the wave ω is then given via the solution of the equation:

$$\det \bar{M} = 0. \quad (2.10)$$

Solving this expression leads to the wavevectors \vec{k} . Note that each eigenstate of the electric field can be subject to its specific wavevector. [3]

2.1.3. Dipole radiation

The description of light emission from excitonic transitions on a molecular frame is achieved by using a classical dipole model [15, 16, 18]. Therein the process of emission can be described as an oscillating dipole, characterized by the transition dipole moment (TDM) of the exciton decay [19]. Using Maxwell's equations and the scalar Hertz potentials, an ansatz chosen by Penninck et al. [16], leads to the following expression for the ordinary (*o*) and extraordinary (*e*) electric field \vec{E} of two orthogonal dipoles, one parallel to the optical axis ($\vec{p}_{c\parallel}$) and one perpendicular ($\vec{c}_{o\perp}$).

$$\vec{E}_o(k_x, k_y, \vec{p}_{c\perp}) = \frac{-i}{8\pi^2} \left[\vec{k}_{o\perp} \times \frac{\mu\omega^2}{|\vec{k}_{o\perp}|^2} \frac{\vec{c} \cdot (\vec{k}_{o\perp} \times \vec{p}_{c\perp})}{k_{z,o}} \vec{c} \right] \quad (2.11)$$

$$\vec{E}_e(k_x, k_y, \vec{p}_{c\perp}) = \frac{-i}{8\pi^2} \left[-\frac{|\vec{k}_{o\parallel}|^2 (\vec{k}_{o\perp} \cdot \vec{p}_{c\perp})}{|\vec{k}_{o\perp}|^2 \varepsilon_{o\perp}} \right] \frac{\vec{k}_{o\perp} - \frac{|\vec{k}_{o\perp}|^2 \varepsilon_{o\perp}}{|\vec{k}_{o\parallel}|^2 \varepsilon_{o\parallel}} \vec{k}_{o\parallel}}{\frac{\varepsilon_{o\perp} + \Delta\varepsilon c_z^2}{\varepsilon_{o\parallel}} \left(k_{z,e} + \frac{\Delta\varepsilon c_t c_z \kappa}{\varepsilon_{o\perp} + \Delta\varepsilon c_z^2} \right)} \quad (2.12)$$

$$\vec{E}_e(k_x, k_y, \vec{p}_{c\parallel}) = \frac{-i}{8\pi^2} \left[\frac{|\vec{k}_{o\parallel}| |\vec{p}_{c\parallel}|}{\varepsilon_{o\parallel}} \right] \frac{\vec{k}_{o\perp} - \frac{|\vec{k}_{o\perp}|^2 \varepsilon_{o\perp}}{|\vec{k}_{o\parallel}|^2 \varepsilon_{o\parallel}} \vec{k}_{o\parallel}}{\frac{\varepsilon_{o\perp} + \Delta\varepsilon c_z^2}{\varepsilon_{o\parallel}} \left(k_{z,e} + \frac{\Delta\varepsilon c_t c_z \kappa}{\varepsilon_{o\perp} + \Delta\varepsilon c_z^2} \right)} \quad (2.13)$$

Therein $\vec{k}_{o\parallel}$ and $\vec{k}_{o\perp}$ denote the components of the wavevector parallel and perpendicular to the optical axis \vec{c} of the system. The same yields for the dielectric constant $\varepsilon_{o\parallel}$ and $\varepsilon_{o\perp}$, while $\Delta\varepsilon$ denotes the difference between the two components of the dielectric constant. [16] The optical axis is assumed to be perpendicular to the film surface throughout this work. While other orientations of this axis could generally be possible, they have never been observed for amorphous or polycrystalline organic semiconductors. It is important to note that these expressions describe the electric field created by the dipole within the k -space. Although real-space expressions are of minor interest within this thesis, they could easily be calculated from Fourier transformations.

2.2. Thin film microcavities

For many applications, the films of organic optoelectronic devices are within a range of several nm [1, 9, 12] allowing for thin film interference effects to occur [3]. Those effects not only change the emission properties of the thin film systems away from Lambertian radiation patterns but also alter some intrinsic properties such as device efficiency as well as radiative lifetimes due to the Purcell effect [1, 16, 20]. For a microcavity to affect the system, the film thickness needs to be within the coherence limit for the light passing the system [3]. Given a visible wavelength between 400 and 800 nm the effects of a microcavity can occur up to a few microns film thickness [1].

2.2.1. Refraction at planar interfaces

To understand the behavior of thin film microcavities, the individual refractions at the planar interface need to be described. Plane waves at an interface are subject to boundary conditions given by Maxwell's equations. Generally, the following equations can be established for electromagnetic waves at planar interfaces and their components parallel and perpendicular to the interface [3]:

$$\vec{D}_{2\perp} - \vec{D}_{1\perp} = \sigma \quad (2.14)$$

$$\vec{H}_{2\parallel} - \vec{H}_{1\parallel} = \vec{K} \quad (2.15)$$

$$\vec{E}_{2\parallel} = \vec{E}_{1\parallel} \quad (2.16)$$

$$\vec{B}_{2\perp} = \vec{B}_{1\perp} \quad (2.17)$$

where \vec{K} denotes the interfacial current density and σ the interfacial charge density.

From these boundary conditions, the Fresnel coefficients relating the electric field amplitudes can be derived. Due to their complexity for anisotropic media, the individual calculations are not given in this work but are used according to literature [3, 16].

2.2.2. Stacked layered media

Stacking multiple thin films onto each other can impact the properties of the resultant microcavity. The introduction of multiple interfaces, as well as different materials of varying optical properties, will enable a wide variety of interactions [3]. Most notably, multiple reflections will occur between the interfaces. The

electrodynamic description of those systems is achieved by applying a matrix transfer formalism. Therein the propagation of the electromagnetic field at an interface or throughout a medium is described by two different matrices.

Yeh gives one approach of calculating the resultant properties of the microcavity via the direct multiplication of matrices [3]. However, as these considerations are subject to computational evaluations, the precision of floating point numbers has to be taken into account, eventually leading to mistakes in the matrix transfer approach. Thus a different ansatz can be made using the scattering matrix approach [21]. Both methods yield the same result. Within this work, the scattering matrix approach was taken for all calculations of thin film microcavities.

2.3. Classical dipoles within one-dimensional microcavities

In the presence of a thin film microcavity, the electric field of a radiative dipole is modulated by interference [1]. This effect can be understood via the reflections of the electric field at the interfaces in the microcavity, generating constructive and destructive interference. Hence the effective electric field of the dipole can be calculated from the properties of the microcavity, leading to the following expression [15].

$$\vec{E}_{\vec{p},\text{eff}} = (1 - R_+ R_-)^{-1} \vec{E}_{\vec{p},\text{dipol},\infty} \quad (2.18)$$

Therein the electric field of the dipole in an infinitely extended medium $\vec{E}_{\vec{p},\infty}$ is modulated by the reflectivity of both half-cavities on top (R_+) and below (R_-). Note that R_- and R_+ are generally matrices taking both eigenstates of the electric field as well as their coupling due to birefringence into account [16].

By considering the electric field in both directions, the electromagnetic radiation leaving the microcavity structure can be calculated. Therein, the transmitted field through one half-cavity consists of the effective field emitted in the direction of outcoupling $\vec{E}_{\vec{p},\text{eff}}$ as well as the contribution from the opposite side $\vec{E}_{\vec{p},\text{eff,opposite}}$ via reflection (R_{opposite}) and the transmittivity of the microcavity T [16, 18].

$$\vec{E}_{\text{out}} = T \left(\vec{E}_{\vec{p},\text{eff}} + \vec{E}_{\vec{p},\text{eff,opposite}} \cdot R_{\text{opposite}} \right) \quad (2.19)$$

2.3.1. Purcell effect

As discussed in the previous paragraph, the electric field of an emissive dipole with the presence of a microcavity is altered. This effect not only changes the electric field of the dipole but further manipulates the emissive properties due to

a difference in the available density of states for the emitted photons. Treating the dipole as an excited state allows for the application of Fermi's golden rule:

$$k_{i \rightarrow f} = \frac{2\pi}{\hbar} \text{DOS}(E_f) |\langle f|V|i \rangle|^2 \quad (2.20)$$

stating that the probability for a radiative decay is proportional to the density of states (DOS) for a given energy E_f in the final state f as well as the expression $\langle f|V|i \rangle$ describing the initial state i , the final state f and the operator V [22, 23]. Consequently, increasing this DOS allows for a faster decay, hence a lower radiative lifetime of the excited state [20]. This behavior is described by the Purcell effect and can be expressed via the Purcell factor F . The derived quantity relates the available DOS in the microcavity DOS_{cav} to the total DOS of the dipole in a infinitely extended medium (DOS_{∞}).

$$F = \frac{\int \text{DOS}_{\text{cav}}}{\int \text{DOS}_{\infty}} = \frac{k_{\text{cav}}}{k_{\infty}} \quad (2.21)$$

It should be pointed out that the Purcell factor also relates to the radiative rate k of the dipole. An exemplary calculation for a dipole in vacuum and in two different distances (260 nm) and (400 nm) is shown in fig 2.2 [1].

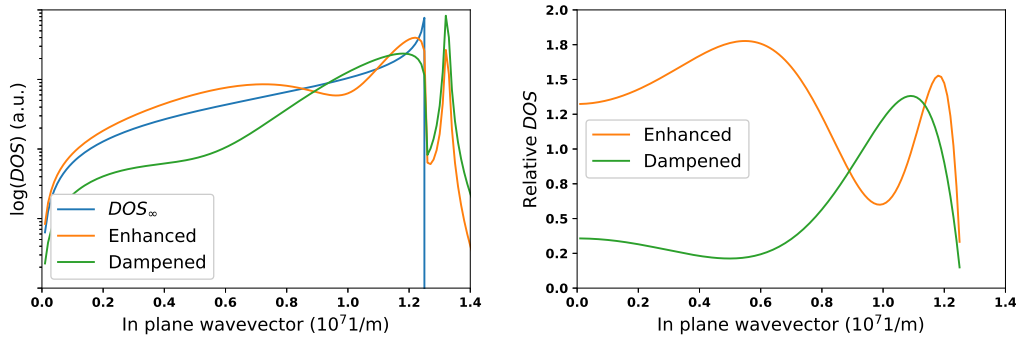


Figure 2.2.: DOS for a dipole in vacuum and in a defined distance to a silver mirror on one side of the dipole (left) and relative change of the DOS when enhanced or damped (right). At 260 nm distance the DOS of the dipole is hampered by the microcavity whereas at 400 nm the DOS increases. Consequently the radiative rate of the dipole is increased for 400 nm and decreased for 260 nm. Note that in close contact to the silver mirror, DOS contributions above an in-plane wavevector of 1.310^7 m^{-1} are induced by near field coupling [1].

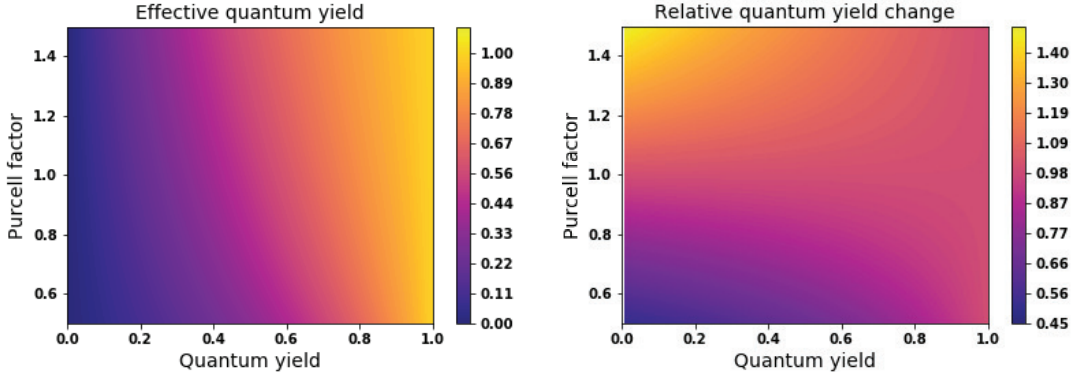


Figure 2.3.: Effective quantum yield of a system for a given intrinsic yield in the presence of a Purcell factor (left). Relative change compared to the intrinsic yield (right).

Interestingly an increase in the radiative decay rate can reduce the fraction of nonradiative decay, allowing to benefit from the Purcell effect [1]. This change of the ratio between the decay rates can be expressed in the quantum yield q , relating the radiative decay rate k_r to the total decay rate as a sum of radiative and nonradiative (k_{nr}) processes [1].

$$q = \frac{k_{\text{eff},r}}{k_{\text{eff},r} + k_{nr}} = \frac{F \cdot k_r}{F \cdot k_r + k_{nr}} \quad (2.22)$$

Further, this effect only shows a pronounced benefit for emissive systems with a contribution from nonradiative processes, having a quantum yield lower than unity. Fig. 2.3 shows the effects of the Purcell factor on a system with a given intrinsic quantum yield.

Therein the effective quantum yield is increased as the Purcell factor rises. However, the effect diminishes for high intrinsic quantum yields. Further, the benefit of this effect can reach as high as 50% for low quantum yield systems while a Purcell factor lower than unity can also hamper the emission and decrease the effective quantum yield accordingly.

2.3.2. Mode coupling

While an increase of the overall DOS can increase the radiative rate of an emissive system, changing this property can further affect the probability of photons being emitted into different modes. For an optoelectronic application, only modes coupled out of the system are contributing to the efficiency. Hence, precise tuning of a microcavity can enhance this fraction while suppressing undesired components [1].

Fig. 2.4 depicts the different modes available within a thin film microcavity. Therein the desired mode is direct outcoupling out of the system. However, the electromagnetic waves can be trapped due to total internal reflection at the various interfaces. It is helpful to distinguish between light trapped inside the incoherent substrate and the waveguided modes within the microcavities. Further interface modes such as surface plasmon polaritons can also hamper the outcoupling efficiency [1].

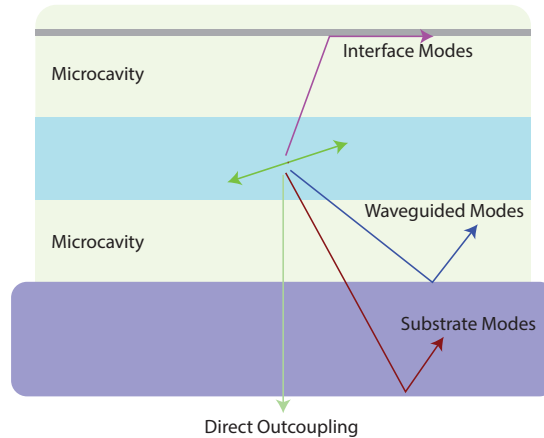


Figure 2.4.: Depiction of different modes within a thin film microcavity. Light leaving the system can be attributed to direct outcoupling, whereas the fraction undergoing total internal reflection at the substrate-air interface is trapped in substrate modes. Further modes include the waveguiding of electromagnetic waves in between the microcavities as well as interface modes inside a microcavity. The latter usually originate from the excitation of surface plasmon polaritons.

In order to attribute the density of states to the different modes, the respective in-plane wavevector can be taken into account. Using this approach, a wave can only be coupled into a certain mode if the in-plane wavevector k_{\parallel} is lower than the maximum wavevector of this mode as higher wavevectors would yield no

2. Dipole radiation in thin film microcavities

energy transfer due to the poynting vector being purely imaginary [1, 7]. Thus the following statements can be made for the coupling into different modes:

$$\text{Direct outcoupling: } k_{\parallel} \leq \frac{2\pi}{\lambda} \quad (2.23)$$

$$\text{Substrate mode: } \frac{2\pi}{\lambda} \leq k_{\parallel} \leq \frac{2\pi}{\lambda} n_{\text{substrate}} \quad (2.24)$$

$$\text{Waveguided mode: } \frac{2\pi}{\lambda} n_{\text{substrate}} \leq k_{\parallel} \leq \frac{2\pi}{\lambda} n_{\text{eff,microcavity}} \quad (2.25)$$

$$\text{Near field coupling: } \frac{2\pi}{\lambda} n_{\text{eff,microcavity}} \leq k_{\parallel} \quad (2.26)$$

$$(2.27)$$

where λ denotes the wavelength of emission in air, $n_{\text{substrate}}$ the refractive index of the substrate. Waveguided modes are taken into account using the effective refractive index of the microcavity $n_{\text{eff,microcavity}}$. This effective optical constant can be calculated from the individual refractive indices of the waveguiding films and their thickness within the microcavity.

Fig. 2.5 shows the application of this technique to a common organic light emitting diode (OLED) microcavity. This specific device shows direct outcoupling as well as substrate modes. Waveguided modes are almost entirely suppressed but near field coupling into a surface plasmon mode occurs for high in-plane wavevectors.

Note that this method of the determination of mode coupling is an approximation, assuming that states coupling into the lowest possible mode are not trapped in higher modes. E.g., light trapped in lower wavevectors surface plasmon or waveguided modes would not be attributed correctly using this model.

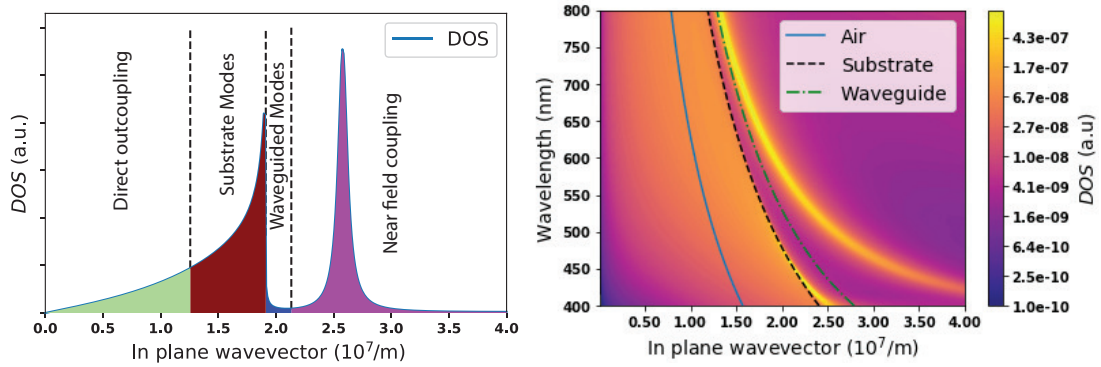


Figure 2.5.: Exemplary mode distribution for a common OLED stack. The analysis for 500 nm (left) reveals almost no contribution to waveguided modes, whereas near field coupling into a surface plasmon mode occurs. Within the whole wavelength range (right) the wavelength dependence of the mode coupling borders becomes visible.

3. Photophysical properties of excitonic light emission

Light emission is generally caused by the radiative decay of an electron-hole pair [2]. In inorganic semiconducting materials the binding energy of the exciton is relatively low. Therefore the resultant excited state is called a "Mott-Wannier" exciton, characterized by the large distance of the electron to the hole as depicted in fig. 3.1. In contrast to this, organic semiconducting molecules exhibit much smaller dielectric constants, increasing the binding energy. Therefore these "Frenkel" excitons usually reside within one molecule, at which point charge transfer states give the exception. Therein the two charge carriers are located on adjacent molecules forming a bound state [2].

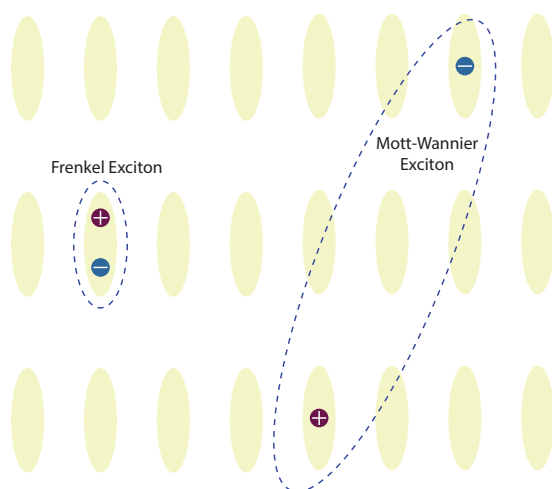


Figure 3.1.: Depiction of Frenkel- and Mott-Wannier excitons. In the former, electron and hole reside in close contact with each other, while the latter extends to a much larger radius between the two charge carriers. Picture adapted from [2].

After excitation the quasi-particle can either transfer its energy through the medium in a diffusive motion or stays located on a molecule, depending on the

energy landscape of the material. Finally, it will decay radiatively or nonradiatively into the ground state [2]. All of those processes will be discussed within the sections of this chapter.

3.1. Generation of excitons in thin films

Two different pathways enable the creation of an exciton. Upon the absorption of a photon having sufficient energy, an electron can be excited into the lowest unoccupied state (LUMO), leaving a hole in the highest occupied state (HOMO) [2].

As a second possibility, an exciton can be formed from an electron and a hole present in the material. Close contact of the two charge carriers will bind them into the excitonic state. However, due to the spin-statistics, the two charge carriers will either form a singlet or a triplet state in which the total spin is one [2].

Despite both processes resulting in an exciton, there are several notable differences. First, the multiplicity of the state being singlet or triplet is an essential factor when investigating exciton properties of organic and inorganic semiconductors. Excitation via photons almost always results in the formation of a singlet state while electrical excitation also yields triplets. Thus from purely optical experiments, no information about the triplets can be obtained, if no intersystem crossing from the singlet to the triplet state occurs. Further, the optical excitation of an exciton does not require charge carriers to be transferred to the emissive site.

Generally higher states above the S_1 and T_1 levels can be excited on an emissive species. However, Kasha's rule leads to rapid conversion to the lowest state for a given multiplicity [24]. It should be pointed out that the energetic landscape of organic semiconductors is further influenced by vibronic substates leading to broad emission and absorption spectra of the thin films [2].

3.2. Radiative decay of excitonic states

The radiative decay of an exciton results in the emission of a photon, whereas the exciton could also decay nonradiatively through thermal dissipation. In the case of optoelectronic applications, radiative decay is desired where the wavelength of the emitted photon should be within the visible range. Note that other applications than displays or lighting could also aim for near-infrared wavelengths [25].

In a simplified picture including only the singlet and triplet state, as depicted

in fig. 3.2, several emission mechanisms are present for organic semiconductors. These mechanisms will be discussed in the following paragraphs. Note that a vast amount of other processes can occur within organic and hybrid thin films, whose discussion would exceed the boundaries of this brief introduction [2].

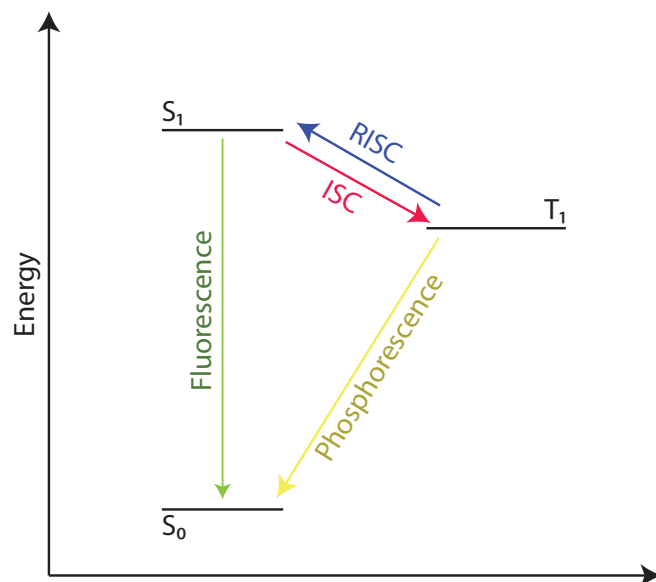


Figure 3.2.: Depiction of fluorescent and phosphorescent decay of excitons from the singlet and triplet state respectively. While the two multiplicities are generally separated, RISC and ISC allow for transfer between the states.

The first organic thin film light emitting devices were only emitting from the singlet state [9]. This most basic process of photon emission is fluorescence - the radiative decay of an exciton from a singlet state back into the ground state. Therein, the electron in the LUMO level decays back into the HOMO. Most notably this process can only occur for singlet states due to the conservation of spin. Hence systems utilizing this kind of emitting species can not harvest triplets which would limit their performance in optoelectronic devices to 25%. Note that within photoluminescence applications the quantum yield can still reach as high as 100%.

Contrary to fluorescence, phosphorescence describes the radiative decay of a triplet exciton. While this process is generally forbidden in simple aromatic hydrocarbons, strong spin-orbit coupling such as given by heavy atoms like Iridium or Platinum can enable this decay pathway. Note that spin-orbit coupling also allows for a rapid intersystem crossing (ISC) of singlets into the triplet states.

Hence excitons on a phosphorescent emitting species are generally converted into triplets within a timeframe shorter than the fluorescent and phosphorescent decay times. Due to this effect, the emission in phosphorescent materials originates only from the triplet state [13, 26].

Another process enabling the use of triplet excitons is thermally activated delayed fluorescence (TADF). While the radiative emission process on systems exhibiting this mechanism is fluorescence, the molecular structure of such a molecule allows for reverse intersystem crossing (RISC). This process enables the conversion of triplet into singlet states via thermal activation. One crucial requirement for this process is the spatial separation of the HOMO and the LUMO state, reducing the overlap of their respective wavefunctions. This feature lowers the energy gap between the singlet and the triplet state and thus enables the RISC process. However, as a drawback, this also reduces the oscillator strength and thereby the decay rate of the exciton. Further, the conversion rates between singlet and triplet states are slower than the fluorescence decay rate leading to a slow decay rate limited by the reverse intersystem crossing rates. Note that several other processes are involved in the TADF mechanism, which are not discussed within this brief overview [14, 27].

3.3. Diffusion of excited states in thin films

After creation, an exciton can transfer its energy to nearby sites via two different mechanisms. One possible process is the Förster resonance energy transfer (FRET) [28]. Therein nonradiative dipole-dipole coupling exchanges the energy from an exciton to a different molecule. The first entity transfers back to the ground state whereas the receiving molecule is altered to the first excited state, as depicted in fig. 3.3. The Förster radius R_F determines the rate of this process k_{FRET} . Further, the intrinsic lifetime of the excited state τ and the separation between the two exchanging sites r affect this process.

$$k_{\text{FRET}} = \frac{1}{\tau} \left(\frac{R_F}{r} \right)^6 \quad (3.1)$$

The Förster radius as used in the formula is defined as the distance where the transfer efficiency has dropped to 50%. Note that this radius is proportional to the overlap between the emission spectrum of the donating molecule and the excitation spectrum of the accepting entity. Further, the orientation between the dipoles is crucial for an efficient FRET process [28].

The second process of energy transfer is given by the Dexter process, which is shown in fig. 3.4 [29]. Therein electrons are transferred between an excited

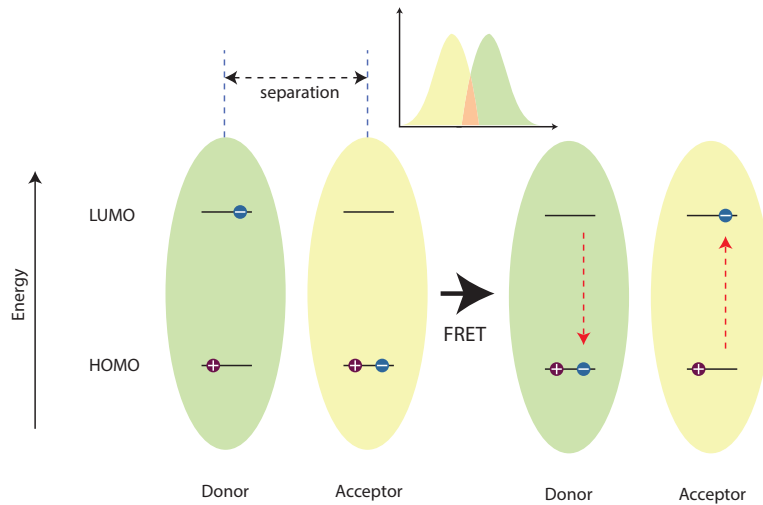


Figure 3.3.: Depiction of the FRET process. Induced by dipole interactions, the electron of the donor is transferred back to the ground state while the acceptor molecule is excited. This process relies on both the separation between the two entities as well as their spectral overlap in the emission of the donor and the excitation of the acceptor [28].

molecule and an adjacent molecule in the ground state. As this process relies on the exchange of electrons, an overlap between the respective wavefunctions is required. This dependency leads to an exponential relationship to the distance between the transferring sites [13]. Hence, lower separation distances are required for an efficient energy transfer compared to the FRET process.

In summary, two different energy transfer mechanisms exist for the diffusion of an excited state within a thin film. While the transfer of the excited state via FRET directly exchanges the energy of the excitation, Dexter transfer relies on the transfer of electrons between the involved sites.

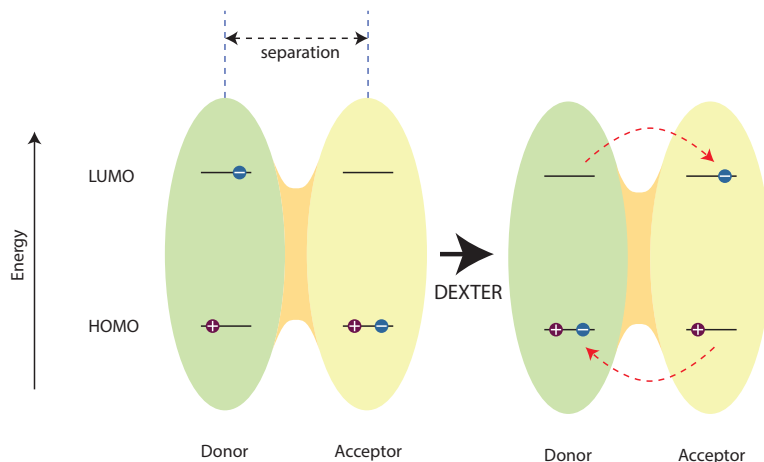


Figure 3.4.: Illustration of the dexter energy transfer between two molecules. The electron from the donor is transferred via intermolecular coupling to the LUMO of the acceptor, whereas an electron in the HOMO of the acceptor is transferred to the ground state of the donor [29].

3.4. Decay rates of excitons in fluorescent and phosphorescent systems

Various factors determine the excited state lifetime of an excited molecule. Each excited state has various possible events altering the state and eventually returning to the ground state. For a simple fluorescent molecule, these events would be radiative and non-radiative decay of the first excited state. Note that higher excited states rapidly decay to the lowest excited state due to Kasha's rule and thus the radiative decay only occurs from this state [24]. Further, the radiative decay from the triplet state is forbidden in a fluorescent molecule, thus only non-radiative processes can occur. The observable exciton lifetime τ_F can thus be written as [2]:

$$\tau_F = \frac{1}{k_F} = \frac{1}{k_{S,R} + k_{S,NR}}. \quad (3.2)$$

If the excited state is embedded within a microcavity, it is important to take the Purcell effect for radiative decay into account. For the sake of simplification, this will not be written explicitly within the following paragraphs. Interestingly the decay rates of the triplet state cannot be observed for fluorescent molecules due to the absence of any interaction between the states [1]. As a rule of thumb, fluorescent lifetimes usually are within a few nanoseconds.

The same approach is valid for phosphorescent emitter such as organometallic

Ir-complexes [13]. In this species, the excited singlet state rapidly transfers to the triplet state due to spin-orbit coupling with the heavy metal atom. This intersystem crossing rate k_{ISC} is in the range of 10^{12} s^{-1} and thus exceeds the fluorescent decay of the exciton. Hence the observable lifetime τ_{P} is analogous to the fluorescent case:

$$\tau_{\text{P}} = \frac{1}{k_{\text{P}}} = \frac{1}{k_{\text{T,R}} + k_{\text{T,NR}}}. \quad (3.3)$$

Note that in this scenario, the radiative and nonradiative rates from the triplet state determine the excited state lifetime. Due to the required spin-orbit coupling for a radiative transfer from the excited triplet state back into the ground state, the observable excitonic lifetimes for phosphorescent emitters usually are within the microsecond range [13].

In excitonic systems in which coupling between the singlet and triplet state occurs, these effects need to be taken into account. The most prominent example for this effect are TADF molecules, but other processes such as triplet-triplet annihilation could also allow for interactions between the singlet and triplet state. In this case, the rates cannot be given intuitively but have to be determined from solving the rate equations [14]. An example of this procedure is given in section 7.1.3.

4. Anisotropy in thin film media

Anisotropic behavior of thin films is a common phenomenon induced by the low thickness and preparation conditions of the layers. While many phenomena, such as magnetism and conductivity, can be affected by anisotropic properties of thin films, this section will focus on the optical effects. Further, the described effects will concentrate on anisotropy perpendicular to the film while considering in-plane properties as isotropic. It should be pointed out that the following quantifications of the optical anisotropy rely on the preferential alignment of the TDM with respect to the surface of a thin film.

4.1. Birefringence

One of the notable effects of preferential alignment in organic thin films is optical birefringence. Therein the polarizability of the media is anisotropic with respect to an optical axis. Due to the amorphous nature of organic materials, the state-of-the-art method for the determination of birefringent properties is variable angle spectroscopic ellipsometry (VASE). Many organic materials were found to be uniaxial anisotropic with an optical axis perpendicular to the surface. These properties arise from the glassy or polycrystalline morphology of the thin films. Within this description, the materials are characterized using ordinary and extraordinary optical constants. Therein, the former describes the polarizability for electric fields perpendicular to the optical axis and vice versa. Hence, the extraordinary parameters need to be taken into account if the electric field of an electromagnetic wave has a component parallel to the optical axis [3, 30–33].

To express the degree of molecular orientation within birefringent thin films, the order parameter S can be calculated via:

$$S = \frac{3 \langle \cos^2 \theta \rangle - 1}{2} = \frac{k_e^{\max} - k_o^{\max}}{k_e^{\max} + 2k_o^{\max}}. \quad (4.1)$$

Therein the order parameter S is defined via $\langle \cos^2 \theta \rangle$, the quadratic average of the absorbing TDM angle with respect to the substrate. This parameter can be calculated from the maximum values of the ordinary k_o^{\max} and extraordinary

k_e^{\max} absorption as measured via VASE [33].

It should be pointed out that the birefringence of thin films in OLEDs is an essential factor for device performance. Therein the optimization of the microcavities concerning the mode coupling in the device leads to increased device performance [34, 35].

4.2. Anisotropy of emissive transitions

The focus of this work lies in the anisotropic properties of the emissive transitions. Hence, the orientation of the TDMs responsible for the emission of visible photons within a thin film device. Contrary to birefringence, this effect does not necessarily alter the optical properties of the film itself but changes the observable radiation pattern of the system. This emission pattern of dipoles within a one-dimensional microcavity depends on the positioning of the dipole with respect to the cavity surfaces as well as the microcavities itself.

Dependence of the radiation pattern on the TDM orientation

For the theoretical description of radiative emission in a thin film, the individual contributions of an ensemble of TDMs are calculated. Therein it is important to note that the power dissipation of a single TDM can be separated into contributions from the projections of the dipole moment parallel and perpendicular to the film surface:

$$P_{\text{total}}(\vec{p}, \phi, \theta, \lambda) = \sum_i P(\vec{p}_i, \phi, \theta, \lambda) = \sum_i \left(P(\vec{p}_{\parallel, i}, \phi, \theta, \lambda) + P(p_{\perp, i}, \phi, \theta, \lambda) \right). \quad (4.2)$$

Within this expression, \vec{p}_i denotes the i -th TDM within the ensemble of dipoles and \vec{p}_{\parallel} and \vec{p}_{\perp} describe the components of that TDM parallel or perpendicular to the surface of the thin film. This radiation pattern is dependant on the polar- and azimuth angles ϕ and θ , as well as the emission wavelength λ . Note that further dependencies such as refractive index and film thickness are not explicitly written in those equations.

For further refinement of this expression, the power dissipation from TDM components parallel to the film surface can be separated into the contributions of s- (P_s) and p-polarized (P_p) electromagnetic waves. Note that the TDM perpendicular to the film surface only emits p-polarized light as the electric field only has a component parallel to the incident plane.

$$P_{\text{total}}(\vec{p}, \phi, \theta, \lambda) = \sum_i \left(P_s(p_{\parallel, i}, \phi, \theta, \lambda) + P_p(p_{\parallel, i}, \phi, \theta, \lambda) + P_p(p_{\perp, i}, \phi, \theta, \lambda) \right) \quad (4.3)$$

The total radiated power of one of the three TDM components is directly proportional to the square of that component. Hence, the individual emission terms can be separated as follows:

$$\begin{aligned}
 P_{\text{total}}(\vec{p}, \phi, \theta, \lambda) &= \sum_i \left(O_{\text{p},\parallel}(\phi, \theta, \lambda) \cdot p_{\parallel}^2 + O_{\text{s},\parallel}(\phi, \theta, \lambda) \cdot p_{\parallel}^2 + O_{\text{p},\perp}(\phi, \theta, \lambda) \cdot p_{\perp}^2 \right) \\
 &:= X + Y + Z.
 \end{aligned} \tag{4.4}$$

Therein $O_{\text{s/p},\parallel/\perp}$ denotes the proportionality factor containing the dependencies on the angles as well as the wavelength. Note that the individual terms within this expression can also be denoted as X , Y , and Z . Fig 4.1 shows exemplary radiation patterns for these terms. Therein the characteristic radiation patterns of a thin film into a glass substrate are shown. It should be pointed out that each component shows distinct features enabling the characterization of the TDMs within a system.

For the quantification of the TDM orientation within an experiment, the s- and p-polarized (P_{s} and P_{p}) radiation patterns are observed individually. Note that the determination would be possible without the introduction of a polarizer but the separation of the two eigenstates leads to more precise results. The expression for the two polarization states writes as follows:

$$\begin{aligned}
 P_{\text{s}}(\vec{p}, \phi, \theta, \lambda) &= \sum_i (O_{\text{s},\parallel}(\phi, \theta, \lambda) \cdot (p_{\parallel})^2) = \sum_i (Y) \\
 P_{\text{p}}(\vec{p}, \phi, \theta, \lambda) &= \sum_i (O_{\text{p},\parallel}(\phi, \theta, \lambda) \cdot (p_{\parallel})^2 + O_{\text{p},\perp}(\phi, \theta, \lambda) \cdot p_{\perp}^2) = \sum_i (X + Z).
 \end{aligned}$$

These equations reveal the s-polarized emission only depending on the power dissipation of TDMs parallel to the surface. Contrary to this, the p-polarized radiation pattern is a superposition of contributions from the horizontal and vertical TDMs. Hence the p-polarized emission enables the determination of a relation between dipoles parallel and perpendicular to the film surface.

4. Anisotropy in thin film media

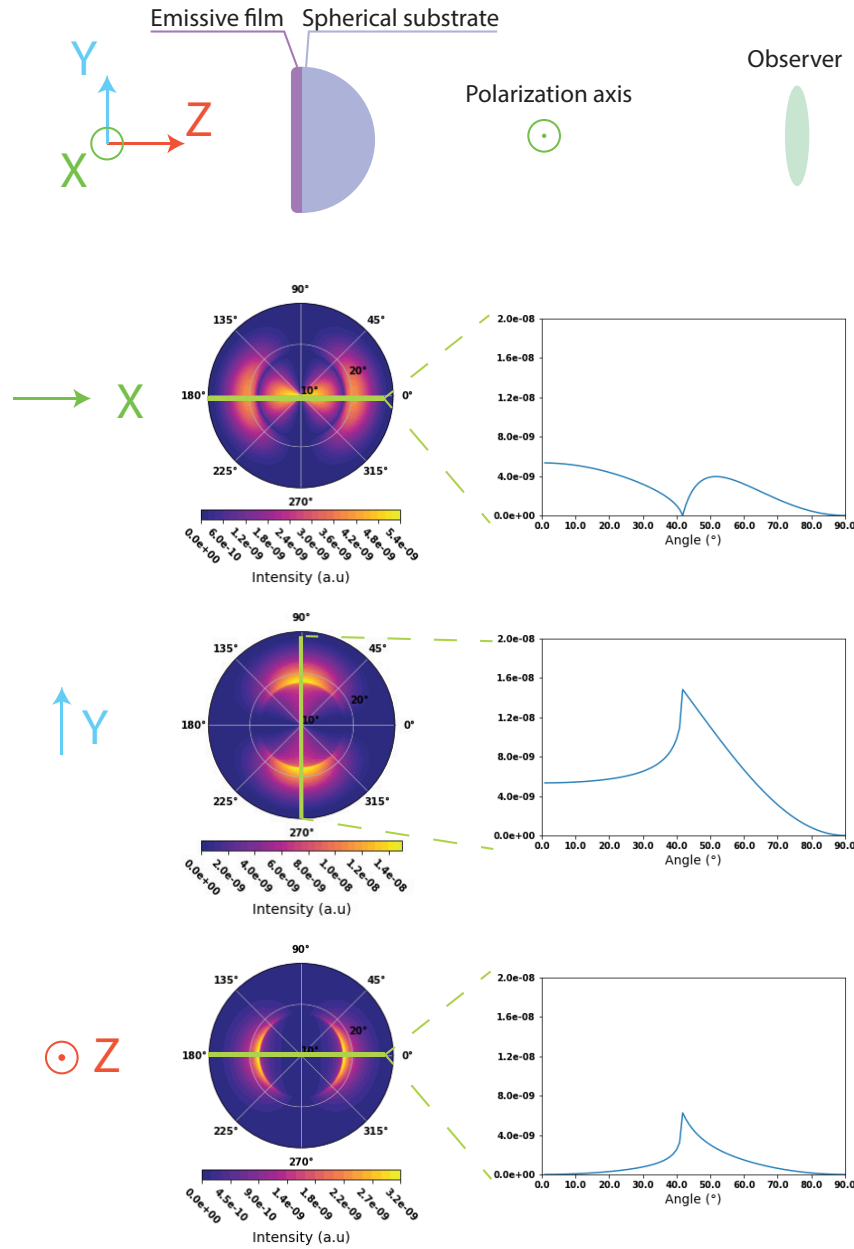


Figure 4.1.: Emissions of dipoles along three orthogonal axes (X, Y, Z) when observed with a polarizer along the indicated axis. The energy dissipation spectra originate from an oscillating dipole on a planar glass surface and illustrate the emission into the glass substrate. The heatmaps indicate emission of a dipole within the half sphere for the three orthogonal dipoles. Further, the radiation pattern along a single line within is depicted on the right side.

Quantifying the orientation of emissive transitions

The previously described factors X , Y , and Z represent the energy emitted by their respective TDM components. This allows for the quantification of the TDM orientation via the orientation parameter Θ . This quantity describes the fraction of energy emitted from TDMs perpendicular to the film surface. Hence, Θ can be calculated via the ratio of emission from perpendicular TDMs, given by Z and the total power dissipation of the system [36, 37].

$$\Theta = \frac{P(p_{\perp})}{P(p_{\parallel}) + P(p_{\perp})} = \frac{Z}{X + Y + Z} \quad (4.5)$$

Further, Θ relates to the TDM components as follows:

$$\Theta = \frac{\sum_i (p_{i,z})^2}{\sum_i (\vec{p}_i)^2} \quad (4.6)$$

due to the power emitted by a dipole being proportional to the square of the dipole moment \vec{p} . Within the orientation parameter Θ , an isotropic system consisting of equally distributed TDMs along the x-, y- and z-plane is given by $\Theta = 0.33$. Values below the isotropic border can be concluded as preferentially horizontal, where $\Theta = 0.0$ is an alignment parallel to the film surface. Θ values above 0.33 express a preferentially vertical alignment of the emissive dipoles limited by each TDM being perpendicular to the film surface yielding $\Theta = 1.0$ [36, 37].

Unraveling the angle of emissive TDMs in a thin film

For further simplification all TDMs are assumed to be oriented with the same angle φ with respect to the surface, whereas they are equally distributed concerning the polar angle. In this case the following expression can be found, in which φ describes the angle of \vec{p} with respect to the film surface:

$$\begin{aligned} P_{\text{total}}(\vec{p}, \phi, \theta, \lambda) &= \sum_i (\quad \quad \quad) \quad (4.7) \\ &= \sum_i (O_{p,\parallel}(\phi, \theta, \lambda) \cdot (|p| \cos(\varphi))^2 + \\ &\quad O_{s,\parallel}(\phi, \theta, \lambda) \cdot (|p| \cos(\varphi))^2 + \\ &\quad O_{p,\perp}(\phi, \theta, \lambda) \cdot |p| \sin(\varphi)^2) \\ &= \sum_i (X + Y + Z) \end{aligned}$$

Analogous to the orientation parameter Θ , this can be described via the components of the emissive TDM \vec{p} .

$$\Theta = \frac{p_z^2}{\vec{p}_i^2} = \frac{(|\vec{p}| \sin(\varphi))^2}{|\vec{p}|^2} \quad (4.8)$$

Note that due to the system being described by a single TDM, the angle φ can be determined:

$$\varphi = \arcsin(\sqrt{\Theta}) \quad (4.9)$$

It is worth noting that this procedure will yield an average angle $\langle \varphi \rangle$ of the TDM if the system is amorphous. However, if the system consists only one angle φ of the TDM with respect to the film surface, this expression can be used to reveal this quantity [37, 38].

Quantification of the radiation pattern of a thin film

For the determination of the effect of preferential alignment on the performance of thin film devices, another quantity is crucial. Given by the electric field of an emissive dipole, its radiation pattern not only depends on the orientation of the TDM but also on the refractive index n of the medium surrounding it. Using the approach presented in [38] the following relationship between the quantities can be found:

$$\frac{P(p_{\parallel})}{P(p_{\perp})} \cdot n^4 = \text{const.} \quad (4.10)$$

The full derivation of this relationship can be found in the appendix. Analogous to the orientation parameter Θ , the alignment constant ζ can be defined by describing the radiation pattern in a refractive index of unity:

$$\zeta = \frac{P(p_{\perp}, n = 1.0)}{P(p_{\parallel}, n = 1.0) + P(p_{\perp}, n = 1.0)} \quad (4.11)$$

Further, a relationship between the energy contributed by the individual TDM components can be found. This connection between the orientation parameter Θ and the more generalized alignment constant ζ is [38]:

$$\Theta = \frac{P(p_{\perp}, n)}{P(p_{\parallel}, n) + P(p_{\perp}, n)} = \frac{n^4 \zeta}{1 + \zeta(n^4 - 1)}. \quad (4.12)$$

It is crucial to note that the dependence on the refractive index is approximately to the power of four. Hence the dependence of the orientation parameter Θ relies on a precise determination of the refractive index. In the case of systems with

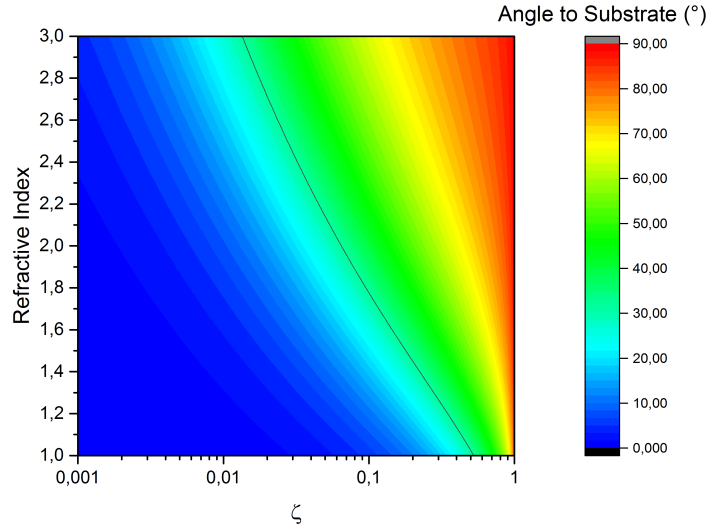


Figure 4.2.: Relationship between the refractive index of an emissive thin film, its alignment constant ζ and the angle of the TDM with respect to the film surface. The black line denotes the angle of an isotropic system $\varphi = 35.4^\circ$. Picture taken from [38].

only a single TDM, ζ can also be related to the angle φ [38].

$$\varphi = \arcsin(\sqrt{\Theta}) = \arcsin\left(\frac{n^4\zeta}{1 + \zeta(n^4 - 1)}\right) \quad (4.13)$$

This relationship, as depicted fig. 4.2, reveals a vast dependence of the radiation pattern not only on the angle of the emissive TDM but also the refractive index of the medium. The dependence of the performance of thin film devices on this quantity will be given in the following section.

5. Light emission from thin film optoelectronic devices

One of the reasons for the investigation of optical processes within thin film microcavities is the application to optoelectronic devices. Although the findings within this chapter are also extendable to other systems, such as lasing and sensor purposes, the following section will be limited to electrically driven light emitting diodes. The following sections are based on earlier work as cited, especially [1]. Note that the calculation of optical processes was performed as described in the computational methods chapter.

Generally, the operation of an organic light emitting device utilizing excitonic emitters can be divided into five different steps as depicted in fig. 5.1 [1, 2].

1. Injection of the charge carriers into the device.
2. Transport of the charge carriers to the emissive layer or multilayer structure.
3. Formation of excitons from the arriving holes and electrons.
4. Radiative decay of the exciton with the emission of a photon.
5. The photon exiting the assembly.

Concerning the external outcoupling efficiency (EQE), each of these processes has a different effect on the total performance of the device. Hence the EQE, defined via the amount of photons leaving the device per injected charge carrier can be written as [39].

$$\eta_{\text{EQE}} = \gamma \cdot \eta_{\text{Exc}} \cdot q_{\text{eff}} \cdot \eta_{\text{out}}. \quad (5.1)$$

Therein the different factors describe the properties of the device as follows:

- γ : This factor represents the charge carrier balance in the emissive structure. As charge transport in thin-film devices is determined by charge carrier injection as well as their mobility in the respective materials. Hence, both these quantities determine this factor. Further, it is important to note that low charge carrier concentrations not necessarily lead to a loss in efficiency since only leakage current through the device is a loss of charge carriers.

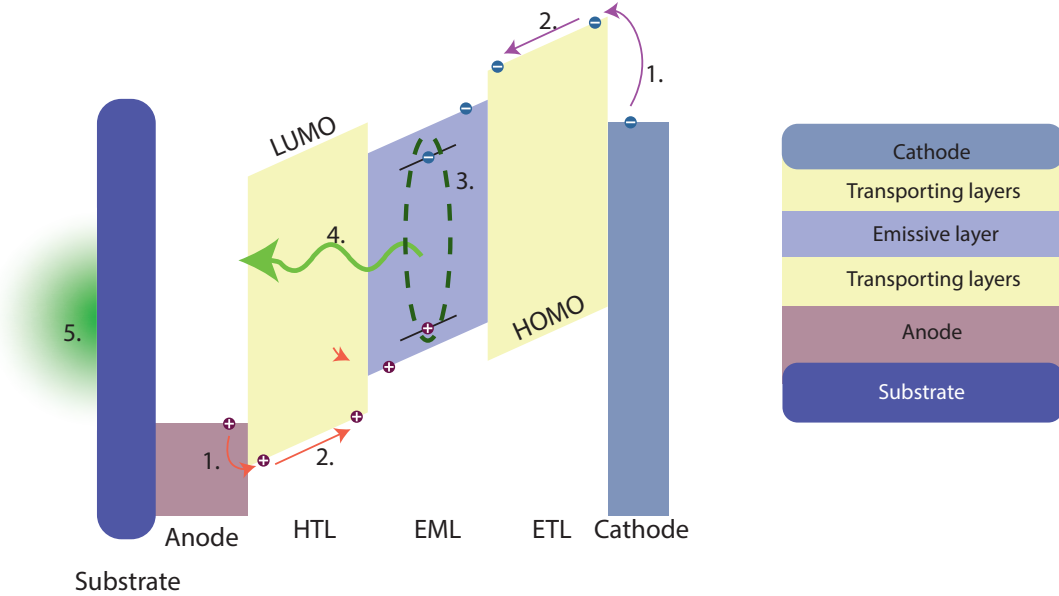


Figure 5.1.: Schematic diagram of the energy levels involved in the electrical operation of an OLED (left) and simplified layer structure (right). In this depiction, the band diagrams are illustrated for a voltage applied in the forward direction. After excitation (1) the holes and electrons are transported on the HTL and ETL respectively (2). Upon reaching the EML, the charge carriers form a bound exciton state (3) which eventually decays via the emission of a photon (4). The microcavity of the device limits the fraction of photons leaving the thin-film device (5). Illustration adapted from [7].

η_{Exc} : The fraction of excitons contributing to light emitting processes. Often this quantity is described as the ratio of singlets because in fluorescent molecules only singlet excitons can decay radiatively. However further advances in organic lighting applications lead to the ability to harvest up to 100% of excitons [13, 14].

q_{eff} : The effective quantum efficiency of the emissive system, describes the relationship between radiatively and non-radiatively decaying excitons. This quantity should carefully be separated from the factor η_{Exc} as it can be affected by the Purcell effect.

η_{out} : The successful decay of an excited state into a visible photon does not necessarily lead to a contribution to light emission out of the devices. Due to the thin film device structure, classical optics limit the fraction of pho-

tons leaving the assembly. As the refractive index of the emissive structure usually is above unity, total internal reflection can occur. Further, the formation of waveguided modes (WGMs) or surface plasmon polaritons (SPPs) also hampers the outcoupling efficiency as described in chapter 2.3.2 [1].

Within the following sections, a brief overview of different considerations in the design of thin film light emitting devices is given. Therein the focus is emphasized on the optical properties such as outcoupling efficiency and the emissive color of the device.

5.1. Electrical operation

The generation of visible photons from the application of an electrical voltage relies on the formation of excitons from electrons and holes within an emissive layer. Hence, it is necessary to inject both types of charge carriers from different contacts into the device and guide them to the emissive film. Further, it is essential to take the work functions of the electrodes as well as the highest occupied molecular orbital and the lowest unoccupied molecular orbital into account.

Fig. 5.1 shows an idealized energy diagram for the electrical operation of an OLED [1, 2]. Therein the charge carriers are injected into the transport layers from the cathode and anode respectively. Efficient charge transport to the emissive layer is achieved via individual transport layers for electrons (ETL) and holes (HTL). To avoid leakage current into the opposite transport layer, functional blocking layers, not shown in the depiction, can be introduced. These films usually are only a few nm thick and enclose the emissive layer (EML) [1, 7]. From an electrical point of view, especially the transport layers require high conductivity, while the thin injection layers and blocking layers should exhibit suitable HOMO and LUMO energies.

To achieve efficient light outcoupling out of the device one of the contacts needs to be transparent for the desired wavelengths, usually visible light. Common choices for the anode are tin-doped indium oxide (ITO) or other transparent and conductive materials [1, 40]. Besides this, thin metal contacts can also exhibit sufficient transparency for lighting applications. The opposite contact has to be reflective to benefit from a tunable microcavity. One example of an electron injecting contact is a thin film of calcium followed by silver or aluminum.

5.2. Optical mode distribution

The coupling of radiative exciton decay into the different optical modes ultimately determines the optical outcoupling efficiency of an OLED. This section will discuss the optical mode distribution of an exemplary OLED stack. These considerations are essential for the performance of light emitting devices. Although the exact optical properties of a thin film device depend on many different factors, the results of this exemplary discussion are representative to many other OLED systems.

Fig. 5.2 shows an exemplary stack for a common green OLED employing the organometallic Ir-complex Ir(ppy)₃ as emissive dye molecule. By varying the thicknesses of the ETL and HTL layers, in this particular case NPB as HTL and Alq₃ as ETL, the mode contributions change. Note that other film thicknesses could be varied as well, but generally the transport layers exhibit the highest conductivities if they are doped and therefore are most suitable for thickness adjustments without affecting the electrical performance.

From an optical point of view, the variation of the two films affects the microcavities surrounding the emissive dipoles in the EML. In the given layout the bottom contact consists of the transparent material ITO. Hence only a small fraction of the light passing through this microcavity is reflected back to the dye molecules. This effect leads to a rather small change in the emissive properties. Contrary to the HTL, the opposite microcavity incorporates a highly reflective material. The high reflectivity of the layer does not allow for transmission out of the device. Thus most of the electromagnetic radiation is reflected to the emissive dipoles and consequently into the bottom microcavity. Due to this behavior, the efficiency of the device is mostly determined by the microcavity between the EML and the reflective contact.

Fig 5.2 shows the coupling of the radiative emission into the different optical modes. Therein only direct outcoupling contributes to the performance of the device, whereas substrate, waveguided and SPP modes can be treated as an energetic loss. When varying the thicknesses of the transport layers, the direct outcoupling reaches values ranging from 25% down to 5% depending on the thicknesses of both films. However the ETL has the most crucial impact on the device performance, reaching maxima at 60 nm and 210 nm. The HTL thickness only shows a minor impact on the efficiency, altering the direct outcoupling between 25% and 18% for a given ETL thickness of 60 nm.

Contrary to direct outcoupling, loss modes show different behavior. Substrate coupling behaves similarly to direct outcoupling. However, the individual maxima are located at different thicknesses. Note that using specialized light extraction techniques can enable the outcoupling of substrate modes, which thereby

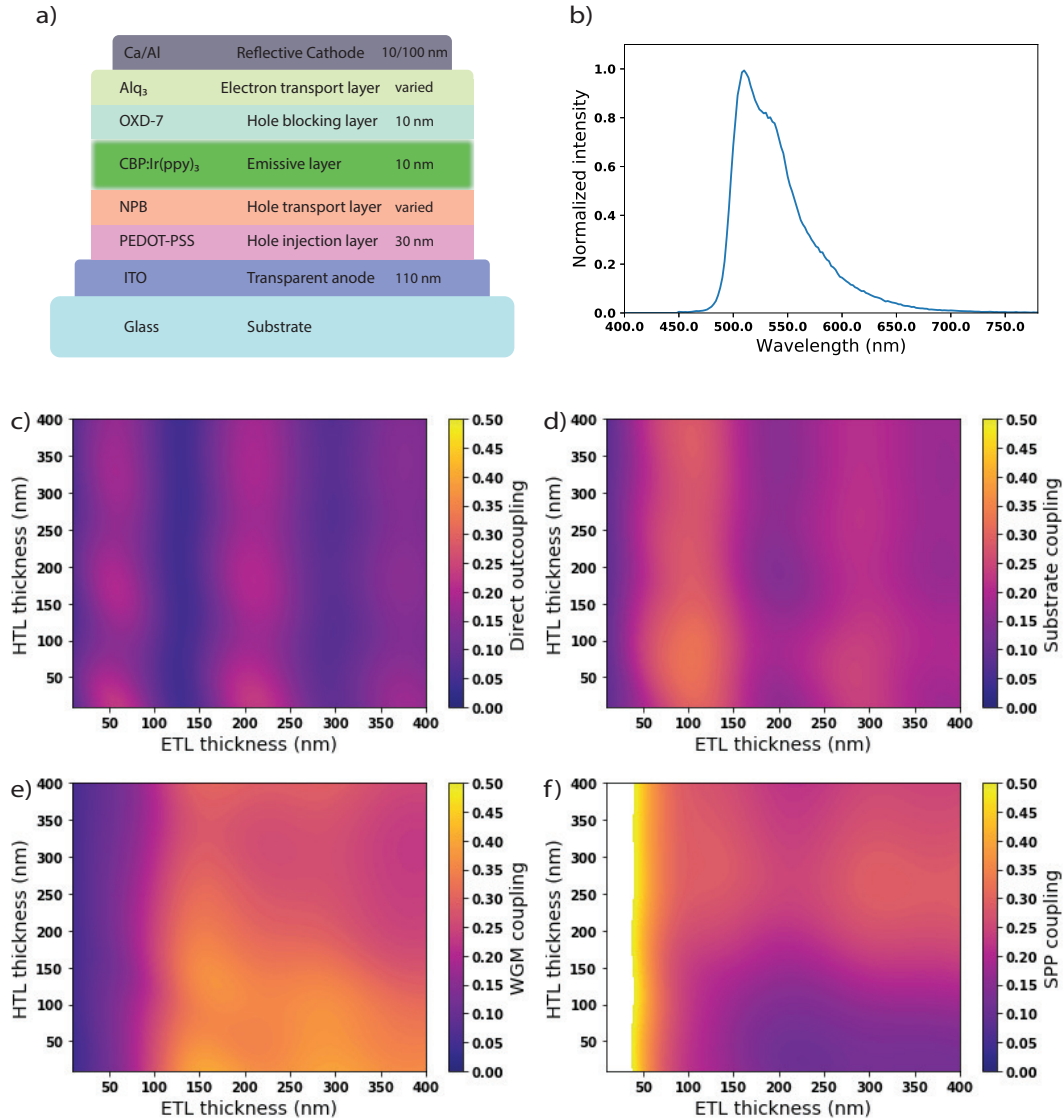


Figure 5.2.: Coupling into the different modes of a LED when varying the thicknesses of both electron and hole transporting layers of an exemplary stack (a). The emissive dye molecules Ir(ppy)₃ emits a predominantly green spectrum (b). For direct outcoupling (a), a strong dependence on the ETL thickness can be observed while the HTL only has a minor impact on this. For the modes not contributing to the device performance, low thicknesses activate a huge contribution into SPP modes (f), whereas higher thicknesses lead to pronounced waveguided modes (e). Substrate modes (d) show minima and maxima depending on the film thicknesses.

contribute to lighting purpose. In this case, the optimized outcoupling performance would be a combination of both, direct outcoupling and substrate modes.

Waveguided modes only occur for a sufficient thickness of the ETL. This effect can be explained via the minimum thickness required for a waveguided mode to be present in the microcavity of the system. Again this effect only shows a small dependence to the HTL thickness.

Finally, the coupling to surface plasmons is most dominant for low ETL thicknesses. Due to the low distance to the metallic cathode, near field coupling into the SPP modes can occur. This effect is draining a significant fraction of emissive radiation. Due to this loss channel, a minimum distance between the emissive film and metallic layers in an OLED is required.

5.3. Color tuning of thin film devices

The coupling to modes within a light emitting device depends on the emitted wavelength. Hence, the visible color of an OLED is changing as the microcavity is altered. Therein, suppressing and promoting parts of the emissive spectrum of the dye allows for an effect on the visible color. It is important to point out that this effect is not altering the intrinsic emission of the EML but rather tunes the probability of coupling into a specific visible mode. Further, adjusting the device towards a particular color can alter the microcavity away from the configuration optimized for overall light outcoupling, hence lowering the performance of the device.

For the quantification of the emissive color, the CIE color diagram is used. Therein each visible color is mapped to certain coordinates. For a given spectrum the color coordinates can be calculated from the color matching functions representing the sensitivity of the human eye to red, green and blue light [41].

Fig. 5.3 shows the resultant CIE coordinates and thus the visible color of the stack given in fig. 5.2 for the variation of both, ETL and HTL thickness. Crucial changes in the emission color do not occur within the high efficiency regions residing at ETL thicknesses of about 50 nm and 210 nm. However near the cavity minima at 130 nm and 300 nm thickness, the CIE color coordinates drastically change due to the properties of the microcavity. Note that the shown calculations only depict the apparent color at an emission angle perpendicular to the device surface.

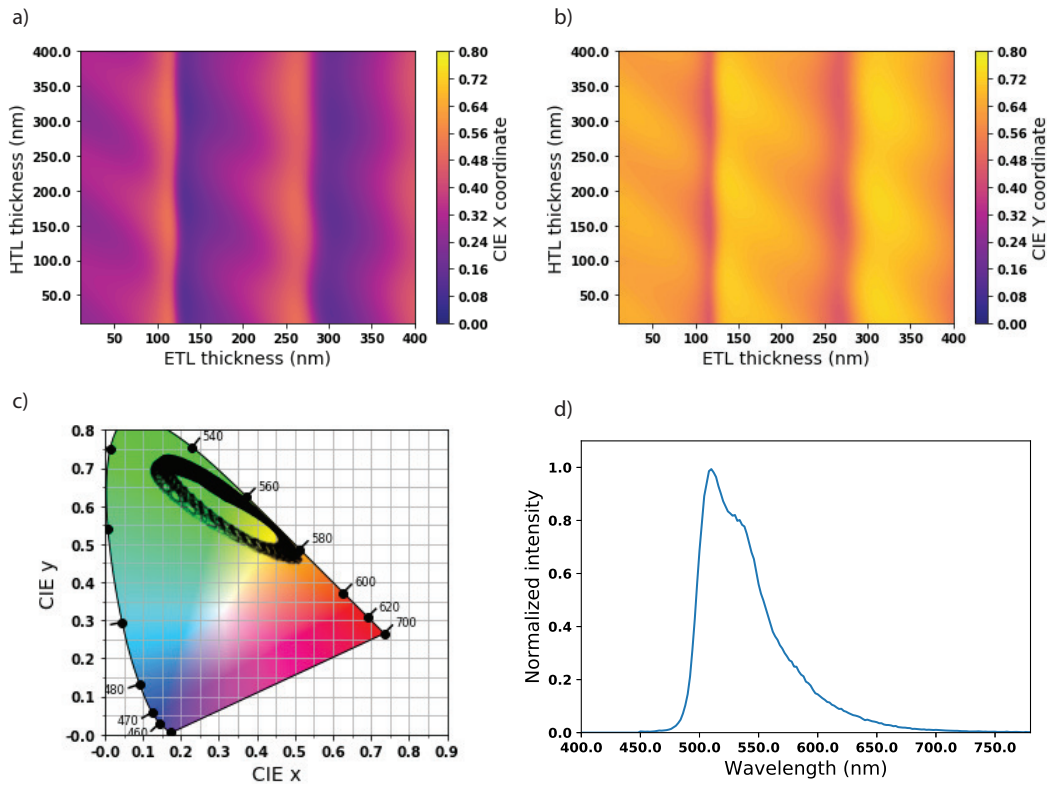


Figure 5.3.: Variation of the emissive CIE x- (a) and y- (b) coordinates when changing the ETL and HTL thickness within the device shown in fig. 5.2. The resultant CIE coordinates (c) cover a wide range of colors. Therein each black dot indicates a CIE coordinate reachable by tuning the microcavity. This vast amount of colors ranging from orange to green is reached despite the dye molecule $\text{Ir}(\text{ppy})_3$ emitting a predominantly green spectrum (d).

5.4. Effects of preferential alignment on device performance

When investigating the efficiency of light emitting devices from an optical point of view, the orientation of the emissive TDM plays an important role [1, 34]. As depicted in fig. 5.4, the fraction of energy coupled into the optical modes is different for the TDM being parallel or perpendicular to the device surface. Dipoles parallel to the surface show a huge fraction being coupled out of the device, while the transitions perpendicular mostly contribute to waveguided or surface plasmon modes. For an isotropic dye molecule, the emission of a device consists of one-third of the energy originating from perpendicular TDMs and two-thirds arising from horizontal dipoles. However changing this distribution by tuning the orientation of the TDM and changing its radiation pattern, the device efficiency can be improved.

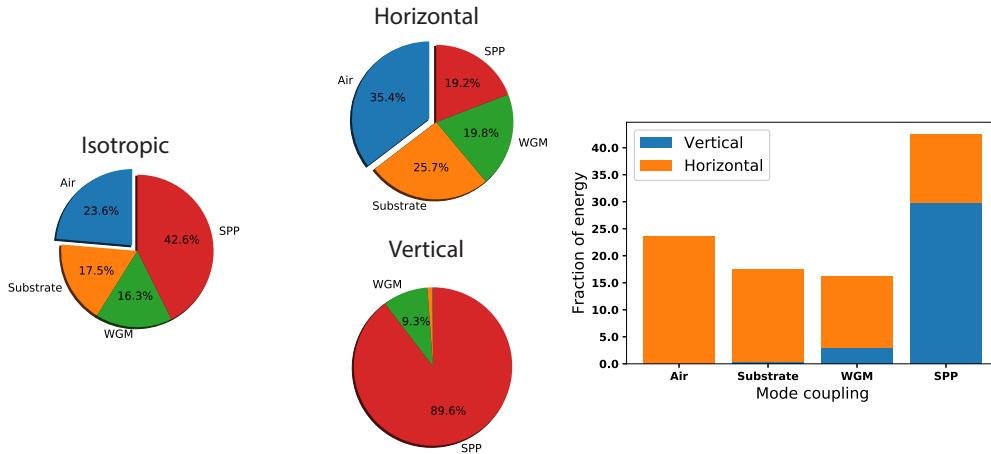


Figure 5.4.: Mode distribution within a device having an isotropic distribution of the TDMs. While 35.4% of the horizontal dipoles contribute to the device performance, less than 1% of the energy emitted by vertical dipoles contributes to the lighting application. Instead, the energy emitted by vertical dipoles is lost into surface plasmon excitation and waveguided modes. It should be pointed out that the presented efficiencies are optimized for an isotropic dipole distribution.

For a given stack layout the variation of the orientation parameter Θ and thereby the energy emitted from horizontal and perpendicular components of the TDMs reveals a direct correlation to the outcoupling efficiency. As depicted

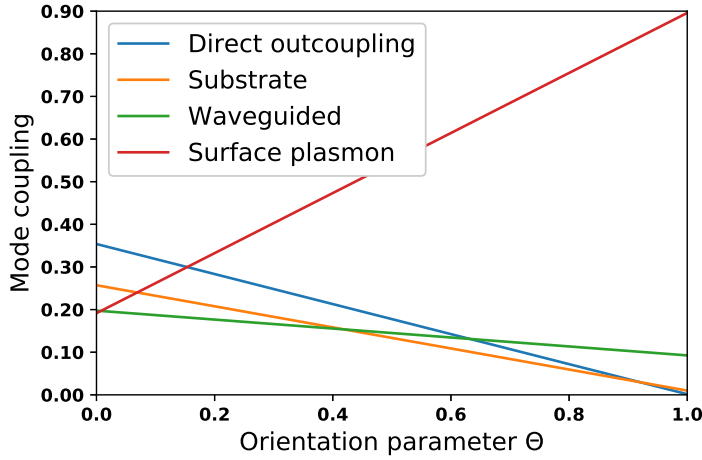


Figure 5.5.: Change of the outcoupling efficiency as well as coupling into different modes when varying the orientation parameter Θ . A complete vertically aligned TDM distribution will yield an outcoupling efficiency of less than one percent while distributing 90% of the energy into surface plasmon modes. Note that the shown simulations are for a given stack layout optimized for light outcoupling of an isotropic TDM distribution.

in fig. 5.5, an increase of the orientation parameter leads to a decrease in outcoupling efficiency while promoting the coupling to surface plasmon modes. Further, the substrate mode coupling shows similar behavior to direct outcoupling. Interestingly the fraction of waveguided modes only shows a minor dependence to the orientation parameter.

The descriptions in the previous chapter lead to the conclusion that not only the orientation but also the refractive index of the emissive medium is essential when investigating the device performance. Given the equivalence of changing the refractive index compared to varying the TDM orientation, the alignment constant ζ , combining both effects should ultimately determine the device efficiency. To illustrate this phenomenon, two different stack layouts were simulated. In one the emissive layer was assumed to be infinitely thin. In a second simulation, this film was changed to be 30 nm. The two different film thicknesses as depicted in fig. 5.6 are essential to investigate, as a change in the refractive index of the layer will affect not only the radiation pattern of the emitter but also the effective refractive index of the microcavity and therefore the coupling into waveguided modes.

5. Light emission from thin film optoelectronic devices

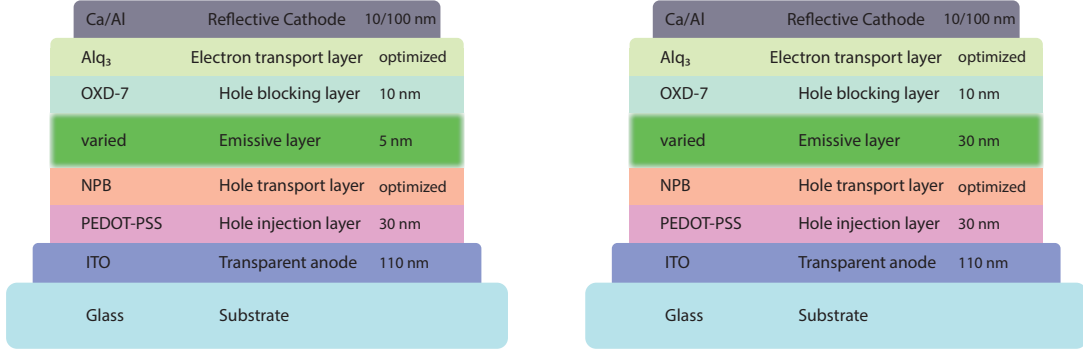


Figure 5.6.: Depiction of two different stack layouts to investigate the different EML thicknesses. The device with the thin EML (left) has a film thickness as low as 5 nm whereas the other stack (right) shows an EML thickness of 30 nm. For both devices the refractive indices of the EML were varied. Further, for each optical constant the thicknesses of the ETL and HTL were optimized for maximum light out-coupling.

For an infinitely thin emissive layer, the optimized ETL thickness can be assumed to stay constant while varying the refractive index of the EML. However, for a thick layer, this optimized thickness will vary. Hence, for the 30 nm EML system the ETL thickness was optimized for each refractive index individually yielding the results shown in fig. 5.7. Therein each refractive index of the 30 nm thick emission layer can be attributed to an individual optimized ETL thickness. This effect occurs due to the refractive index of the film changing the optical path between the emissive dipole and the reflective cathode.

For both systems, the individual contributions to direct outcoupling, substrate modes, waveguided modes as well as surface plasmon modes were calculated for a variation of the angle of the emissive TDM as well as the refractive index of the EML.

The results for a system with a thin emissive film are depicted in fig. 5.8. Therein, an increase in outcoupling efficiency can be observed for a rising refractive index. The same effect occurs when lowering the TDM angle. Consequently, the fraction of surface plasmon modes decreases in the same manner. Interestingly both substrate coupling, as well as waveguided modes, show similar behavior to the outcoupling efficiency. This effect indicates that the increase in outcoupling efficiency, given by both the rise of the refractive index as well as lowering the TDM, originates from a decrease in SPP coupling. For the alignment constant ζ , which describes the effects of both the TDM angle as well as the

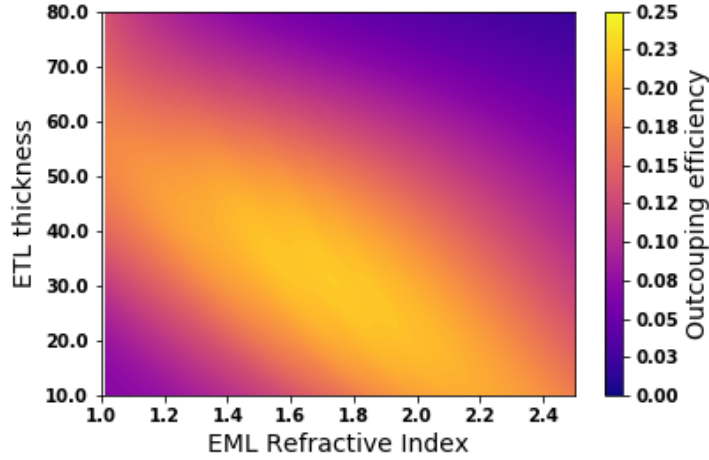


Figure 5.7.: Outcoupling efficiency for an emissive system with an EML of 30 nm thickness when varying the ETL thickness as well as the refractive index of the EML. Due to the change in the optical path between the emissive dipoles and the reflective cathode each refractive index can be assigned an ideal ETL thickness. The emission of the TDM was assumed to be centered in the EML.

refractive index on the radiation pattern of the emissive species, each value can be attributed to a line within the heatmap. These lines follow along pathways with constant coupling efficiency into the different modes. Hence the alignment constant combines the refractive index and the TDM angle into a single quantity ultimately determining the outcoupling efficiency out of the system.

Increasing the thickness of the EML to 30 nm changes the dependence of mode coupling to the alignment constant as depicted in fig. 5.9. While lowering the TDM angle still yields an increase in outcoupling efficiency, the behavior of the refractive index changed. Opposed to the thin emissive film, increasing the refractive index in this system yields an increase in WGM coupling and therefore a decrease in the outcoupling efficiency. Interestingly, the behavior for SPP mode coupling also changed towards a higher fraction of energy lost into these modes as the refractive index is increasing. The indicated lines for the individual ζ values do not follow a path of constant coupling efficiency anymore. These simulations lead to the conclusion that the alignment constant ζ is only valid for thin emissive films in the range of 10 nm while thick layers require a more detailed analysis of the mode coupling within the system.

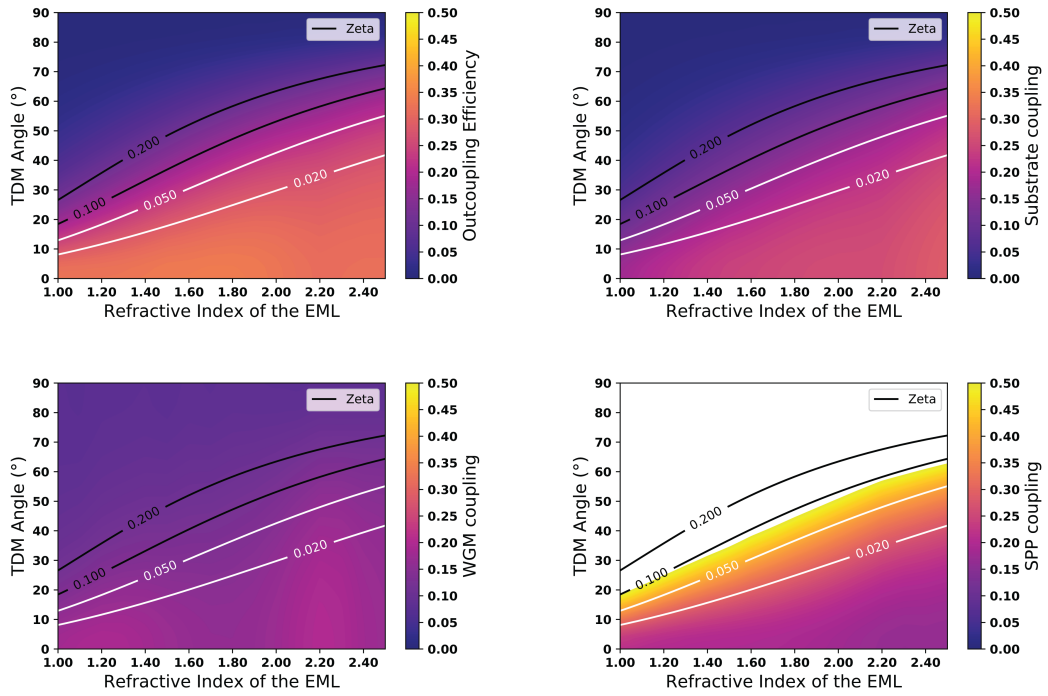


Figure 5.8.: Individual mode coupling contributions for a LED system utilizing a thin emissive layer. The Outcoupling efficiency (top left) increases for rising values of the refractive index as well as lower TDM angles. The achieved boost in performance can be attributed to less surface plasmon coupling (bottom right). Interestingly both waveguided modes (bottom left), as well as substrate modes (top right), are also increased accordingly to the outcoupling efficiency. The alignment constant ζ , as depicted within the heatmaps, follows along regions of constant coupling efficiency. Note that the calculations were performed at a single emission wavelength of 460 nm.

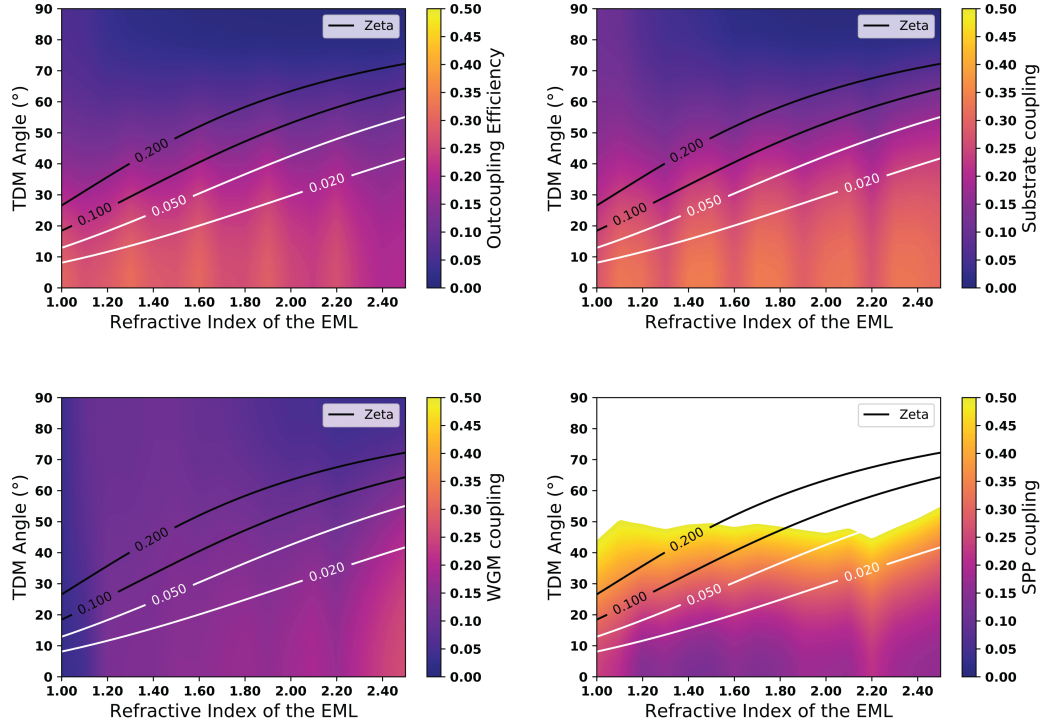


Figure 5.9.: Fraction of radiative emission distributed into the different optical modes for a LED with a thick emissive layer of 30 nm thickness. Contrary to the thin emissive layer, an increase in refractive index leads to more pronounced WGM coupling. Further, a maximum for the coupling to SPP modes at high refractive indices arises. Note that anomalous periodic minima for low TDM angles are due to numerical limitations of the optical simulation. Contrary to the thin emissive layer, ζ does not indicate regions of equal coupling. Again the simulations were performed for an emission wavelength of 460 nm.

Part II.

Methods - Extracting molecular properties to quantify thin film anisotropy

In the matter of physics, the first lessons should contain nothing but what is experimental and interesting to see. A pretty experiment is in itself often more valuable than twenty formulae extracted from our minds.

Albert Einstein

6. Computational methods

The determination and prediction of the preferential alignment of anisotropic molecular glasses rely on several computational methods. Given an organic molecule, the exact knowledge of its anisotropic properties, such as transition and permanent dipole moment is required. Further, the behavior of those molecules within an ensemble and its development in time can be of crucial importance. Finally, knowing these systems allows for the calculation of state-of-the-art light emitting devices and factors limiting their efficiency.

6.1. Calculation of molecular properties

Computing the properties of single molecules relies on the application of density functional theory (DFT). Hence this section introduces the basic concept of density functional theory in the context of current challenges within the field of organic semiconductors. Most of the equations and conclusions are taken from references [4, 42] to give a brief overview of the topic. For more detailed information the reader is referred to a set of review papers from the field of computational chemistry. The idea DFT itself is based on the Hohenberg-Kohn theorem [42, 43], which states that the energy $E(\rho)$ of the ground state for a many electron system can be expressed as:

$$E(\rho) = T_s(\rho) + V_{\text{ne}}(\rho) + J(\rho) + E_{\text{xc}}(\rho) \quad (6.1)$$

using the electron density ρ of the system. However only parts of this energetic description can be precisely described as follows:

1. The kinetic energy for a system of non-interacting particles can be calculated from the electron wavefunctions Φ_i .

$$T_s(\rho) = \sum_i \langle \Phi_i | -\frac{1}{2}\Delta^2 | \Phi_i \rangle \quad (6.2)$$

Therein Φ_i describes a set of single particle Kohn-Sham orbitals, leading

6. Computational methods

to the electron density of the system via:

$$\rho(\vec{r}) = \sum_i |\Phi_i(\vec{r})|^2 \quad (6.3)$$

2. The expression V_{ne} describes the potential energy between the nuclei and the non-interacting electrons:

$$V_{\text{ne}}(\rho) = \int \rho(\vec{r}) \left(\sum_A \left(\frac{Z_A}{|\vec{r} - \vec{R}_A|} \right) \right) d\vec{r} \quad (6.4)$$

3. Coulomb repulsion due to electron-electron interactions is covered as follows:

$$J(\rho) = \frac{1}{2} \int \int \frac{\rho(\vec{r})\rho(\vec{r}')}{|\vec{r} - \vec{r}'|} d\vec{r}d\vec{r}' \quad (6.5)$$

This description leaves the exchange energy E_{xc} as the main challenge for state-of-the-art DFT calculations. In the context of computational chemistry the expression for E_{xc} is referred to as "functional" and the set of wavefunctions Φ_i is described as "basis set", a set of terms describing the electronic wavefunctions.

One approach to providing a simple solution to E_{xc} is the famous B3LYP functional as derived by Becke and Lee-Yang-Parr. This description derives the correlation energy as a combination of Hartree Fock interaction E_{HF} , local density approximation (LDA) E_{LDA} , generalized gradient approximation represented by the B88 functional E_{B88} and the two functionals LYP and VWN [42, 44–47].

$$E_{\text{xc}}^{\text{B3LYP}} = 0.2E_{\text{HF}} + 0.8E_{\text{LDA}} + 0.72\Delta E_{\text{B88}} + 0.81E_{\text{LYP}} + 0.19E_{\text{VWN}} \quad (6.6)$$

In this equation, the prefactors to the energetic contributions have been derived experimentally to fit a wide range of known measurements. Although this functional is performing exceptionally well in many cases, it is known to underestimate long-range interactions especially within large molecules or intermolecular interactions. Nevertheless, it is still the functional of choice for the calculation of molecular properties of organic molecules as described in the following chapter.

Two other functionals worth mentioning in the context of this work are M06 and M06-2X as part of the Minnesota functionals often referred to as Myz. All of those functionals are in the class of hybrid functionals based on the meta-GGA approximation having terms depending on the kinetic energy density. Similar to B3LYP those functionals are also parameterized and benchmarked to reliable measurements. This set is continuously improved with the most recent being the MN15 family. However many of those functionals lack sufficient testing in

the context of organic semiconductors and are therefore not discussed in further detail [48–51].

Another important part of DFT is the extension to time dependence (TD-DFT). This method allows for the calculation of transition states. In analogy to time-independent DFT, this method relies on the Runge-Gross theorem. Therein the energy of a system is extended by a time dependent external scalar field $V_{\text{ext}}(t)$ [4, 52]:

$$E(\rho) = T_s(\rho) + V_{\text{ne}}(\rho) + J(\rho) + E_{\text{xc}}(\rho) + V_{\text{ext}}(\rho, t). \quad (6.7)$$

The Runge-Gross theorem states that, for this system the external potential is only defined by the electron density of the system.

Basically, the TD-DFT calculation is based on the frequency dependent linear response of the system when being affected by a time-dependent external perturbation. This response, the polarizability $\alpha(\omega)$ yields the behavior of the system given an external excitation with frequency ω [4]. The dependence of α to the electronic spectrum can be shown to depend on

$$\alpha(\omega) = \sum_i \frac{f_i}{\omega_i^2 - \omega^2}. \quad (6.8)$$

Therein the excitation energies ω_i are taken into account as poles in the polarizability of the molecule while f_i denotes the oscillator strength, which corresponds to the probability of the transition. Further, it is possible to determine the TDM \vec{p} describing the probability P_i of a transition from the excited state Ψ_i back into the ground state Ψ_0 via [53]:

$$P_i^2 = \frac{2\pi}{\hbar} \text{DOS}(E_i) |\langle \Psi_i | \vec{p} | \Psi_0 \rangle|^2. \quad (6.9)$$

Where the DOS of the final state $\text{DOS}(E_i)$ further affects the transition rate. For emissive transitions in the presence of spin-orbit coupling (SOC), special methods need to be used for a proper description of the system within TD-DFT. Standard functionals such as B3LYP can not predict those systems. Hence, different methods for the description of SOC within TD-DFT have been developed [54–66], this work will focus on the relativistic ZORA (zero-order regular approximation) method [61–63]. This approximation has been used to determine the time-dependent properties of molecules showing SOC. Especially organometallic heavy-metal containing molecules such as Ir-complexes can be described using the ZORA approximation [67–72]. The calculations within this work using the ZORA method were performed according to the method described in [34].

6.2. Amorphous molecular ensembles

Calculating the properties of amorphous molecular ensembles, such as formed in an organic thin film, can be done using classical molecular dynamics simulations. Therein, the temporal evolution of a system can be calculated by applying Newtonian mechanics using the positions, velocities of the individual atoms as well as the forces on the respective particles.

Within this work, the molecular dynamics engine Desmond as available via the Schrödinger Materials Science Suite [73] was used for all shown calculations. Calculations were performed using an Nvidia Quadro P4000 GPU. The descriptions of the molecular dynamics procedure are described based on the initial publication of the Desmond algorithm [74].

Two different methods were used to perform molecular dynamics simulations on amorphous organic systems throughout this thesis. First, the calculation of bulk properties such as density and dipolar interactions was performed from random, disordered systems. As a second method, the application of molecular dynamics to thin film deposition by subsequent placement of the molecules was evaluated. Both of these methods are described in the following sections.

6.2.1. Molecular dynamics simulations

Solving the temporal evolution of an ensemble of molecules and their individual atoms can be done by using molecular dynamics. Therein the system is calculated by applying Newtonian mechanics via [74]:

$$F(\vec{x}, t) = \vec{\nabla}U(\vec{x}, t) = m \cdot \dot{\vec{v}}(t) \quad (6.10)$$

$$v(t) = \dot{\vec{x}}(t) \quad (6.11)$$

Where the force F acting on a particle is given by the gradient of the potential U . This force changes the velocity \vec{v} of the entity with mass m and thereby also its position \vec{x} . From these equations, it is obvious that the proper description of the system relies on the potential U . Within molecular dynamics simulations, this potential is described using force field approximations. Several different force fields suitable for various scenarios can be used. Within the field of organic semiconductors, the OPLS3 [75] force field as developed by Schrödinger shows excellent results. Thus only this description will be used for calculations. This forcefield, as well as other similar potentials such as AMBER [76], GROMOS [77] or CHARMM [78], describe the potential energy E of a system as a sum of

three different energies:

$$E = E_{\text{bond}} + E_{\text{ES}} + E_{\text{vdW}} \quad (6.12)$$

Therein the bonding energy E_{bond} describes the intermolecular forces given by the covalent bond structure. These terms involve at least two atoms, but can also involve three or four atoms describing angular and torsional relations. Electrostatic forces as well as van der Waals interactions are described by E_{ES} and E_{vdW} respectively. Both of them do not rely on bonding but are affected by the whole system. Van der Waals interactions generally are limited to short ranges between 9Å and 12Å and therefore can be sufficiently described using a cutoff radius around the respective particle. Electrostatic forces, however, need to be calculated for the whole system requiring a large amount of computational power. To overcome this limitation, the electrostatic interactions are also only calculated within a certain radius, while suitable approximations cover long-range interactions [74].

Note that the molecular dynamics approach taken within this work is purely classical. While this involves inter- and intramolecular forces as described within a force field approximation, quantum mechanical interactions between molecules cannot be taken into account.

Molecular dynamics simulation steps

After successful preparation of a molecular dynamics system, the actual computation is performed. Depending on the investigated problem, several different possibilities regarding thermodynamics are given as implemented in the Materials Science Suite [73]:

NVE : In this class of simulation the number of particles (N), the volume (V) and the entropy of the system (E) is kept constant. Due to the constant volume, the simulation box will not be reduced in size. Thus, if performed on initial state systems, an isolated cluster of molecules will be formed.

NVT : Instead of fixing the entropy as in the previous case the experimentally accessible temperature is kept at a constant value.

NPT : In this case both pressure (P) and temperature are being kept constant, simulating an ambient condition for a film of organic molecules.

NPAT : Additionally to the previous case the area (A) of the system is fixed to a constant value. Although this is sometimes suitable for thin film

simulations, it is important to keep in mind that the simulation does not necessarily result in a flat surface being formed.

NP γ T : Herein not the area but the surface tension γ is kept constant.

Usually, a relaxation step is performed using a protocol provided by the Schrödinger Material Science Suite [73]:

1. a brownian minimization state
2. 20 ps of NVT at 300 K
3. 20 ps of NPT at 100 K
4. 100 ps of NPT at 300 K

Bulk molecular dynamics

One application for molecular dynamics is the calculation of material densities. This simulation involves an NPT molecular dynamics within a sufficient time-frame for the system to reach its lowest density. Further, an initial relaxation is performed to avoid the system being stuck in an artificial state. The system is calculated in periodic boundary conditions. Hence, number of molecules should be chosen as high as possible to avoid self-interaction between the molecules. As a rule of thumb, the spatial extension of the system should be larger than the electrostatic cut-off radius between the atoms.

Exemplary results for the Coumarin6 dye molecule are depicted in fig. 6.1. Therein the relaxation to a tight box takes a few ns, after which the system is only slowly changing its density. Due to the density of the system fluctuating as throughout the molecular motion, the last 15 ns of the simulation are averaged with the standard deviation as the error value. Note that this bulk density is only an approximation for thin films deposited from TVD as the morphology within a subsequently deposited system will most likely be slightly different.

The preparation of a disordered system is required as a starting point for molecular dynamics simulations. Therein, the initial positions of the atoms are determined. This system should avoid clashes between the individual molecules as well as sufficient room for the molecules to relax into a suitable morphology. The full amorphous system can be prepared by randomly placing all molecules within a simulation box using randomized orientations of the entities. Throughout this work, the algorithm as provided within the Schrödinger Material Science Suite was used for the preparation of disordered systems.

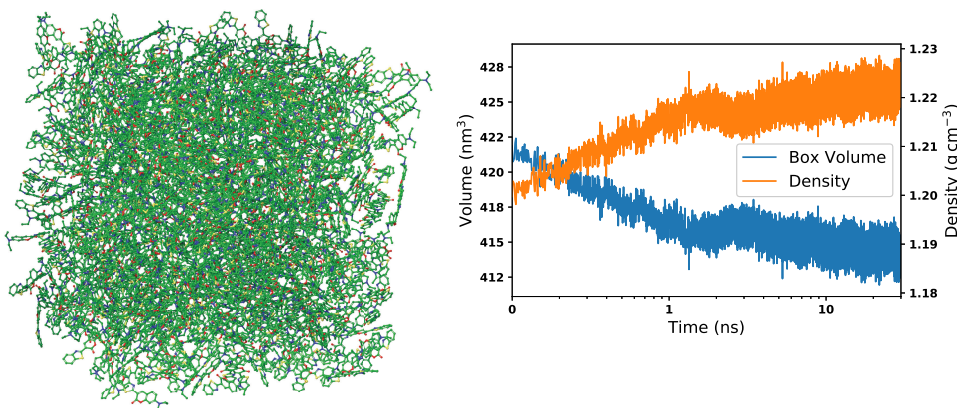


Figure 6.1.: Final simulation box for 30 ns of molecular dynamics simulation with 870 Coumarin6 molecules (left). Within the first nanosecond, most of the relaxation takes place as depicted by the box volume and density of the system (right).

Calculating thin film deposition

In order to calculate the film morphology of an experimental sample prepared via step-by-step deposition techniques such as thermal vapor deposition, the subsequent formation of the film needs to be simulated. While several significant publications approached this problem using specific methods [79–81], the following paragraphs will introduce the technique by using the unrefined OPLS3 forcefield in a default molecular dynamics simulation [75].

At first, a substrate is prepared. Generally, a bulk system consisting of the underlying layer in the thin film system can be used in this case. Other publications also introduced a layer of C_{60} as an inert substrate. Note that the lower parts of the substrate have to be immobilized within the simulation as the film will otherwise deform on the impact of the deposited molecules. The substrate further needs to be relaxed into its ground state before deposition, which was achieved by calculating at least 30 ns of molecular dynamics.

One important factor to be aware of when modeling this process is to estimate the rate of molecules arriving on the surface. Assuming a deposition rate of 1 \AA/s , a material density of 1.4 g/cm^3 and a molar mass of 500 g mol^{-1} , this can be estimated to:

$$\frac{\text{molecules}}{\text{nm}^2\text{s}} = \frac{1.4 \text{ g/cm}^3}{500 \text{ g mol}^{-1}} \cdot 6.022 \cdot 10^{23} \text{ mol}^{-1} \cdot 0.1 \text{ nm s}^{-1} \approx 0.17 / \text{nm}^2\text{s} \quad (6.13)$$

This translates into an average time between two molecules of 50 ms in a simulation box of 10×10 nm. Hence leading to two consequences for the simulation:

1. Between the individual deposition of the molecules, a sufficient timeframe for relaxation needs to be calculated. This was chosen to 6 ns. It should be pointed out that this value was only limited by the available computational power.
2. As the real time between the subsequent arrivals of the molecules is much larger than the available range for molecular dynamics, slow processes affecting the morphology cannot be predicted using this approach.

An investigation of this deposition protocol was performed for the dye molecule $\text{Ir}(\text{ppy})_2(\text{acac})$ doped into the host material CBP. The results for this calculation and its agreement to experimental values are given in 9.2.2.

6.3. Predicting optical device properties

In order to calculate the optical properties of a thin film optoelectronic device, the methods described in sections 2 and 5 are employed. Therein the emissive dye molecules are treated as classical dipoles, and their mode coupling to the microcavity ultimately determines the system properties. In order to perform these calculations, several input parameters are required. The calculations within this work were done using the self-developed simulation software TOASTER, which is based on earlier work by Bert Scholz [82] who started the development of the preceding software BOOST as well as Jörg Frischeisen [7], Nils Reinke [83] and Stefan Nowy [84] and their work with the MAPLE program PDCalc. Calculations were performed using Nvidia CUDA as well as the Intel Compiler Collection and Qt. For CUDA capabilities a Nvidia GTX 770 GPU was used.

The computation requires the optical properties of the system as an input. The required properties include the refractive indices of all involved materials as well as the film thicknesses. Further, the region of the device contributing to waveguided modes is necessary, which is defined by the set of organic layers around the emissive dye - limited by the reflective contact and the substrate. Further, the location or emission profile, as well as the spectral distribution of the emission, need to be specified. Numerical parameters for the simulation involve the step size of the in-plane wavevector, its minimum and maximum values to calculate, wavelengths to calculate and the angles of emission that should be derived from this. For the in-plane wavevector, empirical values adapted from earlier simulations were used, in which this parameter k_{\parallel} is calculated for

$k_{\parallel} = 10^5 \text{ m}^{-1} - 4 \cdot 10^7 \text{ m}^{-1}$ in 10^5 m^{-1} steps. Note that the computational requirements scale linearly with the amount of in-plane wavevectors calculated for the simulation [1].

After input, the individual steps of the simulation are performed as depicted in fig. 6.2. At first, the Fresnel coefficients of the microcavities are calculated for each combination of wavelength, and in-plane wavevectors using a matrix transfer formalism. Utilizing these coefficients, the z-components of the respective Poynting vectors are calculated, representing the emission out of the device. Note that this is a highly parallel computation due to the individual data points, the in-plane wavevectors, and wavelengths, being independent from each other.

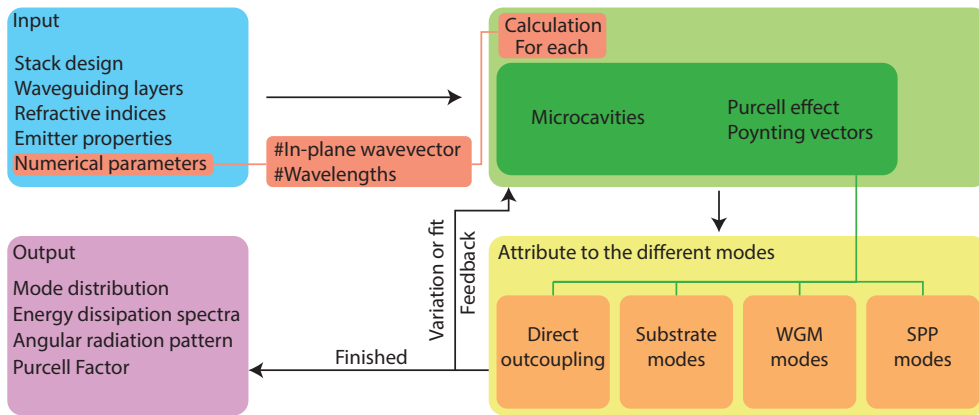


Figure 6.2.: Workflow of an optical simulation to predict the optical properties of a photoluminescent or electroluminescent thin film system using the TOASTER software. After setting up the simulation parameters such as stack design and emitter properties, the microcavity and subsequently the emission of the classical dipole are calculated for each combination of in-plane wavevector and wavelength. Afterward, the calculated power dissipation is attributed to the different modes by numerical integration within the respective boundaries. In the case of a parameter variation within the system or the fit to experimental data, the calculation is repeated as often as necessary. Finally, the output involves the mode distribution, energy dissipation spectra and angular radiation patterns for the individual dipoles describing the emissive system.

After successful computation, the calculated energetic contributions are attributed to their modes in the system depending on the in-plane wavevector. The total mode distribution is computed by numerical integration for the respective wavevector range [1].

7. Experimental methods

The experimental techniques for the investigation of preferential alignment in thin films involve both optical and electrical characterization methods. The following sections in this chapter will introduce the basic concepts of these characterizations and emphasize on important techniques. Therein, the optical methods involving the orientation of organic molecules have been developed within earlier work and were only refined during this thesis [85]. The same holds for the electrical characterization which was developed by Lars Jäger, Alexander Hofmann, and Markus Schmid [10, 11].

It should be pointed out that sample preparation methods are not explicitly discussed during this chapter. Films were generally deposited via thermal vapor deposition (TVD) in a vacuum chamber at a pressure of $4 \cdot 10^{-7}$ mbar and deposition rates of $1 \text{ \AA}/\text{s}$ or via solution from spin coating. Selected samples were also prepared from organic vapor phase deposition (OVPD).

7.1. Optical spectroscopy

Throughout this thesis, several experimental methods require the characterization of the light emitted from a luminescent sample. The desired quantities can be either the spectral distribution, hence the energy emitted per wavelength and time in the visible range, the polarization of the electromagnetic waves, the time-resolved intensity of the luminescence or a combination of all of these. Throughout this chapter, basic methods to investigate those effects will be given and explained in their respective experimental setups.

7.1.1. Spectroscopy of visible light

The detection of electromagnetic radiation in the visible wavelength range is of crucial importance for the investigation of light emitting materials. This section will introduce the basic concepts of monochromators and optical detectors and give an insight into light guiding considerations for optical applications.

Monochromators and light detection

The general approach to characterize visible (VIS) or near-infrared (NIR) light is the detection of the separated wavelengths on a photodetector. The photodetector is usually a semiconducting photodiode, made from a suitable material such as silicon for VIS applications or InGaAs for NIR measurements. However, more complicated methods, such as photomultiplier tubes or microchannel plates are also used.

The separation of the individual wavelengths is usually done using Czerny-Turner-Monochromators as depicted in fig 7.1 [86]. Therein the incoming optical wave is reflected at a grating and subsequently focused through an optical slit (the output slit). At the position of the slit, the wavelengths are spatially separated, allowing for only a small bandwidth of the signal passing through the slit.

Both input slit and the outgoing slit affect the bandwidth of the signal. Therein, smaller slit-widths increase the spectral resolution, whereas larger slits increase the amount of light passing through the device. Of further importance is the focal length of the parabolic mirrors used in the Czerny-Turner setup. This quantity determines the distance of the reflecting surfaces to the optical grating. Upon increasing the length of the optical path, the spectral resolution is again increased, at the expense of light intensity reaching the optical detector.

Using the described setup, a photodetector mounted behind the slit can detect a small interval of wavelengths. Further, if the center wavelength of the monochromator is subsequently changed, complete spectra of an incoming signal can be detected at a significant expense of time. To further reduce the measurement time for a complete spectral characterization, an array of photodetectors, such as a CMOS detector can be used. Mounting this array to the outgoing exit of a monochromator allows for the detection of different wavelengths on each of the pixels of the detector, as shown in fig. 7.1. This method enables the quick measurement of optical spectra [86].

All detection techniques suffer from thermal noise due to ambient temperatures, limiting their detection capabilities. In order to overcome this problem, some photodetectors can be cooled down to lower temperatures. This improvement allows for a significant decrease of dark signal and therefore higher signal-to-noise ratios. This improvement benefits the experiment in two ways, by either decreasing measurement times or allowing for the detection of lower signals [87].

Coupling light into optical setups

Due to the setup of monochromator devices, only a finite set of angles can enter the optical path and reach the detection exit, as shown in fig. 7.2. The amount

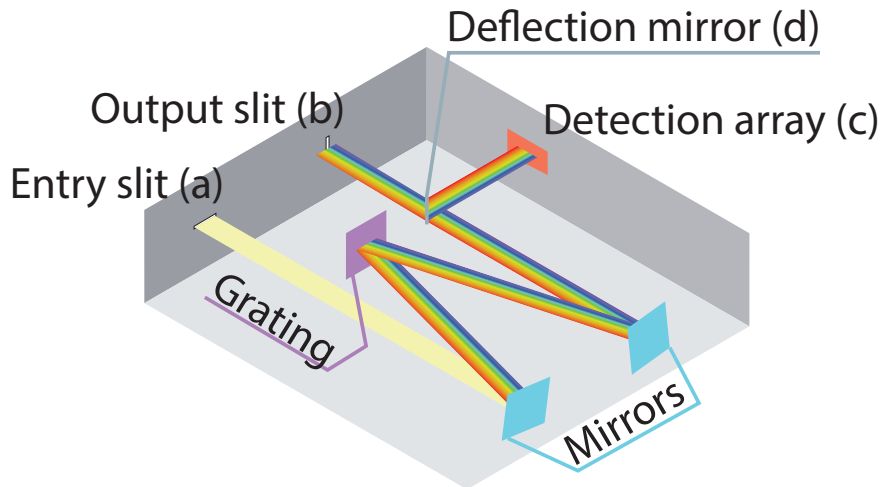


Figure 7.1.: Setup of a Czerny-Turner-Monochromator using an optical slit (b) or a detection array (c) to measure and characterize optical signals. The slitwidths (a) and (b) determine the bandwidth of the signal, whereupon smaller widths increase the spectral resolution. The optional deflection mirror (d) allows for the choice of the outgoing pathway.

of light entering the device can be described by an acceptance angle, which is determined by the focal length of the monochromator.

In order to guide an optical signal into a spectral detection setup, several considerations need to be taken into account. Throughout these steps, the optical invariant will be of crucial importance, limiting the fraction of light that can be pulled into a certain configuration. This quantity connects the minimum diameter of an optical image (z) to the divergence angle of the same ray (ϕ), as shown in fig. 7.3 [88].

$$z_1\phi_1 = z_2\phi_2 = \text{const} \quad (7.1)$$

According to this equation, the finite size of an optically guided ray can only be decreased at the expense of a higher diverging angle. As a second important relation for the guiding of optical rays, the lens equation needs to be taken into account, which is illustrated in fig 7.4 [88]:

$$\frac{1}{f} = \frac{1}{O} + \frac{1}{I}. \quad (7.2)$$

Therein the focal length f is related to the distance of the object O to the plane of the lens as well as the respective distance of the focused image I . Further, the

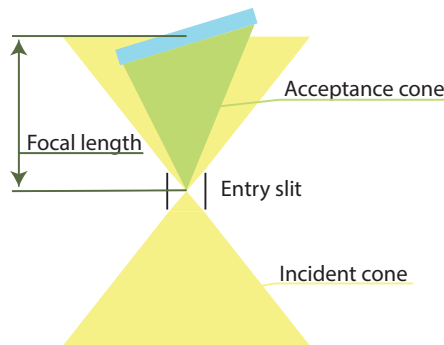


Figure 7.2.: Acceptance cone of a Czerny-Turner monochromator. The focal length and the size of the mirror determine the fraction of the incident cone being guided onto the grating. Note that within real monochromators, an additional aperture would be present to prevent stray light within the device [86].

size of the object and its respective image are also related through the following equation.

$$\frac{\text{Object}}{\text{Image}} = \frac{O}{I} \quad (7.3)$$

Careful consideration of the optical equations allows for precise control of a light ray by using optimized lens systems. In the context of optical spectroscopy, a lens is often used to guide light through the entrance slit of a detector.

Application of light coupling to spectroscopy of small-area emissive samples

Optical spectroscopy of thin films often involves the measurement of light emitting features being excited either via optical or electrical excitation. Therein it is desirable to collect as much light as possible in order to reduce integration times and increase signal-to-noise ratios. In order to reach this, the total optical performance of the collection system needs to be taken into account. It is important to note that the spectroscopic methods within this work rely on a fiber delivery into the spectrograph, which introduces further losses. In summary, the losses can be attributed to the following effects.

1. The fraction of light coupled into the light collection optics.
2. The size of the image projected onto the optical fiber concerning the fiber core size.

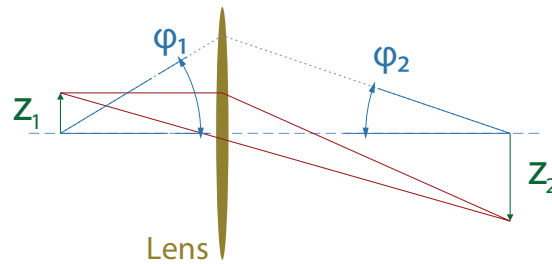


Figure 7.3.: Optical invariant depicted via the refraction at a converging lens. By passing the lens in this illustration, the optical ray is focused at a larger distance, decreasing the divergence angle ϕ_2 . Hence the size of the focused beam will be larger compared to the initial size z_1 [88].

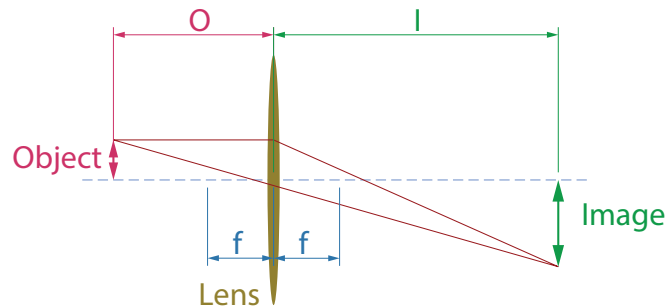


Figure 7.4.: Illustration of equation 7.2 and 7.3. The ratio between image and object size is equivalent to the ratio of their distances to the focal plane of the lens. Further the distances O and I yielding a sharp image are connected to the focal length f of the lens.

3. The numerical aperture of the setup determined by the fraction of light projected onto the fiber below the acceptance angle.
4. Losses at the fiber ends as well as absorption losses in the fiber.
5. The fraction of light entering the spectrograph and ultimately reaching the detector.

The loss channels up to the coupling into the optical fiber are illustrated in fig. 7.5. Therein the different loss channels can be attributed to steradian losses, image size losses, and numerical aperture losses.

7. Experimental methods

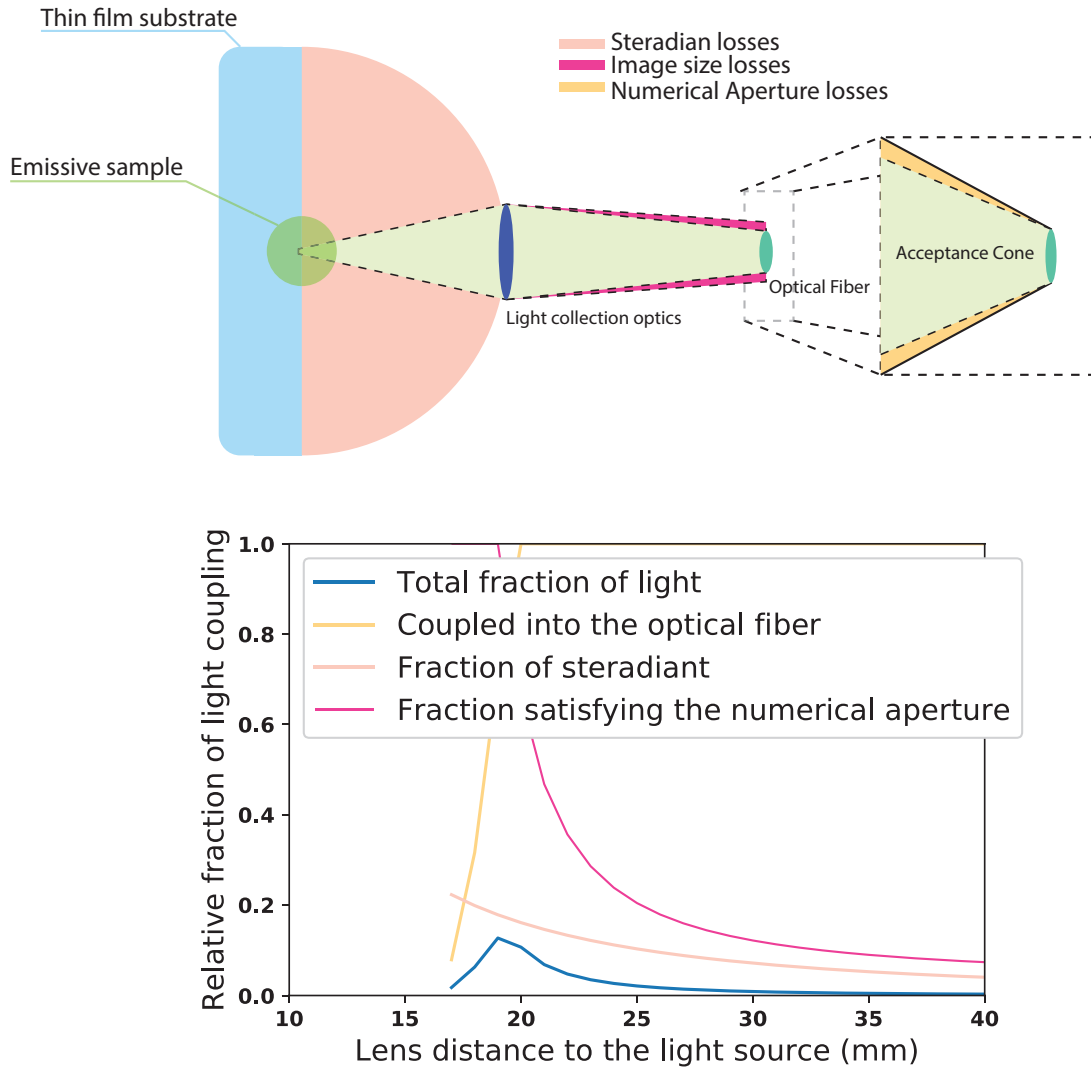


Figure 7.5.: Illustration of optical loss channels when coupling light from an emissive sample into an optical fiber. A large fraction of light is lost due to the steradian covered by the light collection optics. Further losses include the fraction of light not reaching the optical fiber due to the projected image being larger than the fiber core as well as the fraction outside of the angular acceptance cone of the fiber. The graph illustrates the optical loss due to the steradian and image size for a lens with a focal length of 16 mm and a diameter of 1 inch. Note that the steradian coupling is relative to a fixed distance to the sample. Hence the given coupling efficiency is only relative but still able to reveal the ideal distance of the lens.

7.1.2. Polarization anisotropy

Polarization anisotropy occurs if the excitation of a sample with linear polarized light leads to an at least partially polarized emission of the emissive molecules. While this is a common technique for samples within a solution, this section will discuss polarization anisotropy within emissive thin films. At first, different technologies for light polarization are discussed, followed by basic principles of fluorescence anisotropy measurements [89].

Polarization optics

For the polarization of both laser beams as well as emitted light from luminescent samples, two different optical approaches were used throughout this work.

Wire grid polarizers employ a grid of microwires patterned parallel to each other. Thus, incident light in which the electric field is parallel to the wire structure will be absorbed or reflected while the perpendicular component of the electric field will be transmitted through the polarizer [89].

A different approach is taken in birefringent polarizers such as Glan-Thompson or Glan-Taylor prisms [90–92]. Therein the incident beam is guided through a birefringent medium splitting the eigenstates of polarization. Via the proper choice of a cut through the prism, a total internal reflection will occur for only one of the states whereas the other polarization will pass the prism.

Wire grid polarizers can be of much smaller size compared to the birefringent variant. However birefringent polarizers exhibit much higher polarization ratios compared to the thin-film variant. Further, if spaced by only air the damage threshold and wavelength range exceed the microwire grids.

Measuring polarization anisotropy

In order to measure the polarization anisotropy of a thin film sample, photoluminescence needs to be excited by using linearly polarized light. The emission of the sample is then measured using a second polarizer oriented either parallel or perpendicular to the exciting beam. This procedure yields measurements for the intensity parallel to the exciting beam I_{\parallel} as well as the intensity I_{\perp} perpendicular to the excitation. Both measurements can then be refined to quantify the polarization anisotropy [89].

Quantifying polarization anisotropy

Polarization anisotropy can be quantified by a factor r . This quantity is defined via the two intensities I_{\perp} and I_{\parallel} as well as a device calibration factor G . This

factor includes the device specific discrepancies between the polarization states. However, the determination of this calibration factor will not be discussed within this work, but the reader is referred to [89].

$$r = \frac{I_{\parallel} - G \cdot I_{\perp}}{I_{\parallel} + 2 \cdot G \cdot I_{\perp}} \quad (7.4)$$

Generally, this quantity is limited between -0.5 and 1.0 . However, due to photoselection, for an ensemble of molecules the maximum achievable anisotropy factor is 0.4 while the minimum is limited to -0.2 . An anisotropy value of zero indicates a complete depolarization which can be attributed to energy transfer mechanisms as the molecular rotation is not present within solid thin films.

7.1.3. Time resolved spectroscopy

Transient measurements of a luminescence decay can be of huge interest when investigating emissive thin films and their properties. Several different methods, such as time-correlated single photon counting, ICCD systems or streak camera experiments exist. Within this work, only the latter method was used and will be described in detail. Nevertheless, the evaluation methods for luminescence decay data obtained from all these experiments are similar.

Streak Camera

The experimental setup used within this work to determine the exciton lifetime of thin film samples consisted of a spectrograph attached to a streak camera. While the spectrograph generates a spatial separation between the wavelengths of the laser light, a streak camera can resolve the time dependency of the signal. Therefore, the emissive sample needs to be excited by a pulsed light source with a suitable pulse width below the exciton decay time. The thereby generated photons are guided onto a photocathode, to convert the light into electrons. These can then be accelerated and deflected by suitable cathodes using a varying deflection voltage to achieve spatial separation in the time domain. Further enhancement of the signal is done via a microchannel plate (MCP) to multiply the incident electrons. These are guided onto a phosphor screen which can be measured to obtain two-dimensional images showing both wavelength and time dependence of the sample signal. Fig. 7.6 depicts this setup and the respective light paths [93].

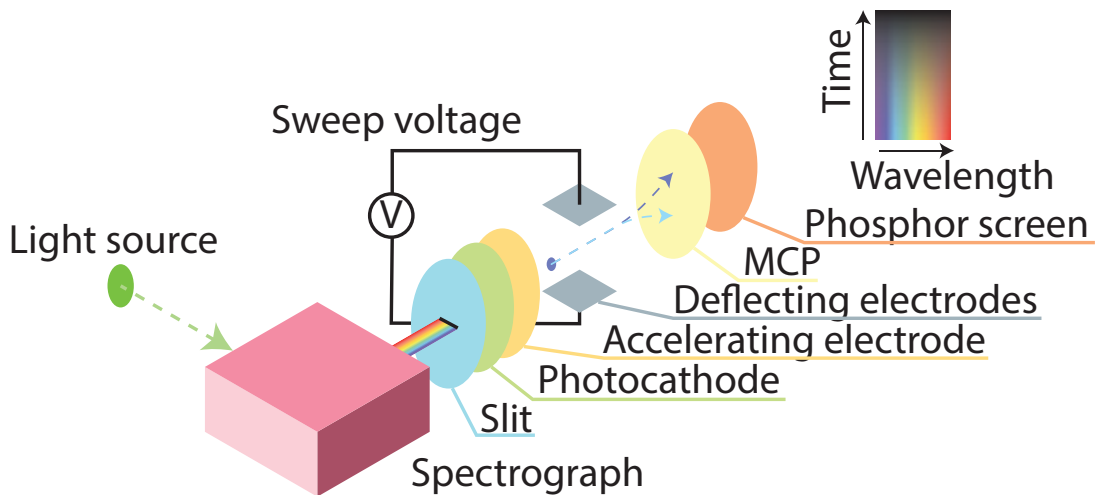


Figure 7.6.: Illustration of a streak camera setup. The light generated in short pulses is guided through a spectrograph to achieve a spatial wavelength separation. Afterward, the beam passes a slit followed by a photocathode to convert the light into electrons. The generated charge carriers can be accelerated and deflected by a sweep voltage to achieve a separation in the time when the photon entered the setup. Finally, a MCP is used for multiplication of the electrons which are then guided onto a phosphor screen. The resultant image separates the signal in both wavelength and time. Picture adapted from [53].

Evaluating luminescence decay

Given the luminescence decay from time-resolved spectroscopy experiment, it is often necessary to obtain intrinsic properties of the investigated system. However, the feasibility to achieve this is limited by the effects involved in the decay process. Given a fluorescent organic semiconductor, the decay rate k of the exciton can be described as the following equation involving both radiative (k_{R}) and nonradiative (k_{NR}) decay of the exciton:

$$k = k_{\text{R}} + k_{\text{NR}}. \quad (7.5)$$

The decay rate determines the transient luminescence decay of the system via the number excitons decaying per time:

$$\dot{n}(t) = -kn(t) = -(k_{\text{R}} + k_{\text{NR}})n(t) \quad (7.6)$$

where $n(t)$ describes the total amount of excited states within the system. Using this expression, the luminescence decay function $L(t)$ can be found as:

$$L(t) = A \cdot \exp(-k \cdot t) + C. \quad (7.7)$$

Therein A and C usually are fitting constants without physical meaning, while k is the only available quantity from the measurement. Interestingly it is not possible to distinguish between radiative and non-radiative decay rates within this experiment. It is important to note that other processes linear to the exciton count also cannot be distinguished, such as an excitonic state with two different decay paths without an intermediate state.

However other systems allow for the extraction of additional information. For example TADF emitting molecules have excitons within both the singlet and the triplet state. This leads to a coupled equation for the excitonic decay [94]:

$$\begin{aligned} \dot{S}(t) &= -(k_{\text{R},\text{S}} + k_{\text{NR},\text{S}})S(t) + k_{\text{RISC}}T(t) - k_{\text{ISC}}S(t) \\ \dot{T}(t) &= -k_{\text{NR},\text{T}}T(t) + k_{\text{ISC}}S(t) - k_{\text{RISC}}T(t). \end{aligned} \quad (7.8)$$

Therein the triplet state is assumed to only decay nonradiatively with a rate of $k_{\text{NR},\text{T}}$. Further, singlets $S(t)$ can be converted into triplets $T(t)$ via intersystem crossing (k_{ISC}) and vice versa (k_{RISC}). As the solution to this equation is too long to be explicitly written within this work, the intersystem crossing rate k_{ISC} is assumed to be very low to give a suitable approximation.

$$L(t) = A \cdot \exp(-(k_{\text{R},\text{S}} + k_{\text{NR},\text{S}}) \cdot t) + B \cdot \exp(-(k_{\text{NR},\text{T}} + k_{\text{RISC}}) \cdot t) + C. \quad (7.9)$$

Interestingly, the luminescence decay in this expression reveals two different time constants. Therein one denotes the rapid decay that can be attributed to the fluorescent signal, while the other involves the non-radiative rate of triplet decay as well as the reverse intersystem crossing rate.

7.1.4. Determination of the radiation pattern and orientation parameters

In order to determine the angular dependent emission intensity of a sample, it is necessary to perform an angularly resolved measurement. Two different methods can perform this measurement. Angular dependent measurements were performed at the University of Augsburg where the experimental setup was improved during the master theses of Philippe Linsmayer and Felix Höhnle. Further, back focal plane imaging was performed in cooperation with Carissa Eisler at the Molecular Foundry in the Lawrence Berkeley National Laboratory.

One experimental procedure for the determination of the radiation pattern of a thin film sample is angular dependent photoluminescence spectroscopy (ADPL) [85]. Therein the sample is rotated with respect to a detection optic attached to a spectrometer. This method allows for the subsequent acquisition of a wavelength-resolved spectrum for each emission angle. Contrary to this, the back focal plane (BFP) imaging aims to determine the radiation pattern within one measurement by observing the back focal plane of a high numerical aperture objective [95, 96]. In this plane, each angle of incidence on the objective can be resolved at a different location of the image. Both methods are shown in fig 7.7. This section will introduce ADPL measurements as the main method of determination for orientation parameters. Further exemplary measurements will be given and compared to BFP imaging techniques as a second experimental technique.

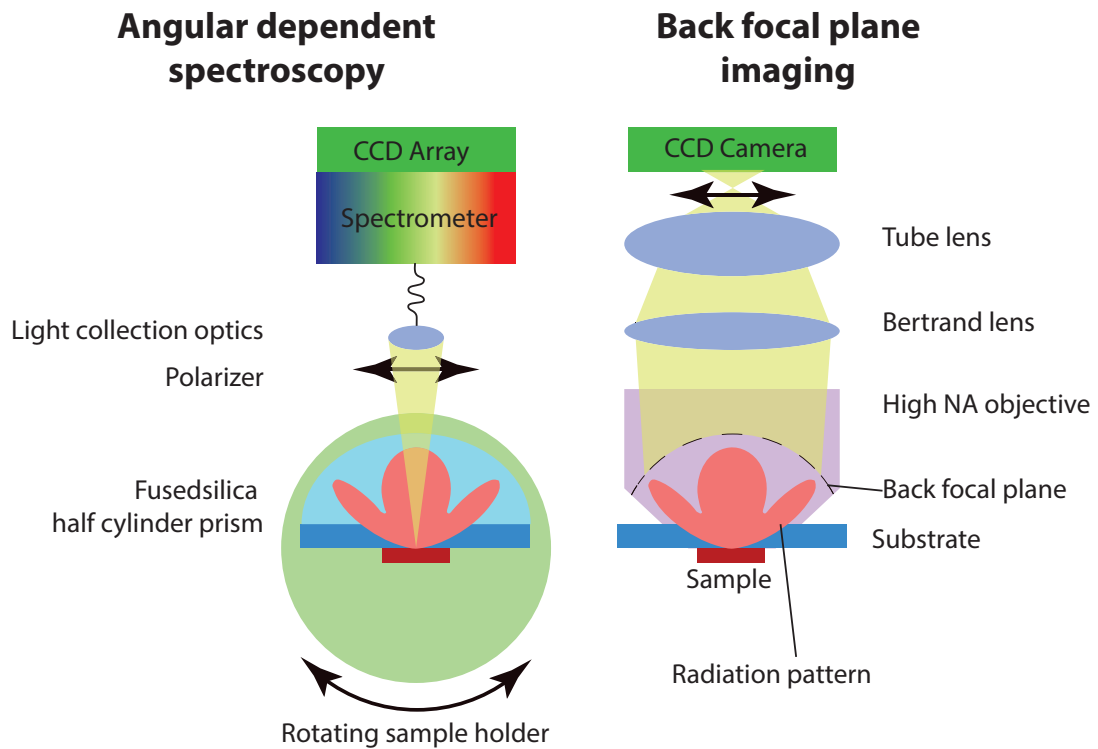


Figure 7.7.: Illustration of two methods able to determine the radiation pattern of an emissive sample. In the angular dependent spectroscopy (left) sample and detector are rotated with respect to each other, whereas back focal plane imaging (right) allows for the determination within one measurement via high numerical aperture microscopy.

ADPL Measurements

Angular resolved measurements of the radiation pattern of a thin film can be performed by different experimental configurations that will be explained within the following section. Generally, two parts of the experiments can be distinguished. The excitation of the emissive thin film is usually achieved via a laser beam guided onto the sample. Additionally, the light emitted from the excited sample needs to be collected using suitable optics. For the excitation of the sample, several aspects need to be taken into account:

1. The polarization state of the incident laser beam.
2. The energy of the exciting laser.
3. The excitation angle on the emissive sample.

Further, the incident beam needs to be adjustable in both translation and gimbal to guide the light onto the sample. For control of polarization and incident energy of the excitation beam, two polarizers and a $\lambda/2$ waveplate were used. Stringing together two polarizers allows for precise control of the energy of the laser via the difference in the polarization planes of the two components. Further, guiding the output of the second polarizer through the waveplate enables the rotation of the polarization plane without changing the energy of the beam. Note that these components are optional and an unpolarized beam with a single power level can also be used. To enable the beam path being adjustable with respect to the rotating sample holder, either two mirrors or a four-axis stage need to be introduced. Finally, to guide the beam onto the sample, a suitable lens is used to reduce the size of excitation spot, which is crucial for the sensitivity of the measurement.

Regarding the detection optics, several considerations need to be made. The lens or lens system should be able to guide the whole excited spot into the detector. Within this work, an optical fiber was used to lead the collected light into a spectrometer. Hence the image size of the system needs to be smaller than the fiber core, which was $550\ \mu\text{m}$ throughout for all experiments. If the light collection is incomplete, measurement errors can occur leading to false orientation data. Further, it is important to note that the optical properties of the system should be suitable for the investigated wavelengths. For spectra of organic dyes, an achromatic optical system is necessary. Besides the chromatic aberration, the spherical aberration of the lens can also alter the observed data. Especially if using low focal length optics, aspherical shapes should be used within the system to prevent these errors from occurring.

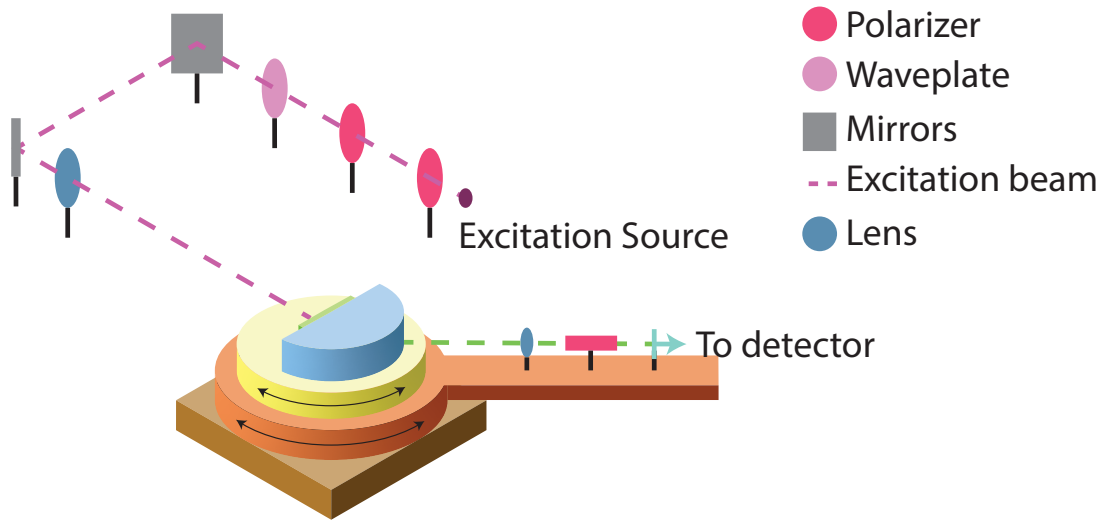


Figure 7.8.: Depiction of an experimental setup for ADPL measurements. The excitation light source is guided through polarizers and a waveplate to adjust both power and polarization of the incident beam. Afterward, the beam is reflected by two adjustment mirrors and guided through a lens focusing the beam onto the sample. The light emitted by the sample is collected via a lens and guided into the detector, often connected via an optical fiber. Adding a polarizer into the detection path enables independent measurements of the radiation pattern for s- and p-polarized light.

For the separation of s- and p-polarized light as well as fluorescence anisotropy measurements, a polarizer needs to be introduced into the detection path. While wire grid polarizers are sufficient for the respective components of the radiation pattern, sensitive fluorescent measurements require a higher extinction ratio such as provided by birefringent polarizers.

Both the excitation and detection pathways need to be aligned with respect to the optical axis of the system. To be able to detect misalignment during the determination of the radiation pattern, measurements should be performed covering symmetrical angles. For example, a measurement of the radiation pattern should be performed from -80° to $+80^\circ$, and the corresponding symmetrical parts should match each other.

It should be emphasized that both excitation and emission can be mounted onto the rotating part of the setup. However, if the polarization state of the exciting laser beam is of interest, fixing this section of the setup to an optical table is recommended.

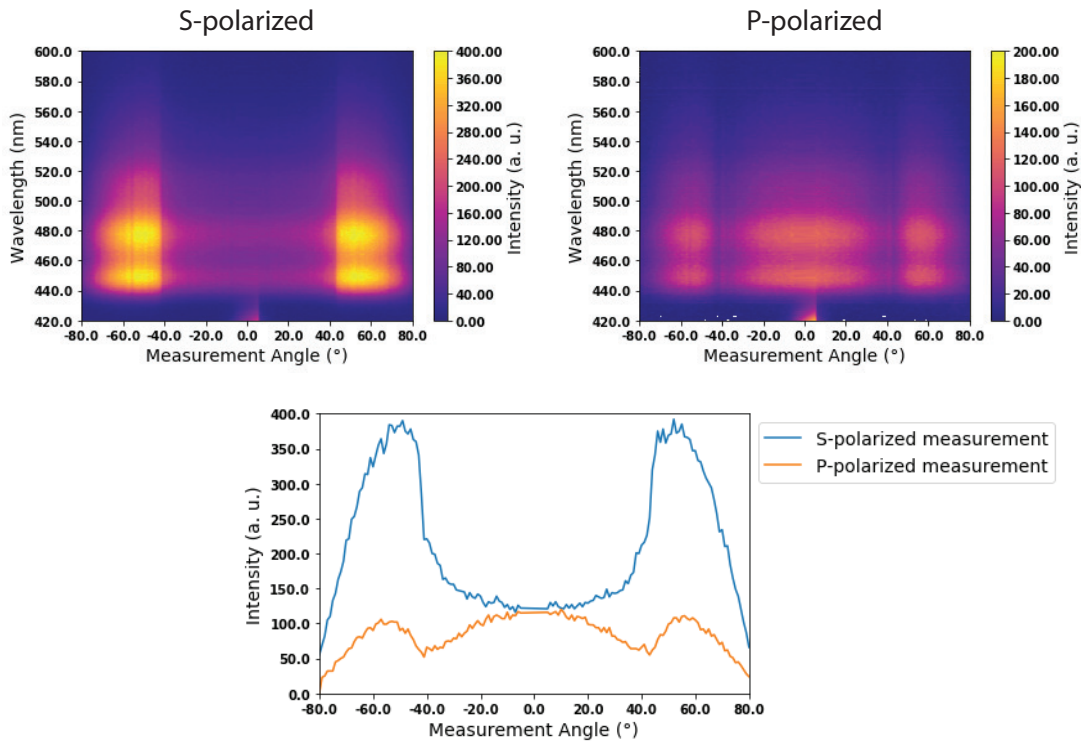


Figure 7.9.: Exemplary measurements for s-polarized (left) and p-polarized (right) emission spectra from a thin film sample. The radiation pattern at 480 nm (bottom) shows characteristic shapes for a thin film sample. The sample consisted of the dye molecule fac-1295-A doped into a DPEPO host medium.

Taking all these considerations into account, a setup for angular dependent spectroscopy consists of the sections given in fig. 7.8. Therein the experimental setup is shown for the detection light path onto a rotatable assembly whereas the excitation light path is fixed.

An ADPL measurement results in a single spectrum for each angle. This whole radiation pattern as depicted in fig 7.9 also allows for the extraction of the radiation pattern of individual wavelengths which will be used for the analysis of the emissive TDMs within the system.

Extraction of TDM properties from ADPL measurements

In order to extract the various orientation parameters describing the alignment of the emissive TDM, the experimental data needs to be fitted to the optical simulation model [15, 16, 85] as presented in sections 5 and 6.3. At first, the

7. Experimental methods

s-polarized measurement is utilized to calculate the thickness of the emissive film. This procedure can either be applied to the full measurement, selected wavelengths or each wavelength individually. As the thickness should be constant for the full wavelength range, deviations in the fit result for different wavelengths indicate mistakes in the system modeling, being either false refractive indices or missing additional layers of the system. An exemplary fit is depicted in fig 7.10, revealing a thickness of 35 nm.

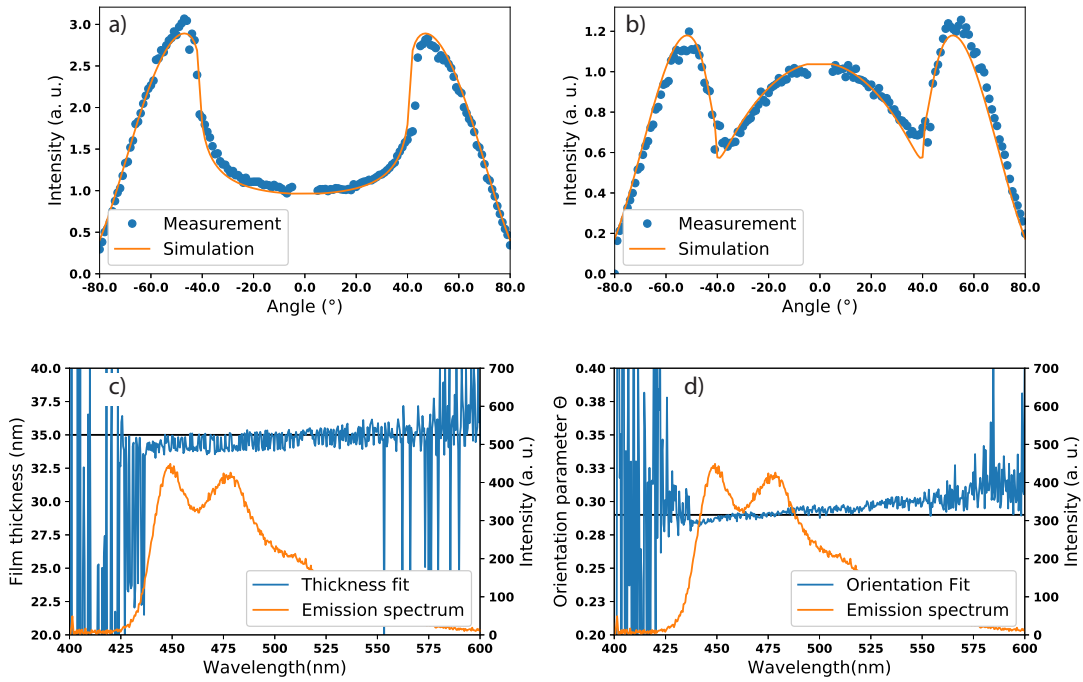


Figure 7.10.: Exemplary analysis of the measurement data shown in fig 7.9. (a) s-polarized fit of the measurement data at 480 nm wavelength resulting in 35 nm film thickness. (b) corresponding fit of the p-polarized measurement. (c) and (d) show the results of the procedure for each individual wavelength and the emission spectrum of the dye molecule. Although a small deviation within the emission range is visible, this does not affect the outcome for this experiment.

Note that the calculation generally is using a single emissive dipole centered within the film to describe the radiation pattern. If the thickness exceeds 50 nm, this simplification cannot be applied anymore. Hence, the simulation of an emission profile along the film is required in this case.

As a second step, the p-polarized measurement is fitted to the optical sim-

ulation while weighting the contributions from horizontal and vertical dipoles. Hence, the resultant weights of the two contributions lead to the quantities for preferential alignment as described in section 4.2. As a rule of thumb, it can be concluded that the height of the emission peak at angles above 40° indicates the fraction of vertical dipoles.

Utilizing BFP imaging for the extraction of optical properties

BFP imaging has rarely been used to determine the preferential alignment of TDMs. Especially for amorphous organic systems the technique has rarely been applied. Hence, in order to establish the method as a second technique besides ADPL, two different types of emissive systems were chosen. Organic guest-host mixtures, such as Ir(mdq)₂(acac) doped into NPB, are widely used in organic lighting applications [8, 36, 37, 97]. The preferential alignment of the organometallic dye molecules depends on the preparation technique [36, 37]. In this work, the investigated films were deposited either from solution via spin-coating or from thermal evaporation in a vacuum chamber. The different deposition techniques affect the alignment of the dye molecules, leading to isotropic radiation patterns for the solution processed samples and preferentially horizontal orientation for the samples prepared from thermal evaporation [36, 37].

As a second emissive system self-organized CsPbBr₃ nanocrystals were investigated. This material exhibits a narrow green emission band, high photoluminescence quantum yields, and almost zero stokes shift [98–100]. Further, this material has recently been found to exhibit vertically aligned transition dipole moments despite their high brightness [38].

The detailed processes leading to the alignment properties of the systems will be discussed in the following chapters.

BFP imaging results for both systems are shown in figure 7.11. Measurements without polarizer already show different intensities of the outer ring, indicating isotropic orientation for the guest host system and vertical alignment for the perovskite nanocrystals. This agreement is further confirmed by a detailed analysis of the BFP measurements with a polarizer. The p-polarized lines within the BFP image reveal the exact quantities for the alignment properties of the material, whereas the s-polarized lines do not contain any information about this property.

In order to verify the BFP images for future application, the data was compared to ADPL results as shown in figs. 7.12 a and b . Therein the data extracted from the BFP images are in good agreement to ADPL spectra. To further demonstrate the correctness of the method, different alignment quantities were extracted and compared to the respective literature values, shown in fig. 7.12 c. All three values, Θ , ζ and the TDM angle to the surface are in excellent

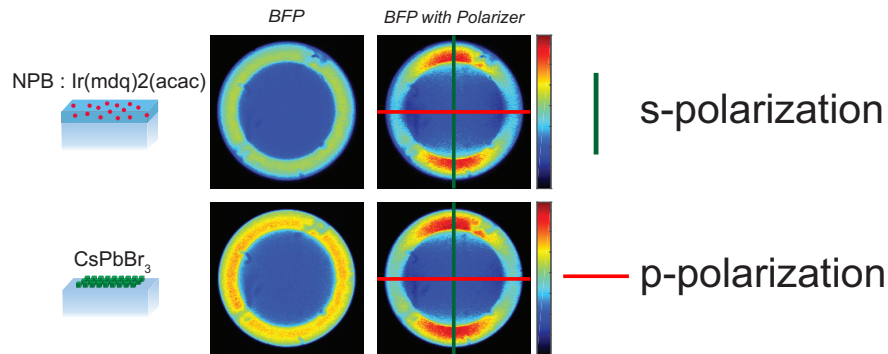


Figure 7.11.: BFP measurements for two different emissive systems. The images are shown without polarizer (left) and with polarizer (right). In contrast to ADPL measurements, both polarizations can be investigated within one image. The corresponding lines to the s- and p-polarized ADPL measurements are shown as green (s-polarized) and red (p-polarized) lines.

agreement to the known literature values.

In conclusion, BFP imaging is an equally effective method to determine the radiation pattern of emissive thin films compared to ADPL measurements. For all investigated systems the results were in agreement between the measurement techniques, leading to correct orientation data. Especially for nanocrystal systems or quantum dots featuring narrow emission spectra, BFP imaging is a compelling and efficient technique as only one image of the emission has to be measured. Further, the presented technique is not affected by degradation of the sample.

Polarization anisotropy and its effects on the radiation pattern

An anisotropic excitation of the emissive species can have a crucial impact on the proper determination of the radiation pattern. For samples exhibiting polarization anisotropy, incomplete energy transfer between the emissive sites is present. As a consequence of this effect, the emissive sites within the film are not excited isotropically. Hence, upon excitation with a laser, the orientation of the emitting molecules will seem to be preferentially aligned within the plane of excitation. Within the previously described setup using perpendicular incidence of the laser beam, the procedure would preferentially excite in-plane molecules leading to a false determination of the orientation parameters.

To investigate this problem, multiple concentrations of a guest host system were prepared. The samples consisting of PMMA doped with Coumarin6 were

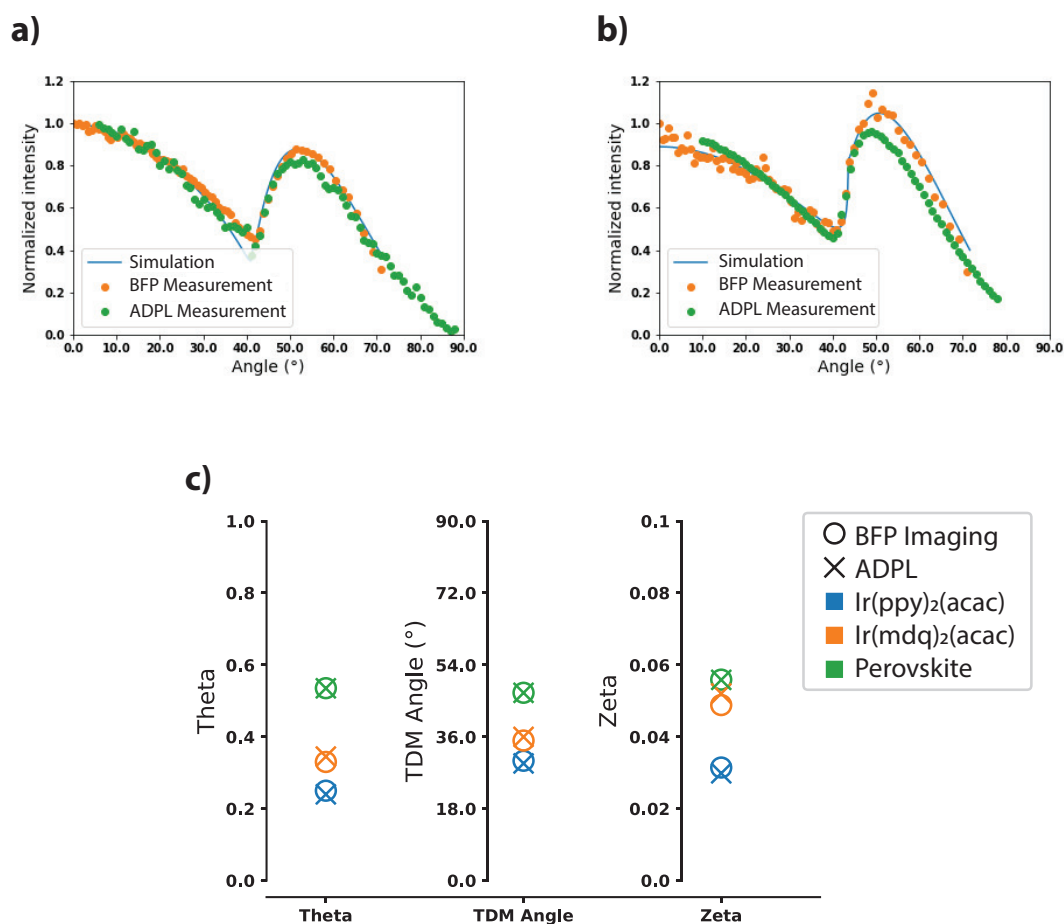


Figure 7.12.: Comparison of BFP imaging to ADPL measurements. a) and b) show the direct comparison of measurements, showing the radiation pattern extracted from the BFP image (orange circles) as well as the ADPL measurement (green circles) for Ir(ppy)₂(acac) in CBP (a) and perovskite nanocrystals (b). Further, the fit of the optical simulation to the BFP result is shown as the blue line. It should be pointed out that ADPL and BFP imaging were performed using different substrates. Hence, the orientation values can be equal despite the fact that the measurements do not match each other. (c) depicts the results for the three different quantifications of preferential alignment, the orientation factor Θ , the angle of the emissive TDM to the substrate and the alignment constant ζ . In all three cases, the results match each other.

7. Experimental methods

deposited from solution to ensure the isotropic distribution of the molecules and their transition dipole moments. The concentrations varied from 0.01% wt. up to 10% wt.. The photoluminescence of the samples was excited using a 442 nm laser.

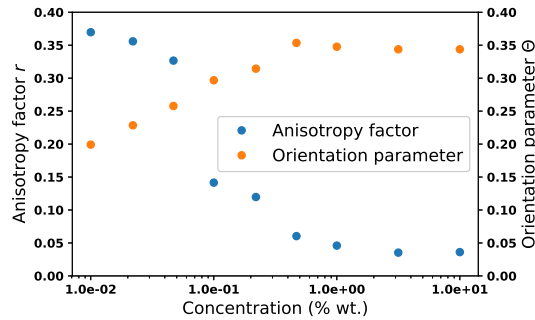


Figure 7.13.: Anisotropy factor r and corresponding Θ values for Coumarin6 doped into PMMA at various concentrations. Due to the samples being prepared from solution, the molecules are isotropically distributed within the guest host system. However, upon lowering the concentration the orientation parameter begins to decrease whereas the polarization anisotropy increases.

Measurements of both the anisotropy factor and the orientation parameter Θ for the sample series, as depicted in fig. 7.13, reveal a connection between the increasing anisotropy and the decreasing orientation parameter. Note that the samples were excited perpendicular to the interface, preferentially exciting horizontal molecules. This behavior indicates an arising measurement error as the excited states are not equally distributed within the system due to the incomplete energy transfer between the Coumarin6 molecules.

7.2. Electrical characterization

Evaluation of the electrical properties of a thin film optoelectronic device can yield detailed information about the system. Using current-voltage characteristics combined with the luminance, the light emission of the device, allows for a quick determination of basic device properties. Yet, the detailed quantification is only possible if combined with further techniques. While several methods for the quantification of mobilities, injection properties as well as quenching mechanisms exist, this section will be limited to impedance spectroscopy as a method to analyze preferentially aligned permanent dipole moments (PDMs).

7.2.1. Extracting interfacial sheet charge density from impedance measurements

Measurements of the impedance of an electrical system aim to determine capacitance, inductivity, and resistance of a given system. Within the context of thin film semiconductors, inductivity can be neglected and will not be further investigated. For this measurement technique, a voltage signal is applied to the sample. This signal consists of a constant offset as well as a small alternating component, usually in the range of a hundred millivolts. Hence the current flow through the system will have a constant as well as an alternating component. Further, it will exhibit a phase shift concerning the applied voltage, as depicted in fig. 7.14.

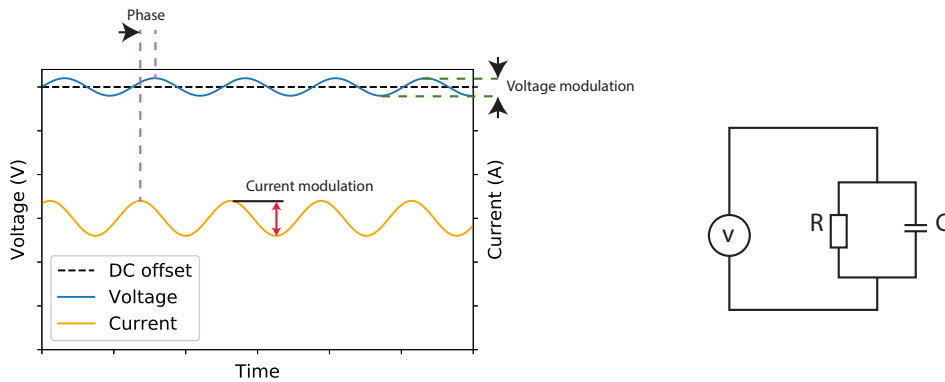


Figure 7.14.: Illustration of an impedance measurement (left). The applied voltage consists of a DC offset as well as a small alternating modulation. The resultant current shows a constant as well as an alternating component. Further, the modulated current is phase shifted with respect to the applied voltage. Using an appropriate circuit model such as shown on the right side of the picture, capacitance and resistivity of the system can be determined.

Taking these experimentally obtained values into account, it is possible to calculate the impedance Z of the system, described by a complex number. Further, the capacitance of the system can be obtained from a circuit model as illustrated in fig 7.14. For the depicted system the capacitance can be analytically calculated from the measured impedance and the frequency of the AC modulation f :

$$C = -\frac{1}{2\pi f} \frac{\text{Im}(Z)}{|Z|^2}. \quad (7.10)$$

7. Experimental methods

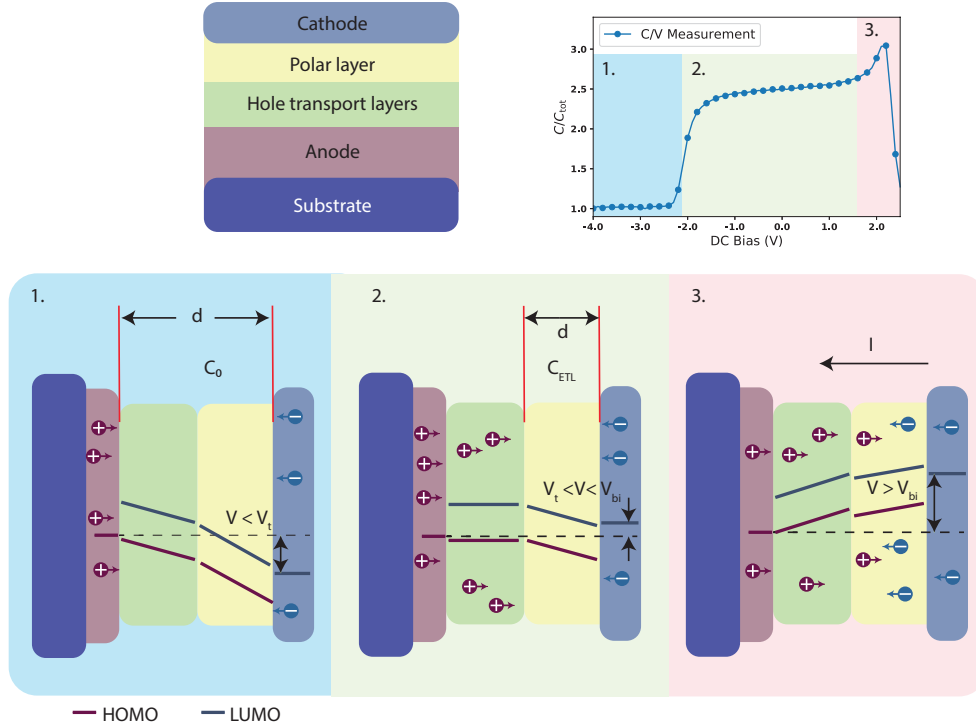


Figure 7.15.: Schematic processes inside a bilayer device with a polar ETL. At low offset voltages (1) the measured capacitance corresponds to the thickness of both the HTL and the polar layer. Upon exceeding a certain threshold voltage holes are being injected into the HTL and accumulate at the interface to the polar layer (2). Further increase of the voltage eventually leads to the injection of electrons from the cathode or holes into the polar layer, making the device conductive (3) [101].

Within this measurement technique, the magnitude of the DC offset, as well as the frequency of the signal, can be of interest. While the latter will not be investigated within this work, a sweep of the voltage offset can reveal intrinsic properties of the thin film system such as an internal surface charge.

In order to determine the interfacial sheet charge density of a polar film, usually a bilayer device with two contacts is used as depicted in fig 7.15 [10]. The capacitance-voltage (C-V) dependence of this system is divided into three different regions. At first, neither holes nor electrons are injected into the system. In this case, the whole device acts as a capacitor and the resultant capacitance resembles the thickness of the whole system. Upon reaching a specific transition voltage, holes are being injected into the hole transport layer but not into the po-

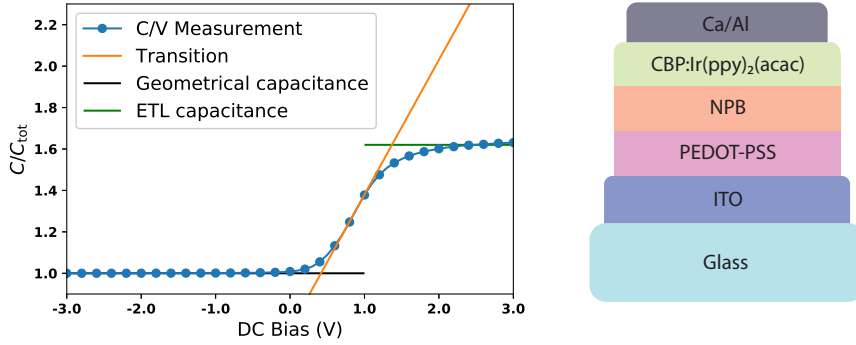


Figure 7.16.: Depiction of a capacitance voltage measurement for a bilayer device incorporating a polar ETL. The transition marks the injection of holes into the HTL which leads to the increase in capacitance. Although not shown the bias voltage V_{bi} can be easily obtained from the voltage at which the capacitance collapses to zero.

lar film. At this point, the effective thickness of the capacitor decreases as holes accumulate at the HTL-ETL interface. Thereby the capacitance is increased. Finally, as both charge carriers are injected when reaching the bias voltage, a current is flowing through the device, and the capacitance decreases to zero.

The exemplary C-V measurement shown in fig. 7.16 depicts the approach to determine the interfacial sheet charge density within a bilayer device. Therein the transition voltage V_T as well as the bias voltage V_{bi} yield the interfacial sheet charge density σ_{IF} of the polar material [10].

$$\sigma_{IF} = \frac{\varepsilon_0 \varepsilon_r}{d_{ETL}} (V_T - V_{bi}) = \frac{C_{ETL}}{A} (V_T - V_{bi}) \quad (7.11)$$

Therein either the thickness d_{ETL} and the relative permittivity ε_r of the film need to be known or the capacitance C_{ETL} of the film and the area A of the device.

7.2.2. Determination of the preferential alignment of PDMs

Evaluating the orientation of aligned PDMs within a thin film allows for conclusions about molecular alignment within the system. The determination can be achieved by knowledge of the interfacial sheet charge density of both the experimental sample and an idealized, perfectly aligned sample. The ratio between the two thus yields the degree of orientation for the investigated film [10, 11].

The maximum possible polarization of a film can be calculated by knowing

7. Experimental methods

the individual PDM of a single molecule μ as well as the amount of contributing PDMs (N) in the volume of the prepared film (V).

$$\sigma_{\text{IF}} = \mu \cdot \frac{N}{V} = \mu \cdot d \cdot \frac{\rho \cdot N_{\text{A}}}{M} \quad (7.12)$$

This can be calculated from the thickness d of the film as well as the density ρ , the molar mass of the contributing molecule M and the Avogadro constant N_{A} . In the case of a diluted system in which only one polar entity contributes to the sheet charge density of the system, the concentration needs to be taken into account:

$$\sigma_{\text{IF,MAX}} = \mu \cdot \frac{N_{\text{dopant}}}{V_{\text{total}}} = \mu \cdot \frac{d_{\text{dopant}}}{d_{\text{total}}} \cdot \frac{\rho_{\text{dopant}} \cdot N_{\text{A}}}{M_{\text{dopant}}}. \quad (7.13)$$

Therein the individual density ρ_{dopant} , and molar mass M_{dopant} of the dopant need to be taken into account. Further total thickness d_{total} and the individual thickness of the dye film d_{dopant} as detected during sample preparation via co-deposition are necessary [11].

As the density of the dopant in a thin film often is not available, this quantity can easily be accessed by molecular dynamics simulations. Usually, an ensemble of several hundred molecules is calculated for at least 30 ns in order to achieve the necessary precision for the density [11].

The relation between the experimentally obtained interfacial charge σ_{IF} and the maximum possible charge $\sigma_{\text{IF,MAX}}$ leads to the orientation parameter Λ [11]:

$$\Lambda = \frac{\sigma_{\text{IF}}}{\sigma_{\text{IF,MAX}}}. \quad (7.14)$$

This parameter expresses the fraction of PDMs aligned perpendicular to the film surface. Note that Λ is also tied to the orientation of the PDMs within a sample, assuming that all dipoles are aligned with the same angle α with respect to the surface and no compensation effects are present [11].

$$\Lambda = \sin(\alpha) \quad (7.15)$$

Part III.

Results - Understanding and predicting optical anisotropy in amorphous thin films

Not only is the Universe stranger than we think, it is stranger than we can think.

Werner Heisenberg

8. Anisotropy of small fluorescent molecules

Preferential alignment of small molecules and their emissive TDMs can occur in many organic systems. As a starting point, this chapter will focus on fluorescent molecules only emitting from the singlet state. This approach provides the advantage of less resource intensive computational descriptions as well as simple molecules. The materials investigated within this chapter as shown in fig. 8.1 exhibit a single TDM for Coumarin6 and two nearly parallel TDMs for DCM. Further, both dyes have a PDM, making them polar entities within an organic film.

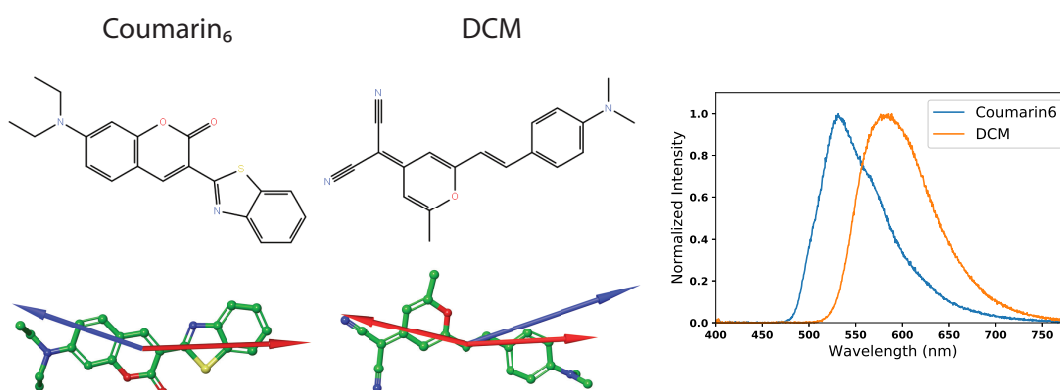


Figure 8.1.: The two polar dye molecules Coumarin6 and DCM with their respective PDMs (blue arrows) and TDMs (red arrows). Note that DCM exhibits two dominant TDMs with slightly different directions. Solution spectra for the two molecules in Chloroform at a concentration of 1 mg ml^{-1} show a predominantly green emission for Coumarin6 and a red spectrum for DCM.

The following sections will investigate two different effects related to the emissive TDMs of the molecules. First, the possible influence of dipolar interaction within films will be evaluated. Further, the preferential alignment of the dye molecules within neat films and organic guest-host systems will be investigated

using ADPL measurements. Finally, the molecule Coumarin6 will be taken as an exemplary molecule for fluorescence anisotropy within organic guest-host systems.

Further, given the high polarity of the molecules, a solid state solvent shift is expected. This effect lowers the gap of the organic dye as the polarity of the surrounding medium is increased [102, 103].

Investigations of the preferential alignment of Coumarin6 and DCM were performed by Thomas Gimpel within his Bachelor’s thesis while being supervised by Thomas Morgenstern. Further refinement to the experimental data was performed within this thesis using novel evaluation methods. Polarization anisotropy was measured by Felix Höhnle within his Masters thesis.

8.1. Alignment mechanisms of small polar dyes

The orientation of small molecule organic semiconductors is a topic of great interest. After the first application of ADPL to the rod-like molecule, BDASBi [85] a vast amount of organic systems have been investigated for their preferred alignment. Those different molecular approaches include classical fluorescent small molecules, such as Coumarin6, donor-acceptor assemblies exhibiting TADF processes as well as organometallic complexes including phosphorescent Iridium or Platinum compounds [8, 36, 37, 104–106]. Within this section, only polar and non-organometallic molecules will be discussed.

The dipolar property of polar dye molecules makes them susceptible to dipole-dipole interactions. For two given dipole moments $\vec{\mu}_1$ and $\vec{\mu}_2$, as well as the vector \vec{r} separating the two entities, this can be expressed as:

$$V(r) = \frac{1}{4\pi\epsilon_0|r|^3} \left(\vec{\mu}_1 \cdot \vec{\mu}_2 - 3 \frac{(\vec{\mu}_1 \cdot \vec{r})(\vec{\mu}_2 \cdot \vec{r})}{|r|^2} \right) \quad (8.1)$$

where ϵ_0 denotes the dielectric constant. In the case of an antiparallel configuration of two dipoles next to each other, this energy simplifies to

$$V(r) = -\frac{\vec{\mu}_1 \cdot \vec{\mu}_2}{4\pi\epsilon_0 r^3}. \quad (8.2)$$

To evaluate whether the magnitude of the molecular PDM affects the film formation, the dipolar interaction potential energy can be compared to the thermal energy of the molecules, where each entity can be attributed with $E_{\text{thermal}} = \frac{3}{2}k_{\text{B}}T$ via the Boltzmann constant k_{B} and the temperature T .

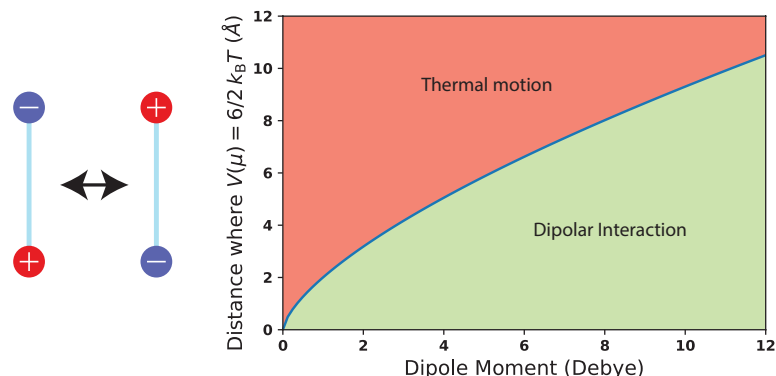


Figure 8.2.: Interaction potential of two antiparallel dipoles compared to their thermal energy $\frac{6}{2}k_B T$. If the average distance between two molecules exceeds the critical separation, the PDM will not be able to affect the morphological properties of the film.

Using this, the maximum distance at which the dipole potential exceeds the thermal energy can be expressed:

$$r = \sqrt[3]{\frac{\mu^2}{4\pi\epsilon_0 \frac{6}{2}k_B T}}. \quad (8.3)$$

It is important to note that two molecules contribute to the total thermal energy. From the above expression, it is possible to calculate the minimum PDM for any given distance that can affect the film formation, as depicted in fig. 8.2. Most notably, the distance between the molecules required for an effect of the dipolar interaction is within the range of several Å, as expected within an amorphous thin film. Hence, the following section will employ molecular dynamics simulations to get an estimate to this quantity.

8.1.1. Dipolar interactions Coumarin6 and DCM

The photophysical properties of the investigated molecules Coumarin6 and DCM make both of them suitable fluorescent dyes which are prone to dipolar interaction. Coumarin6 is a green polar dye molecule, exhibiting a PDM of 7.894 Debye. As a second molecule, DCM mostly emits light in the red regime and has a large PDM of 10.16 Debye. Both values were obtained from DFT calculations using the B3LYP functional and 6-31G** basis set.

For the Coumarin6 molecule, the possibility of the PDM affecting the film morphology can be estimated. At first, the average molecular distance was de-

ducted from molecular dynamics simulations. Therein a dense system of 870 Coumarin6 molecules is calculated for a duration of 30 ns using the OPLS3 force field. The analysis of the system for the separation between the dye molecules yields an estimate to the average molecular distance. The resultant values, as depicted in fig 8.3 revealed a minimum distance of the molecular centers of masses of 3 Å. Further, the integration of the probability, leads to the average amount of molecules within a given distance. In the example within a separation of 6 Å at least one other molecule will be located.

This simplified model indicates that for the Coumarin6 molecule in neat film concentrations the morphology of the film will be dominated by dipolar interaction. These findings can be deduced from the threshold distance of about 7 Å below which the dipolar interaction strength overcomes the thermal energy of the molecules. Further investigations were done by diluting the system. The lower dye content increases the intermolecular distance up to a value at which this effect becomes negligible.

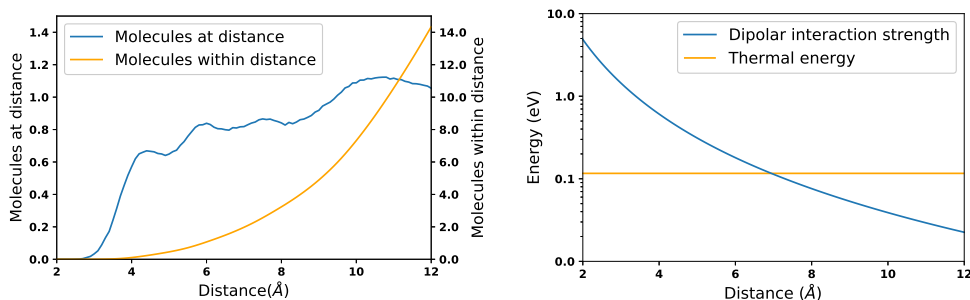


Figure 8.3.: Average molecular separation of C6 molecules within a simulated box of 870 molecules (left) and dipolar interaction strength as compared to thermal energy of the two interacting molecules (right).

An even more pronounced behavior is found for the DCM molecule exhibiting a PDM of 10.16 Debye. Therein, as shown in fig. 8.4, the average intermolecular distance is even lower due to the smaller molecular geometry. Thus, the lowest value for intermolecular separation can be determined to 2.1 Å. Further, at least one molecule is within a distance of 5.8 Å while the saturation distance of the dipolar interaction exceeds 8 Å. This distance again indicates domination of dipolar interaction for films consisting of the DCM dye.

To investigate the solid state solvent shift, Coumarin6 as the less polar molecule was doped into Alq₃ having a dipole moment of 4.29 Debye as well as the non-polar matrix Spiro2-CBP. Measured emission spectra from the thin film are shown in fig. 8.5. Therein the solid state solvation shift is visible. However,

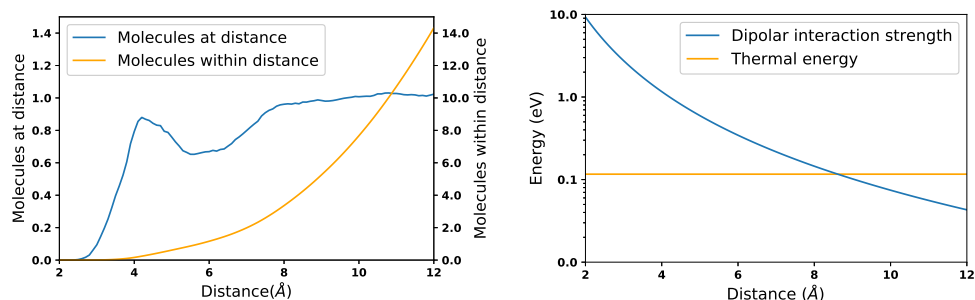


Figure 8.4.: Average molecular separation of DCM molecules within a simulated box of 870 molecules (left) and dipolar interaction strength as compared to thermal energy of the two interacting molecules (right).

for the polar host material, the shift is saturating at a concentration of around 30% and the resultant spectrum is broader than the low concentration emission. The same effect is observable for the non-polar matrix. Again the emission spectra are shifted to higher wavelengths while vastly broadening the spectrum with increasing concentration. Further, the initial emission in this material is at higher energies due to the missing polarity of the host molecule. In comparison to the solution spectra, shown in fig. 8.1, the shape of the spectra indicates emission from an aggregate of molecules. However, further experiments would be necessary to confirm this assumption.

Measurements of the dye molecule DCM were performed in the polar host molecule Alq₃ as well as the less polar NPB it is important to note that despite its structure the latter medium also exhibits a permanent dipole moment of 0.6 Debye. Measured spectra for both experiments are shown in fig 8.6. Therein the solid state solvation shift is visible as the emission maximum is continuously shifted towards lower energies as the concentration of the polar dye is increased. Further, the initial emission spectrum at low dye content is at higher energies for the non-polar host medium compared to the polar matrix. Interestingly, DCM features a broader spectrum within the non-polar material as compared to the polar medium.

The presence of the solid-state solvent shift in both systems confirms the polar properties of both molecules. Further, it can be expected that a dilution of the system would tune the polarity of the film and consequently the dipolar interaction between the molecules.

In order to quantify the interaction strength of both dye molecules within their respective polar and non-polar host materials, molecular dynamics simulations were performed. For each of the four systems, DCM doped into NPB, DCM

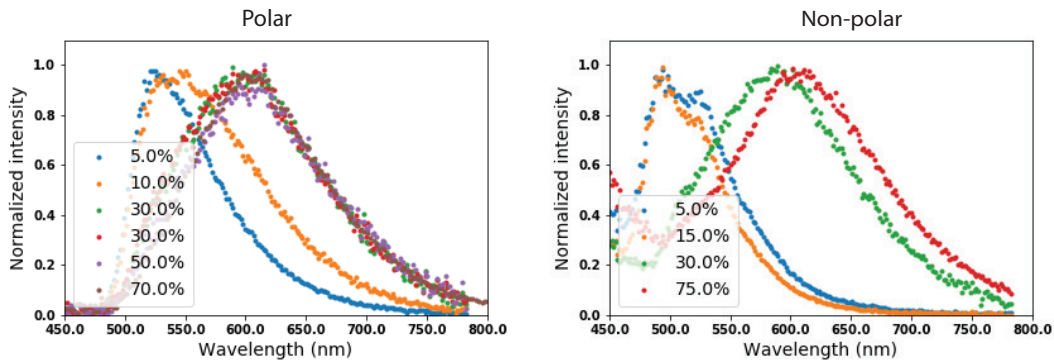


Figure 8.5.: Emission spectra of Coumarin6 doped into Alq_3 (left) and Spiro2-CBP (right) at various concentrations. For the measurements in the polar host material, 5% and 10% concentrations yield the green spectrum of the dye, whereas higher concentrations show a broad red spectrum almost independent of the dye concentration. The same effect is observable for the non-polar host material, although the low concentration spectrum occurs for slightly higher energies.

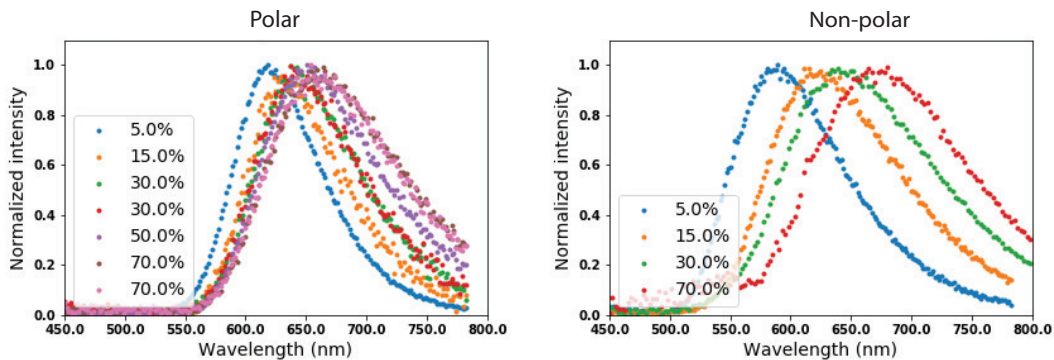


Figure 8.6.: Measured emission spectra for DCM in a Alq_3 matrix (left) as well as NPB as host material (right). In both cases the continuous red-shift of the emission is observable. For the non-polar host medium the initial emission maximum is located below 600 nm, whereas this is above 600 nm for the polar medium.

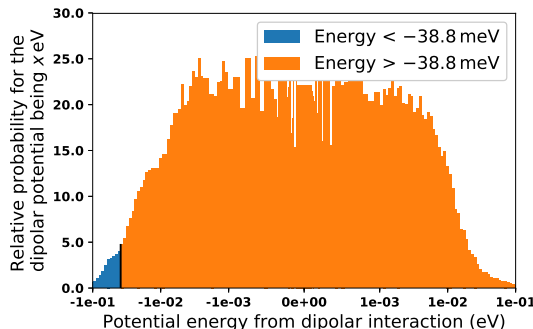


Figure 8.7.: Histogram of the dipolar interaction potentials within a molecular dynamics system consisting of 50% Coumarin6 and 50% NPB. The data can be divided by the thermal energy of an individual molecule being 38.8 meV. Molecules with a dipolar interaction potential lower than this energy are bound by the potential, whereas other molecules can overcome the dipolar interaction. Note that the widths of the histogram bins are logarithmic. Hence most of the molecules show high, positive or negative potential.

doped into Alq₃, Coumarin6 doped into Spiro2–CBP and Coumarin6 doped into Alq₃, different concentrations were calculated. Each simulation included a total of 870 molecules with dye concentrations of 10%, 30%, 50%, 70% and neat films. After initial relaxation a total of 30 ns were calculated. Further the first 15 ns were required for the system to reach the ground state. Hence only the final 15 ns were taken into account for the analysis.

After simulation, the systems were analyzed for their dipolar interactions. Contrary to the approximation given in fig. 8.2, the exact interaction strength was calculated. Hence, for each dye molecule, both the dipolar interaction with the other dye molecules and the interaction with the host molecules were calculated separately and for each frame of the molecular dynamics simulation. The following paragraphs will summarize the analysis for exemplary systems and depict the results for all performed simulations.

At first, the dipolar interaction potential for each dye molecule within each calculation snapshot was calculated. 15 ns involve 500 individual snapshots of the molecular dynamics simulation. Afterward, these energies can be analyzed statistically for their frequency of appearance within the system as depicted in a histogram in fig. 8.7.

Further, each molecule was investigated for the total energy as a sum of the dipolar potential V_{dipole} and the thermal energy $E_{\text{Therm}} = \frac{3}{2}k_{\text{b}}T = 38.8 \text{ meV}$.

Hence, if the condition

$$V_{\text{dipole}} + E_{\text{Therm}} \leq 0 \quad (8.4)$$

is fulfilled, the molecule is bound to the dipolar interaction. Repeating this procedure for the whole system yields insight into the fraction of molecules being bound to the dipolar potential. While the applied procedure is only an approximation, the calculations yield information if dipolar interaction dominates the morphology of the system or if other processes define it.

Further, the distance to the nearest neighbor for each dye molecule can be investigated. As dipolar interaction is vastly dependent on the separation between the dipoles, this yields further insight into the role of dipolar interaction within the system according to fig. 8.4 and 8.3. Fig. 8.8 shows the increasing gap to the nearest neighbour for various concentrations of Coumarin6 doped into NPB. Therein the separation to the closest next dye molecule is below 5 Å for neat films of the dopant with some molecules being as close as 3 Å. Lowering the dye concentration increases this distance and broadens the distribution with an average distance of more than 10 Å for concentrations of 10%. From this analysis, it is obvious that the dipolar interaction will increase as the concentration rises. Additionally, the dipolar interaction does not seem to induce serious aggregation within the simulation due to the molecules being more separated at lower concentrations.

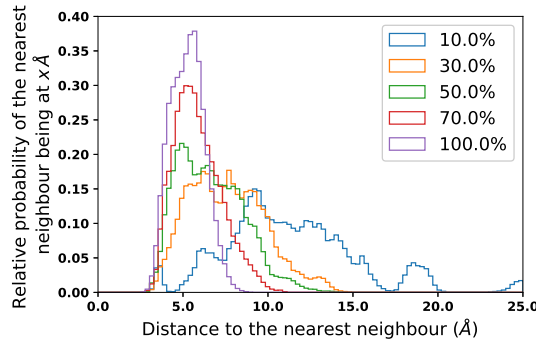


Figure 8.8.: Statistical illustration of the distance to the nearest dye molecule for a system of Coumarin6 doped into NPB. While neat films of the dye reveal an average distance of less than 5 Å, low concentrations increase this value to more than 10 Å. This leads to the conclusion that no serious aggregation be induced by the dipolar interaction in this film.

For a variety of dopant contents within the system, the fraction of dopant molecules being bound in their dipolar potential can be calculated for each system

individually. Thus, it can be concluded how a change in dye concentration will behave within the experiment. Fig. 8.9 shows exemplary data for this procedure while indicating the energetic threshold given by the thermal energy. Note that the absolute value given at a potential of zero depends on the fraction of polar molecules being attracted or repelled by the interaction and thus is given by the randomness of the molecular dynamics simulation. Hence, the calculated fractions of bound molecules will be normalized to the value at a potential of zero. The results depicted in fig. 8.10 show a rising fraction of bound molecules within this model system.

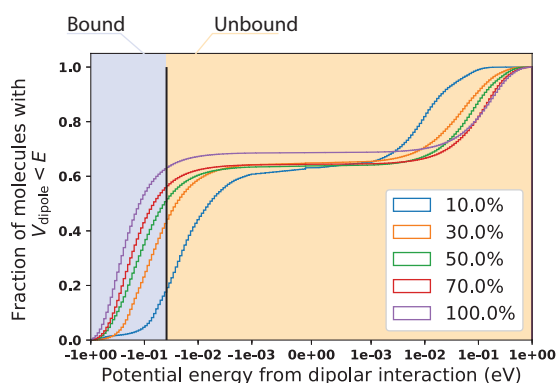


Figure 8.9.: Cumulative fraction of Coumarin6 molecules prone to dipolar interaction. The black line indicates the thermal energy of a single molecule. Thus the fraction of molecules below this threshold is bound to the dipolar potential.

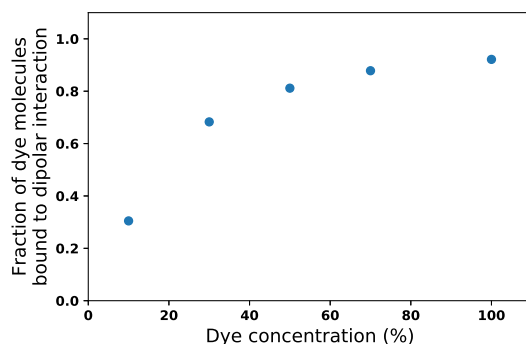


Figure 8.10.: Fraction of Coumarin6 molecules bound due to the dipolar potential for various dye concentrations in a non-polar host. As the polarity of the system is increasing, the fraction of bound molecules is rising.

8. Anisotropy of small fluorescent molecules

The described procedure was performed for all investigated systems. In the case of polar host materials, the values were distinguished between host and dopant interactions. At first, the distance to the nearest neighbor in each system was determined as depicted in fig. 8.11. In all systems, an increase in the distance to the nearest dye molecule upon diluting the system can be observed. This separation indicates that despite the strong dipolar interaction no serious aggregation occurs within an already formed thin film. Note that this situation could be different if the films are deposited subsequently. Further, the lowest observable separation is at about 3 Å for all investigated systems even in neat films.

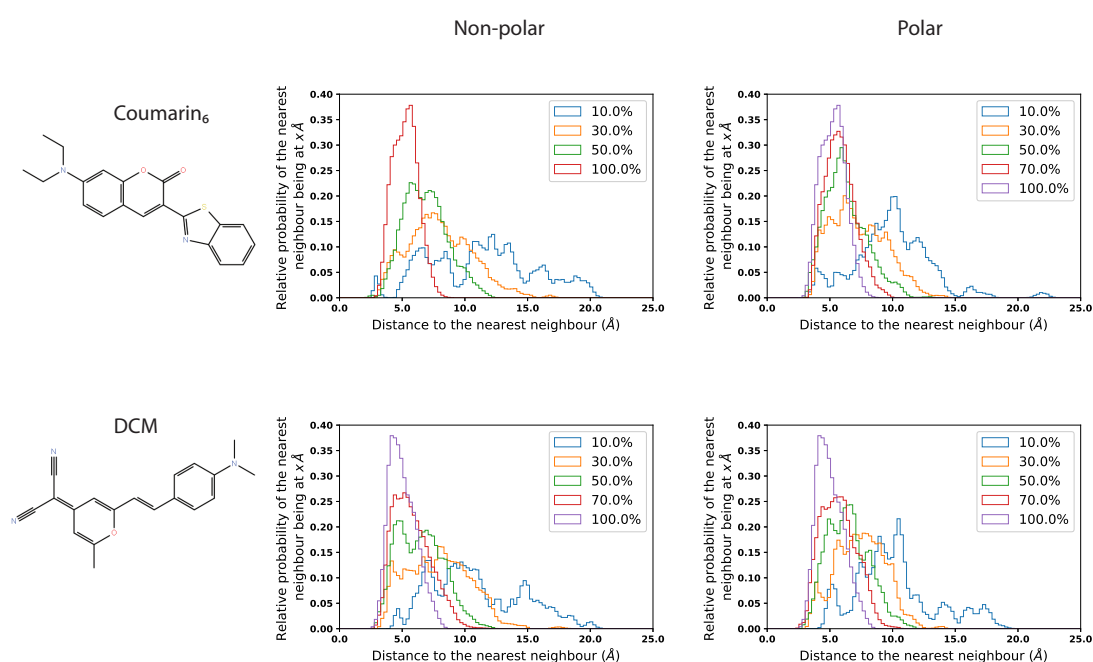


Figure 8.11.: Histograms of the distance to the nearest neighbor for both Coumarin6 and DCM doped into polar and non-polar host materials. As indicated by the graphs, the distance distribution only depends on the concentration of the dye molecules and shows no visible effect of the host material.

Investigations of the green dye within a non-polar host material, as depicted in fig. 8.12, reveal a rising fraction of bound molecules upon an increasing dye concentration. For a low concentration of dye molecules of 10% only 30% of the dopant is trapped in a dipolar potential lower than the thermal energy. This would low potential allows for a molecular motion almost independently of the

dipolar interaction during the film formation. Increasing the dye fraction changes the fraction of bound dopant molecules. Most notably, the increase of bound molecules is changing at a concentration of 50%, at which only a small rise up to the highest value of 90% can be observed. This situation changes in the presence of the polar host material Alq₃, exhibiting a PDM of 4.3 Debye. Due to the polar environment, the fraction of bound molecules is as high as 80% even for low dilutions of the dopant. While this value does not change throughout the variation of the concentration, a change in the individual contributions between the host and dopant molecules can be observed. The contribution of the dopant for only 10% dye content is 40%, which is higher than expected from the non-polar host material. This behavior indicates an aggregation of the dopant molecule within the Alq₃ host. Further, the dipolar interaction of the host is decreasing for concentrations above 30%, indicating that in this scenario the dopant once again dominates the dipolar interaction in the film.

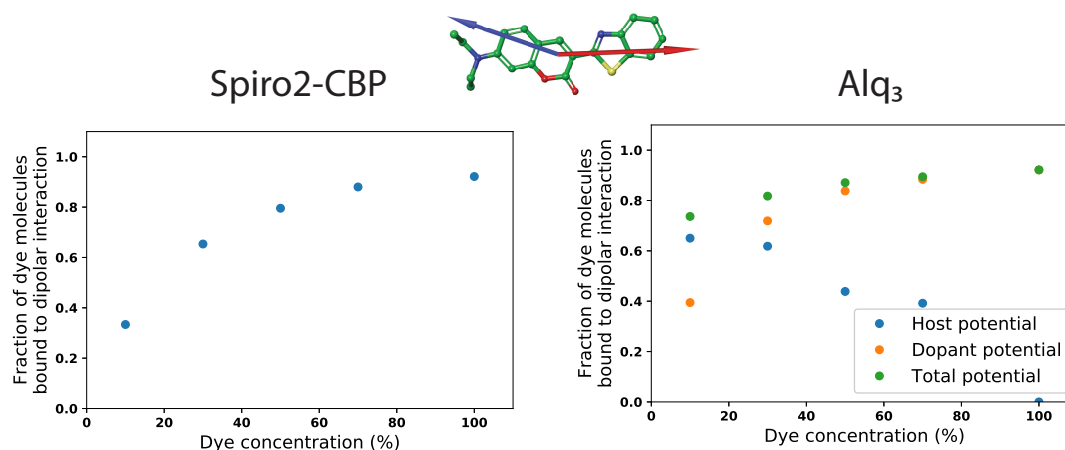


Figure 8.12.: Dipolar interaction of the green dye molecule Coumarin6 doped into the non-polar host material Spiro2-CBP as well as the polar matrix Alq₃. For the non-polar host material, the fraction of molecules bound to dipolar interaction is as low as 30%. Note that the maximum value of 90% is almost reached even for a one to one ratio, yielding 80% bound molecules. For the polar molecule, the fraction of bound molecules is around 80% even for low concentrations, with almost no dependence to the concentration. Most notably, the contribution from the dye molecules to the dipolar interaction is higher than in the non-polar material, which indicates aggregation processes within this host.

As a second dopant molecule DCM was investigated. Compared to the green dye, this dopant exhibits an even higher PDM and slightly smaller spatial extent. Based on the experimental values presented in the following section, this dye was calculated in the non-polar host material NPB as well as the polar matrix Alq₃. While the general behavior for this dye is similar to Coumarin6 small differences can be observed. Most notably the concentration of saturation within the non-polar host is lower, reaching a plateau value even for 30% dye content for the polar material. The same is true for the polar host Alq₃, in which the saturation of dopant potential is also reached for concentrations as low as 30%. Further, the contribution of the host material decreases for high dye concentrations.

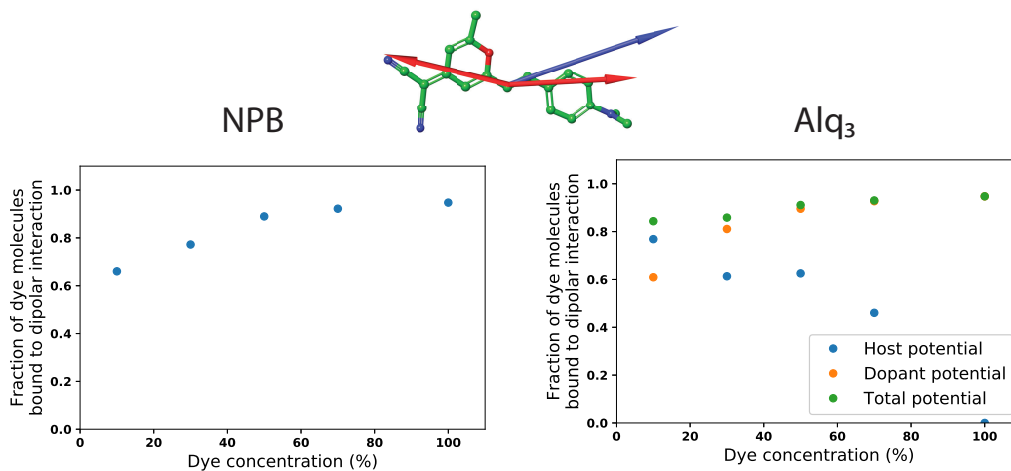


Figure 8.13.: Dipolar interaction of the red dye molecule DCM doped into the non-polar host material NPB as well as the polar matrix Alq₃. In the non-polar material the fraction of molecules bound to the dipolar interaction is rising for low concentrations, saturating at value of about 80%. Within the polar material the total potential is already saturated even at low concentrations, with the Alq₃ contribution decreasing upon a rising dye content.

In conclusion, the results indicate an active involvement of the PDM in the film morphology. Only very low dopant concentrations in the range of 1 – 2% will sufficiently increase the intermolecular separation, while higher concentration leads to a dominant effect of the dipolar interaction between the dopant molecules. It should be noted that the investigated processes depend on the temperature of the system. Hence, cooling or heating polar guest-host systems during film preparation could lead to different behavior during the deposition of the film.

8.1.2. Preferential alignment of polar dyes in diluted guest host systems

When using polar dye molecules, the question if the strong dipole moments affect the film morphology arises. As shown in a previous section, the polarity of the two investigated molecules Coumarin6 and DCM will most likely affect the molecules during film growth and therefore change the amorphous properties of the thin film.

To investigate this phenomenon, the two dyes were prepared in a polar and a non-polar host system at varying concentrations ranging from 5% to 70%. Note that due to crystallization processes not all samples could be measured successfully. Caused by the same problem, the determination of the refractive indices of the individual films was not possible. Hence the samples were analyzed for their emissive properties using the alignment constant ζ . Further Θ was calculated based on the refractive index of the host material. In order to yield a single representative value, the resultant values were calculated for each wavelength and averaged weighted with their respective emission spectrum.

It is worth noting that the Coumarin6 molecule has been investigated for its preferential alignment in earlier work [104]. However, in that data, the concentration of the dopant was low. Hence the dipolar interaction between the molecules could not affect the morphology of the film, leaving the presented alignment process for the dopant.

Fig. 8.14 depicts the alignment constant of both dye molecules in their respective host materials. Therein the green dye Coumarin6 shows a slight increase in the alignment constant for rising concentrations in the non-polar host Spiro2-CBP. The same trend is apparent for the polar host material Alq₃. However, at low concentrations, the alignment constant is 0.02 within this material.

Approximations of the orientation parameter Θ were calculated using the refractive index of the host material. Therein, as depicted in fig. 8.15, Coumarin6 reveals almost isotropic behavior for all samples except low dye concentrations within the polar host material. This behavior indicates that the polarity of Alq₃ within films prepared from TVD induces a preferential alignment of the dye molecule. Taking the calculations of the dipole interaction within those systems into account, the increase of the orientation parameter at concentrations of 30% and above coincides with the dipolar interaction between the dopants becoming dominant. Consequently, at low concentrations the dipolar interaction is determined by the matrix material, leading to the preferential alignment of the dye. This observation leads to the conclusion that dipole potential of Coumarin6 itself does not contribute towards preferential alignment of the molecule.

This scenario is different for the red dye DCM. This molecule reveals a de-

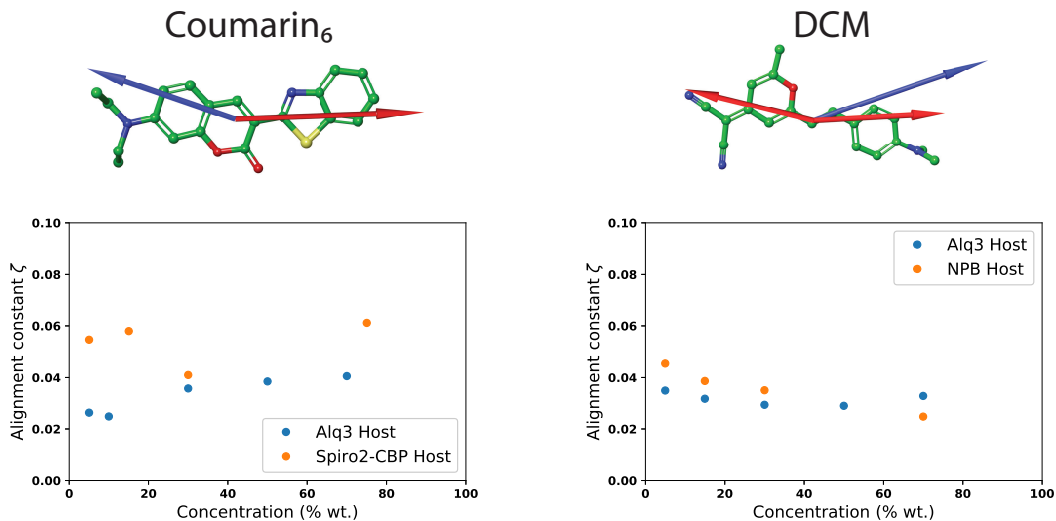


Figure 8.14.: Alignment constant ζ for Coumarin₆ (left) and DCM (right) doped into a polar and an unpolar host material. For Coumarin₆, an increase in dye concentration yields a rising alignment constant for both host materials. However, at diluted concentrations ζ reveals a value close to 0.02 in the polar matrix Alq₃ compared to $\zeta = 0.05$ in the non-polar material. The red dye DCM reveals a decreasing alignment constant for the non-polar materials whereas the polar host yields no change.

crease of the orientation parameter Θ as the concentration of the polar dye is increasing within a non-polar matrix. From molecular dynamics simulations, the dopant interaction reveals to be dominant at concentrations above 30% while only affecting 40% of the molecules at 10% dye content. This limit coincides with the horizontal preferential alignment being formed for dye concentrations above 30% within the experimental values. Within a polar host material, the dipole interaction is dominated by the polar dye Alq₃ at low concentrations leading to preferentially aligned molecules as already observed for the green dye molecule.

In conclusion, the alignment mechanisms for the polar dye molecules Coumarin₆, and DCM can be pinpointed to the dipolar interaction within the system. From the combination of molecular dynamics simulations and experimental guest-host systems, it could be shown that both dopant-dopant and host-dopant interactions, contribute towards the morphology of the system. While the green dye Coumarin₆ revealed to show preferential alignment within a polar matrix, the dopant-dopant interaction leads to isotropic dye orientations. A different be-

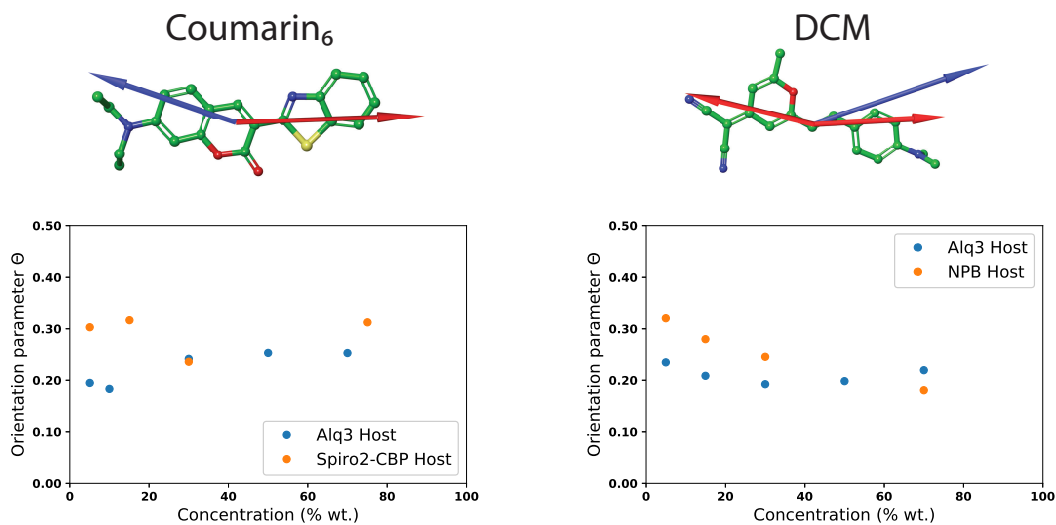


Figure 8.15.: Orientation parameter Θ for the results shown in fig. 8.14. The green dye Coumarin6 only shows a significant horizontal alignment if prepared at low concentrations using the polar host material Alq₃. Contrary to this, the red emitting dye DCM reveals a more pronounced horizontal alignment as the dopant concentration is increasing within the non-polar material NPB. Within the Alq₃ host material, the alignment shows horizontal behavior with no significant dependence to the dye concentration.

havior could be found for the more polar DCM where both host-dopant and dopant-dopant interactions induced preferentially horizontal alignment of the dye within the guest-host system. It should be pointed out that the computational approximation does not include the mobility of the molecule during deposition into account and therefore can not be used to investigate the effect of the glass transition temperature on film morphology.

8.2. Fluorescence anisotropy in organic guest-host systems

The basic concept of fluorescence anisotropy is widely used in different scientific fields. Therein the basic concept relies on polarized light from an emissive species, which itself was excited with a polarized source. Hence, if no depolarization occurs within the system, the emission will itself be polarized with respect to photoselection rules. The resultant depolarization ratio yields further

information about the depolarization effects within the system [89].

Despite its usefulness, this method is mostly applied to solvent or bulk samples, while little attention is given in the field of organic thin films. Thus, this section will investigate the fluorescence anisotropy for Coumarin6 as an exemplary molecule within a diluted organic system. Most of the experiments were performed and evaluated by Felix Höhnle within his master's thesis while being supervised by Thomas Morgenstern.

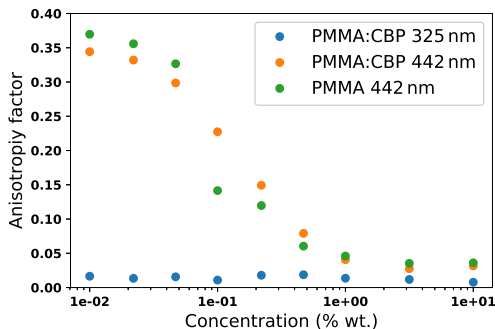


Figure 8.16.: Polarization anisotropy of Coumarin6 doped into either PMMA or a mixed host of 20 %wt. CBP and 80 %wt. PMMA. Incident laser light at a wavelength of 442 nm only excites the green dye and therefore polarization anisotropy occurs for low dopant concentrations. Contrary to this, exciting the PMMA–CBP mixed host with 325 nm light leads to the exciton being formed on the CBP molecule, subsequently transferring its energy to the dye molecule. This process includes total depolarization and thus no anisotropy factor can be observed. Note that samples of the dopant in the PMMA host could not be measured when excited with a 325 nm laser.

For any organic photoluminescent system, a crucial requirement for fluorescence anisotropy to occur is an incomplete depolarization. As the investigated systems are in the solid state the only process to induce depolarization is the energy transfer of the excited state. Both energy transfers, Forster and Dexter transfer, rely on a low separation distance between the exchanging sites. Hence a variation of the dye concentration allows for control of the intermolecular separation and therefore the energy transfer efficiency. To investigate this process the green dye Coumarin6 was doped into a PMMA host at various concentrations. In order to reach compositions of less than 1% dye concentrations, the samples were prepared from solution. To further investigate energy transfer in the presence of an organic matrix material a second set of samples was prepared

using a mixed host consisting of 20 %wt. CBP and 80 %wt. PMMA. Contrary to PMMA, CBP can be excited using ultraviolet light with 325 nm.

The polarization anisotropy factor r was investigated for both sets of samples using two different excitation wavelengths. While 325 nm allows for direct excitation of the host material, 442 nm can only excite the green dye directly. Note that the samples without the mixed host did not show sufficient photoluminescence when excited with UV light.

The results, shown in fig. 8.16, reveal the polarization anisotropy of the Coumarin6 dye when excited with 442 nm light. In the PMMA matrix material, polarization anisotropy starts to occur at concentrations below 5 %wt., indicating an incomplete energy transfer between the dye molecules. This behavior leads to the conclusion that efficient energy transfer between the dye molecules is possible at concentrations of 10 % and above and excitons will most likely not decay on the same molecule they were excited.

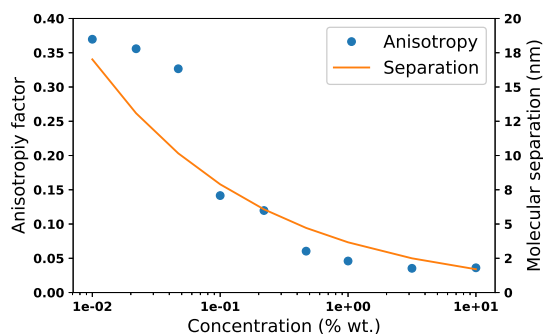


Figure 8.17.: Polarization anisotropy of Coumarin6 doped into PMMA in various concentrations. Measurements were performed using 442 nm as excitation wavelength, revealing the anisotropy of the system at low concentrations. From equation 8.5 the average molecular separation, shown as the orange line, can be calculated. Based on the polarization anisotropy, incomplete depolarization begins to occur at molecular separations above 5 nm.

In order to refine this measurement the average distance of two dopant molecules was calculated using the densities and molar masses of the respective components. Therein the density of Coumarin6 was calculated as $\rho_{C6} = 1.22 \text{ g/cm}^3$ and PMMA has a density of $\rho_{PMMA} = 1.18 \text{ g/cm}^3$. Further the molar mass M of

8. Anisotropy of small fluorescent molecules

the dye is $350.43 \text{ g mol}^{-1}$. Using the equation

$$r_0 = \sqrt[3]{\frac{\left(\frac{w_{C6}}{\rho_{C6}} + \frac{1-w}{\rho_{PMMA}}\right) M}{w_{C6} N_A}} \quad (8.5)$$

the average distance between two dye molecules r_0 can be calculated depending on the concentration w_{C6} of dopant in the system.

Fig. 8.17 shows the measurements for Coumarin6 doped into PMMA as compared to the average molecular separation between two dye molecules. Therein the onset of the polarization anisotropy can be compared to the respective separation distance. This procedure reveals an incomplete depolarization for molecular separations above 5 nm. Note that the slow increase of the anisotropy factor is most likely due to the non-uniformity of the film with some molecules being aggregated due to their strong dipole interaction.

9. Preferential alignment of organometallic Ir-complexes

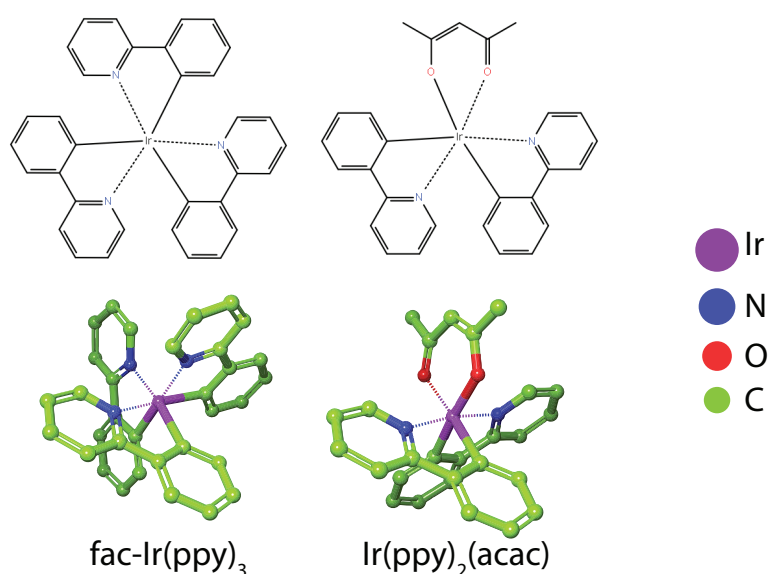


Figure 9.1.: The two organometallic Ir-complexes Ir(ppy)₃ (left) and Ir(ppy)₂(acac) (right) shown in their three-dimensional geometry as well as the Lewis structure. Three ligands surround the center Iridium atom (purple). The homoleptic compound Ir(ppy)₃ consists of three equal ppy ligands while the heteroleptic Ir(ppy)₂(acac) dye has one ppy replaced by an aliphatic acac group. Additional hydrogen atoms are not shown in this illustration and dashed lines are used for a cleaner illustration of the complex but still resemble the indicated coordination bonds.

One of the core problems limiting the performance of organic lighting applications has been the dye molecule for a long time. In particular, the spin-statistics limit the achievable ratio of radiatively decaying excitons to only 25% [1]. To overcome this limitation, new dye molecules were synthesized exploiting heavy

atoms for their strong spin-orbit coupling [13]. This effect enables a fast transfer from the singlet state to the triplet while providing a radiative decay channel for the triplet excitons. Although the excitonic lifetimes rise to a value of about 1 μ s, those dyes were finally able to achieve a real singlet to triplet ratio of unity while maintaining a high quantum yield. The first efficient molecules exhibiting these unique properties was Tris[2-phenylpyridinato-C₂,N]iridium(III) (Ir(ppy)₃) as shown in fig. 9.1. This homoleptic Ir-complex consisted of three equal phenylpyridine (ppy) ligands coordinated to a center Iridium atom [13, 107].

Interestingly another molecule in the synthesizing route of the Ir(ppy)₃ dye drew attention to lighting applications. The Ir(ppy)₂(acac) complex (fig 9.1), although consisting of only two conjugated ligands and one acetylacetonate (acac) ligand, shows a high quantum yield and surprisingly high device efficiencies exceeding those of the Ir(ppy)₃ molecule. This unexpected behavior was found to be caused by a preferential alignment of the emissive transition dipole moments of the Ir(ppy)₂(acac) molecule which improves the performance in lighting applications [108]. While this effect turned out to apply to many dye molecules in state-of-the-art OLEDs, Ir-complexes exhibit some unique effects which will be discussed in this chapter [8, 37].

The organometallic dyes discussed in the following sections can further be classified concerning their symmetric properties. Generally, Ir-complexes contain several organic ligands bound to the center atom in an octahedral shape. Homoleptic compounds only consist of one type of ligand, whereas heteroleptic molecules include at least a second type of ligand [8]. This degree of freedom allows for more variety in the design of the organometallic dyes. It is important to note that within this work only materials with three ligands were investigated. Other approaches such as dye molecules with only two ligands were not investigated.

Besides the composition of the ligands, their symmetry further affects the molecular properties. For homoleptic dyes, the ligands can either be in meridional or facial symmetry, both cases are illustrated in fig. 9.2. Most notably the facial configuration is more symmetric and therefore desired in the design of the dye molecules. However, in some individual cases, the symmetry only has a minor effect on the photophysical properties of the complex. It is important to mention that the homoleptic compounds also exhibit different chiralities which will not be discussed in this work [109].

For heteroleptic compounds, similar symmetries exist but have not found any application in organic dye molecules so far. Hence the usual symmetry is *cis*. The by far most common additional ligand for heteroleptic Ir-complexes is acetylacetonate (acac). Although this molecule was only used in a final step for the first synthesis of the Ir(ppy)₃ complex, compounds containing this side group have

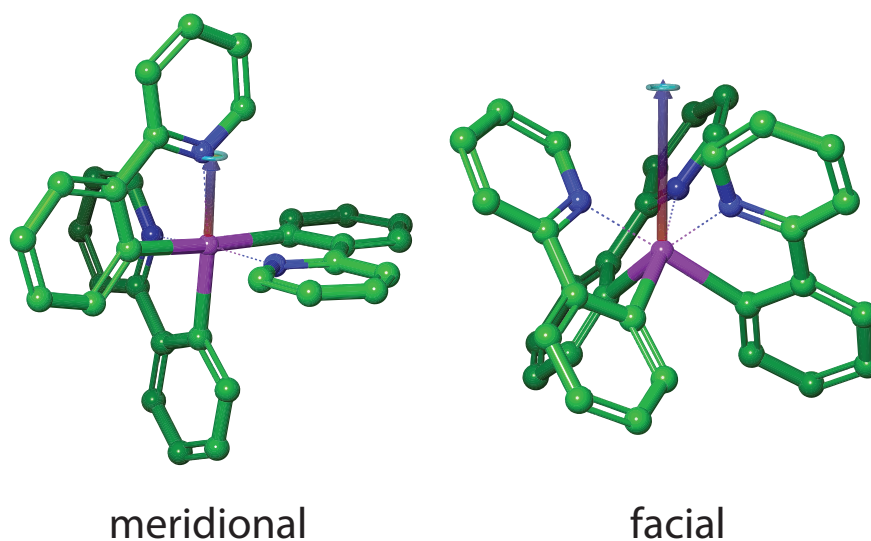


Figure 9.2.: Meridional (mer) and facial (fac) symmetries of the $\text{Ir}(\text{ppy})_3$ molecule. The facial species has a C_3 symmetry while the meridional molecule shows no symmetry. The arrows indicate the PDM of the molecules. Most notably the PDM is parallel to the C_3 symmetry axis for the facial molecule, whereas it is pointing towards a Ir–N bond in the meridional configuration.

drawn significant attention due to their unique preferential alignment properties as discussed in section 9.2.2 [8, 37].

9.1. Photophysics of phosphorescent Ir-complexes

One of the extraordinary features of organometallic Ir-complexes is the strong spin-orbit coupling due to the heavy Iridium atom. This effect allows for a fast intersystem crossing from the singlet to the triplet state as well as efficient radiative decay from the triplet to the ground state. The radiative decay process, as depicted in fig 9.3, allows for the use of both singlet and triplet excitons within optoelectronic devices, significantly boosting the performance [13, 107].

Note that Ir-complexes are subject to the Jahn-Teller distortion [110, 111]. This effect will lead to a break of the symmetry if the molecule is excited. Consequently, the excitation will be mostly within one ligand and the center heavy-metal atom, forming a metal to ligand charge transfer (MLCT) state. Due to this radiative decay being uniquely from the triplet state, the lifetime of the excited state significantly differs from fluorescent molecules. Common exciton

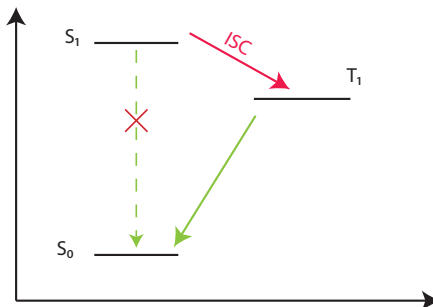


Figure 9.3.: Emission process of phosphorescent Ir-complexes. Due to the strong spin-orbit coupling, singlet excitons (S_1) rapidly perform intersystem crossing (ISC) to the triplet state. This process is several orders of magnitude faster than the singlet decay, effectively removing the decay channel from the singlet. Finally, the excitons decay to the ground state (S_0) via phosphorescence from the T_1 level.

decay times range between $1\mu\text{s}$ up to several ms [34].

As the decay path of the excited states in this type of molecules is via the triplet state, it is essential to pay attention to the surrounding medium of the emissive dye. A neat film of the emissive molecules gives rise to triplet-triplet annihilation (TTA) and triplet-polaron-quenching (TPQ) due to the close contact of the dyes [112]. To overcome these quenching mechanisms, diluting the system in a host material forming a guest-host system is a standard method. Usual concentrations of this approach are 6 – 8% wt. to maintain a dye-only emission while reducing TTA [113]. Choosing this approach requires the host material to exhibit a sufficiently high triplet level, higher than the level of the dye molecule. Fig. 9.4 shows a variety of common host materials for the use in guest-host systems with organometallic Ir-complexes.

In many applications, carbazole-based molecules are taken as the host material, such as CBP, mCP, mCBP, and TCTA [72, 114–117]. However, the triplet level of the carbazole being in the range of 2.9 eV limits the application of these materials for deep blue dye molecules [122–124]. In those cases, phosphonates such as DPEPO or PO9 have turned out to be viable replacements, although the stability of those molecules limits the application for long-lived devices [120, 125].

Besides the traditional guest-host system, mixed host approaches have turned out to be superior in the field of lighting applications. The two-host advance separates the charge carriers on the emissive film, efficiently suppressing TPQ processes. Further, this allows for thicker emissive films, effectively reducing the local triplet density and thereby avoiding TTA [115].

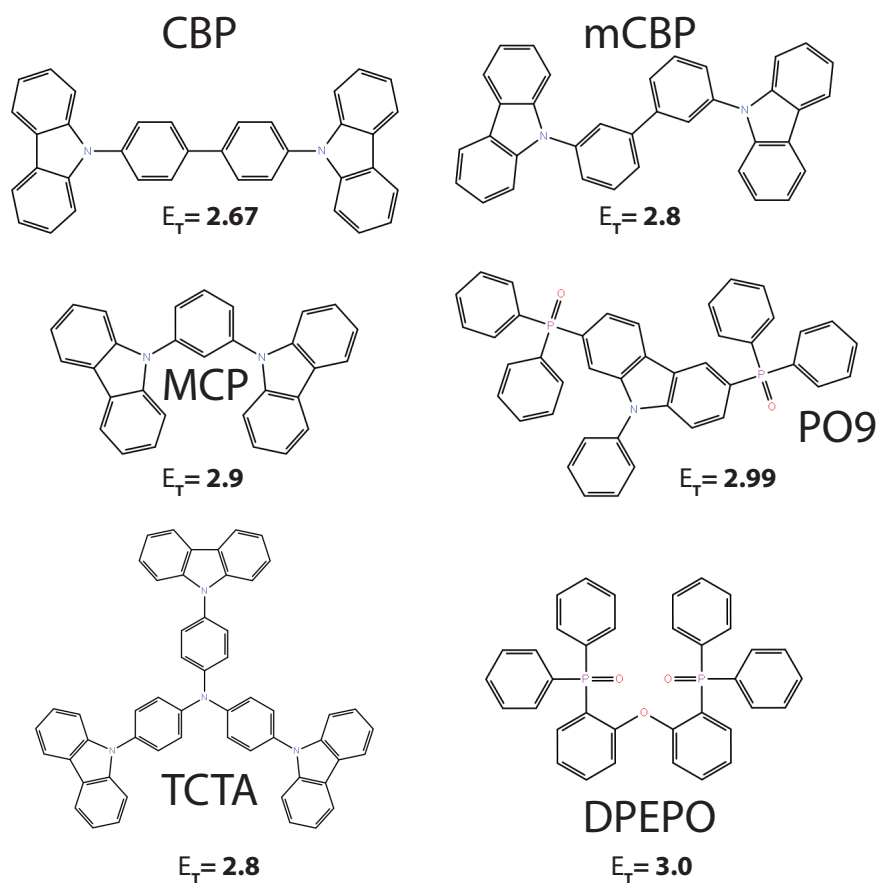


Figure 9.4.: Different host materials suitable for the use in phosphorescent guest host systems. The carbazole based materials CBP, mCBP, MCP, and TCTA are mostly used for green dye molecules. Due to their high triplet level E_T , DPEPO and PO9 are suitable host materials for deep blue dopant molecules [106, 118–121].

9.2. Preferential alignment of heteroleptic Ir-complexes

Organometallic Ir-complexes containing two different ligands have drawn significant attention in their application in OLEDs. Especially complexes containing partially aliphatic parts, such as acac, tmd, and similar species, lead to the preferential alignment of the dye molecules [37, 97, 104, 108, 114, 126–128]. The origin of this unique feature has been in the focus of research for several years, and different approaches have been taken to identify the processes behind this effect [37, 81, 129, 130]. In this section, the methods to pinpoint the molecular orientation as well as considerations for understanding and predicting the preferential alignment will be given.

9.2.1. Pinpointing the molecular orientation

Determination of the exact alignment of a molecular ensemble within an organic thin film is of crucial importance for understanding its properties. This section will give insight into the experimental and computational methods required to pinpoint the alignment of $\text{Ir}(\text{ppy})_2(\text{acac})$ as an exemplary molecule. The experimental results base on two publications and further data. The investigations were supported by Markus Schmid, Alexander Hofmann, Lars Jäger, Tobias Schmidt, and Matthew Jurow. Further work about the organic vapor phase deposition process was supported by Matthew Jurow, Francisco Navarro and John Facendola.

Within this section, two different quantities expressing the molecular orientation were investigated. The preferential alignment of the emissive TDMs can be probed by using optical methods such as angular dependent spectroscopy or back focal plane imaging [37, 85]. However, due to the procedure only taking the second moment of the TDM into account, the meaningfulness of this value alone is limited. As a second quantity, the permanent dipole moment can be taken into account as probed via Kelvin probe measurements or impedance spectroscopy [10, 11, 131]. This method can reveal the general orientation of the molecule, pointing away or towards the film surface as well as a more profound insight into the preferential alignment of the PDM if combined with computational methods. The combination of both experiments yields either an exact molecular orientation or a small range of possible outcomes depending on the amount of disorder taken into account [11].

9.2. Preferential alignment of heteroleptic Ir-complexes

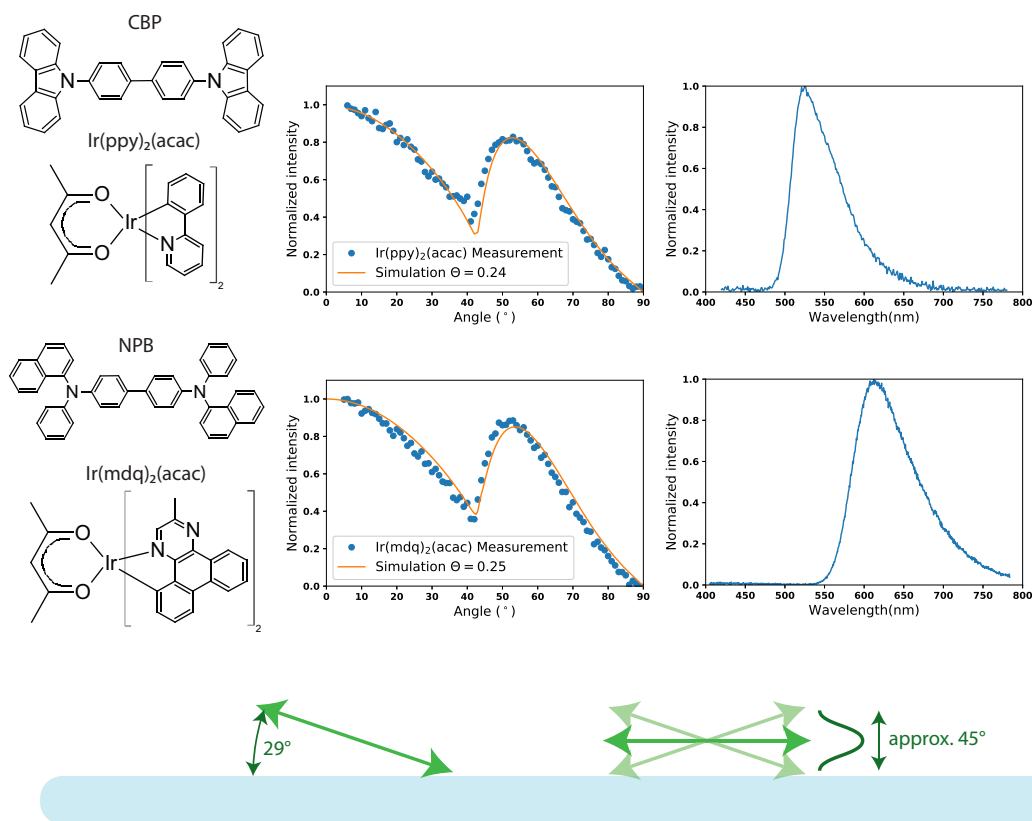


Figure 9.5.: Orientation measurements and photoluminescence spectra for Ir(ppy)₂(acac) doped into CBP (top) and Ir(mdq)₂(acac) in NPB (bottom) as prepared from thermal vapor deposition. The orientation was determined using the corresponding peak wavelength from the emission spectrum shown on the right side. Both measurements reveal a preferential alignment of the dye molecule resembled in the orientation factor $\Theta = 0.24$. The bottom illustration depicts the alignment of the emissive TDM with respect to a film surface as revealed by the orientation factor $\Theta = 0.24$. The TDM has to be either aligned with an angle of 29° or a distribution with a broadening of approximately 45°.

In the context of heteroleptic Ir-complexes, the determination of the TDM orientation resembled in the factor Θ is of particular interest due to its effect on the EQE of light emitting devices [36, 37]. Therein the emissive molecule is often diluted into a host material such as CBP or NPB. Hence these systems give a suitable starting point for their investigation.

Fig 9.5a shows the experimental result for two exemplary systems known from literature. Both shown dye molecules, $\text{Ir}(\text{ppy})_2(\text{acac})$ and $\text{Ir}(\text{mdq})_2(\text{acac})$ reveal a horizontal preferential alignment of $\Theta = 0.24$ and $\Theta = 0.25$ in their respective host materials. This behaviour indicates an orientation of the emissive TDMs of 29° with respect to the surface or a Gaussian distribution with a mean value of zero degrees and a broadening of 45° as depicted in fig. 9.5.

This degree of preferential alignment of $\text{Ir}(\text{C-N})_2(\text{O-O})$ complexes, where C-N is a cyclometalated ligand, and O-O is a diketonate ligand such as acetylacetonate (acac), is the same for many different guest host systems [34, 37]. Studies revealed almost no effect of the host material and its properties such as glass transition temperature on the preferential alignment of the dye [104]. Further, it is surprising that many different C-N ligands reveal the same orientation in the corresponding organometallic complex if combined with an acac ligand [34, 37].

Contrary to this behavior, heteroleptic complexes without a O-O diketonate ligand, such as the $\text{Ir}(\text{bppo})_2(\text{ppy})$ dye, do not exhibit any preferential alignment from an optical point of view. This absence of preferential alignment indicates a dependence to the acac ligand, as discussed in a later section [37].

Dependence on the preparation technique

In the context of organic semiconductors, although TVD is a highly controllable form of thin film deposition, other preparation techniques have drawn attention due to being more accessible to apply or more cost-effective. Especially solution processing is a much more accessible process and possibly applicable to printing technology. Hence, the question arises if the deposition technique alters the alignment behavior of organometallic Ir-complexes.

To investigate this effect different material systems were chosen and deposited from either TVD or solution processing via spin-coating. The two red dye molecules $\text{Ir}(\text{mdq})_2(\text{acac})$ and $\text{Ir}(\text{piq})_2(\text{acac})$ were doped into the host material NPB. Further, the heteroleptic green dye $\text{Ir}(\text{ppy})_2(\text{acac})$ was doped into different host materials, being CBP, PMMA, and Spiro2-CBP. Therein PMMA is not an organic small molecule semiconductor but a polymer matrix. In order to verify the results to a known isotropic dye, samples containing the homoleptic dye $\text{Ir}(\text{ppy})_3$ were also investigated.

The experimental results as shown in fig. 9.6 include several remarkable effects on the preferential alignment of the dye molecule. As expected from earlier work [108, 114], the heteroleptic dye molecules exhibit horizontally aligned TDMs. Note that the host PMMA as a polymer cannot be processed via TVD. The homoleptic dye $\text{Ir}(\text{ppy})_3$, which was included for reference reasons, does not exhibit preferential alignment in neither of the preparation techniques. Interestingly changing the film deposition to solution processing, removes the preferential alignment from the heteroleptic dye molecules. In none of the four different host materials horizontally aligned TDMs could be observed.

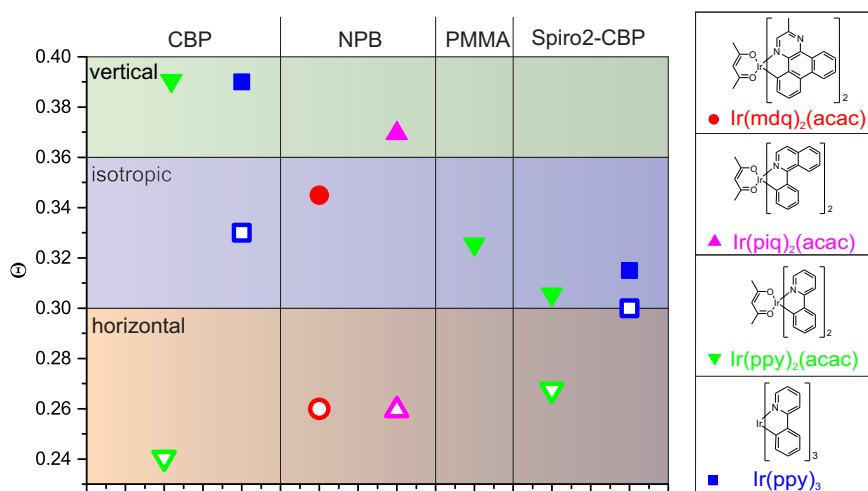


Figure 9.6.: Orientation measurements of four organic compounds doped into their respective host materials as indicated. Samples were prepared either from TDV (open symbols) or via spin-coating from solution (closed symbols) at a dye concentration of 8% wt. The heteroleptic dyes exhibit a preferred horizontal alignment when prepared from TVD, whereas the solution processed approach yields an isotropic to vertical orientation. Contrary to this, the homoleptic compound retains its isotropic behavior. The host materials are shown in an ascending manner to the glass transition temperature. Picture taken from [36].

For solution processing the host material also shows an effect on the dye orientation, whereas this could not be observed for the TVD samples [36, 104]. Therein a decreasing glass transition temperature seems to increase the vertical alignment of the dye molecules. One explanation for this effect could be a vertical alignment of the host molecule, inducing the same behavior for the dye molecule due to the two species coupling to each other. However, in this work

it cannot be excluded that the optical properties of the solution-processed films change compared to the TVD preparation. This behavior would lead to false conclusions due to different refractive indices.

As a third preparation technique, organic vapor phase deposition (OVPD) was investigated. Similar to TVD, this procedure is a step-by-step deposition technique by transporting the molecules via a carrier gas to the substrate at comparable rates to TVD [132–136]. Contrary to TVD, this method involves the presence of a carrier gas and a pressure of 8 mbar. Thus, the deposition conditions differ from the high vacuum present during the TVD process.

Investigations of the dye Ir(ppy)₂(acac) doped into CBP are in agreement to preparation from TVD, yielding a value for the orientation parameter Θ of 0.24. Note that the substrate temperature was kept at ambient conditions during the film deposition. These findings indicate no effect of the carrier gas or the vapor phase deposition on the preferred orientation compared to sample preparation from traditional TVD.

In summary, the preparation technique of organic guest-host systems containing heteroleptic Ir-complexes doped into a host material depends on the deposition process being a subsequent deposition of the individual molecules or a one-step process such as spin-coating. Therein the step-by-step techniques allow for the preferential alignment of the dye molecule, whereas solution processing keeps the dye orientation in an isotropic or possibly slightly vertical behavior.

Investigation of the dye concentration

Given the polarity of most of the heteroleptic dye molecules, a high concentration of the polar species could enhance intramolecular interactions and therefore change the TDM orientation. Most investigations in this context use concentrations ranging from 2 % wt. up to 20 % wt. in systems prepared from TVD. This limited range originates from the application to light emitting devices. Therein low concentrations usually lead to an incomplete energy transfer from the host to the dye molecule and high concentrations promote quenching mechanisms such as TTA. Within this work, two systems were also investigated for their high concentration properties up to the behavior of neat films of the dye.

Taking literature data as well as experimental results into account, heteroleptic Ir-complexes show no dependence on the concentration of the emissive species, as shown in fig. 9.7. This surprising behavior is caused by the unique alignment mechanism as discussed in a later section.

Investigations of the emission spectrum of the guest host systems were performed using the molecule Ir(ppy)₂(acac) doped into CBP. Therein it could be expected to reveal a solid state solvation shift due to a change in the polarity of

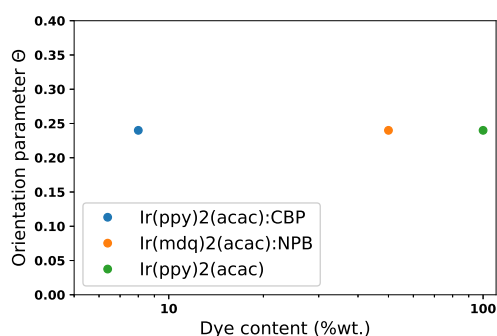


Figure 9.7.: Preferential alignment of different emissive species at various concentrations within a guest-host system prepared from TVD. The preferential alignment of heteroleptic Ir-complexes shows no dependence to the dye concentration despite all shown molecules having a permanent dipole moment along their C2 axis [11].

6

the surrounding medium, whereas CBP in contrast to the dye molecule is non-polar. However, the results in fig. 9.8, showing the photoluminescence spectra of the respective systems, yield no signs of this behavior. The emission spectrum of the organic film is almost constant for a wide range of concentrations. Hence, the polarity of the molecule is not sufficient to significantly alter the emission spectrum of the film. It is important to note that higher concentrations yield a much lower intensity signal due to quenching processes.

Influence of the host medium

Given the fact that triplet emitters such as organometallic Ir-complexes are almost uniquely used in guest-host systems due to their susceptibility to TTA, the matrix is another factor possibly influencing the preferential alignment. Using TVD, a vast amount of different host materials were investigated for their influence on the alignment of the emissive TDM. However, with only a few exceptions, the host medium could not be shown to affect this behavior as depicted in fig. 9.9. One special case yields only an isotropic orientation of the dye molecule. The material UGH-2 suppresses the preferential alignment of the dye molecules even if prepared from TVD. This effect can be understood by taking the glass transition temperature of the material into account. This quantity is exceptionally low [137, 138], making the system to develop a random orientation due to the high mobility of the host material. Further, it is important to note, that the electrostatic interaction between this host material and some dye molecules can

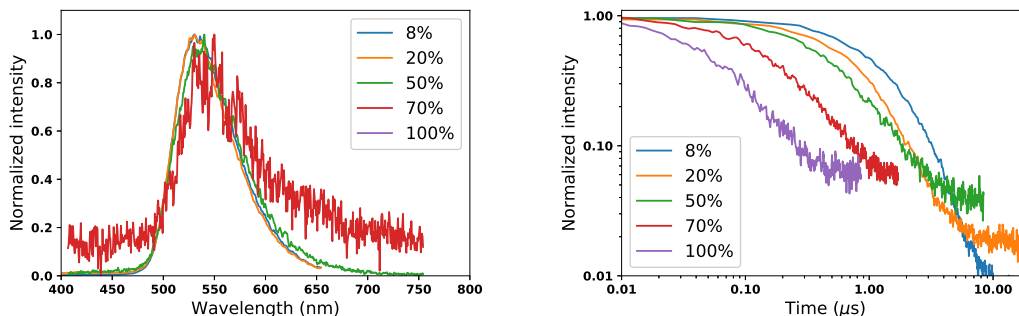


Figure 9.8.: Photoluminescence spectrum of the organic guest-host system $\text{Ir}(\text{ppy})_2(\text{acac})$ doped into CBP at various concentrations (left) and corresponding exciton decay rates (right). The thin films do not show any significant shift in the emissive spectrum for the whole concentration range. It should be pointed out that the spectra were measured using a spectrometer with a large slit width. Hence the spectral features of the $\text{Ir}(\text{ppy})_2(\text{acac})$ spectrum cannot be identified. Further, due upon a rising concentration the exciton decay time and therefore the quantum yield rapidly decreases due to TTA.

be shown to be repulsive. Hence due to the repellent interaction between the guest and host molecules, no preferential alignment can be formed.

Contrary to film deposition via TVD, in solution processed systems the matrix material can change the preferential alignment of heteroleptic dye molecules. However, it is essential to distinguish between small molecule semiconductors, such as CBP or NPB, and polymer matrix materials. For the latter, it could be shown that polymerization of the host material can induce the preferential alignment of the dye in certain circumstances [105].

For non-polymer films, the heteroleptic dye molecules form isotropic systems as shown previously. However, due to the preparation technique, those samples are prone to crystallization processes. This film morphology can have a significant impact on the radiation pattern of the emissive films. Hence no neat films of the dye molecules were prepared via spin-coating.

Effect of the substrate temperature

When investigating the effects of different host materials on the preferential alignment of heteroleptic Ir-complexes, the dynamics of those molecules can play an important role. Hence, instead of changing the properties of the host molecule, it is also possible to vary the temperature of the system during deposition to

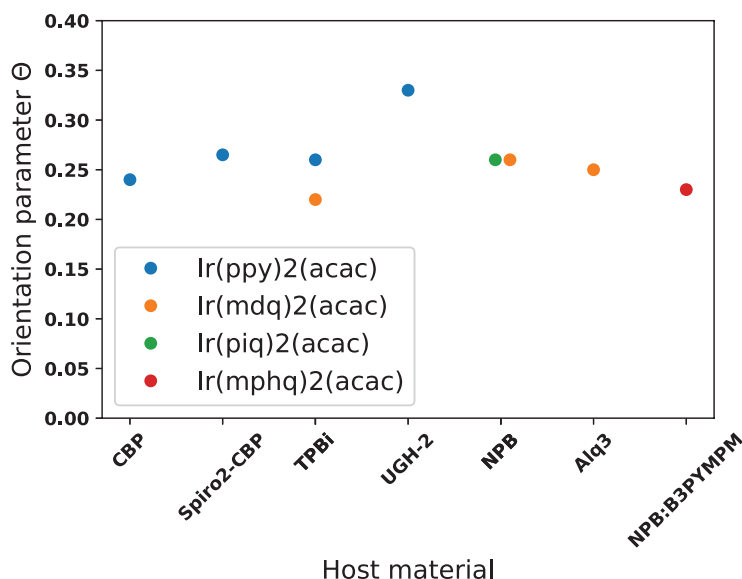


Figure 9.9.: Orientation factor for several emissive dyes in various host materials. With only a few exceptions the host material does not change the preferential alignment of the investigated dye molecules when prepared from TVD. Values taken from refs [11, 36, 104, 130, 130].

study the effects of the molecular mobility.

Small molecular emitters have been investigated in several studies revealing their effects on the orientation of the amorphous systems. Many rod-like molecules show vertical or isotropic behavior when deposited at ambient conditions or even elevated temperatures. However cooling the substrate, effectively decreasing the molecular motion of the system during deposition, leads to a horizontal alignment originating from the lack of thermal energy [106, 139].

In the case of organometallic Ir-complexes, the dye molecules Ir(ppy)₂(acac) and Ir(bppo)₂(acac) doped into CBP and Spiro-2CBP were chosen. Due to experimental limitations the guest-host systems were only deposited via OVPD in a temperature range from ambient conditions at 25° C down to –100° C. The experimental results, shown in fig. 9.10, were compared to samples prepared from TVD and solution processing both at ambient temperatures.

For 25° C the orientation factor is in agreement with the TVD system as discussed in a previous section. Reducing the temperature of the substrate does not affect the resultant alignment of the TDM down to a temperature of about –50° C. Reducing the thermal energy further removes the preferential alignment of the emissive dye in samples prepared at –100° C.

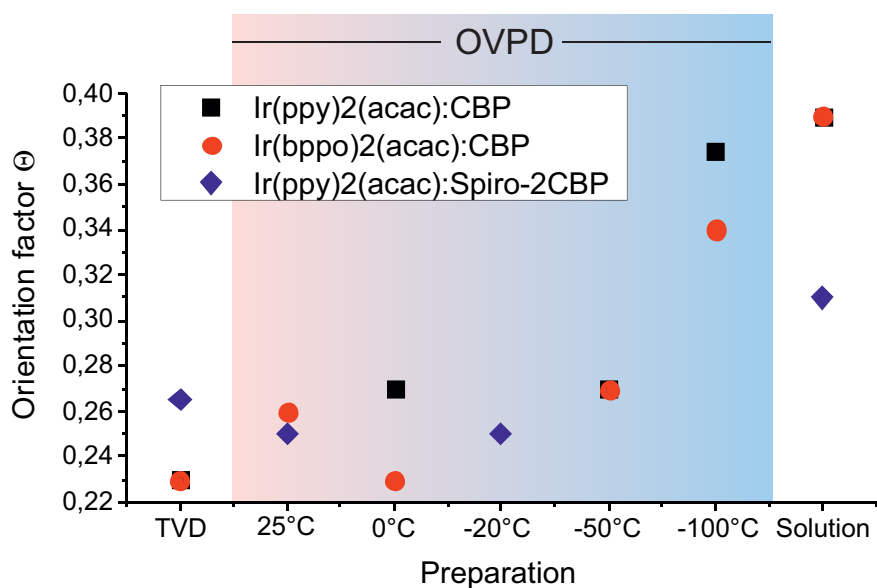


Figure 9.10.: Experimentally obtained orientation values for Ir(ppy)₂(acac) doped into CBP as well as Spiro-2CBP and Ir(bppo)₂(acac) doped into CBP. All investigated material systems were prepared with a concentration of 8% wt. Further, the preparation technique was varied between TVD, solution processing, and OVPD. Therein for the OVPD process, the substrate temperature was varied between ambient conditions at 25°C and –100°C.

This behavior indicates a thermal activation of the orientation process of the heteroleptic dye molecules. The experiments give a rough estimate of the required energy for this process between 173 K and 223 K or 15 meV and 19 meV. These findings are contrary to prior observations for rod-like molecules, which assume a more horizontal orientation at lower ratios of the substrate temperature to the glass transition temperature [104, 106, 140]. Thus, the alignment process of heteroleptic phosphors can further be distinguished from other dye molecules to a unique surface effect and the different properties of the ligands of Ir-complexes.

Unfortunately, the dependence on the substrate temperature could not be investigated further due to complications with the substrate cooling of the deposition chamber.

Investigating the alignment from an electrical point of view

While the preferential alignment of the TDM for $\text{Ir}(\text{ppy})_2(\text{acac})$ is a frequently investigated feature, knowledge about its exact orientation is not sufficient to pinpoint the exact molecular alignment within a thin film. From geometrical considerations, it can be concluded that at least two independent molecular properties need to be investigated. The respective orientation of the two quantities then allows to derive the exact positioning of the dye molecule. Moreover, measurements of the emissive TDM leave further room for uncertainties due to the experimental technique probing the second moment of the TDM with respect to the film surface. Hence, as shown in fig. 9.11, several configurations exhibiting the same orientation factor exist.

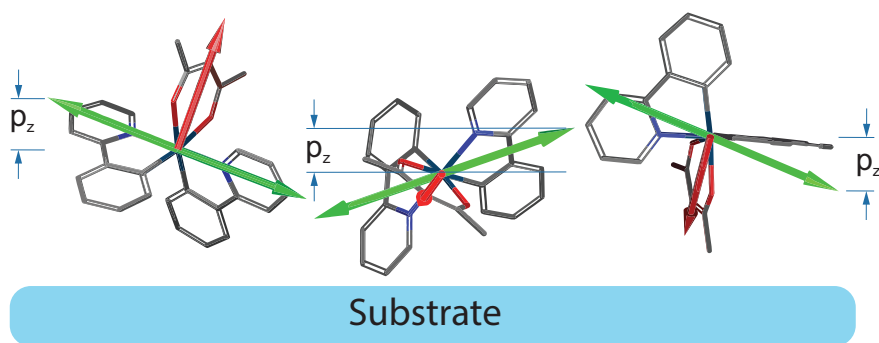


Figure 9.11.: Optically equivalent orientations of the $\text{Ir}(\text{ppy})_2(\text{acac})$ molecule with respect to the preferential alignment of the emissive TDM. Green arrows indicate the TDM on the molecular frame, whereas the red arrows depict the C_2 symmetry axis. In all three molecular orientations, the p_z component of the TDM vector has the same amplitude, making the illustrated orientations equivalent in an optical experiment.

Heteroleptic Ir-complexes containing an (acac) ligand usually exhibit a permanent dipole moment perpendicular to their C_2 symmetry axis. This molecular property is almost perpendicular to the emissive TDM pointing approximately in the direction of the C–N bond. Thus the PDM is an excellent candidate as a second quantification of the molecular alignment of the dye molecules.

Using impedance spectroscopy the preferential alignment of the PDM can be quantified in the orientation parameter Λ , expressing the relative fraction of PDMs being aligned perpendicular to the film surface. Fig 9.12 shows the impedance measurement for $\text{Ir}(\text{ppy})_2(\text{acac})$ doped into CBP at a low concentration of 6%. A bilayer device consisting of NPB as hole transport layer and the

investigated guest host system was used to perform the electrical measurements.

The results after applying the evaluation procedure as described in the corresponding methods section indicate a negative sheet charge density of -0.5 mC/m^2 . The sign of the sheet charge density indicates that the PDM of the dye molecule points away from the film surface.

Contrary to this behavior, when doping the dye into a UGH-2 host, the polar properties of the film vanish and no transition voltage can be detected using impedance spectroscopy. This result is in agreement with the optical orientation parameter $\Theta = 0.33$ for this guest-host system. Hence the results confirm the isotropic distribution of dye molecules within the host material UGH-2.

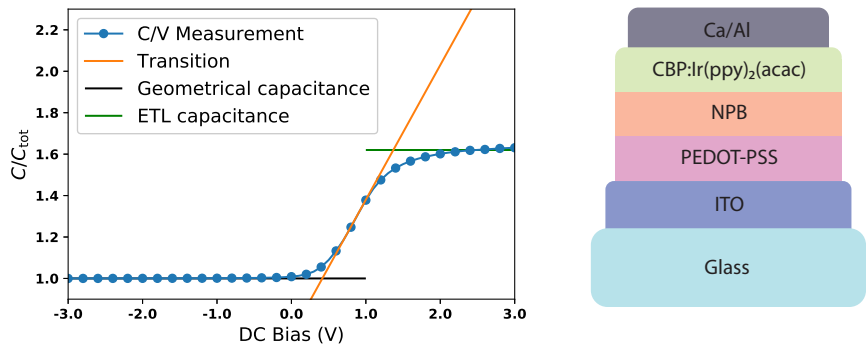


Figure 9.12.: C-V Measurement for $\text{Ir}(\text{ppy})_2(\text{acac})$ doped into CBP (left) using low concentration of 6%. The capacitance values are normalized to the geometrical capacitance of the device. Lines indicate the fitting process as described in the corresponding methods section. Measurements were performed using the bilayer device depicted in the right-hand side of the figure [11].

From DFT calculations the PDM of $\text{Ir}(\text{ppy})_2(\text{acac})$ was determined as 2.01 Debye. Further quantities required for the calculations of the orientation parameter Λ involve the density, which was calculated as 1.508 kg/m^3 using molecular dynamics simulations, and the molar mass of the molecule being $599.70 \text{ g mol}^{-1}$. From these values and the sheet charge density of -0.5 mC/m^2 , Λ can be calculated as 0.8. This value corresponds to 80% of the maximum possible interface polarization.

Unraveling the preferential alignment of Ir(ppy)₂(acac)

The correlation between both optical and electrical alignment quantifications allows for the determination of the dye alignment within thin films. Therefore it is necessary to calculate possible molecular orientations satisfying the two different measurements. Therein

$$\Theta = \sum_i \frac{p_{z,i}^2}{|\vec{p}_i|^2} \quad (9.1)$$

is given for the optical alignment parameter and

$$\sin(\phi) = \Lambda \quad (9.2)$$

for the electrical value. The z-component of the TDMs (\vec{p}_i) as well as the tilt of the C2-axis ϕ with respect to the film surface then determine the molecular orientation.

Taking the Ir(ppy)₂(acac) molecule as an example where the PDM is parallel to the C2-symmetry axis and the two TDMs point within an angle of 85° to this axis, the following considerations can be made:

1. For the sake of simplicity the PDM μ is assumed to be aligned perpendicular to the film as a starting point:

$$\vec{\mu} = |\vec{\mu}| \begin{pmatrix} 0 \\ 0 \\ 1 \end{pmatrix} \quad (9.3)$$

2. The two TDMs of the molecule, \vec{p}_1 and \vec{p}_2 are within the x-z plane, where ϕ_L describes the angle of the TDM with respect to the C2 symmetry axis.

$$\vec{p}_1 = |\vec{p}_1| \begin{pmatrix} \sin(\phi_L) \\ 0 \\ \cos(\phi_L) \end{pmatrix} \quad (9.4)$$

$$\vec{p}_2 = |\vec{p}_2| \begin{pmatrix} -\sin(\phi_L) \\ 0 \\ \cos(\phi_L) \end{pmatrix} \quad (9.5)$$

These quantities can be rotated around the z- and y-axis using rotation matrices M_y and M_z . While rotation of the x-axis would also be possible, it is not necessary to take all molecular orientations into account. Note that this changes

when taking random ensembles in consideration as given later in this section.

$$M_y = \begin{bmatrix} \cos(\phi_y) & 0 & \sin(\phi_y) \\ 0 & 1 & 0 \\ -\sin(\phi_y) & 0 & \cos(\phi_y) \end{bmatrix} \quad M_z = \begin{bmatrix} \cos(\phi_z) & -\sin(\phi_z) & 0 \\ \sin(\phi_z) & \cos(\phi_z) & 0 \\ 0 & 0 & 1 \end{bmatrix} \quad (9.6)$$

These transformations allow for the investigation of the experimentally determined quantities for all possible rotations of the molecule:

$$\begin{aligned} \Theta &= \frac{1}{2} (M_y \cdot M_z \cdot \vec{p}_1)_z^2 + \frac{1}{2} (M_y \cdot M_z \cdot \vec{p}_2)_z^2 \\ &= \frac{1}{2} \left((-\sin(\phi_y) \cos(\phi_z) \cos(\phi_L) - \cos(\phi_y) \sin(\phi_L))^2 \right. \\ &\quad \left. + (\sin(\phi_y) \cos(\phi_z) \cos(\phi_L) + \cos(\phi_y) \sin(\phi_L))^2 \right) \end{aligned} \quad (9.7)$$

$$\Lambda = \frac{(M_y \cdot M_z \cdot \vec{\mu})_z}{|\vec{\mu}|} = \cos(\phi_y) \quad (9.8)$$

However, the analytical approach does not take the amorphous nature of organic thin films into account. An approach including this requires the introduction of a distribution function for the molecular alignments. Due to in plane properties of the films being amorphous, this distribution is most likely only dependent on the angle of the molecular symmetry axis to the film surface. One example of a function describing these amorphous properties is a Gaussian distribution given by

$$\Phi(\varphi) = \frac{1}{\sqrt{2\pi b^2}} \exp \left\{ -\frac{(\sin(\varphi) - \sin(\varphi_m))^2}{2b^2} \right\}. \quad (9.9)$$

Therein b describes the broadening of the amorphous distribution and φ_m the preferred alignment angle of the investigated molecule as shown in fig. 9.13.

Via a statistical approach using an ensemble of randomly generated rotation matrices, all possible rotations of the investigated molecule can be calculated and weighted with respect to the distribution function. This procedure allows for the calculation of the orientation parameters Θ and Λ for any given distribution function. The Φ function as given in equation 9.9 yields the results as shown in fig. 9.14.

Therein all possible values for Θ and Λ are mapped to their corresponding φ_m and b values. From this it can be concluded that Λ can range from -1.0 up to $+1.0$ whereas Θ has a limited range from near zero up to 0.5 for the investigated

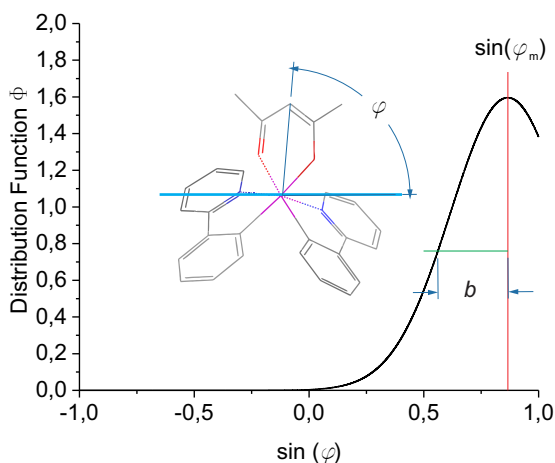


Figure 9.13.: Distribution function as shown in equation 9.9. The broadening of the distribution b and the center value φ_m yield a probability for any given molecule to orient within a certain angle ϕ to the film surface. Picture taken from [11].

molecule. Note that Λ will always be within this range as there can be only one PDM within a molecule. Contrary to this the range of Θ will depend on the amount of emissive TDMs and their direction with respect to the symmetry axis.

By using the experimental values obtained from both electrical and optical measurements, it is possible to determine the set of φ_m and b values satisfying both orientation parameters. From the determination of the cross section between the areas, the molecular orientation can be pinpointed to a limited set of possible orientations. Using this procedure for the $\text{Ir}(\text{ppy})_2(\text{acac})$, as shown in fig. 9.15, reveals a limited range of distribution functions varying from a delta distribution at $\varphi_m = 48^\circ$ up to a broad amorphous behaviour with $\varphi_m = 90^\circ$ and $\Delta\varphi = 17^\circ$. These values allow for the conclusion of an extreme preferential alignment of the molecular C2 axis with only up to 17° degrees broadening.

Within this work $\text{Ir}(\text{ppy})_2(\text{acac})$ was chosen as an exemplary molecule to investigate the combination of both, electrical and optical orientation measurements. However, this procedure is not limited to heteroleptic Ir-complexes. Generally, it can be applied to all organic dye molecules exhibiting visible luminescence and a PDM. Further, it is essential that those two quantities are not parallel to each other but ideally in orthogonal relation.

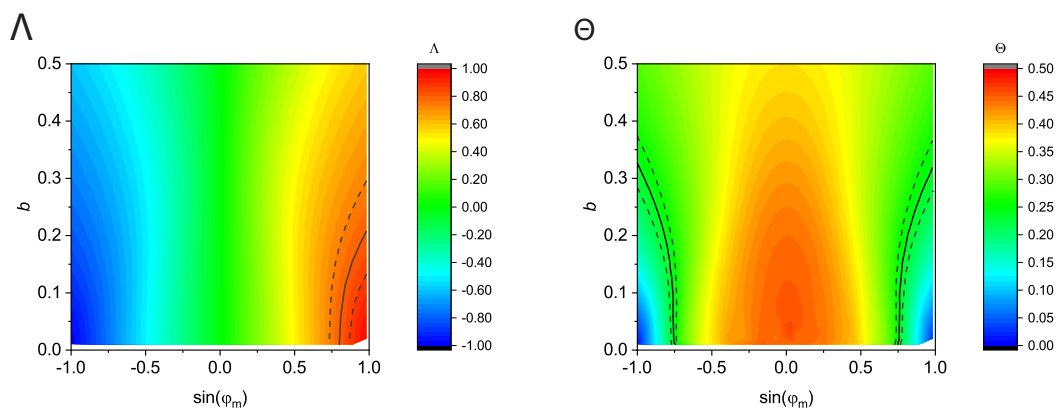


Figure 9.14.: Calculated values for Λ (left) and Θ (right) from applying the distribution function Φ to a randomly generated set of molecular orientations. The black lines indicate measured values whereas the dashed lined depict the possible range of the values when taking measurement errors into account. Pictures taken from [11].

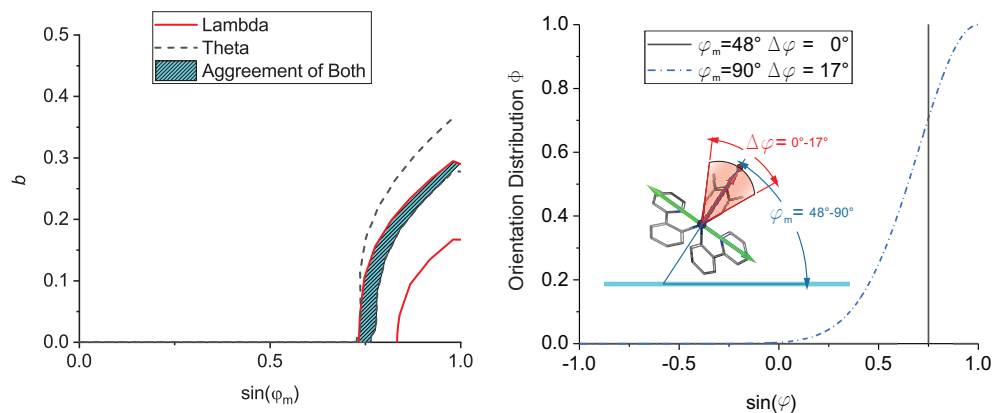


Figure 9.15.: Possible distribution functions for the given set of measurement values (left), ranging from a delta distribution with $\varphi_m = 48^\circ$ up to an amorphous behaviour with $\varphi_m = 90^\circ$ and $\Delta\varphi = 17^\circ$. Both distribution functions are shown in the right side of the picture illustrating the small range of possible orientations given for the $\text{Ir}(\text{ppy})_2(\text{acac})$ molecule. Pictures taken from [11].

Aggregation of polar heteroleptic Ir-complexes

Using the electrical orientation parameter Λ as well as the optical quantification Θ allows for the investigation of dye aggregation effects for heteroleptic Ir-complexes. Interestingly high concentrations did not show any effect on the preferential alignment for optical investigations. Hence, the emissive TDMs and their preferred alignment are independent from the concentration. To investigate the real orientation of the dye molecules in those films, Λ was determined for various concentrations ranging from 2% up to 100% dopant concentration. The resultant C-V measurements, as well as extracted sheet charge densities, are shown in fig 9.16.

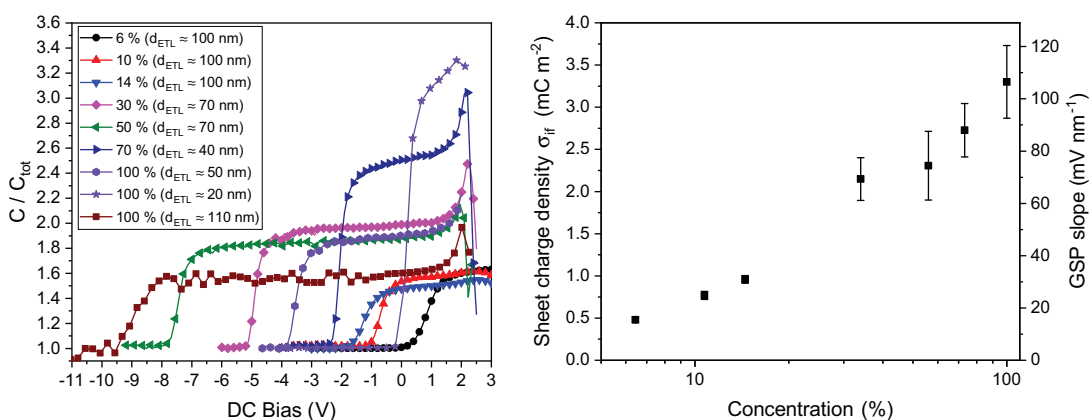


Figure 9.16.: Capacitance-Voltage measurements for various concentrations of $Ir(ppy)_2(acac)$ doped into CBP (left). Note that not all concentrations were prepared with the same polar film thickness to maintain a suitable measurement window for the impedance spectroscopy. The individual measurements were analyzed for their respective sheet charge density within the bilayer device. The resultant values are shown on the right-hand side of the picture. Pictures taken from [11].

The sheet charge density ranges from $0.5 mC/m^2$ up to more than $3 mC/m^2$, corresponding to an electric field of more than $1 \cdot 10^7 V m^{-1}$. It should be pointed out that the measurements were performed using different film thicknesses to adjust the position of the transition voltage. The measurements reveal an increasing sheet charge density as the dopant concentration is increased. This continually increasing behavior is different from observations of another organometallic complex Alq_3 , in which the interfacial polarization yields a maximum value at around 50% dopant concentration [10].

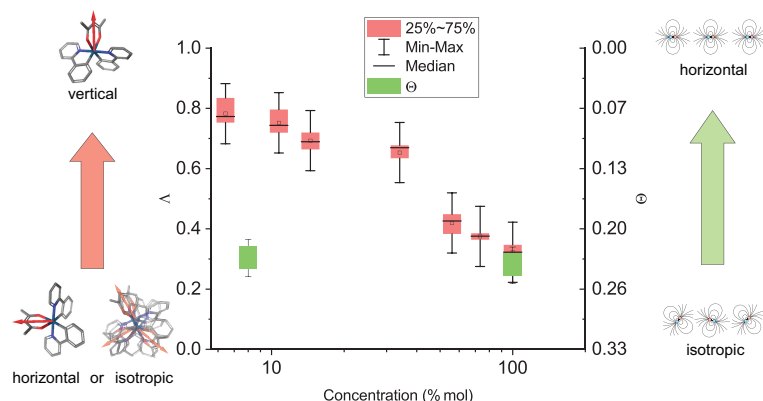


Figure 9.17.: Electrical and optical orientation parameters for various concentrations of Ir(ppy)₂(acac) doped into CBP. Interestingly, the optical orientation Θ remains constant throughout the variation, while the electrical parameter Λ shows a decreasing behavior. Picture adapted from [11].

Calculations of the orientation parameter Λ for the different dye concentrations, as depicted in fig. 9.17, reveal a decrease of the degree of alignment. Hence, a rising fraction of dye molecules within the film leads to a change in the interfacial sheet charge density induced per polar molecule. The reason behind the decrease of the orientation parameter could originate from different effects. At first, an increase in dopant content within the film could neglect the underlying processes for the preferential alignment and lead to a more isotropic film. However, due to the alignment of the TDMS not changing as the film composition is altered, this scenario seems unlikely.

Hence, the more natural cause for this effect on the alignment of the PDMs would be an aggregation of the dye molecules in an antiparallel or at least partially compensating manner. In this case, two different scenarios could explain the experimentally obtained results. First, the aggregated dye molecules could be prone to quenching mechanisms. Hence these non-polar structures would not emit anymore, leaving the observable radiation pattern to the still separated molecules and leading to the observed orientation parameter Θ . As a second possibility, the dye molecules could attach in an antiparallel fashion while preserving the optical orientation parameter. Although the presence of neither of these scenarios can be verified within this system, the second possibility will be investigated in detail within the following paragraphs.

For the sake of simplification, the aggregation was described via two antiparallel distribution functions. Using the same formalism as for the unraveling of the

exact dye orientation, the distribution function can be used to determine a range of distribution functions which explain both the observed electrical and optical orientation values. The results of this procedure are depicted in fig 9.18 and reveal an increasing fraction of dye molecules. Further, the error bars represent the possible range of dye fractions when taking all allowed distribution functions into account. Interestingly, the radiative lifetime of the emissive films coincides with the increased aggregation of the dye molecules. This decrease of excitonic lifetime further confirms the assumption of the formation of aggregates.

Note that the alignment of the molecular C2 axis parallel to the film surface as proposed within literature [141] is not in agreement with the measured data. Due to the TDMs of the molecule being perpendicular to the symmetry axis, this scenario can not yield a Θ value of 0.24.

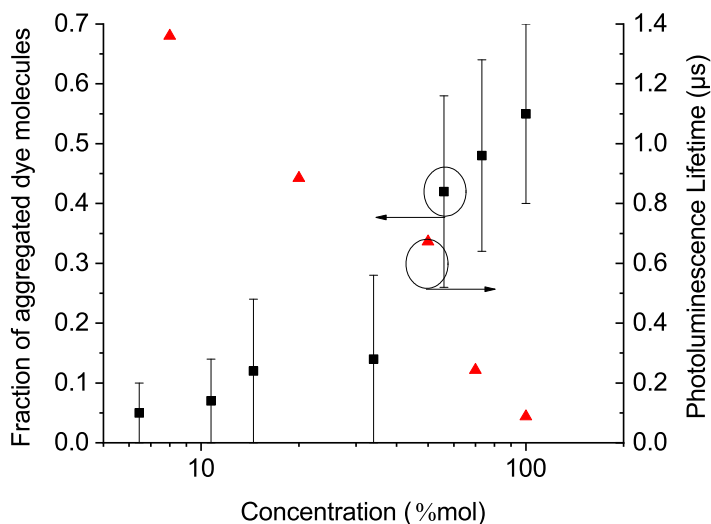


Figure 9.18.: Fraction of aggregated dye molecules in various concentrations of $\text{Ir}(\text{ppy})_2(\text{acac})$ doped into CBP. As the dye content is increasing, more molecules are aggregating leading to a decrease of the interfacial sheet charge density induced per molecule. Further, the aggregation is in agreement with the decrease of the exciton lifetime. Picture taken from [11].

9.2.2. Understanding and predicting the alignment mechanisms

At first, the preferential alignment of the molecule is surprising due to the bulky shape of many heteroleptic complexes such as $\text{Ir}(\text{ppy})_2(\text{acac})$. The aspect ratio of the molecular axes of this particular dye is almost unity, as shown in fig 9.19. Hence, other effects need to be investigated to explain and predict the preferential alignment of heteroleptic Ir-complexes.

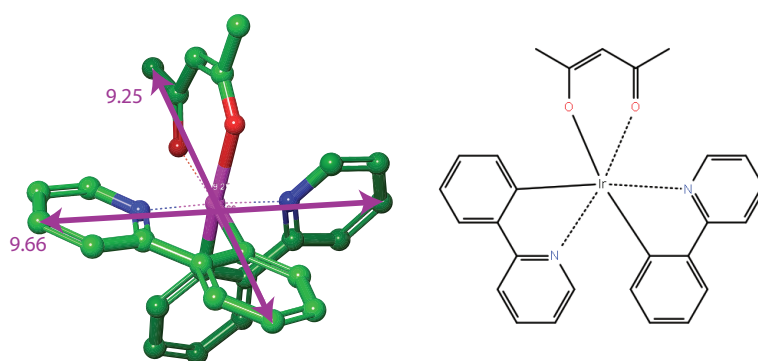


Figure 9.19.: The aspect ratio of the $\text{Ir}(\text{ppy})_2(\text{acac})$ molecule is rather bulky, hence a preferential alignment of the dye molecule cannot be caused by the shape of the molecule. The molecular geometry was optimized using the B3LYP functional and LACVP** basis set.

Several other features of the molecules such as the permanent dipole moment, electrostatic potential of the molecule as well as local discrimination in aromaticity, depicted in fig 9.20, could be involved in the orientation process [37, 129, 130]. This section will focus on the underlying processes of preferential alignment for organometallic $\text{Ir}(\text{C}-\text{N})_2(\text{O}-\text{O})$ complexes. The discussion is based on the theoretical and experimental results of [37].

Due to the asymmetry of heteroleptic Ir-complexes, they exhibit permanent dipole moments ranging from 1 Debye to more than 8 Debye [129]. This property could lead to effects similar to small molecules such as DCM or Coumarin6. Graf et al. tried to correlate the permanent dipole moment to some organometallic complexes being aligned, while others showed isotropic behavior [129]. While the approach seems reasonable, this would most likely lead to isotropic orientations in films consisting of high dye concentrations, such as neat films of $\text{Ir}(\text{ppy})_2(\text{acac})$. Interestingly, this material system still maintains the preferential alignment of the dye [11]. Further, the synthesis of the $\text{Ir}(\text{bpp})_2(\text{acac})$ dye dismantled this approach, as it maintained the preferential alignment despite its high PDM exceeding 8 Debye [37, 142].

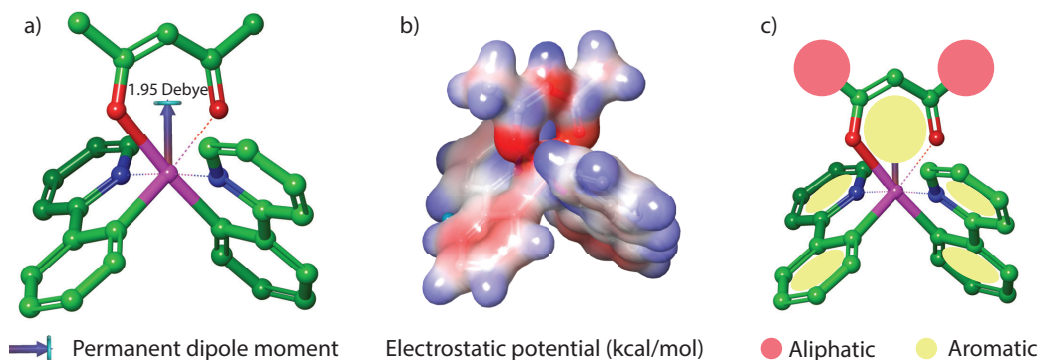


Figure 9.20.: Heteroleptic Ir-complexes exhibit several features possibly responsible for their preferential alignment. The permanent dipole moment (a) points along the C2 axis of the molecule towards the acac ligands. In the case of $\text{Ir}(\text{ppy})_2(\text{acac})$ the permanent dipole moment is 1.95 Debye. Further, the electrostatic surface (b) of the molecule offers possible interactions with the surrounding medium. Besides these features, the aromaticity of the molecule, leading to distinct Van-der-Waals forces could also influence the preferential alignment of the molecule [37, 129, 130].

Another interesting molecular feature is asymmetric electrostatic surface interacting with the surrounding material. This hypothesis, proposed by J.J. Kim et al. [130], claimed that the electrostatic surface of the dye molecules leads to the orientation of the Ir-complex via an attracting force between the guest and the host molecule within doped films. This theory is further supported by the fact, that films consisting of $\text{Ir}(\text{ppy})_2(\text{acac})$ doped into UGH-2 reveal an isotropic orientation of the dye molecule while the interaction between guest and host is repulsive. This approach can be investigated by comparing the two molecules $\text{Ir}(\text{ppy})_2(\text{acac})$ and $\text{Ir}(\text{ppy})_2(\text{bppo})$ [37]. Both species have comparable electrostatic surfaces. Hence, if the electrostatic surface of the molecules was an important molecular property for the formation of preferential alignment, both molecules should show preferential alignment. Interestingly, the experimental results reveal preferential alignment of $\text{Ir}(\text{ppy})_2(\text{acac})$, while $\text{Ir}(\text{ppy})_2(\text{bppo})$ does not show any signs of molecular orientation. This leads to the conclusion that the electrostatic surface is not the factor leading to preferential alignment [37].

A third explanation for the preferential alignment of heteroleptic Ir-complexes is the aromaticity of the investigated ligands. In organic $\text{Ir}(\text{C}-\text{N})_2(\text{O}-\text{O})$ complexes, the C-N ligand usually exhibits aromatic groups due to its organic nature. Contrary to this, the O-O ligand contains aliphatic groups. It is important

to note that the acac ligand was shown to be partially aromatic and thus, only the part of the entity can be considered aliphatic [37].

Within this approach the organic ligands of the complex interact with the surface of the underlying film, leading to the aromatic groups being attracted to the film surface while the aliphatic O–O entity is pointing away from the surface. This hypothesis satisfies the preferential alignment of Ir(ppy)₂(acac) and Ir(bppo)₂(acac) while simultaneously agreeing to the isotropic orientation of Ir(bppo)₂(ppy) and Ir(ppy)₂(bppo) due to the missing aliphatic entity. Further, the orientation of the acac group away from the film surface could be confirmed using impedance spectroscopy [11, 37].

It is important to note that this effect requires an exposed film surface during deposition as well as a step-by-step deposition technique such as TVD or OVPD. Hence the isotropic orientation of guest-host systems prepared from solution processing is a direct consequence of this process. Therein the molecules are deposited within one step without the possibility to interact with an aromatic surface, suppressing their preferential alignment [36]. However, in this system, the strong interaction of the dye molecules to the host medium, caused by electrostatic interaction, can still affect the preferential alignment of the dopant by manipulating the host medium. This effect was confirmed using polymerizing host materials, inducing preferential alignment of the dye after deposition via spin-coating [105].

Within the process of alignment via aromatic-aliphatic discrimination, the interface of the exposed film plays an important role. This area is usually exposed to vacuum in a TVD process, and thus the orientation could also be affected by the vacuum. Using OVPD deposition, this can also be investigated. Therein the film surface is not exposed to vacuum but a nitrogen atmosphere. Despite this difference, Ir(ppy)₂(acac) doped into CBP still maintained its preferential alignment, indicating that the atmosphere which the film is exposed to does not affect the alignment properties of heteroleptic Ir-complexes.

When investigating organometallic dyes doped into the high gap material UGH₂, it could be expected that the dye orients within the film due to this effect interacting with the aromatic host. However, it is essential to take the dynamics of the system into account, which is partially represented by the glass transition temperature of the host material. In the case of UGH₂, this temperature is very low [138], leaving the system highly mobile within the deposition chamber as well as in room temperature. These conditions cause isotropy of the system within a short time, neglecting the alignment effects happening at the film surface during deposition. Taking this effect into account, the preferential alignment of the dye can be expected to vanish if the film is heated to elevated temperatures approaching the glass transition temperature of the host.

Unfortunately, this experiment cannot be performed due to most organic systems crystallizing at those temperatures, making a proper determination of the radiation pattern impossible.

The dynamics of the system given by the temperature also play a vital role in the formation of preferential alignment. When cooling down the substrate during a deposition process such as OVPD, the molecular orientation vanishes below a certain threshold temperature. While further investigations are necessary to understand this process entirely, this indicates that the formation of preferred orientation takes place after deposition and requires thermal energy for the molecule to align itself.

Accessing the preferential alignment via molecular dynamics simulations

Recently, molecular dynamics simulations of heteroleptic Ir-complexes doped into organic guest-host systems were performed by several researchers using different approaches. Tonnelé et al. [79], as well as Friederich et al. [80] confirmed the orientation of the molecule in several different host and dye molecules by simulating the step-by-step deposition process. Hence, single molecules were dropped onto a prepared film surface and calculated for an extended timeframe before another entity was introduced into the system. Another approach investigated the movement of a single dye molecule on a film surface. Therein it was claimed that Van-der-Waals forces are responsible for the preferential alignment of the guest molecule on the film surface [81].

Using the Desmond molecular dynamics engine and the OPLS3 force field, the deposition of Ir(ppy)₂(acac) onto CBP was simulated within this work. The film was formed on a pre-calculated NPB substrate to mirror the conditions within an OLED stack. Between each molecular deposition event, 6 ns of molecular dynamics were calculated to ensure the relaxation of the system. Note that this timeframe is shorter than the average time between two molecules arriving on the film surface in an experimental deposition process performed at 1 Å/s. However, the time window is limited by the computational performance of the simulation. The resultant system consisted of 200 deposited molecules in total, 40 of which were dye molecules. Hence, a molar concentration of 20% was calculated. From the final geometry, the last 6 ns were taken to determine the values for both Λ and Θ . Note that the determination of the alignment of the TDMs was simplified by assuming the TDM parallel to the N–N axis of the Ir(ppy)₂(acac) dye.

The investigation of the PDM of the film reveals a vast difference to experimentally obtained values. The results as depicted in fig. 9.21 reveal values different from experimental parameters. The calculated films only show a mean Λ of 0.17 as well as a mean Θ of 0.35. Hence, the optical orientation parameter

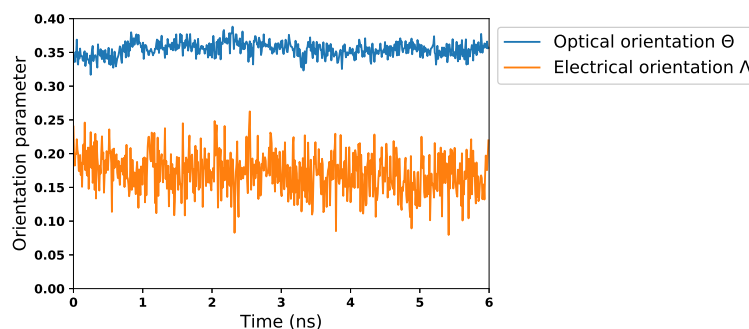


Figure 9.21.: Computational results for a system of Ir(ppy)₂(acac) doped into CBP on a NPB substrate. In total 200 molecules were deposited, 20% of which were dye molecules. During the subsequent deposition procedure, each molecule was calculated for 6 ns before the introduction of another molecule to ensure the relaxation of the system.

was not able to resemble the expected value of $\Theta = 0.24$. Further, the electrical parameter Λ is not in agreement with the values obtained from impedance spectroscopy, which revealed a strong orientation with $\Lambda = 0.8$. This discrepancy shows that this simple molecular dynamics approach is not able to reproduce the complex conditions within organic guest-host systems and therefore cannot easily give access to their alignment mechanisms. Despite these drawbacks, the general direction of the PDM and its parallel C2 axis could be determined to point away from the surface.

In conclusion, the simplified approach via the OPLS3 force field and the desmond molecular dynamics engine is not able to reproduce the experimentally obtained results. However, comprehensive approaches using specific force-fields characterized using in-depths DFT calculations as used in literature [79, 80] can adequately describe the preferential alignment of the TDMs. Unfortunately, none of the mentioned publications determined the electrical orientation parameter Λ .

9.3. Orientation mechanisms of homoleptic C-C complexes

Contrary to the heteroleptic organometallic Ir-complexes, exhibiting different aromatic ligands, homoleptic dyes cannot exploit this feature. However, there are some examples of preferentially aligned homoleptic dyes which will be discussed in this section.

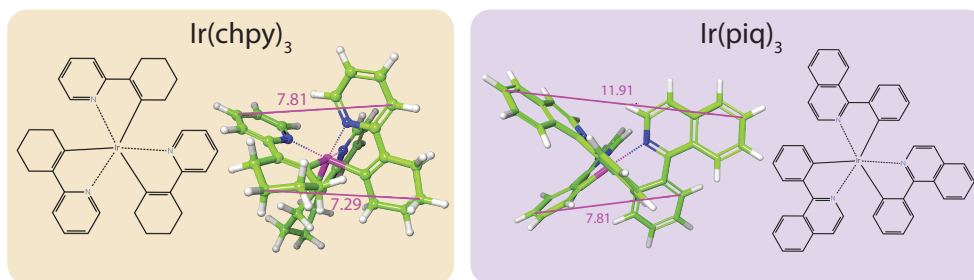


Figure 9.22.: Structure and Lewis formulas of the homoleptic Ir-complexes $\text{Ir}(\text{chpy})_3$ (left) and $\text{Ir}(\text{piq})_3$ (right) for the facial symmetries in both cases. Due to the larger ligand, the $\text{Ir}(\text{piq})_3$ dye has an asymmetric aspect ratio while $\text{Ir}(\text{chpy})_3$ remains in a bulky shape. Further, chpy ligand offers discrimination in aromaticity of the molecule while the piq substructure does not show this feature. Length units shown are given in Å.

The two red dye molecules $\text{Ir}(\text{piq})_3$ and $\text{Ir}(\text{chpy})_3$ shown in fig. 9.22 offer the feature of preferential alignment as known from the literature [129]. However, the fundamental processes behind this effect were not investigated in detail. For the $\text{Ir}(\text{chpy})_3$ complex this behavior could be caused by the discrimination in aromaticity of the chpy ligand. Due to the non-aromatic ring of the chpy substructure, this could cause the same effect as for the heteroleptic Ir-complexes.

Contrary to this, the $\text{Ir}(\text{piq})_3$ molecule does not offer discrimination of the aromaticity. Although the piq substructure does offer two differently large conjugated systems, this cannot be responsible for the preferential alignment. Further, the heteroleptic counterpart $\text{Ir}(\text{piq})_2(\text{acac})$ does not show any different behavior compared to other heteroleptic complexes. However, this homoleptic dye molecule deviates from the usual bulky structure of many Ir-dyes, leading to an asymmetric aspect ratio with the long axis measuring 11.91 Å, while the short axis only extends to 7.81 Å. It is important to note that the literature values known for $\text{Ir}(\text{piq})_3$ could not be reproduced within several experimental attempts.

To investigate the alignment processes of homoleptic Ir-complexes another, easily modifiable, molecule was chosen [143, 144]. The blue-emitting dye 1295 consists of three equal ligands, each containing a imidazole as well as a dibenzofuran group as shown in fig. 9.23. All dye molecules in the following section were synthesized at the Technical University of Braunschweig by Kristoffer Harms and Hans-Hermann Johannes.

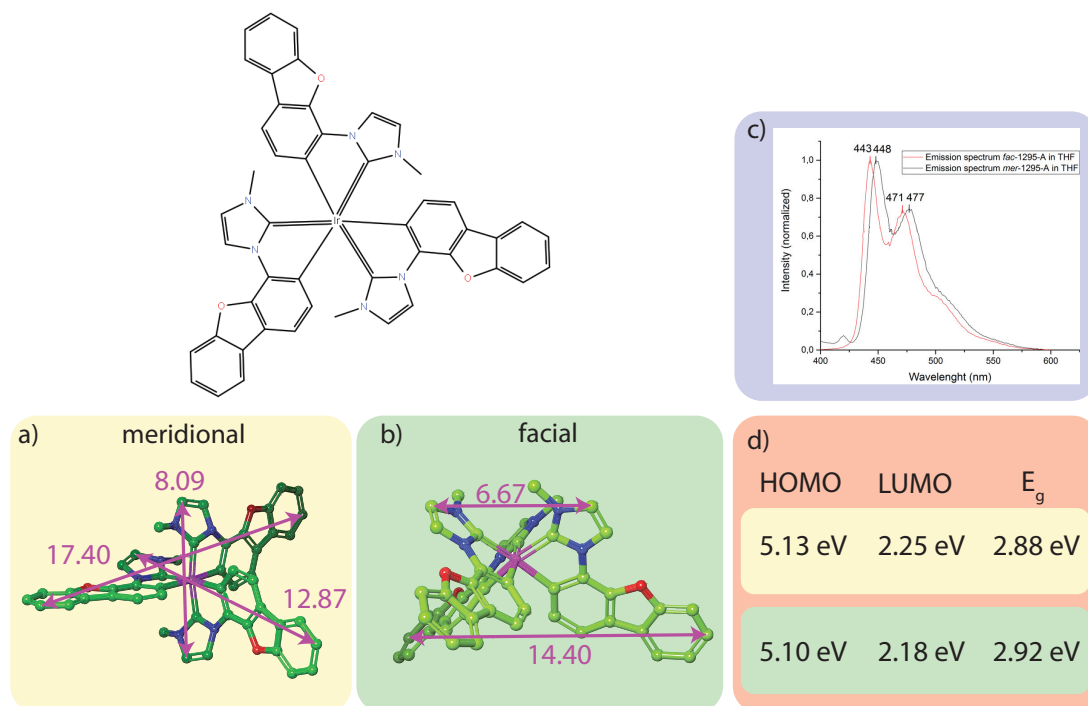


Figure 9.23.: The molecule 1295 containing three equal ligands in both meridional (a) and facial (b) symmetry. (c) An emission spectrum of the two dyes molecule from THF solution. (d) Photophysical properties of the 1295 dye molecule in both symmetries. HOMO values were calculated via cyclic voltammetry relative to ferrocene in DMF. LUMO energies were determined from E_g and the HOMO level. The energy gap E_g was determined from the emission edge.

9.3.1. Photophysical properties of sky-blue Ir-complexes

Synthesis of efficient and stable sky-blue Ir-complexes is still in the focus of research [145–154]. Due to the involvement of high-energy triplets in those material systems, several challenges arise such as suitable host materials and stability of both, host and guest molecule in the presence of those [1]. Further blue emitting organometallic complexes often yield a high triplet lifetime, enabling quenching processes in lighting applications. Contrary to the two preferentially aligned homoleptic molecules in the previous section, this molecule is a C-C complex. Hence the atoms coordinating to the center Iridium are both carbons. Another unique feature to the 1295 dye molecule is the similarity of the facial and meridional enantiomers. Whereas for $\text{Ir}(\text{ppy})_3$ those two symmetries show a huge difference in their photophysical properties, this is not the case for 1295. However,

this feature gives rise to problems in separating the enantiomers during chemical synthesis.

Another challenge for guest-host systems incorporating this blue emitting complex is the high triplet level of the dye. Experiments with carbazole-based host materials such as Spiro2-CBP revealed an incomplete energy transfer to the guest molecule. This behavior can be demonstrated either by investigating the emission spectrum of the guest host system or the radiative lifetime of the emissive spectrum. Both techniques are shown in fig. 9.24.

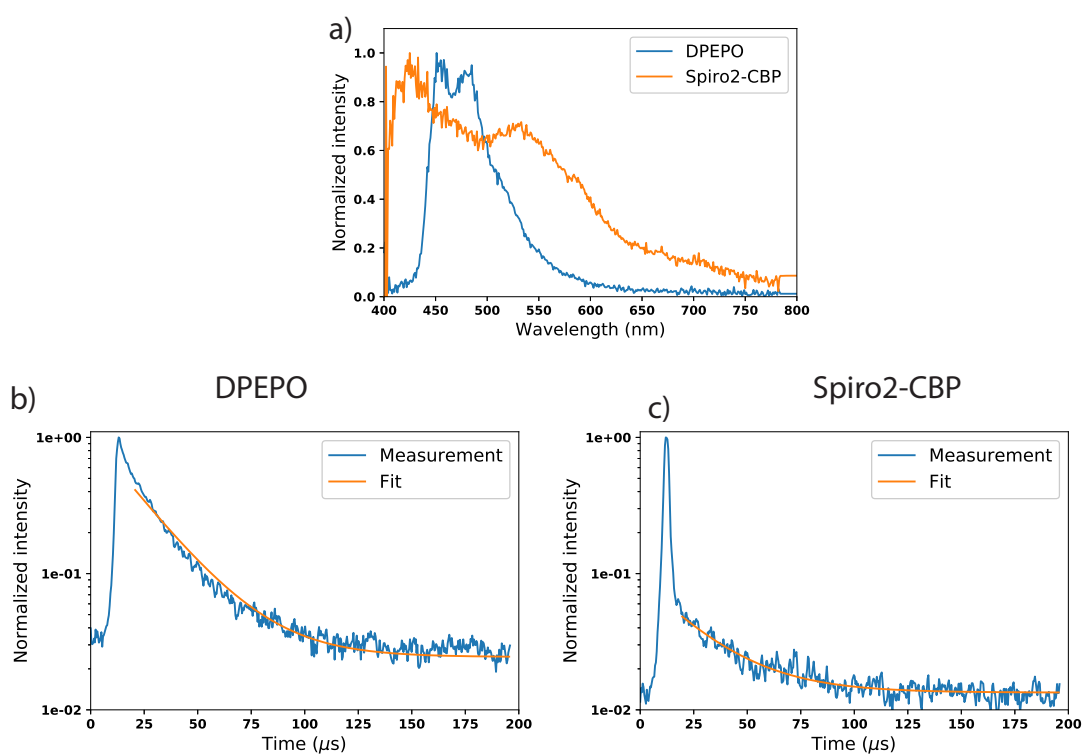


Figure 9.24.: Emission spectra (a) and exciton lifetime measurements of the 1295 dye in two different host materials, Spiro-2CBP (b) and DPEPO (c). The carbazole based host material Spiro-2CBP reveals a contribution to the emission spectrum as well as a excitonic lifetime component in the ns range, indicating an involvement of the host medium. The sample with the Spiro2-CBP host material reveals an exciton lifetime of 25 μs whereas the DPEPO host has a shorter lifetime of 22 μs .

9. Preferential alignment of organometallic Ir-complexes

From these measurements, the host molecule DPEPO was chosen as one possible host material due to the clean dye emission spectrum and the lack of a short exciton lifetime component. Additionally another matrix material, PO9 also was found to be a suitable host material [144].

Based on the 1295 dye, a new derivate was chosen as depicted in fig 9.25, aiming to modify the properties of the molecule. The derivate 1295-B adds an additional phenyl group to the imidazole. This modification has two effects on the structural behavior of the molecule. At first, the aspect ratio is changed away from the almost plate-like shape of the 1295-A dye. Second, this group shields the imidazole from the interaction with the surrounding medium. Hence, if this part of the molecule is responsible for the preferential alignment of the emissive TMDs, the modification should take away this feature.

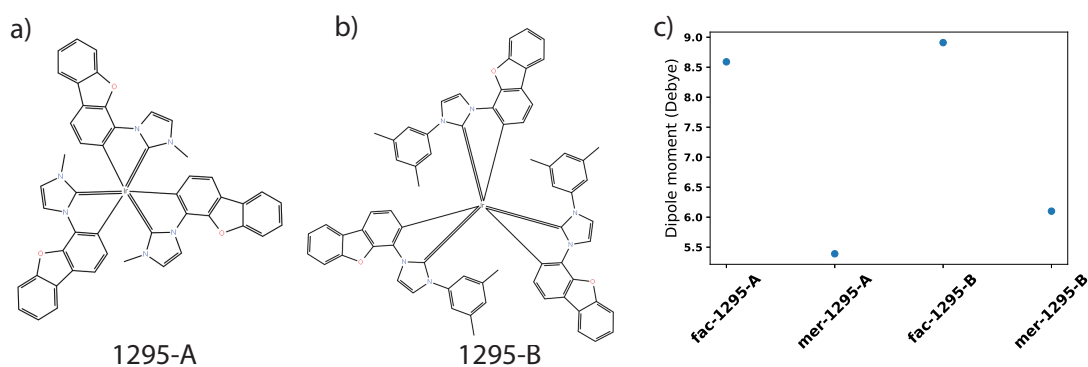


Figure 9.25.: Lewis formulas of the two investigated molecules 1295-A and -B. For the -B variant an additional phenyl group was added to the imidazole. Both molecules were investigated in their facial and meridional symmetries. The permanent dipole moments of the structures as calculated from DFT are depicted in (c). Therein the facial variants always exhibit the higher PDM compared to their meridional counterparts. Furthermore, the additional phenyl group slightly increases the dipole moment compared to 1295-A.

To investigate the effects of symmetry and the additional phenyl group on the photophysical properties of the molecule calculations were performed for both 1295-A and -B in their respective configurations. The results are shown in fig. 9.26 and depict the dominant TDMs for each molecule. Unfortunately, fac-1295-B could not be calculated successfully. The directions of the emissive TDMs on the molecules reveal several interesting features. For the only facial symmetry calculated, fac-1295-A, three equivalent TDMs have to exist due to the symmetry of the molecules. However given by the Jahn-Teller distortion, only one of those

redundant transition states is calculated. Interestingly the TDMs of fac-1295-A reveal an angle of 90° with respect to the permanent dipole moment and thereby the C3 axis of the molecule. This angle would make the facial symmetry of this molecule an excellent candidate for the preferential alignment of these TDMs as a perfect orientation could be achieved if the symmetry axis is aligned perpendicular to the film surface.

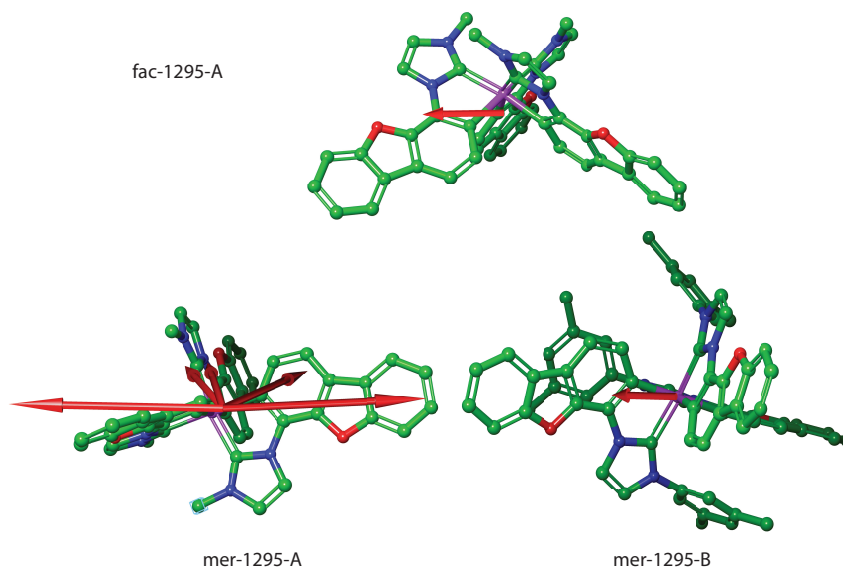


Figure 9.26.: Transition dipole moments of 1295-A in both facial and meridional symmetry as well as the TDM for mer-1295-B. For the facial molecule, only one of the three equivalent TDMs is shown which has an angle of 90° with respect to the C3 symmetry axis of the molecule. The respective calculations for the meridional molecules reveal only a single TDM for the 1295-B derivative while 1295-A has five equivalent TDMs spread along the molecule. Interestingly, the emissive TDMs are within the plane of the molecule which allows for their simultaneous alignment within a thin film. Note that the TDMs for mer-1295-A are scaled by a factor of ten to enhance their visibility.

For meridional symmetries, the angular relation of the TDMs is within $\pm 20^\circ$ with respect to the PDM. However, for those molecules, the -A and -B derivatives show different behavior. In the case of the molecule without an additional phenyl group, five different TDMs with almost equal contributions can be found. Interestingly, the TDMs lie within a plane along the long axis of the molecule.

Contrary to this behavior upon adding a phenyl group as in the 1295-B molecule only a single TDM can be found, which again is aligned within a plane along the long axis of the molecule.

Despite their differences of the TDMs, the emissive spectra as well as the exciton lifetimes of all the investigated molecules, as depicted in fig. 9.27 show no significant difference despite their changes in structure and symmetry. Further, the lifetime of the excited state does not have a significant dependence on the used host material being DPEPO or PO9, indicating that both materials are suitable to be used as matrix material. This eligibility is further confirmed by the emissive spectra showing no contribution of the host material.

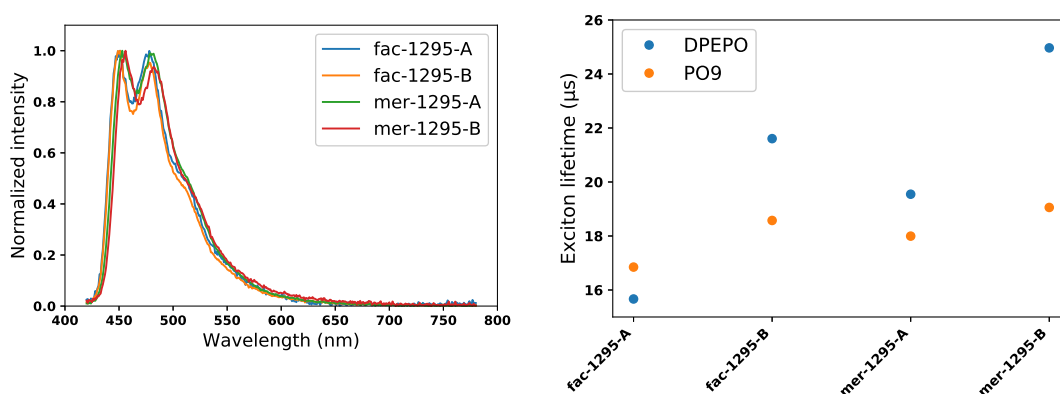


Figure 9.27.: Photoluminescence spectra of 1295-A and -B for both symmetries measured within a PO9 matrix (left). Surprisingly, the molecules show almost no difference in their spectra. The radiative lifetimes of the molecule as measured in two different host materials, DPEPO and PO9, also do not exhibit any substantial changes depending on the structure of the molecule or the host material.

9.3.2. Preferential alignment of homoleptic C-C complexes

Surprisingly, homoleptic 1295-A dye exhibits a preferential alignment of its three equal transition dipole moments. In the host material PO9, the orientation factor Θ could be determined to 0.24. Given that no distinct aliphatic groups are present as for heteroleptic dyes, the question arises what the origin of this orientation behavior is within the group of homoleptic C-C complexes. Interestingly, despite not being discussed in detail, samples of fac-1295-A in DPEPO show no preferential horizontal alignment when prepared from solution (THF, 5 mg ml⁻¹)

but a slightly vertical alignment of $\Theta = 0.4$. This value again indicates a dependence on the deposition technique similar to heteroleptic Ir-complexes.

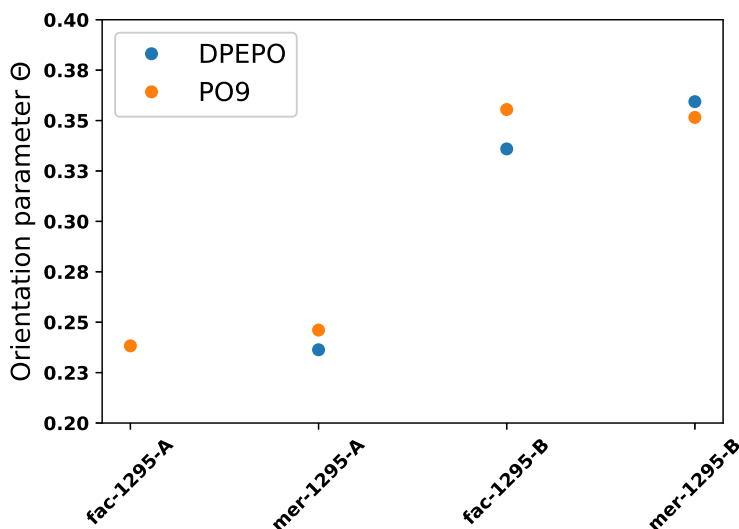


Figure 9.28.: Orientation parameter Θ for the investigated molecules. Interestingly both the meridional and facial configurations of 1295-A reveal a preferential alignment of their emissive TDMS with the same value for the orientation parameter Θ . Contrary to this, both symmetries for 1295-B show isotropic behaviour. Note that fac-1295-A was not measured in DPEPO.

When prepared from TVD, different orientations ranging from 0.24 up to 0.35 can be observed for the 1295 dye family doped into either DPEPO or PO9 at a concentration of 8% wt.. These results, as depicted in fig 9.28 depend on the dye molecule being either 1295-A or 1295-B, in which the -A variant exhibits horizontally aligned TDMS while the -B derivative does not show any signs of preferential orientation. Further, the host material being either DPEPO or PO9 show no effect on this alignment behavior of the dye molecules.

Within another experiment using a neat film of fac-1295-A, the surface potential and thereby the interfacial sheet charge density could be determined to be positive. This sign indicates the PDM of this molecule pointing towards the film surface during deposition, which is opposed to heteroleptic dye molecules. Note that this experiment was not performed for other dye molecules so far due to the material requirements. Further, it cannot be performed in doped films containing a polar host material such as DPEPO, which itself is known to exhibit preferential alignment of the PDMs and thereby could not be distinguished from

the dopant.

For the family of 1295 molecules, different alignment mechanisms could affect the film morphology. Although an aliphatic group is missing, a strong interaction section of the molecule could orient parts of the dye towards the exposed film surface. Another possibility is the shape of the molecule itself having a preferred orientation on a surface and thereby orienting the emissive TDMS. Both of these possibilities will be discussed in the following paragraphs.

Dependence of preferential alignment to the molecular aspect ratio

Given the unique shape of the 1295 dye family, the shape of the molecules could generally affect the preferential alignment of the molecule. Planar molecules such as Pt-complexes or phthalocyanines have been investigated in great detail for their morphology in thin films showing different alignment features [155, 156]. Further, some other dye molecules within more amorphous systems are also known to preferentially align due to their aspect ratio [157]. Fig. 9.29 depicts the aspect ratios between the longest and shortest axes within the molecules as calculated from DFT. The facial molecules fac-1295-A and fac-1295-B both show a C₃ symmetry and thus are rotationally symmetric with respect to the C₃ axis. However, the spatial extension of either the dibenzofuran or the imidazole group is vastly different, where the axis between two dibenzofuran groups extends to about 14.4 Å while the imidazole only requires 6.5 Å of space. Further the length of the molecule along the symmetry axis is only 6.49 Å giving the molecule a cone-like shape. Note that 1295-B, despite its modifications still has a length along the C₃ axis of only 7.4 Å, retaining the cone-like shape. This unique format of the molecule would indicate a preferential alignment of the dibenzofuran groups towards the substrate within a step-by-step deposition technique. However, this is not the case as discussed later within this section.

Contrary to their facial counterpart, the two meridional complexes do not exhibit any rotational symmetry. Hence, the orthogonal axes along the longest axes within the molecule were investigated. For both dyes, the shortest axis is along the opposing imidazole groups measuring only 8.6 Å. Surprisingly, the additional phenyl group does not affect this for 1295-B as the additional entity fits into the plate-like structure of the molecule. The other two axes put up the flat structure of the molecule, measuring about 17.3 Å and 13.0 Å each. Again the values show only small differences between the -A and -B derivatives of the 1295 dye.

Regarding the question whether the shape of the molecules affects the preferential alignment, several observations can be made. For the meridional molecules, the planes of the two long axes need to be preferentially aligned parallel to the

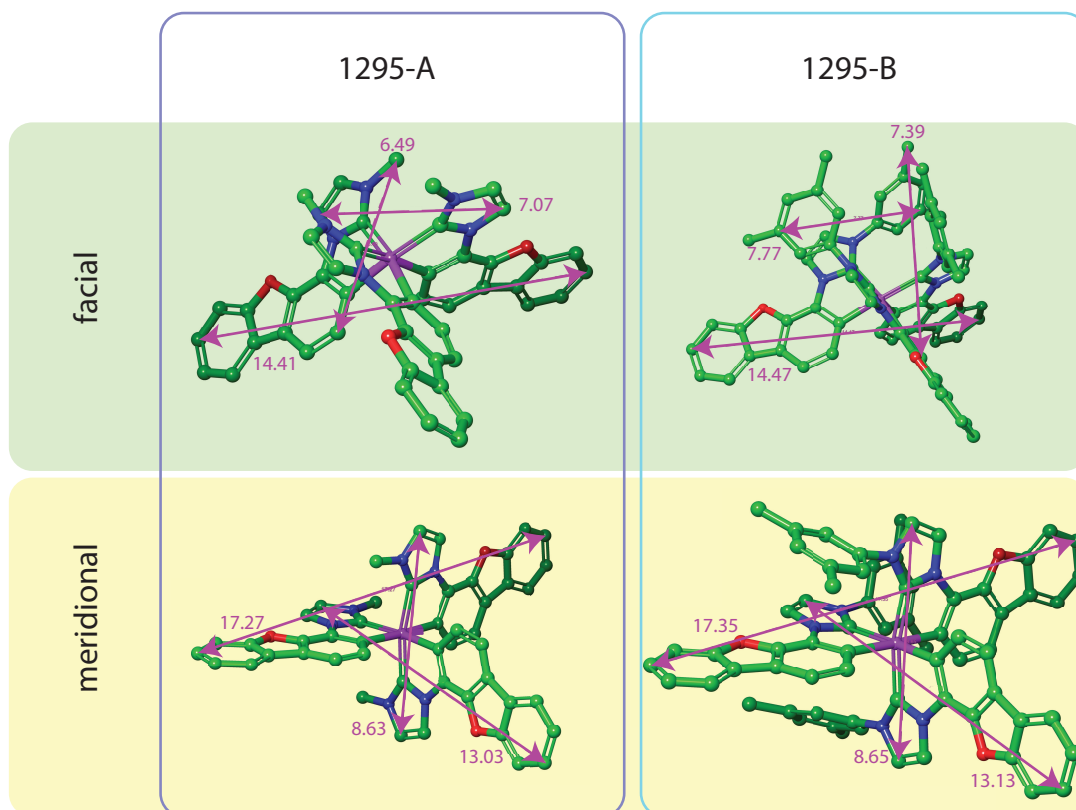


Figure 9.29.: Aspect ratios for the different symmetries of 1295-A and -B. The lengths of the different axes are shown in Å. In both symmetries, the ratio of the longest axis to the shortest axis shows no significant difference between the two derivatives. In the case of the facial configuration, this ratio is 2.22 for 1295-A and 1.95 for 1295-B. In the case of meridional symmetry, these values change to 2.01 and 2.00 respectively. Note that meridional configurations have a planar shape as two long axes with more than 10 Å while facial molecules have a long axis at the bottom of the molecule and a short axis on the top.

film substrate in order to yield the observed horizontal alignment. However, only the 1295-A variant exhibited this behavior while the 1295-B dye did not show any preferential orientation. Given their almost equal aspect ratios, the shape of the molecules cannot be the driving force towards the preferential alignment. A similar observation can be made for the facial configurations. While the lateral extension along C3 symmetry axes of the molecules shows minor differences, the general shape is the same for both molecules. However, the orientation behavior differs as only fac-1295-A shows preferential alignment while the dye with an additional phenyl group is isotropically distributed within a thin film. Further, due to electrical measurements for neat films, the smaller imidazole groups are expected to point towards the film surface, neglecting the intuitive orientation given by the aspect ratio.

Imidazole as interaction center towards preferential alignment

As the previous section showed, the aspect ratio of the molecule has no influence on the orientation of the 1295 dye molecules. Further, the extent of the molecules is too large for efficient dipole-dipole interaction towards changing the morphology. Hence, only the specific interaction of subgroups of the molecules during a step-by-step deposition is able to induce the preferential alignment of the dye. Given the structure of the molecules, two entities could be responsible for this effect. First, the imidazole group bound to the center atom could interact with the film surface and thereby align the molecule. The second possibility is the dibenzofuran group and its extensive aromatic system.

To conclude whether the imidazole ligands is responsible for the preferential alignment of the molecule, it was modified by attaching an additional group. This extension shields the ligands from interaction with the film substrate and thus would hamper the alignment processes. This behavior, as depicted in fig 9.30, is confirmed by the orientation parameter of fac-1295-B of $\Theta = 0.35$. Further, the interfacial sheet charge density of neat films of fac-1295-A was found to be positive, indicating the PDM of the molecule pointing towards the film surface and thus orienting the imidazole ligand towards the interface.

For the meridional configurations, a similar behavior was observed. In the case of the preferentially aligned mer-1295-A, the plane along the long axes of the molecules needs to be parallel to the film surface. This observation leaves only two imidazole groups left to interact with the interface of the so far deposited film and again indicates the involvement of this section of the molecule in the alignment properties. For mer-1295-B however, the same groups are still exposed to the surface with the only difference of one nitrogen not being attached to a methyl but a much larger phenyl. From the lack of preferential alignment of mer-

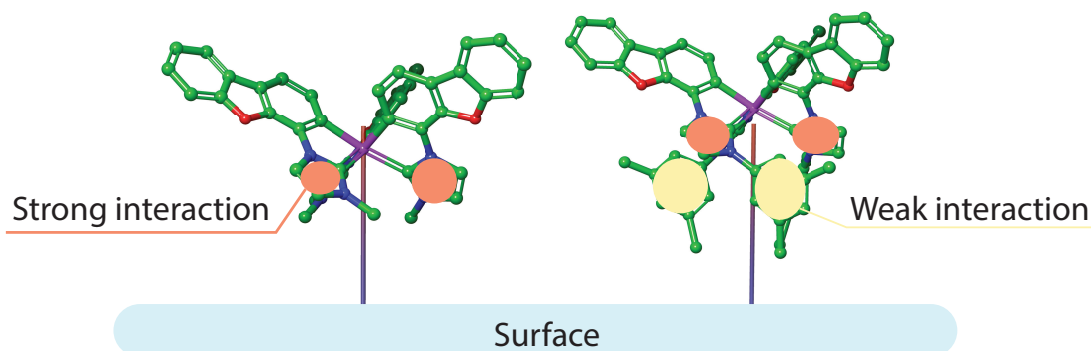


Figure 9.30.: Interaction of facial 1295 assuming the PDM of 1295-A pointing towards the film surface. The strongly interacting imidazole group leads to the preferential alignment of the latter. However, shielding this entity with an additional chemical group neglects the beneficial interaction and leads to isotropically oriented molecules.

1295-B, this nitrogen atom can be identified as a crucial factor for the orientation of 1295 molecules.

9.3.3. Confirming the isotropic nature of $\text{Ir}(\text{ppy})_3$

Due to the symmetrical nature of homoleptic Ir-complexes, the TDMs can theoretically align in an orthogonal manner. This behavior would lead to a constant fraction of the TDMs being perpendicular to the film surface as the molecule is rotated. Hence, in this case, the orientation of the emissive species could not be determined from optical experiments. This consideration leads to the question if homoleptic Ir-complexes that were assumed to be isotropically oriented could show preferential alignment despite an optical orientation parameter of $\Theta = 0.33$. To investigate this possibility, the homoleptic dye molecule $\text{Ir}(\text{ppy})_3$ was analyzed for a preferential alignment of the PDM using impedance spectroscopy [11].

Experimental results were obtained for $\text{Ir}(\text{ppy})_3$ doped into CBP as well as neat films of the dye molecule. Both measurements do not show any obvious preferential alignment [11, 108]. Especially the C-V measurements, depicted in fig. 9.31, do not yield a transition voltage and indicate no interfacial charge density within the bilayer devices. Further, it is important to note that the TDMs of $\text{Ir}(\text{ppy})_3$ were found to be not orthogonal but almost in-plane to each other [8]. Hence, by applying the same procedure as used to unravel the alignment of $\text{Ir}(\text{ppy})_2(\text{acac})$, the possible orientation of $\text{Ir}(\text{ppy})_3$ can be investigated. The results, shown in fig. 9.32, limit the possible alignment of the molecule. The optical orientation parameter Θ only allows for values that are either extensive

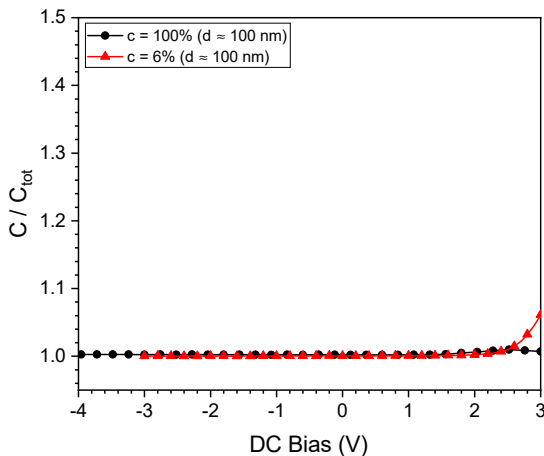


Figure 9.31.: Impedance spectroscopy measurements of Ir(ppy)₃ doped into CBP as well as neat films of the dye molecule. Neither of the two measurements reveals a preferential alignment of the molecular PDMS. Picture taken from [11].

distributions close the isotropic behavior or sharp distributions for specific angles. Note that the latter are the alignments in which the TDMs align close to the magic angle of 35.4° which yields the isotropic Θ value of 0.33. As a second quantity, the electrical parameter Λ only allows for distributions close to the C3 axis of the molecule being parallel to the surface, as represented by $\sin(\varphi_m) = 0$.

Due to the limitations given by both measurements, the preferential alignment Ir(ppy)₃ would require a minimum broadening of 1.2 to satisfy the two conditions. Interestingly, all possible distribution functions given by fig. 9.32 are close to an isotropic behavior of the systems. From these observations, the absence of preferential alignment from the Ir(ppy)₃ molecule is the most likely scenario, confirming the previously assumed behavior.

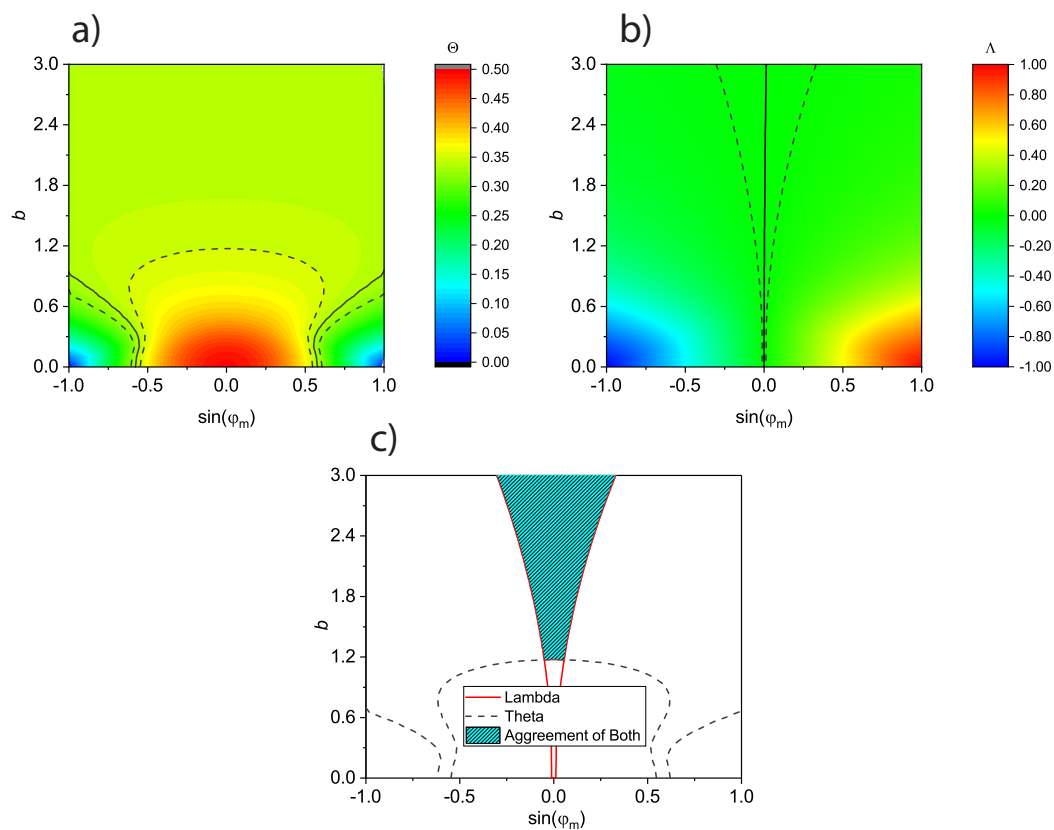


Figure 9.32.: Possible values for the orientation parameters Θ (a) and Λ (b) for the homoleptic Ir-complex $\text{Ir}(\text{ppy})_3$. The solid lines indicate the measured values and the dashed lines the corresponding upper and lower limits given by the measurement error. (c) denotes the possible range of distribution functions satisfying both conditions. It should be pointed out that the minimum required broadening of the distribution of 1.2 is very close to isotropically distributed molecules. Picture taken from [11].

10. Tunable anisotropic light emission in lead-halide perovskite nanocrystals

Lead-Halide Perovskites (LHPs) such as CsPbBr_3 have drawn significant attention due to their promising properties including high quantum yield photoluminescence [98–100], emission from the triplet state [158] and excellent light absorption [159, 160]. Recently the record performance for perovskite photovoltaics exceeded 20%, outperforming purely organic devices. As several similarities between efficient photovoltaics and lighting applications exist, the application of perovskite emitters in LEDs is an obvious step [161].

The often used perovskite MAPbI_3 , enabling outstanding photovoltaic performance [162], is not suitable as an emissive material due to the band gap being too low for visible lighting. Hence the color of the perovskite needs to be tuned. This change can be done by altering the material composition, especially the halide in the crystal lattice. Replacing Iodide with Bromide changes the dominant wavelength towards higher energies making the material an ideal candidate for green devices. Further tuning into the blue regime can be done via the use of chlorine. Interestingly, mixed halide concentrations enable a smooth variation between the photoluminescence wavelengths [163]. However, in this work the focus is set to purely inorganic CsPbBr_3 nanocrystals (NCs). The application of this material as light emitting nanocrystal is a promising concept for perovskite light emitting devices (perovskite LEDs). Recently, devices employing this emissive crystal have exceeded 20% quantum yield [164–168].

Perovskites generally describe the crystal structure of a compound with ABX_3 as stoichiometry. Therein B is coordinated by six X, forming an octahedron BX_6 . The octahedrons are corner sharing arranged, leaving a gap in between which is occupied by A. Within the gaps between the so formed crystal structure, A is located. Due to their unique properties, this work is limited to the CsPbBr_3 perovskite crystal. Within this structure the heavy metal lead is surrounded by Bromide and Caesium is utilized as cation [98].

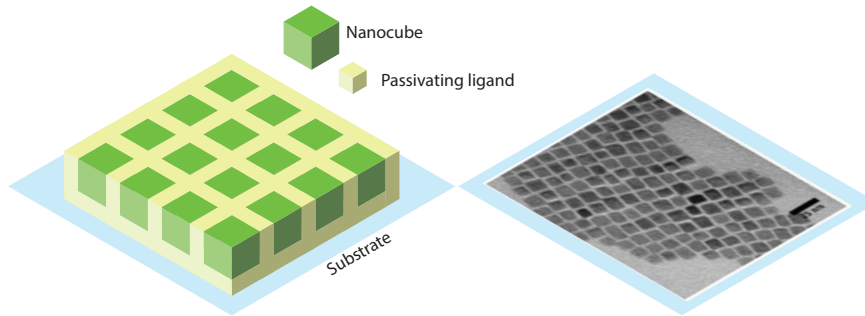


Figure 10.1.: Illustration of a self-assembled nanocube system (left). The individual green nanocubes are surrounded by the passivating ligand, preventing interaction between the nanocrystals. The right-hand side shows an experimentally obtained SEM image of a self-assembled nanocube film. The dark squares indicate the nanocrystals, whereas the space between the individual cubes is filled by the ligand[38].

To investigate the photophysical properties of CsPbBr_3 nanocrystal assemblies the focus is set on the characteristics of the transition dipole moment and its orientation within the film. The nanocrystals for this work were either synthesized by Matthew Jurow at the Lawrence Berkeley National Laboratory or Carola Lampe in the Nanospectroscopy group at the Ludwig-Maximilians University in Munich. Results regarding nanocubes are published in [38], whereas nanoplates were published in [169]. BFP imaging was performed by Carissa Eisler.

The investigated LHP NCs within this chapter consist of CsPbBr_3 , passivated with an oleic acid ligand [98]. Due to the interparticle interaction, films of this material tend to self assemble within a cubic lattice forming a so-called supercrystal. Fig. 10.1 depicts the structure of a self-assembled nanocrystal film, and a corresponding scanning electron microscope (SEM) image of an LHP NC monolayer deposited onto a substrate [38].

10.1. Carrier dynamics in CsPbBr_3 nanocrystals

Contrary to organic molecules and polymers, perovskites are crystalline. Within this lattice Mott-Wannier Excitons are formed that are highly mobile and extend over multiple unit cells in the nanocrystal. [170, 171].

To prevent excitons from quenching at crystal defects, boundaries or other anomalies, it is necessary to passivate the surface of the CsPbBr_3 nanocrystals. During synthesis, this is achieved using oleic acid and oleyl amine as ligands, after

which the oleic acid will attach to the crystal surface [172]. While this vastly improves quantum efficiencies of the NCs, it will also hamper charge injection into the LHP for optoelectronic applications. Interestingly, this does not prevent efficient Forster energy transfer between the nanoparticles maintaining exciton diffusion lengths of several hundred nanometers [173]. Besides the passivation of the nanocrystal surface, additional treatment towards repairing defects in the nanocrystal surface has shown to increase the photoluminescence performance [174].

Classical core-shell nanoparticles such as CdS/CdSe prevent access to the electronic environment of the NC due to the wide bandgap shell [175, 176]. For LHP NCs the crystal is only protected by the ligand material, making the electronic structure of the perovskite susceptible for tuning of the excited state.

10.1.1. Light emission from lead-halide perovskites

Emission in lead-halide perovskites originates from the recombination of an electron in the conduction band bound to a hole within the valence band. Interestingly, the binding energy between the two charge carriers depends on the composition and quantum confinement of the crystal [174, 177, 177–180]. For cubic CsPbBr₃ nanocrystals the binding energy of the charge carriers is only 30 meV. Hence, no stable exciton can be formed but the light emission originates from free charge carrier recombination instead. Upon lowering the thickness of the nanocrystal and thereby quantum confining the excited state, the binding energy is increased and a Mott-Wannier exciton is created [174].

Due to the high order within the perovskite nanocrystal compared to organic semiconductors, the emissive spectrum of the foregoing features narrow bandwidths. Fig. 10.2 shows the emissive spectrum of green CsPbBr₃ nanocubes, featuring a narrow bandwidth as well as a green emission peak at 518 nm [181].

In CsPbBr₃ nanocrystals the bandgap is given by the R point as shown in Fig. 10.3, depicting the calculated band structure. Similar to organic semiconductors, the spin state of the exciton is of crucial importance for the possibility of the excited state to decay radiatively. Becker et al. give an intuitive comparison between organic and inorganic semiconductors regarding the influence of the spin in CsPbBr₃ perovskites. Therein it is stated, that contrary to organic semiconductors, spin is not conserved in the inorganic counterpart due to the strong coupling between spin and the orbital motion of the charge carriers. Consequently, only the total momentum is conserved. The resultant sublevels are described as the fine structure of the semiconductors. In many cases, the lowest level of this structure is a so-called dark exciton having a forbidden transition to the ground state [158, 182].

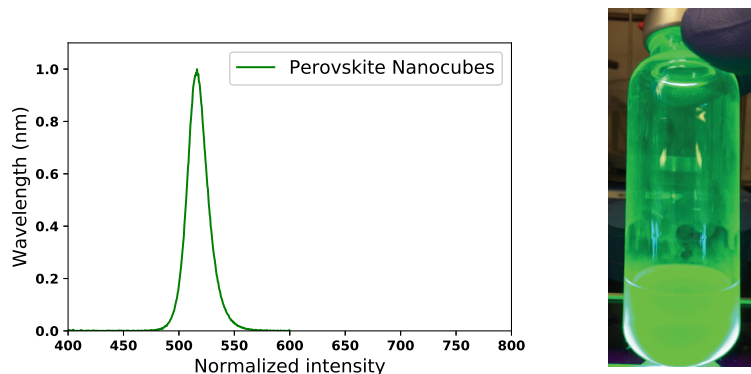


Figure 10.2.: Photoluminescence spectrum of green CsPbBr₃ nanocubes (left) in toluene solution as shown on the right side of the picture.

Interestingly, calculations for CsPbBr₃ indicate the lowest energy state being emissive. This effect was found by Becker et al. using low-temperature excited state lifetimes [158]. Traditional semiconductors, as well as fluorescent organic molecules, exhibit an increase in the radiative lifetime due to the slow emission from the triplet state. Contrary to this, it could be shown that the radiative lifetime of CsPbBr₃ nanocrystals decreases to values below the nanosecond regime while maintaining a high quantum yield at cryogenic temperatures. Most semiconductor nanocrystals exhibit a slow radiative lifetime below one microsecond at low temperatures due to the lowest energy state being dark [183]. Hence, this behavior indicates the presence of an emissive lowest energy state [158].

For the application in light emitting devices, this has further benefits. Due to the emissive lowest energy state, all excitons can be harvested and thus contribute to the lighting purpose. This unique feature also makes CsPbBr₃ nanocrystals competitive to organometallic Ir-complexes [158].

10.1.2. Quantum confining the excited state in perovskite nanocrystals

In the so far described CsPbBr₃ nanocrystals, the lattice is assumed to be infinitely large compared to the electronic wavefunction of the charge carriers. This section will focus on quantum confinement effects occurring if the size of the crystal is decreased below the exciton bohr radius within the crystal, which is about 7 nm in CsPbBr₃ [184].

When investigating quantum confinement in nanocrystals, the density of states is of crucial importance, as it reveals effects on the electronic structure of the

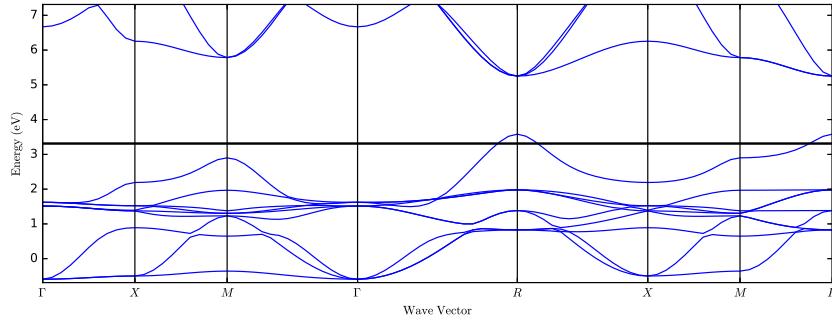


Figure 10.3.: Calculated band structure of a CsPbBr₃ crystal using the GGA functional and PBE basis set in periodic DFT. Note that this low level computation does not resemble the bandgap correctly but still is able to give a qualitative view of the bandstructure.

nanocrystal. Fig 10.4 depicts different extents of quantum confinement and their effects on the DOS within the crystal structure [185, 186].

Using the two dimensional nanoplatelet as an example, a simple model for the quantum confinement can be established. Given an electron within a potential between two infinite barriers in z direction, while being not restricted within the $x - y$ plane, dispersion relations for the conduction and valence band can be established [187]:

$$E_c(k) = E_G + \frac{\hbar^2}{2m_e} (k_x^2 + k_y^2) \quad (10.1)$$

$$E_v(k) = E_G + \frac{\hbar^2}{2m_h} (k_x^2 + k_y^2) \quad (10.2)$$

Therein the energy of the conduction band E_c and valence band E_v are related via the effective mass of the respective charge carriers m_e and m_h as well as their wavevectors within the x - y plane, k_x and k_y . It is important to note that the effective mass of the hole is negative in this description. Further the energy gap E_G is required. Using the Schrödinger equation yields the energies of the eigenstates E_n for the n -th state [188]:

$$H\Psi_n(z) = \left(-\frac{\hbar^2}{2m_{e/h}} \frac{\partial^2}{\partial z^2} \right) \Psi_n(z) = E_n \Psi_n(z) \quad (10.3)$$

$$E_n = \frac{\pi^2 \hbar^2}{2m_{e/h} L^2} n^2 \quad (10.4)$$

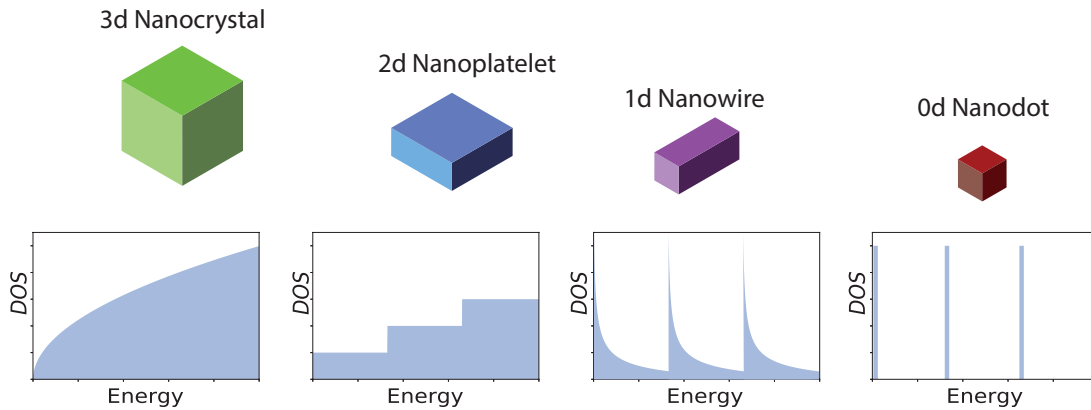


Figure 10.4.: Depiction of quantum confinement in a nanocrystal. From left to right the crystal is confined within several dimensions. At first, the confinement in the thickness leads to a nanoplatelet structure, whereas a further reduction in size shapes nanowires and nanodots. The density of states, as shown on the bottom, reveals significant changes if the wavefunction of the charge carriers is confined within the structure. Picture adapted from [185, 186].

with L denoting the thickness of the two dimensional structure. While a more sophisticated approach is necessary to adequately describe the properties of the quantum confined structure, this approach reveals that the energy of the eigenstates is proportional to $\frac{1}{L^2}$. Thus a decrease in thickness will increase the energy and consequently lower the emission wavelength of the nanocrystal [181, 186].

10.2. Manipulating the emissive transition dipole moment of LHP nanocrystals

Tuning the TDM of LHP nanocrystals is a promising concept to increase the efficiency of lighting applications. While preferential alignment of the TDM is a well-known concept for organic applications, only very little is known for LHP NCs. This section will discuss the properties of the emissive TDM in both cubic NCs and quantum confined nanoplatelets.

10.2.1. Anisotropic emission from self-organized LHP nanocubes

At first nanocube assemblies seem to be isotropic due to their symmetric geometry. However, the physics will be different within a thin film. Due to the close contact to the surrounding media, an LHP nanoparticle within a system is prone to be affected by interfacial charges [38].

To investigate the emissive properties of LHP nanocubes, the radiation pattern of thin films on a glass substrate was investigated. Most samples were investigated using ADPL. Additionally, results were also verified using BFP imaging. Due to the uncertainty of the refractive index, the alignment constant ζ was used within this investigation. Based on this value the orientation parameter Θ and the angle of the TDM with respect to the substrate φ was calculated using approximations for the refractive index [38].

The optical properties of the film can be derived from the individual refractive indices of the components. While the perovskite crystal itself can be estimated to have a refractive index of 2.3, the space in between the cubes is filled with oleic acid and oleyl amine. Those materials exhibit a lower refractive index of 1.45. Using TEM images the ratio between perovskite and ligand within the film could be determined to 70 : 30. Thus the effective refractive index can be calculated to 2.1 using a Bruggeman effective medium approach [38]. Within the following results, this value is assumed to be constant for different concentrations.

Basic characterization of the nanocube films involved powder x-ray diffraction to ensure the perovskite crystal structure as well as absorption and photoluminescence measurements in toluene solution and TEM imaging. These measurements, depicted in fig. 10.5 yield insight into the basic properties of the system. The sharp absorption and emission peaks indicate a narrow particle size distribution as confirmed from TEM measurements [37].

For the characterization of the emissive TDM, glass covered by polymerized hydrocarbon was chosen as a substrate. This material system is promising due to the underlying material promoting the formation of dense monolayers of the self-assembled NCs. The nanocrystals were deposited via spin-coating and the resultant films revealed a self organized pattern. Additionally, measurements were performed for various concentrations of the nanoparticles. Fig. 10.6 shows several SEM images of the nanocubes on the samples. The nanocrystals form monolayers when deposited from solutions containing $610 \mu\text{g mL}^{-1}$, whereas solutions with only $12 \mu\text{g mL}^{-1}$ lead to isolated nanocubes on the surface [38].

Measurements of the TDM angle with respect to the substrate plane for these samples revealed a dependence on the concentration of the nanoparticle solution. When using high concentrations, the angle can be determined at about 50° . De-

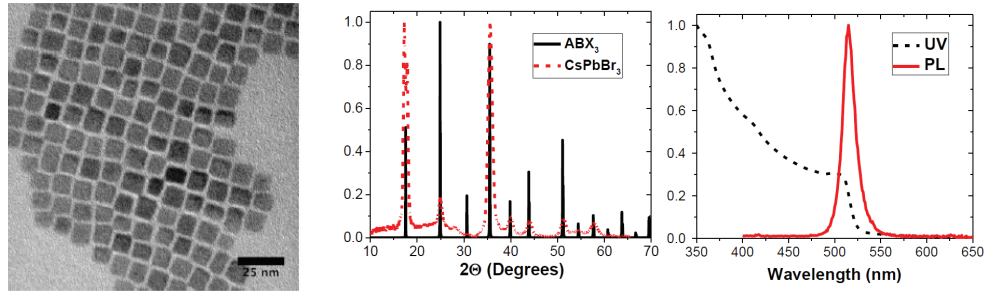


Figure 10.5.: TEM image of a self assembled LHP nanocube film (left). Measured (CsPbBr_3) and calculated (ABX_3) powder x-ray diffraction patterns of LHP nanocubes (middle). Optical absorption and photoluminescence spectra for nanocubes dispersed in toluene (right). Picture taken from [38].

creasing the concentration leads to a more vertical alignment of the TDM. This value reaches as high as 59° when using solutions containing only $12 \mu\text{g mL}^{-1}$ of nanocubes. As a consequence, the alignment constant ζ of the NC films varies between 0.07 for dense films up to 0.125 for isolated nanoparticles. This value indicates a significant dependence on the nanoparticle density for potential optoelectronic applications. It should be pointed out that within those experiments it was not possible to determine if the change in the radiation pattern originates from the different dielectric background of the nanocubes or an intrinsic property of the nanocubes themselves.

10.2.2. Tunability of the anisotropic properties of LHP nanocubes

While the variation of the nanoparticle concentration already revealed a tunability of the TDM, further control of the excitonic state as well as the underlying processes leading to this effect remain to be investigated. Thus, the TDM angle was investigated for additional film substrates at different nanoparticle concentrations. As underlying materials polymerized fluorocarbon (poly C_4F_8), silicon dioxide, bare glass and ITO were chosen and covered with different concentrations of nanoparticle solutions.

The results as obtained from ADPL measurements are shown in fig. 10.7. ITO, as well as poly C_4F_8 , showed the lowest TDM angles while SiO_2 and glass were slightly higher. However, none of the values for the $185 \mu\text{g mL}^{-1}$ solution reached as high as 52° on the poly CH samples. Samples on a glass substrate did not show any dependence on the solution concentration, while the chemically

10.2. Manipulating the emissive transition dipole moment of LHP nanocrystals

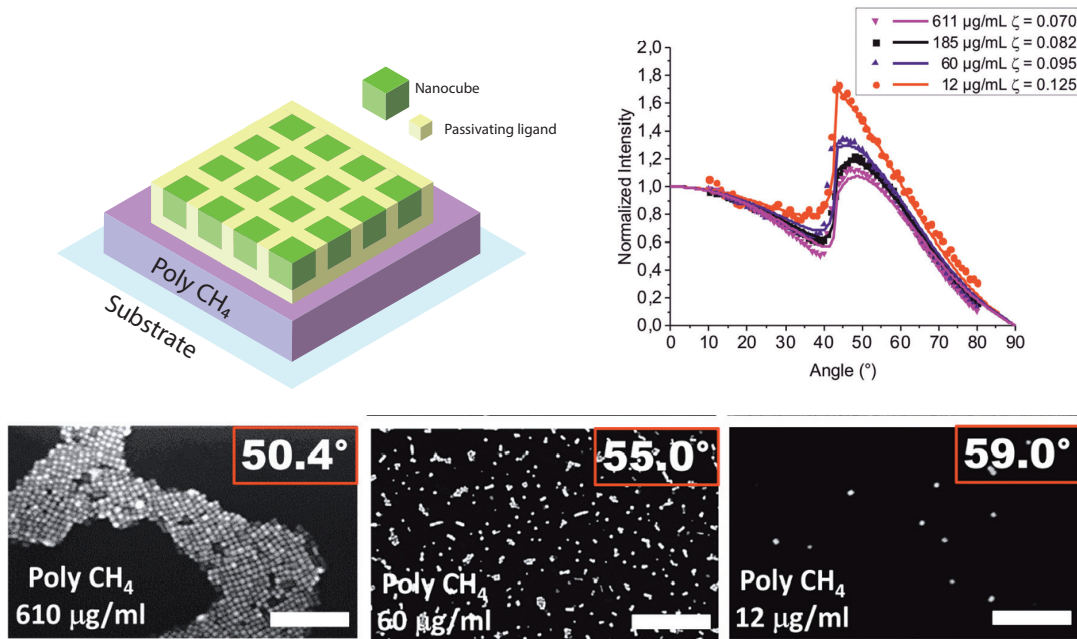


Figure 10.6.: Investigations of LHP nanocubes deposited onto glass covered by polymerized hydrocarbon as depicted in the upper left corner. SEM images of the films as shown on the bottom, range from dense monolayers for high particle concentrations down to isolated nanocubes for low concentrations. The angle of the emissive TDM, as determined by using ADPL, increases upon lowering the concentration of nanoparticles. Therein the values range from a TDM angle of 50° for concentrated films up to 59° for sparse films, depicted in the upper right corner of the image. Further the alignment constant ζ ranges from 0.07 up to 0.125. The picture was taken from [38].

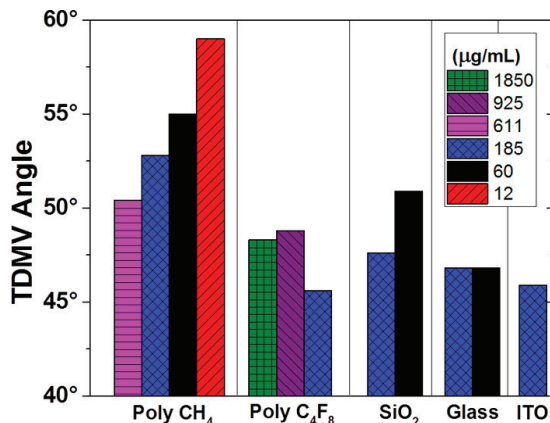


Figure 10.7.: Angle of the emissive TDM with respect to the film surface for different concentrations and substrates. Contrary to the deposition on polymerized hydrocarbon, different orientations can be found when using other substrates. Therein the TDM angles are as low as 45° , making the substrate more suitable for optoelectronic applications. Picture taken from [38].

similar silicon dioxide revealed the expected increase of the TDM angle at lower concentrations. Interestingly, for poly C₄F₈ the TDM angle did not rise upon increasing the concentration up to $1850 \mu\text{g mL}^{-1}$. This behavior could indicate a saturation effect when approaching a closed monolayer on the surface.

Measurements of the quantum yield of the individual films, depicted in fig. 10.8, further support an effect of the underlying substrate on the electronic structure of the nanocubes. For ITO as a substrate, the quantum yield is only 50% of the value obtained for LHP nanocubes on a glass substrate. The high quantum yield is only preserved by the poly C₄F₈ coated substrate, which corresponds to the low TDM angle obtained on this substrate. These values indicate a strong influence of the underlying medium on the quantum yield of the material.

The origin of this dependence on the underlying substrate was investigated using a computational approach. At first, the close contact of a perovskite lattice to silicon dioxide, as depicted in fig. 10.9, was analyzed. Periodic DFT reveals a redistribution of charges at the interface. This redistribution was determined to be $0.006 e/\text{\AA}^2$. Consequently, the anisotropic behavior of the charges lead to the formation of an electric field perpendicular to the film surface.

To take the charge redistribution into account, the band structure was calculated in the neat material as well as in the presence of an electrical field of $0.05 \text{ V}/\text{\AA}$. At first, the conduction and valence band without an electric field show a symmetric distribution of the band structure within the crystal. How-

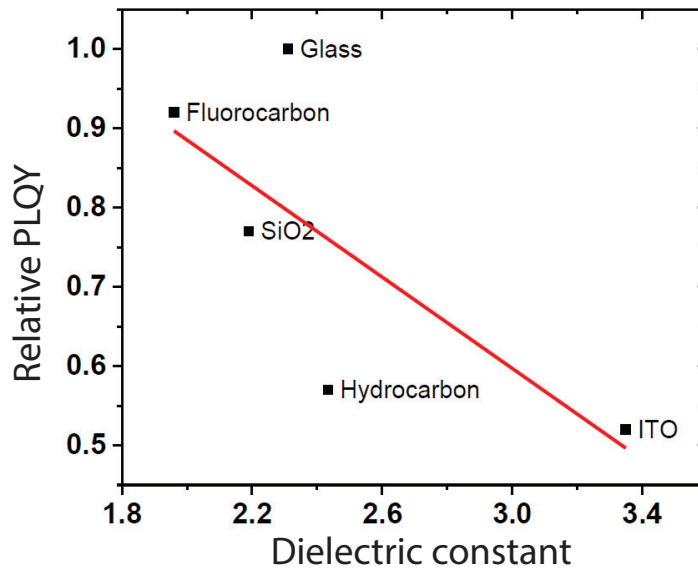


Figure 10.8.: Relative quantum yields of the LHP nanocubes on various substrates compared to the value on bare glass. Picture taken from [38].

ever, the introduction of the electric field induces a spatial separation of the corresponding bands. This observation confirms the previously observed effect of the underlying substrate on the emissive structure.

To unambiguously confirm this effect, TD-DFT calculations were performed by Jun Kang at the Lawrence Berkeley National Laboratory [38]. The computations allow for the prediction of the TDM within the LHP. Hence, the results can be compared to the experimental values obtained from the measurement of the radiation pattern. Again, the calculations were performed for an isolated structure as well as in the presence of an electric field of 0.05 V/\AA . The results for the nanocrystal without the external perturbation reveal the isotropic angle of the TDM as 35.4° . Contrary to this result, the introduction of the electric field reveals a TDM angle of 63° with respect to the film surface. This value is very close to the experimentally observed 59° , as depicted in fig 10.10, and cannot agree with an isotropic TDM distribution which would correspond to an angle of 35.4° .

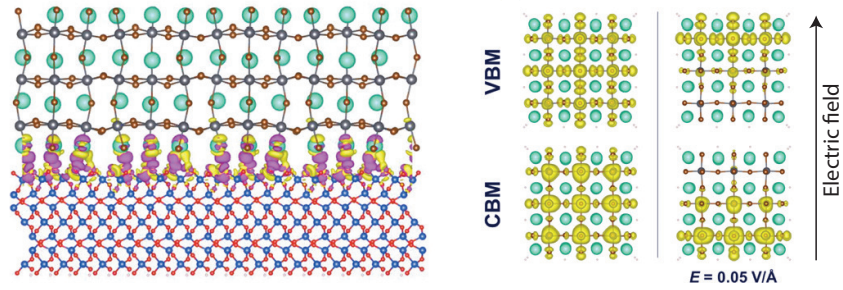


Figure 10.9.: DFT calculations of LHP nanocubes. The close contact of the perovskite lattice to silicon dioxide (right) reveals a redistribution of charges at the interface. This redistribution is as high as $0.006 \text{ e}/\text{\AA}^2$. The thereby induced electrical field of $0.05 \text{ V}/\text{\AA}$ is able to spatially separate the conduction band (CBM) from the valence band (VBM) and thus lead to an anisotropically distributed TDM within the symmetric cubic lattice. Picture taken from [38].

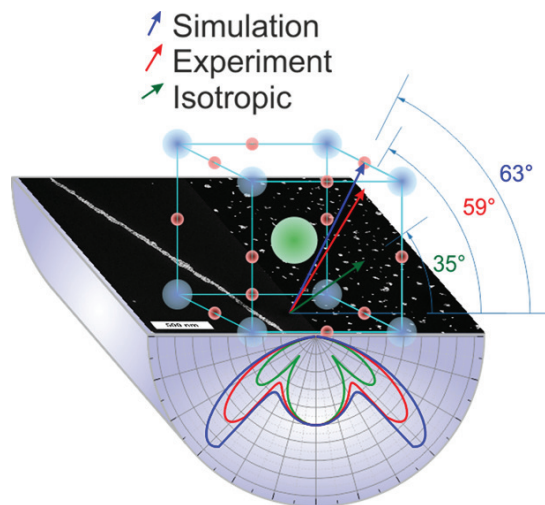


Figure 10.10.: Illustration of the TD-DFT calculations, yielding a TDM angle of 63° , compared to the experimentally obtained value of 59° . Both values can not be in agreement with an isotropic TDM orientation which would correspond to an angle of 35° . Picture taken from [38].

10.2.3. LHP TDM in quantum confined NCs

When investigating the shape of LHP NCs, the quantum confinement (QC) of the exciton is of special interest. Due to the spatial limitation of the electron and hole being comparable to the size of the particle within this effect, their excited state properties change [189]. At first the wavelength of the emitted photons changes to higher energies. This behavior can be explained via the confinement of the exciton within the nanocrystal as described in a previous section.

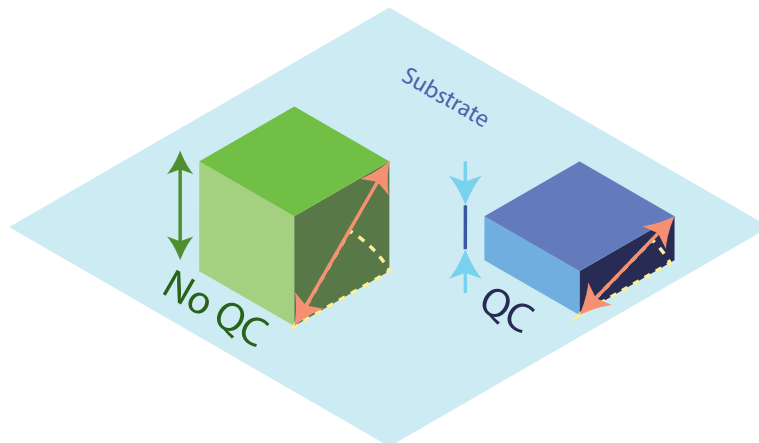


Figure 10.11.: The emissive TDM of a nanocube (green) is at an angle of approximately 45° degrees with respect to the film substrate. Confining the exciton within a nanoplatelet (blue) restricts the TDM within the crystal and tunes the angle towards the substrate. Note that the orientation of the TDM depends on the alignment of the nanoplatelet on the film.

Further, due to the quantum confinement effect, the TDM of the nanocrystal is changed. In the case of a nanoplatelet, the exciton is confined within the thickness of the structure. This effect vastly changes the direction of the TDM and therefore the optical properties regarding the optical alignment constant of a particle film. This effect is illustrated in fig. 10.11.

The synthesis of quantum confined nanoplatelets is comparable to their cubic counterpart. Using the same hot injection process, precise control of the temperature can tune the thickness of the resultant NCs [172]. Further, the investigated nanoplatelets are known for their face-down orientation within a thin film [172].

Before measurements of the TDM angle, nanoplatelet films were investigated using basic measurement techniques, such as TEM, SEM, and optical absorption and emission. The results as depicted in fig. 10.12, reveal the blue emission

properties of the nanoplatelets resulting from quantum confinement. Further atomic force microscopy (AFM) and TEM confirm the face-down orientation of the samples. For comparison, TEM images of edge-on standing nanoplatelets were also taken but not measured for their emissive TDM properties. It should be pointed out that the refractive index of nanoplatelets was estimated to 2.0 based on the SEM characterization.

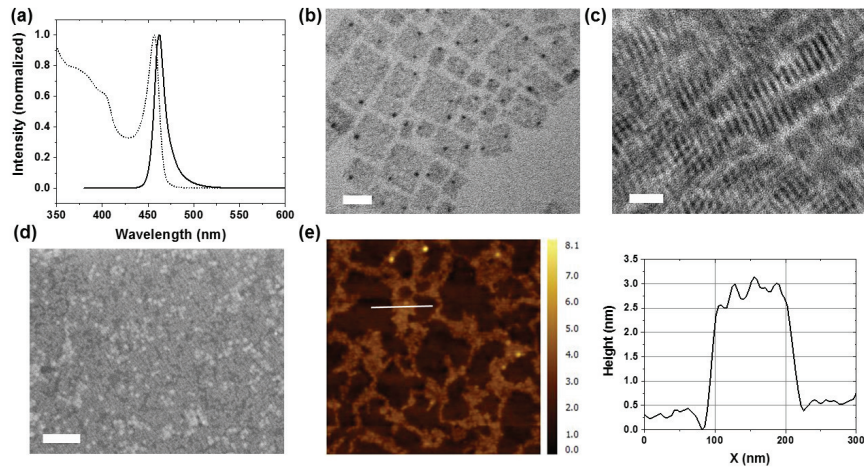


Figure 10.12.: Photoluminescence (solid line) and optical absorption (dashed line) of LHP nanoplatelets in solution (a). TEM images of both flat lying and on edge standing nanoplatelets (b and c). SEM images with a scale bar of 200 nm (d) and atomic force microscopy characterization (e) revealing the face-down orientation of the nanoplatelets. Picture taken from [169].

The results of the nanoplatelets as depicted in fig. 10.13, reveal a strongly horizontal alignment of the TDM within the nanoplatelets. Via ADPL, the alignment constant could be determined to $\zeta = 0.02$ for the dominant emission wavelength of 460 nm. Note that the nanocrystals partially fused into larger structures that are not quantum confined. The second emission peak at 520 nm indicates a contribution of the bulk material. Interestingly, the alignment constant of this contribution is in agreement with measurements for CsPbBr₃ nanocubes.

To further identify the dependence of the TDM to the NC thickness, different nanoplatelets were measured. Note that the CsPbBr₃ samples were synthesized differently from the previously described method. Hence, slightly different values for the alignment constant could occur. The results, as depicted in fig. 10.14, reveal a strong dependence of the TDM alignment to the quantum confinement of the NCs.

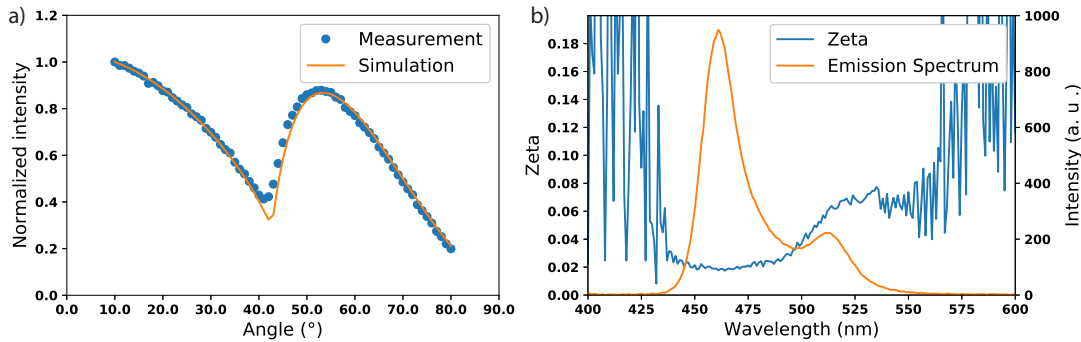


Figure 10.13.: (a) ADPL measurement for the sample of nanoplatelets at 460 nm wavelength. The radiation pattern indicates a strong horizontal alignment yielding $\zeta = 0.02$. (b) Resultant alignment constant for each wavelength. Interestingly, the sample is contaminated with green emitting nanoparticles. The alignment constant of these non-quantum confined particles coincides with the values measured for nanocubes.

10.2.4. Superior optical properties of LHP nanoplatelets

Bare LHP nanoplatelets already showed exceptional optical properties compared to their cubic counterpart. However, within an optoelectronic application, the NCs will be covered by one or more functional layers, further affecting the optical properties of the particles. Based on the results for cubic LHP nanoparticles it can be expected that an additional layer on top of the emissive structure will again affect the excited state properties of the film. As the band separation induced by the substrate will be partially removed, an even more horizontal orientation of the TDM is enabled.

To investigate this effect, films of nanoplatelets were covered with a thin layer of Al_2O_3 and measured using BFP imaging. From the measurements, a further decrease of the TDM angle with respect to the substrate was observed. The presence of the covering layer decreased this from 29° down to 14° . This further reduction in the TDM angle can be confirmed by investigating the BFP image at a given distance from the center as depicted in fig 10.15. Therein the effect can be confirmed due to the lower minimum of the Al_2O_3 coated sample compared to the bare film. Taking the alignment constant ζ into account, this system reaches as low as 0.02, outperforming many organic emitter systems while only aligned CdS/CdSe quantum structures were able to reach below this value [96].

This effect not only yields a superior emissive system compared to organic dye molecules, as discussed in the next section, but also confirms the proposed

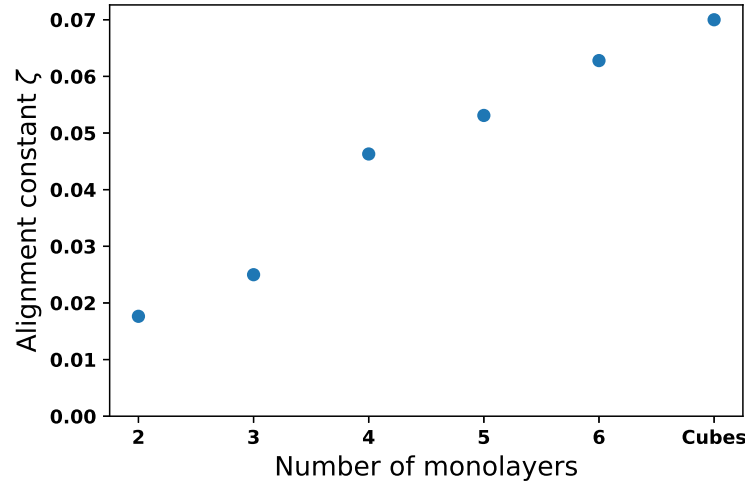


Figure 10.14.: Alignment constant ζ for various thicknesses of LHP nanoplatelets. The values range from 0.07 for not quantum confined structures down to 0.018 for structures of only two monolayers. Value for cubes taken from ref. [38].

tunability of the excited state by manipulating the direct environment of the nanocrystals. Introducing a second interface counteracts to the charge redistribution at the bottom layer, partially compensating the adverse effect of the separation between the valence, and conduction band.

From a computational point of view, this behaviour can be modeled by taking the work functions Φ of the semiconductors into account. Due to their difference, being 5 eV for SiO_2 , 4.7 eV for Al_2O_3 and 3.95 eV for CsPbBr_3 , the direct contact of the materials yields a charge distribution:

$$\sigma_{\text{if}} = \frac{\epsilon_r}{d} (\Phi(a) - \Phi(b)) \quad (10.5)$$

This equation yields the interfacial charge given by the permittivity ϵ_r , the distance between the materials and the difference between the work functions. The results, as depicted in fig. 10.16, indicate a strong charge redistribution if the materials are in close contact. However this effect is lost if the separation between the materials increases. Taking the corresponding electric field into account, the observed effects on the TDM properties are further confirmed.

By using DFT, the TDM angle of a nanoplatelet in the close contact to a Al_2O_3 film can be calculated. Note that the calculations assume an infinitely extended crystal within the plane of the nanoplatelet whereas the actual plate

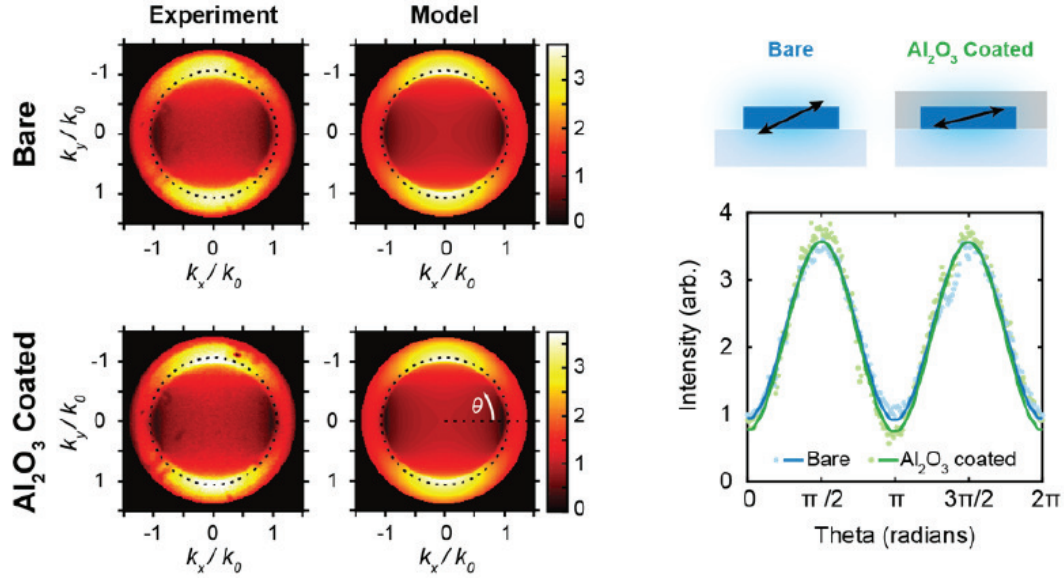


Figure 10.15.: BFP measurements of bare CsPbBr_3 nanoplatelets as well as samples covered with a Al_2O_3 layer. When investigating the measurement traces along the dashed lines (left), the difference between the samples is clearly visible in the plot on the bottom right of the picture. The lower minimum of the coated samples indicates the more horizontal TDM of the covered nanoplatelets. Picture taken from [169].

has a finite extent. Due to this, the calculations will most likely underestimate the TDM angle. The results, illustrated in fig. 10.16, yield a decreasing angle of the emissive TDM for low thicknesses of the nanoplatelets. For four different thicknesses of the nanocrystal the TDM angle increases as the structure is placed in close contact with an Al_2O_3 surface.

For an isolated, 4.2 nm thick nanoplatelet, the angle of the emissive TDM can be calculated as 13° with respect to the substrate. Taking the close contact to a silica substrate into account, this quantity increased to 16° as induced by the electric field. In conclusion, the calculations confirm the increase of the angle compared to a nanocrystal in a vacuum. Further, the decrease of the TDM angle for a low thickness of the investigated system is in agreement to the predictions.

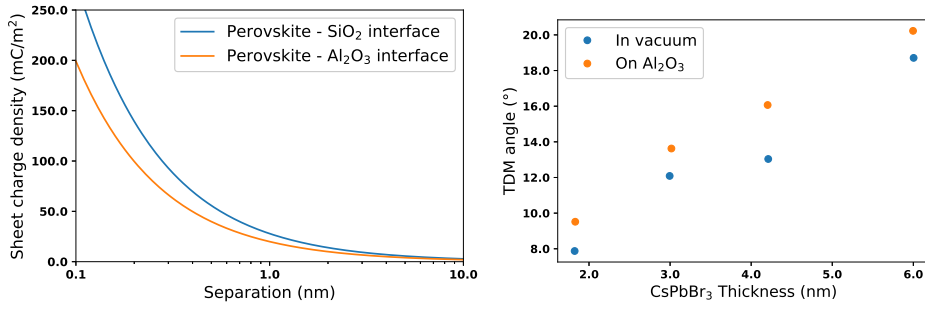


Figure 10.16.: Charge redistribution at a CsPbBr₃ interface in close contact to either SiO₂ or Al₂O₃ according to equation 10.5 (left). Calculated TDM angle in a perovskite nanoplatelet in vacuum (blue) and on top of a Al₂O₃ surface (orange) for various thicknesses. As the quantum confinement is increased the TDM angle is tuned towards the substrate, whereas the contact to Al₂O₃ increases the angle.

10.3. Performance limit of perovskite LEDs

Although the efficiency of perovskite-based light emitting devices has reached a competitive region, many effects of such devices remain to be investigated [164–168]. Within this section, the theoretical performance of perovskite LEDs will be discussed from an optical point of view by determination of the outcoupling efficiency η_{out} . Precise knowledge of the TDMs involved in the emission process, as well as different stack designs, allow for the calculation of this quantity as described in chapter 5.

The overall performance of a perovskite LED is given analog to OLEDs. Hence, the external quantum efficiency η_{EQE} can be written as [161]:

$$\eta_{EQE} = \gamma \cdot \eta_{Exc} \cdot q_{int} \cdot \eta_{out}. \quad (10.6)$$

Therein the charge carrier balance γ is not known and dependent to the specific device architecture. In order to determine the performance limit of this device, γ will be assumed as unity. Further, the fraction of radiatively decaying excitons is known to be unity as well as the emissive state of the perovskite nanocrystals is bright [158]. Consequently, the remaining factors limiting the performance are the quantum yield q_{int} and the outcoupling efficiency η_{out} . Note that the quantum yield will also be affected by the microcavity via the Purcell effect.

From an optical point of view, LHP NCs yield the challenge of a high refractive index compared to purely organic materials. Based on the considerations in sec-

tion 5.4, this has a beneficial effect on the overall device performance. Note that the effect of the refractive index is different for the hole and electron transport layers. Therein the optical constant is desired to be as low as possible to enhance the device efficiency [190].

Besides, the outcoupling efficiency, the emission spectrum and therefore the color of the nanocrystal plays an important role in the fabrication of perovskite LEDs. Compared to traditional organic dye molecules, such as TADF emitters or organometallic Ir-complexes, perovskites feature a very narrow emission spectrum. This behavior, shown in fig 10.17, leads to a very clean emission color and, if taking the shown blue emission of the nanoplatelets into account, a very low CIE-y coordinate.

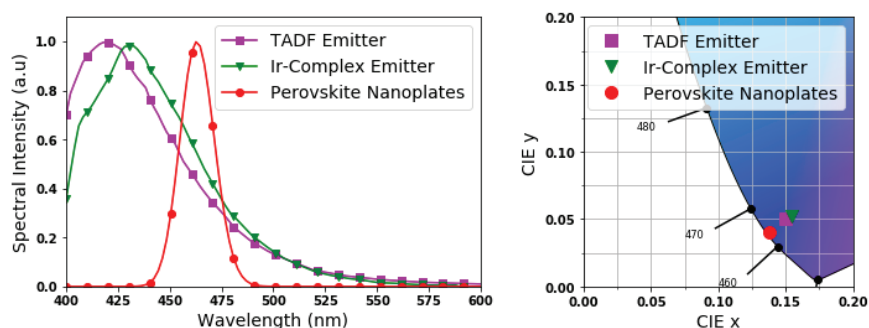


Figure 10.17.: Emission spectrum of a 3 monolayer thick CsPbBr_3 nanoplatelet compared to state-of-the-art blue organic dye molecules. The narrow emission spectrum of the perovskites allows for a deep blue CIE-y coordinate despite the emission peak being at higher wavelengths compared to the organic dyes. Picture taken from [169].

In order to evaluate the outcoupling efficiency of perovskite LEDs, a thin film of only a few monolayers of perovskite was assumed within a common device structure, as depicted in fig. 10.18. Note that a thick layer of this material is not feasible from an experimental point of view. Further, it would harm the overall device performance due to the high refractive index of the material. The hypothetical stack layout consisted of 110 nm ITO, 30 nm PEDOT:PSS, 7 nm NPB, 5 nm of perovskite, 10 nm OXD-7, an optimized thickness of Alq_3 , 10 nm Ca and 100 nm of aluminum, as depicted in fig. 10.18. Note that this theoretical system will not yield a functioning device in an experiment due to misalignment of the energy levels in the HTL to the emissive nanocrystal.

As emissive materials different thicknesses of perovskite nanoplatelets were used and further compared to not quantum confined nanocubes. As these nanocrystals show different emission wavelengths [174], it is important to adjust the film

thicknesses of the device for each emissive wavelength individually. Hence, simulations using different emission wavelengths corresponding to the nanocrystal thicknesses ranging from two to six monolayers were performed. After optimization, each of the investigated emission wavelengths from 520 nm down to 435 nm reached the same outcoupling efficiency of about 25 % if an isotropic distribution of the TDMs was assumed. It should be pointed out that the thickness of the emissive layer was kept constant at 5 nm. Although a monolayer of nanocubes would have a higher thickness, the results are not expected to significantly differ from this scenario.

Within the calculations, the alignment constant of the material was varied to investigate the effect of the quantum confinement within nanoplatelets on the device efficiency. Additionally, experimental values for the alignment constant and quantum yield were taken into account to determine the performance limit within lighting applications. Note that the quantum yield values are taken from [174].

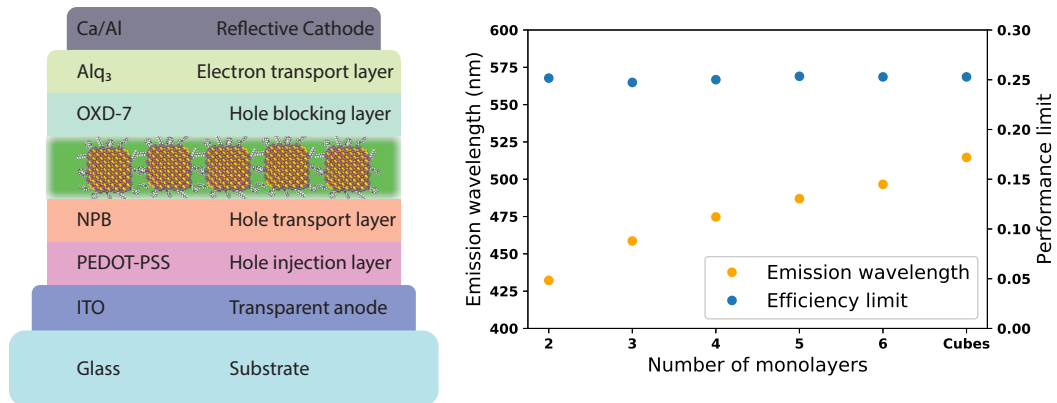


Figure 10.18.: A hypothetical stack layout for a perovskite based LED (left). Note that the device was not fabricated but designed to represent a basic LED structure. For each of the emission wavelengths (right) the thicknesses of the HTL and ETL were individually adjusted. When assuming an isotropic distribution of the TDMs, each emission wavelength reaches the same maximum possible performance of about 25%. Peak Emission wavelengths were taken from ref. [174].

Lowering the TDM angle leads to an increase in the outcoupling efficiency. This benefit is mostly caused by a decrease in surface plasmon coupling. Consequently, a higher angle leads to more pronounced SPP coupling and therefore lower device efficiencies. Further, the computational values reveal an increase of the device performance when increasing the refractive index of the emissive

material. This effect is again caused by a decrease in SPP coupling. Hence, the energy contributed to the other modes, outcoupling, surface coupling and waveguiding, is increased. This behavior is contrary to observations made for the transport layer in traditional OLEDs, in which the refractive index should be as low as possible. Both effects originate from the optimized emission pattern of the emissive dipoles and can be combined into the alignment constant ζ as described in chapter 4.2.

Taking the quantum yield of the perovskite nanocrystals into account leads to the performance limit of perovskite LED devices. The experimentally obtained values need to be adjusted for the Purcell effect. Note that the experimental values are taken from [174]. Combining the internal quantum yield with the outcoupling efficiency from the optical simulations reveals the performance limit of the investigated stack layout.

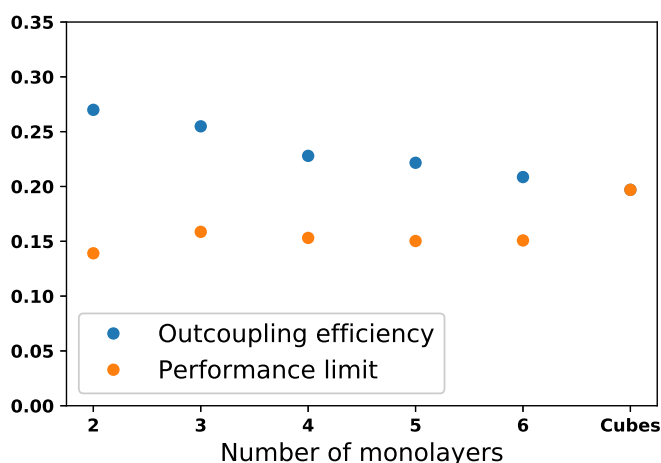


Figure 10.19.: Performance limit of perovskite LEDs for various nanocrystal shapes ranging from two-layer nanoplatelets to a cubic shape. Despite the lower quantum yield, nanoplatelets maintain a device performance comparable to the cubic counterparts due to the lower alignment constant originating from the quantum confinement of the nanocrystals.

For perovskite nanocubes, the measured alignment constant of 0.07 limits the device efficiency to 20% despite the perfect quantum yield [38]. Contrary to this, three-layered nanoplatelets were determined to have an alignment constant of 0.025 for exposed NCs, and even lower values if covered by alumina. For the following predictions, the values of different nanoplatelets on glass were used,

as shown in fig. 10.14. It should be noted that the NCs would be covered by additional layers within a device structure, leading to lower alignment constants. Hence, the estimation yields a lower boundary for the potential device efficiency.

This beneficial alignment of the TDMs allows for an outcoupling efficiency as high as 27%, as shown in fig. 10.19. The maximum possible device performances for all NC shapes range from 20% for nanocubes to less than 15% for 2-layered nanoplatelets having a quantum yield of only 50%. Interestingly, all nanoplatelet structures show similar performance despite the decreasing alignment constant. This effect is occurring due to the quantum yield decreasing for lower thicknesses.

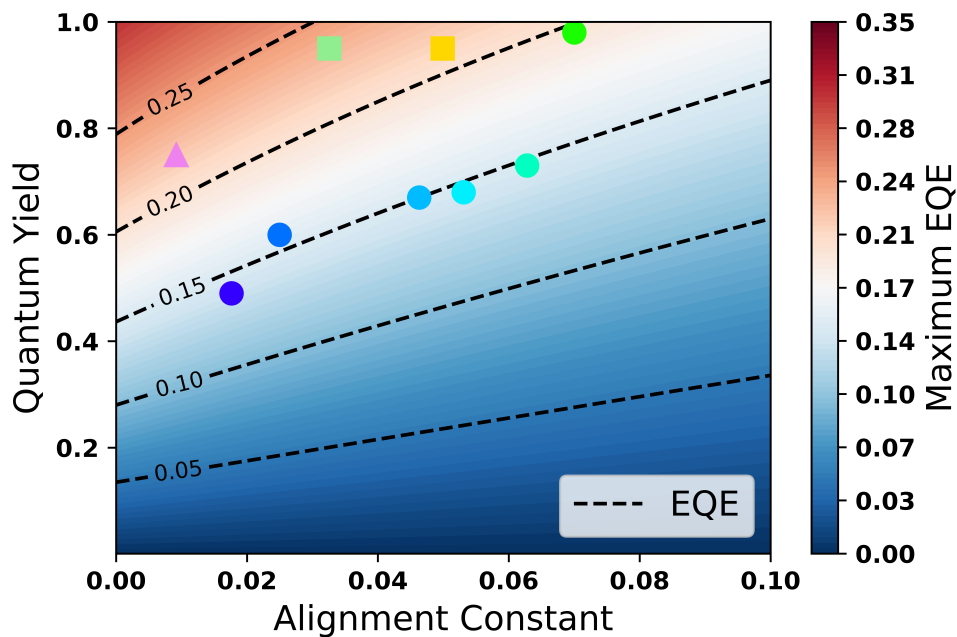


Figure 10.20.: Performance of the stack given in fig. 10.18 for different quantum yields and alignment constants of the emissive nanocrystal. The colored dots indicate the theoretical limit of different CsPbBr₃ nanocrystal shapes. While nanocubes are close to their maximum of about 20%, device performance for the different nanoplatelets could be enhanced by increasing the quantum yield of the emissive perovskite

In summary, the estimations reveal a performance limit of 20% for not quantum confined nanocubes due to their vertical alignment of the emissive TDM. By introducing CsPbBr₃ nanoplatelets, the alignment constant of the emissive species can be tuned towards lower values, increasing the outcoupling but reduc-

ing the quantum yield. Putting these values in perspective towards the maximum possible device performance, as depicted in fig. 10.20, external quantum efficiencies could reach even higher values. In particular, increasing the quantum yield of thin quantum confined nanocrystals, such as two or three monolayer platelets, could boost the EQE to 27%. However, to exceed 30% or more, new methods need to be found to further decrease the alignment constant. Interestingly, state-of-the-art devices for CsPbBr₃ nanoplatelets only reach about 0.3% EQE [191], indicating that quenching processes and an imperfect charge carrier balance severely limit the performance of those nanocrystals LEDs.

Part IV. Summary and Outlook

In summary, three different types of light emitting materials were investigated for their emissive properties and in particular the alignment of their TDMs. At first, the polar dye molecules Coumarin6, and DCM revealed the effect of their large permanent dipole moments on the morphology of the film and the visible spectrum. Introducing a polar host yielded further insight into the alignment properties. The obtained results could be explained from investigations of the dipolar interactions within the films. While these materials are not suitable for the use in state-of-the-art OLEDs, the processes affecting the preferential alignment can be applied to other molecules such as TADF dyes.

As a second class of materials, organometallic Ir-complexes were investigated. Therein the materials were classified into heteroleptic, and homoleptic species. The orientation of the heteroleptic dye molecule was unveiled within this thesis [11] while the mechanisms leading to this behavior were investigated in detail. Further, the effects of different preparation conditions were investigated, revealing a significant temperature dependence of the preferential alignment as well as new effects in solution-processed films. Given the vast amount of processes affecting the film morphology in organic guest-host systems, computational approaches will be crucial for the design of future high-performance Ir-complexes. However, the exact description of the film morphologies is not a straightforward method and requires substantial effort.

For homoleptic Ir-complexes, the processes vastly differ from their heteroleptic counterparts. While the green dye Ir(ppy)₃ was determined to be utterly isotropic within the system, the family of carbene complexes molecules revealed new effects. For these C-C Ir-complexes, new alignment processes are present, which could be tracked down to the interaction of the imidazole group to the film surface. However, due to the opposite alignment of the PDM compared to other materials, devices employing this molecule will not be able to achieve high performance. Nevertheless, this research enables a new design approach for homoleptic Ir-complexes that could be employed in new material designs.

Finally, the methods commonly used for OLEDs were applied to perovskite nanocrystals. Motivated by the surprisingly anisotropic transition dipole mo-

ments of CsPbBr₃ nanocubes, different experiments were performed. Tuning the shape of the nanocrystal towards a quantum confined structure as exhibited by two-dimensional nanoplatelets turned out to affect the angle of the emissive transition within the structure. The experiments confirmed this effect and density functional theory was able to predict angles as low as 10° with respect to the film surface. Due to this effect, CsPbBr₃ nanoplatelets were determined to be almost perfect emissive species for the use in perovskite LEDs with predicted device performances as high as 24%.

Further research towards high quantum yield nanocrystals could boost this value to more than 30%, making the blue emitting nanoplatelets ideal candidates for the application in display technologies. However, the computational predictions need to be confirmed in real devices. Hence, future research will have to focus on the design of efficient perovskite LED stacks to investigate their properties in detail. As for the preferential alignment of TDMs, this research will again benefit from the extensive set of tools developed for the characterization of OLEDs.

Bibliography

- [1] W. Brütting, J. Frischeisen, T. D. Schmidt, B. J. Scholz, and C. Mayr. Device efficiency of organic light-emitting diodes: Progress by improved light outcoupling. *physica status solidi (a)*, 210(1):44–65, 2013.
- [2] H. C. Wolf and M. Schwörer. *Organic molecular solids*. Wiley-VCH, Weinheim, 2007.
- [3] P. Yeh. *Optical waves in layered media*. Wiley series in pure and applied optics. Wiley-Interscience, Hoboken, N.J. and Great Britain, 1998 2005 [printing].
- [4] W. Koch and M. C. Holthausen. *A Chemist's Guide to Density Functional Theory*. Wiley-VCH, Weinheim, second edition edition, 2015.
- [5] Thomas Lampe. *Optische Simulationen zur Lichtauskopplung aus OLEDs*. Bachelor thesis, University of Augsburg, Augsburg, 2012.
- [6] Thomas Lampe. *Optische Simulationen von organischen Leuchtdioden*. Master thesis, University of Augsburg, Augsburg, 2015.
- [7] J. Frischeisen. Light extraction in organic light-emitting diodes, 2011.
- [8] T. D. Schmidt, T. Lampe, D. Sylvinson M. R., P. I. Djurovich, M. E. Thompson, and W. Brütting. Emitter orientation as a key parameter in organic light-emitting diodes. *Physical Review Applied*, 8(3):681, 2017.
- [9] C. W. Tang and S. VanSlyke. Organic electroluminescent diodes. *Journal of the American Chemical Society*, 51(12):913–915, 1987.
- [10] L. Jäger, T. D. Schmidt, and W. Brütting. Manipulation and control of the interfacial polarization in organic light-emitting diodes by dipolar doping. *AIP Advances*, 6(9):095220, 2016.
- [11] T. Morgenstern, M. Schmid, A. Hofmann, M. Bierling, L. Jäger, and W. Brütting. Correlating optical and electrical dipole moments to pin-point phosphorescent dye alignment in organic light-emitting diodes. *ACS applied materials & interfaces*, 10(37):31541–31551, 2018.

- [12] J. H. Burroughes, D. D. C. Bradley, A. R. Brown, R. N. Marks, K. Mackay, R. H. Friend, P. L. Burns, and A. B. Holmes. Light-emitting diodes based on conjugated polymers. *Nature*, 347(6293):539, 1990.
- [13] M. A. Baldo, D. F. O'Brien, Y. You, A. Shoustikov, S. Sibley, M. E. Thompson, and S. R. Forrest. Highly efficient phosphorescent emission from organic electroluminescent devices. *Nature*, 395(6698):151, 1998.
- [14] Z. Yang, Z. Mao, Z. Xie, Y. Zhang, S. Liu, J. Zhao, J. Xu, Z. Chi, and M. P. Aldred. Recent advances in organic thermally activated delayed fluorescence materials. *Chemical Society Reviews*, 46(3):915–1016, 2017.
- [15] W. L. Barnes. Fluorescence near interfaces: The role of photonic mode density. *Journal of Modern Optics*, 45(4):661–699, 2009.
- [16] L. Penninck, P. de Visschere, J. Beeckman, and K. Neyts. Dipole radiation within one-dimensional anisotropic microcavities: a simulation method. *Optics express*, 19(19):18558–18576, 2011.
- [17] A. Sommerfeld. Über die Ausbreitung der Wellen in der drahtlosen Telegraphie. *Annalen der Physik*, 333(4):665–736, 1909.
- [18] K. A. Neyts. Simulation of light emission from thin-film microcavities. *Journal of the Optical Society of America A*, 15(4):962, 1998.
- [19] Nicholas J. Turro, V. Ramamurthy, and Juan C. Scaiano. Modern molecular photochemistry of organic molecules. *Angewandte Chemie*, 122(38):6859–6860, 2010.
- [20] Purcell. Spontaneous emission probabilities at radio frequencies. *Physical Review*, 69:681, 1946.
- [21] D. Y. K. Ko and J. R. Sambles. Scattering matrix method for propagation of radiation in stratified media: attenuated total reflection studies of liquid crystals. *JOSA A*, 5(11):1863–1866, 1988.
- [22] P. A. M. Dirac. The quantum theory of the emission and absorption of radiation. *Proceedings of the Royal Society A: Mathematical, Physical and Engineering Sciences*, 114(767):243–265, 1927.
- [23] E. Fermi. *Nuclear physics*. Univ. of Chicago Press, Chicago, rev. ed., reprint edition, 1974.

-
- [24] M. Kasha. Characterization of electronic transitions in complex molecules. *Discussions of the Faraday Society*, 9:14, 1950.
- [25] X. Yang, H. Guo, X. Xu, Y. Sun, G. Zhou, W. Ma, and Z. Wu. Enhancing molecular aggregations by intermolecular hydrogen bonds to develop phosphorescent emitters for high-performance near-infrared oleds. *Advanced Science*, 51:1801930, 2019.
- [26] H. Yersin. *Highly efficient OLEDs with phosphorescent materials*. Wiley-VCH, Weinheim, 2007.
- [27] M. Aydemir, G. Haykır, F. Türksoy, S. Gümüş, F. B. Dias, and A. P. Monkman. Synthesis and investigation of intra-molecular charge transfer state properties of novel donor-acceptor-donor pyridine derivatives: the effects of temperature and environment on molecular configurations and the origin of delayed fluorescence. *Physical chemistry chemical physics : PCCP*, 17(38):25572–25582, 2015.
- [28] T. Förster. Zwischenmolekulare Energiewanderung und Fluoreszenz. *Annalen der Physik*, 437(1–2):55–75, 1948.
- [29] D. L. Dexter. A theory of sensitized luminescence in solids. *The Journal of Chemical Physics*, 21(5):836–850, 1953.
- [30] H.-W. Lin, C.-L. Lin, H.-H. Chang, Y.-T. Lin, C.-C. Wu, Y.-M. Chen, R.-T. Chen, Y.-Y. Chien, and K.-T. Wong. Anisotropic optical properties and molecular orientation in vacuum-deposited ter(9,9-diarylfuorene)s thin films using spectroscopic ellipsometry. *Journal of Applied Physics*, 95(3):881–886, 2004.
- [31] M. C. Gather and D. D. C. Bradley. An improved optical method for determining the order parameter in thin oriented molecular films and demonstration of a highly axial dipole moment for the lowest energy $\alpha\text{p}-\alpha\text{p}^*$ optical transition in poly(9,9-dioctylfluorene-co-bithiophene). *Advanced Functional Materials*, 17(3):479–485, 2007.
- [32] D. Yokoyama and C. Adachi. In situ real-time spectroscopic ellipsometry measurement for the investigation of molecular orientation in organic amorphous multilayer structures. *Journal of Applied Physics*, 107(12):123512, 2010.

- [33] D. Yokoyama. Molecular orientation in small-molecule organic light-emitting diodes. *Journal of Materials Chemistry*, 21(48):19187–19202, 2011.
- [34] M. Schmid, T. Morgenstern, and W. Brütting. Enabling electron conduction in anisotropic hole transport materials for superior optical properties in organic light emitting diodes. *Organic Electronics*, 62:216–219, 2018.
- [35] M. K. Callens, D. Yokoyama, and K. Neyts. Anisotropic materials in oleds for high outcoupling efficiency. *Optics express*, 23(16):21128–21148, 2015.
- [36] T. Lampe, T. D. Schmidt, M. J. Jurow, P. I. Djurovich, M. E. Thompson, and W. Brütting. Dependence of phosphorescent emitter orientation on deposition technique in doped organic films. *Chemistry of Materials*, 28(3):712–715, 2016.
- [37] M. J. Jurow, C. Mayr, T. D. Schmidt, T. Lampe, P. I. Djurovich, W. Brütting, and M. E. Thompson. Understanding and predicting the orientation of heteroleptic phosphors in organic light-emitting materials. *Nature materials*, 15(1):85–91, 2016.
- [38] M. J. Jurow, T. Lampe, E. Penzo, J. Kang, M. A. Koc, T. Zechel, Z. Nett, M. Brady, L.-W. Wang, A. P. Alivisatos, S. Cabrini, W. Brütting, and Y. Liu. Tunable anisotropic photon emission from self-organized CsPbBr₃ perovskite nanocrystals. *Nano letters*, 17(7):4534–4540, 2017.
- [39] T. Tsutsui, E. Aminaka, C. P. Lin, and D.-U. Kim. Extended molecular design concept of molecular materials for electroluminescence: sublimed-dye films, molecularly doped polymers and polymers with chromophores. *Philosophical Transactions of the Royal Society of London. Series A: Mathematical, Physical and Engineering Sciences*, 355(1725):801–814, 1997.
- [40] J.-W. Kang, W.-I. Jeong, J.-J. Kim, H.-K. Kim, D.-G. Kim, and G.-H. Lee. High-performance flexible organic light-emitting diodes using amorphous indium zinc oxide anode. *Electrochemical and Solid-State Letters*, 10(6):J75, 2007.
- [41] A. R. Robertson. Colorimetry. *Reports on Progress in Physics*, 41(4):469.
- [42] A. J. Cohen, P. Mori-Sánchez, and W. Yang. Challenges for density functional theory. *Chemical reviews*, 112(1):289–320, 2012.

-
- [43] P. Hohenberg and W. Kohn. Inhomogeneous electron gas. *Physical Review*, 136(3B):B864, 1964.
- [44] A. D. Becke. Density-functional thermochemistry. iii. the role of exact exchange. *The Journal of chemical physics*, 98(7):5648–5652, 1993.
- [45] C. Lee, W. Yang, and R. G. Parr. Development of the colle-salvetti correlation-energy formula into a functional of the electron density. *Physical Review B*, 37(2):785–789, 1988.
- [46] P. J. Stephens, F. J. Devlin, C. F. Chabalowski, and M. J. Frisch. Ab initio calculation of vibrational absorption and circular dichroism spectra using density functional force fields. *The Journal of Physical Chemistry*, 98(45):11623–11627, 1994.
- [47] S. H. Vosko, L. Wilk, and M. Nusair. Accurate spin-dependent electron liquid correlation energies for local spin density calculations: A critical analysis. *Canadian Journal of Physics*, 58(8):1200–1211, 1980.
- [48] M. Walker, A. J. A. Harvey, A. Sen, and C. E. H. Dessent. Performance of m06, m06-2x, and m06-hf density functionals for conformationally flexible anionic clusters: M06 functionals perform better than b3lyp for a model system with dispersion and ionic hydrogen-bonding interactions. *The journal of physical chemistry. A*, 117(47):12590–12600, 2013.
- [49] Y. Zhao and D. G. Truhlar. The m06 suite of density functionals for main group thermochemistry, thermochemical kinetics, noncovalent interactions, excited states, and transition elements: Two new functionals and systematic testing of four m06-class functionals and 12 other functionals. *Theoretical Chemistry Accounts*, 120(1-3):215–241, 2008.
- [50] H. S. Yu, X. He, and D. G. Truhlar. Mn15-l: A new local exchange-correlation functional for kohn-sham density functional theory with broad accuracy for atoms, molecules, and solids. *Journal of chemical theory and computation*, 12(3):1280–1293, 2016.
- [51] H. S. Yu, X. He, S. L. Li, and D. G. Truhlar. Mn15: A kohn-sham global-hybrid exchange-correlation density functional with broad accuracy for multi-reference and single-reference systems and noncovalent interactions. *Chemical science*, 7(8):5032–5051, 2016.

- [52] M. A. Marques, K. Burke, E. K. U. Gross, F. Nogueira, A. Rubio, and C. A. Ullrich. *Time-Dependent Density Functional Theory*, volume 706 of *Lecture Notes in Physics*. Springer, Berlin, Heidelberg, 2006.
- [53] T. D. Schmidt. Photophysics of organic light-emitting diodes: Device efficiency and degradation processes.
- [54] F. Wang and T. Ziegler. Time-dependent density functional theory based on a noncollinear formulation of the exchange-correlation potential. *The Journal of chemical physics*, 121(24):12191–12196, 2004.
- [55] F. Wang, T. Ziegler, E. van Lenthe, S. van Gisbergen, and E. J. Baerends. The calculation of excitation energies based on the relativistic two-component zeroth-order regular approximation and time-dependent density-functional with full use of symmetry. *The Journal of chemical physics*, 122(20):204103, 2005.
- [56] I. Tunell, Z. Rinkevicius, O. Vahtras, P. Salek, T. Helgaker, and H. Ågren. Density functional theory of nonlinear triplet response properties with applications to phosphorescence. *The Journal of Chemical Physics*, 119(21):11024–11034, 2003.
- [57] J. Gao, W. Liu, B. Song, and C. Liu. Time-dependent four-component relativistic density functional theory for excitation energies. *The Journal of chemical physics*, 121(14):6658–6666, 2004.
- [58] J. Gao, W. Zou, W. Liu, Y. Xiao, D. Peng, B. Song, and C. Liu. Time-dependent four-component relativistic density-functional theory for excitation energies. ii. the exchange-correlation kernel. *The Journal of chemical physics*, 123(5):054102, 2005.
- [59] Z. Li, B. Suo, Y. Zhang, Y. Xiao, and W. Liu. Combining spin-adapted open-shell td-dft with spin-orbit coupling. *Molecular Physics*, 111(24):3741–3755, 2013.
- [60] S. Perumal, B. Minaev, and H. Ågren. Spin-spin and spin-orbit interactions in nanographene fragments: a quantum chemistry approach. *The Journal of chemical physics*, 136(10):104702, 2012.
- [61] E. van Lenthe, E. J. Baerends, and J. G. Snijders. Relativistic regular two-component hamiltonians. *The Journal of chemical physics*, 99(6):4597–4610, 1993.

-
- [62] E. van Lenthe, E. J. Baerends, and J. G. Snijders. Relativistic total energy using regular approximations. *The Journal of chemical physics*, 101(11):9783–9792, 1994.
- [63] E. van Lenthe, J. G. Snijders, and E. J. Baerends. The zero-order regular approximation for relativistic effects: The effect of spin-orbit coupling in closed shell molecules. *The Journal of chemical physics*, 105(15):6505–6516, 1996.
- [64] W. Liu and W. Kutzelnigg. Quasirelativistic theory. ii. theory at matrix level. *The Journal of chemical physics*, 126(11):114107, 2007.
- [65] W. Liu and D. Peng. Exact two-component hamiltonians revisited. *The Journal of chemical physics*, 131(3):031104, 2009.
- [66] W. Kutzelnigg and W. Liu. Quasirelativistic theory equivalent to fully relativistic theory. *The Journal of chemical physics*, 123(24):241102, 2005.
- [67] K. Mori, T. P. M. Goumans, E. van Lenthe, and F. Wang. Predicting phosphorescent lifetimes and zero-field splitting of organometallic complexes with time-dependent density functional theory including spin-orbit coupling. *Physical Chemistry Chemical Physics*, 16(28):14523–14530, 2014.
- [68] J. M. Younker and K. D. Dobbs. Correlating experimental photophysical properties of iridium(iii) complexes to spin-orbit coupled tddft predictions. *The Journal of Physical Chemistry C*, 117(48):25714–25723, 2013.
- [69] A. R. G. Smith, P. L. Burn, and B. J. Powell. Spin-orbit coupling in phosphorescent iridium(iii) complexes. *Chemphyschem : a European journal of chemical physics and physical chemistry*, 12(13):2429–2438, 2011.
- [70] H. Li, S. Wu, Y. Liao, Z. Su, Y. Kan, and X. Tang. Density functional theory studies on structures and absorption spectra of $[\text{Au}(\text{tpy})\text{Cl}]_2^+$ and its derivatives: Role of basis set, functional, solvent effect, and spin orbit effect. *International Journal of Quantum Chemistry*, 112(6):1642–1653, 2012.
- [71] E. Ronca, F. de Angelis, and S. Fantacci. Time-dependent density functional theory modeling of spin-orbit coupling in ruthenium and osmium solar cell sensitizers. *The Journal of Physical Chemistry C*, 118(30):17067–17078, 2014.

- [72] K.-H. Kim, E. S. Ahn, J.-S. Huh, Y.-H. Kim, and J.-J. Kim. Design of heteroleptic ir complexes with horizontal emitting dipoles for highly efficient organic light-emitting diodes with an external quantum efficiency of 38%. *Chemistry of Materials*, 28(20):7505–7510, 2016.
- [73] Materials science suite 2017-2, schrödinger, llc, new york, ny, 2017.
- [74] K. Bowers, E. Chow, H. Xu, R. Dror, M. Eastwood, B. Gregersen, J. Klepeis, I. Kolossvary, M. Moraes, F. Sacerdoti, J. Salmon, Y. Shan, and D. Shaw. Scalable algorithms for molecular dynamics simulations on commodity clusters. In *SC 06*, page 43, [United States], 2006. [Association for Computing Machinery].
- [75] E. Harder, W. Damm, J. Maple, C. Wu, M. Reboul, J. Y. Xiang, L. Wang, D. Lupton, M. K. Dahlgren, J. L. Knight, J. W. Kaus, D. S. Cerutti, G. Krilov, W. L. Jorgensen, R. Abel, and R. A. Friesner. Opls3: A force field providing broad coverage of drug-like small molecules and proteins. *Journal of chemical theory and computation*, 12(1):281–296, 2016.
- [76] D.A. Case, I.Y. Ben-Shalom, S.R. Brozell, D.S. Cerutti, T.E. Cheatham, III, V.W.D. Cruzeiro, T.A. Darden, R.E. Duke, D. Ghoreishi, M.K. Gilson, H. Gohlke, A.W. Goetz, D. Greene, R. Harris, N. Homeyer, S. Izadi, A. Kovalenko, T. Kurtzman, T.S. Lee, S. LeGrand, P. Li, C. Lin, J. Liu, T. Luchko, R. Luo, D.J. Mermelstein, K.M. Merz, Y. Miao, G. Monard, C. Nguyen, H. Nguyen, I. Omelyan, A. Onufriev, F. Pan, R. Qi, D.R. Roe, A. Roitberg, C. Sagui, S. Schott-Verdugo, J. Shen, C.L. Simmerling, J. Smith, R. Salomon-Ferrer, J. Swails, R.C. Walker, J. Wang, H. Wei, R.M. Wolf, X. Wu, L. Xiao, D.M. York and P.A. Amber 2018.
- [77] C. Oostenbrink, A. Villa, A. E. Mark, and W. F. van Gunsteren. A biomolecular force field based on the free enthalpy of hydration and solvation: the gromos force-field parameter sets 53a5 and 53a6. *Journal of computational chemistry*, 25(13):1656–1676, 2004.
- [78] K. Vanommeslaeghe, E. Hatcher, C. Acharya, S. Kundu, S. Zhong, J. Shim, E. Darian, O. Guvench, P. Lopes, I. Vorobyov, and A. D. MacKerell. Charmm general force field (cgenff): A force field for drug-like molecules compatible with the charmm all-atom additive biological force fields. *Journal of computational chemistry*, 31(4):671–690, 2010.
- [79] C. Tonnelé, M. Stroet, B. Caron, A. J. Clulow, R. C. R. Nagiri, A. K. Malde, P. L. Burn, I. R. Gentle, A. E. Mark, and B. J. Powell. Elucidating

- the spatial arrangement of emitter molecules in organic light-emitting diode films. *Angewandte Chemie (International ed. in English)*, 56(29):8402–8406, 2017.
- [80] P. Friederich, R. Coehoorn, and W. Wenzel. Molecular origin of the anisotropic dye orientation in emissive layers of organic light emitting diodes. *Chemistry of Materials*, 29(21):9528–9535, 2017.
- [81] C.-K. Moon, K.-H. Kim, and J.-J. Kim. Unraveling the orientation of phosphors doped in organic semiconducting layers. *Nature communications*, 8(1):791, 2017.
- [82] B. J. Scholz. Optische Methoden zur Verbesserung der Effizienz und des Abstrahlungsverhaltens von organischen Leuchtdioden.
- [83] N. A. Reinke. Photophysikalische Prozesse und Lichtextraktion in organischen Leuchtdioden.
- [84] S. Nowy. Understanding losses in oleds: optical device simulation and electrical characterization using impedance spectroscopy.
- [85] J. Frischeisen, D. Yokoyama, C. Adachi, and W. Brütting. Determination of molecular dipole orientation in doped fluorescent organic thin films by photoluminescence measurements. *Applied Physics Letters*, 96(7):073302, 2010.
- [86] J. E. Stewart. *Optical principles and technology for engineers*, volume 104 of *Mechanical engineering*. Marcel Dekker, New York, 1996.
- [87] Princeton instruments - pylon ccd cameras for imaging and spectroscopy.
- [88] J. E. Greivenkamp. *Field guide to geometrical optics*, volume FG01 of *SPIE field guides*. SPIE Press, Bellingham, Wash., 2004.
- [89] J. R. Lakowicz. *Principles of fluorescence spectroscopy*. Springer, New York, NY, third edition, corrected at 4. printing edition, 2010.
- [90] J. F. Archard and A. M. Taylor. Improved glan-foucault prism. *Journal of Scientific Instruments*, 25(12):407, 1948.
- [91] Paul Glan. Über einen Polarisator. *Carl's Repertorium*, (16):570, 1880.
- [92] Silvanus Philips Thompson. On a new polarising prism. *Phil Mag.* 5, (12):349, 1881.

- [93] W. Demtröder. *Laserspektroskopie: Grundlagen und Techniken*. Springer Berlin Heidelberg, Berlin, Heidelberg and s.l., Vierte, erweiterte und neubearbeitete Auflage edition, 2000.
- [94] N. Haase, A. Danos, C. Pflumm, A. Morherr, P. Stachelek, A. Mekic, W. Brütting, and A. P. Monkman. Kinetic modeling of transient photoluminescence from thermally activated delayed fluorescence. *The Journal of Physical Chemistry C*, 122(51):29173–29179, 2018.
- [95] M. A. Lieb, J. M. Zavislan, and L. Novotny. Single-molecule orientations determined by direct emission pattern imaging. *Journal of the Optical Society of America B*, 21(6):1210, 2004.
- [96] Y. Gao, M. C. Weidman, and W. A. Tisdale. CdSe nanoplatelet films with controlled orientation of their transition dipole moment. *Nano letters*, 17(6):3837–3843, 2017.
- [97] T. D. Schmidt, D. S. Setz, M. Flämmich, J. Frischeisen, D. Michaelis, B. C. Krummacker, N. Danz, and W. Brütting. Evidence for non-isotropic emitter orientation in a red phosphorescent organic light-emitting diode and its implications for determining the emitter’s radiative quantum efficiency. *Applied Physics Letters*, 99(16):163302, 2011.
- [98] L. Protesescu, S. Yakunin, M. I. Bodnarchuk, F. Krieg, R. Caputo, C. H. Hendon, R. X. Yang, A. Walsh, and M. V. Kovalenko. Nanocrystals of cesium lead halide perovskites (CsPbX₃, X = Cl, Br, and I): Novel optoelectronic materials showing bright emission with wide color gamut. *Nano letters*, 15(6):3692–3696, 2015.
- [99] K. Wu, G. Liang, Q. Shang, Y. Ren, D. Kong, and T. Lian. Ultrafast interfacial electron and hole transfer from CsPbBr₃ perovskite quantum dots. *Journal of the American Chemical Society*, 137(40):12792–12795, 2015.
- [100] S. Colella, M. Mazzeo, A. Rizzo, G. Gigli, and A. Listorti. The bright side of perovskites. *The journal of physical chemistry letters*, 7(21):4322–4334, 2016.
- [101] S. Berleb, W. Brütting, and G. Paasch. Interfacial charges and electric field distribution in organic hetero-layer light-emitting devices. *Organic Electronics*, 1(1):41–47, 2000.

-
- [102] V. Bulović, R. Deshpande, M. Thompson, and S. Forrest. Tuning the color emission of thin film molecular organic light emitting devices by the solid state solvation effect. *Chemical Physics Letters*, 308(3-4):317–322, 1999.
- [103] V. Bulović, A. Shoustikov, M. Baldo, E. Bose, V. Kozlov, M. Thompson, and S. Forrest. Bright, saturated, red-to-yellow organic light-emitting devices based on polarization-induced spectral shifts. *Chemical Physics Letters*, 287(3-4):455–460, 1998.
- [104] C. Mayr and W. Brütting. Control of molecular dye orientation in organic luminescent films by the glass transition temperature of the host material. *Chemistry of Materials*, 27(8):2759–2762, 2015.
- [105] A. Senes, S. C. J. Meskers, H. Greiner, K. Suzuki, H. Kaji, C. Adachi, J. S. Wilson, and R. A. J. Janssen. Increasing the horizontal orientation of transition dipole moments in solution processed small molecular emitters. *Journal of materials chemistry. C*, 5(26):6555–6562, 2017.
- [106] T. Komino, H. Tanaka, and C. Adachi. Selectively controlled orientational order in linear-shaped thermally activated delayed fluorescent dopants. *Chemistry of Materials*, 26(12):3665–3671, 2014.
- [107] M. A. Baldo, S. Lamansky, P. E. Burrows, M. E. Thompson, and S. R. Forrest. Very high-efficiency green organic light-emitting devices based on electrophosphorescence. *Applied Physics Letters*, 75(1):4–6, 1999.
- [108] P. Liehm, C. Murawski, M. Furno, B. Lüssem, K. Leo, and M. C. Gather. Comparing the emissive dipole orientation of two similar phosphorescent green emitter molecules in highly efficient organic light-emitting diodes. *Applied Physics Letters*, 101(25):253304, 2012.
- [109] D. R. Martir, C. Momblona, A. Pertegás, D. B. Cordes, A. M. Z. Slawin, H. J. Bolink, and E. Zysman-Colman. Chiral iridium(iii) complexes in light-emitting electrochemical cells: Exploring the impact of stereochemistry on the photophysical properties and device performances. *ACS applied materials & interfaces*, 8(49):33907–33915, 2016.
- [110] H. A. Jahn and E. Teller. Stability of polyatomic molecules in degenerate electronic states - i—orbital degeneracy. *Proceedings of the Royal Society of London. Series A - Mathematical and Physical Sciences*, 161(905):220–235, 1937.

- [111] A. Heil, K. Gollnisch, M. Kleinschmidt, and C. M. Marian. On the photophysics of four heteroleptic iridium(iii) phenylpyridyl complexes investigated by relativistic multi-configuration methods. *Molecular Physics*, pages 1–16, 2015.
- [112] S. Wehrmeister, L. Jäger, T. Wehlius, A. F. Rausch, T. C. G. Reusch, T. D. Schmidt, and W. Brütting. Combined electrical and optical analysis of the efficiency roll-off in phosphorescent organic light-emitting diodes. *Physical Review Applied*, 3(2):024008, 2015.
- [113] N. C. Erickson and R. J. Holmes. Engineering efficiency roll-off in organic light-emitting devices. *Advanced Functional Materials*, 24(38):6074–6080, 2014.
- [114] M. Flämmich, J. Frischeisen, D. S. Setz, D. Michaelis, B. C. Krummacher, T. D. Schmidt, W. Brütting, and N. Danz. Oriented phosphorescent emitters boost oled efficiency. *Organic Electronics*, 12(10):1663–1668, 2011.
- [115] K.-H. Kim, C.-K. Moon, J.-H. Lee, S.-Y. Kim, and J.-J. Kim. Highly efficient organic light-emitting diodes with phosphorescent emitters having high quantum yield and horizontal orientation of transition dipole moments. *Advanced materials (Deerfield Beach, Fla.)*, 26(23):3844–3847, 2014.
- [116] B. Sim, C.-K. Moon, K.-H. Kim, and J.-J. Kim. Quantitative analysis of the efficiency of oleds. *ACS applied materials & interfaces*, 8(48):33010–33018, 2016.
- [117] S.-J. Yoo, J.-H. Lee, J.-M. Kim, and J.-J. Kim. Hole mobility in various transition-metal-oxides doped organic semiconductor films. *Applied Physics Letters*, 110(5):053303, 2017.
- [118] T. Zhang, Y. Liang, J. Cheng, and J. Li. A CBP derivative as bipolar host for performance enhancement in phosphorescent organic light-emitting diodes. *Journal of Materials Chemistry C*, 1(4):757–764, 2012.
- [119] J. S. Swensen, E. Polikarpov, A. von Ruden, L. Wang, L. S. Sapochak, and A. B. Padmaperuma. Improved efficiency in blue phosphorescent organic light-emitting devices using host materials of lower triplet energy than the phosphorescent blue emitter. *Advanced Functional Materials*, 21(17):3250–3258, 2011.

- [120] Y. Nagai, H. Sasabe, S. Ohisa, and J. Kido. Effect of substituents in a series of carbazole-based host-materials toward high-efficiency carbene-based blue oleds. *Journal of Materials Chemistry C*, 4(40):9476–9481, 2016.
- [121] C. Han, Y. Zhao, H. Xu, J. Chen, Z. Deng, D. Ma, Q. Li, and P. Yan. A simple phosphine-oxide host with a multi-insulating structure: high triplet energy level for efficient blue electrophosphorescence. *Chemistry (Weinheim an der Bergstrasse, Germany)*, 17(21):5800–5803, 2011.
- [122] M. Baroncini, G. Bergamini, and P. Ceroni. Rigidification or interaction-induced phosphorescence of organic molecules. *Chemical communications (Cambridge, England)*, 53(13):2081–2093, 2017.
- [123] P. Baronas, K. Kazlauskas, A. Gruodis, V. Jankauskas, A. Tomkeviciene, J. Simokaitiene, J. Vidas Grazulevicius, and S. Jursenas. High-triplet-energy carbazole and fluorene tetrads. *Journal of Luminescence*, 169:256–265, 2016.
- [124] D. Gudeika, K. Norvaisa, E. Stanislovaityte, O. Bezikonny, D. Volyniuk, P. Turyk, I. Hladka, V. M. Yashchuk, and J. V. Grazulevicius. High-triplet-energy derivatives of indole and carbazole as hosts for blue phosphorescent organic light-emitting diodes. *Dyes and Pigments*, 139:487–497, 2017.
- [125] J. Zhang, D. Ding, Y. Wei, and H. Xu. Extremely condensing triplet states of DPEPO-type hosts through constitutional isomerization for high-efficiency deep-blue thermally activated delayed fluorescence diodes. *Chemical Science*, 7(4):2870–2882, 2016.
- [126] S. Lamansky, P. Djurovich, D. Murphy, F. Abdel-Razzaq, H.-E. Lee, C. Adachi, P. E. Burrows, S. R. Forrest, and M. E. Thompson. Highly phosphorescent bis-cyclometalated iridium complexes: Synthesis, photophysical characterization, and use in organic light emitting diodes. *Journal of the American Chemical Society*, 123(18):4304–4312, 2001.
- [127] S.-Y. Kim, W.-I. Jeong, C. Mayr, Y.-S. Park, K.-H. Kim, J.-H. Lee, C.-K. Moon, W. Brütting, and J.-J. Kim. Organic light-emitting diodes with 30% external quantum efficiency based on a horizontally oriented emitter. *Advanced Functional Materials*, 23(31):3896–3900, 2013.
- [128] J.-H. Lee, G. Sarada, C.-K. Moon, W. Cho, K.-H. Kim, Y. G. Park, J. Y. Lee, S.-H. Jin, and J.-J. Kim. Finely tuned blue iridium complexes with varying horizontal emission dipole ratios and quantum yields

- for phosphorescent organic light-emitting diodes. *Advanced Optical Materials*, 3(2):211–220, 2015.
- [129] A. Graf, P. Liehm, C. Murawski, S. Hofmann, K. Leo, and M. C. Gather. Correlating the transition dipole moment orientation of phosphorescent emitter molecules in oleds with basic material properties. *J. Mater. Chem. C*, 2(48):10298–10304, 2014.
- [130] K.-H. Kim, S. Lee, C.-K. Moon, S.-Y. Kim, Y.-S. Park, J.-H. Lee, J. Woo Lee, J. Huh, Y. You, and J.-J. Kim. Phosphorescent dye-based supramolecules for high-efficiency organic light-emitting diodes. *Nature communications*, 5:4769, 2014.
- [131] K. Osada, K. Goushi, H. Kaji, C. Adachi, H. Ishii, and Y. Noguchi. Observation of spontaneous orientation polarization in evaporated films of organic light-emitting diode materials. *Organic Electronics*, 58:313–317, 2018.
- [132] M. A. Baldo, V. G. Kozlov, P. E. Burrows, S. R. Forrest, V. S. Ban, B. Koene, and M. E. Thompson. Low pressure organic vapor phase deposition of small molecular weight organic light emitting device structures. *Applied Physics Letters*, 71(21):3033–3035, 1997.
- [133] M. Baldo, M. Deutsch, P. Burrows, H. Gossenberger, M. Gerstenberg, V. Ban, and S. Forrest. Organic vapor phase deposition. *Advanced materials (Deerfield Beach, Fla.)*, 10(18):1505–1514, 1998.
- [134] R. R. Lunt, B. E. Lassiter, J. B. Benziger, and S. R. Forrest. Organic vapor phase deposition for the growth of large area organic electronic devices. *Applied Physics Letters*, 95(23):233305, 2009.
- [135] M. Shtein, J. Mapel, J. B. Benziger, and S. R. Forrest. Effects of film morphology and gate dielectric surface preparation on the electrical characteristics of organic-vapor-phase-deposited pentacene thin-film transistors. *Applied Physics Letters*, 81(2):268, 2002.
- [136] F. F. Navarro, P. I. Djurovich, and M. E. Thompson. Metal deposition for optoelectronic devices using a low vacuum vapor phase deposition (VPD) system. *Organic Electronics*, 15(11):3052–3060, 2014.
- [137] J.-J. Lin, W.-S. Liao, H.-J. Huang, F.-I. Wu, and C.-H. Cheng. A highly efficient host/dopant combination for blue organic electrophosphorescence devices. *Advanced Functional Materials*, 18(3):485–491, 2008.

-
- [138] H. Bozec and V. Guerschais. *Molecular Organometallic Materials for Optics*, volume 28. Springer Berlin Heidelberg, Berlin, Heidelberg, 2010.
- [139] I. Lyubimov, M. D. Ediger, and J. J. de Pablo. Model vapor-deposited glasses: Growth front and composition effects. *The Journal of chemical physics*, 139(14):144505, 2013.
- [140] J. Jiang, D. M. Walters, D. Zhou, and M. D. Ediger. Substrate temperature controls molecular orientation in two-component vapor-deposited glasses. *Soft matter*, 12(13):3265–3270, 2016.
- [141] C. Murawski, C. Elschner, S. Lenk, S. Reineke, and M. C. Gather. Investigating the molecular orientation of Ir(ppy)₃ and Ir(ppy)₂(acac) emitter complexes by x-ray diffraction. *Organic Electronics*, 53:198–204, 2018.
- [142] X. Ren, M. E. Kondakova, D. J. Giesen, M. Rajeswaran, M. Madaras, and W. C. Lenhart. Coumarin-based, electron-trapping iridium complexes as highly efficient and stable phosphorescent emitters for organic light-emitting diodes. *Inorganic chemistry*, 49(4):1301–1303, 2010.
- [143] P. Strohriegel, D. Wagner, P. Schrögel, S. T. Hoffmann, A. Köhler, U. Heine-meyer, and I. Münster. Novel host materials for blue phosphorescent oleds. In F. So and C. Adachi, editors, *Organic Light Emitting Materials and Devices XVII*, SPIE Proceedings, page 882906. SPIE, 2013.
- [144] H. Sasabe, J.-i. Takamatsu, T. Motoyama, S. Watanabe, G. Wagenblast, N. Langer, O. Molt, E. Fuchs, C. Lennartz, and J. Kido. High-efficiency blue and white organic light-emitting devices incorporating a blue iridium carbene complex. *Advanced materials (Deerfield Beach, Fla.)*, 22(44):5003–5007, 2010.
- [145] L. He, Y. Lan, D. Ma, X. Song, and L. Duan. Fluorine-free, highly efficient, blue-green and sky-blue-emitting cationic iridium complexes and their use for efficient organic light-emitting diodes. *Journal of Materials Chemistry C*, 6(6):1509–1520, 2018.
- [146] T. Sajoto, P. I. Djurovich, A. Tamayo, M. Yousufuddin, R. Bau, M. E. Thompson, R. J. Holmes, and S. R. Forrest. Blue and near-UV phosphorescence from iridium complexes with cyclometalated pyrazolyl or n-heterocyclic carbene ligands. *Inorganic chemistry*, 44(22):7992–8003, 2005.

- [147] Z. Song, R. Liu, Y. Li, H. Shi, J. Hu, X. Cai, and H. Zhu. Aie-active Ir(III) complexes with tunable emissions, mechanoluminescence and their application for data security protection. *Journal of Materials Chemistry C*, 4(13):2553–2559, 2016.
- [148] Y. Wang, Y. Lu, B. Gao, S. Wang, J. Ding, L. Wang, X. Jing, and F. Wang. Single molecular tuning of the charge balance in blue-emitting iridium dendrimers for efficient nondoped solution-processed phosphorescent oleds. *Chemical Communications*, 52(77):11508–11511, 2016.
- [149] C.-H. Lin, Y.-Y. Chang, J.-Y. Hung, C.-Y. Lin, Y. Chi, M.-W. Chung, C.-L. Lin, P.-T. Chou, G.-H. Lee, C.-H. Chang, and W.-C. Lin. Iridium(iii) complexes of a dicyclopentylphosphite tripod ligand: strategy to achieve blue phosphorescence without fluorine substituents and fabrication of OLEDs. *Angewandte Chemie (International ed. in English)*, 50(14):3182–3186, 2011.
- [150] H. Chen, W. Liang, Y. Chen, G. Tian, Q. Dong, J. Huang, and J. Su. Efficient blue fluorescent organic light-emitting diodes based on novel 9,10-diphenyl-anthracene derivatives. *RSC Advances*, 5(86):70211–70219, 2015.
- [151] R. D. Costa, E. Ortí, H. J. Bolink, F. Monti, G. Accorsi, and N. Armatori. Luminescent ionic transition-metal complexes for light-emitting electrochemical cells. *Angewandte Chemie (International ed. in English)*, 51(33):8178–8211, 2012.
- [152] X. Yang, G. Zhou, and W.-Y. Wong. Functionalization of phosphorescent emitters and their host materials by main-group elements for phosphorescent organic light-emitting devices. *Chemical Society reviews*, 44(23):8484–8575, 2015.
- [153] J. Lee, H.-F. Chen, T. Batagoda, C. Coburn, P. I. Djurovich, M. E. Thompson, and S. R. Forrest. Deep blue phosphorescent organic light-emitting diodes with very high brightness and efficiency. *Nature materials*, 15(1):92–98, 2016.
- [154] C.-Y. Kuei, W.-L. Tsai, B. Tong, M. Jiao, W.-K. Lee, Y. Chi, C.-C. Wu, S.-H. Liu, G.-H. Lee, and P.-T. Chou. Bis-tridentate ir(iii) complexes with nearly unitary rgb phosphorescence and organic light-emitting diodes with external quantum efficiency exceeding 31%. *Advanced materials (Deerfield Beach, Fla.)*, 28(14):2795–2800, 2016.

-
- [155] C. Mayr, M. Taneda, C. Adachi, and W. Brütting. Different orientation of the transition dipole moments of two similar Pt(II) complexes and their potential for high efficiency organic light-emitting diodes. *Organic Electronics*, 15(11):3031–3037, 2014.
- [156] M. Taneda, T. Yasuda, and C. Adachi. Horizontal orientation of a linear-shaped platinum(ii) complex in organic light-emitting diodes with a high light out-coupling efficiency. *Applied Physics Express*, 4(7):071602, 2011.
- [157] C. S. Oh, C.-K. Moon, J. M. Choi, J.-S. Huh, J.-J. Kim, and J. Y. Lee. Relationship between molecular structure and dipole orientation of thermally activated delayed fluorescent emitters. *Organic Electronics*, 42:337–342, 2017.
- [158] M. A. Becker, R. Vaxenburg, G. Nedelcu, P. C. Sercel, A. Shabaev, M. J. Mehl, J. G. Michopoulos, S. G. Lambrakos, N. Bernstein, J. L. Lyons, T. Stöferle, R. F. Mahrt, M. V. Kovalenko, D. J. Norris, G. Rainò, and A. L. Efros. Bright triplet excitons in caesium lead halide perovskites. *Nature*, 553(7687):189, 2018.
- [159] J. Liang, C. Wang, Y. Wang, Z. Xu, Z. Lu, Y. Ma, H. Zhu, Y. Hu, C. Xiao, X. Yi, G. Zhu, H. Lv, B. Ma, T. Chen, Z. Tie, Z. Jin, and J. Liu. All-inorganic perovskite solar cells. *Journal of the American Chemical Society*, 138(49):15829–15832, 2016.
- [160] J. S. Manser, J. A. Christians, and P. V. Kamat. Intriguing optoelectronic properties of metal halide perovskites. *Chemical reviews*, 116(21):12956–13008, 2016.
- [161] S. D. Stranks, R. L. Z. Hoyer, D. Di, R. H. Friend, and F. Deschler. The physics of light emission in halide perovskite devices. *Advanced materials (Deerfield Beach, Fla.)*, page e1803336, 2018.
- [162] Z. Shi and A. H. Jayatissa. Perovskites-based solar cells: A review of recent progress, materials and processing methods. *Materials*, 11(5), 2018.
- [163] V. A. Hintermayr, A. F. Richter, F. Ehrat, M. Döblinger, W. Vanderlinden, J. A. Sichert, Y. Tong, L. Polavarapu, J. Feldmann, and A. S. Urban. Tuning the optical properties of perovskite nanoplatelets through composition and thickness by ligand-assisted exfoliation. *Advanced materials (Deerfield Beach, Fla.)*, 28(43):9478–9485, 2016.

- [164] J. Li, X. Shan, S. G. R. Bade, T. Geske, Q. Jiang, X. Yang, and Z. Yu. Single-layer halide perovskite light-emitting diodes with sub-band gap turn-on voltage and high brightness. *The journal of physical chemistry letters*, 7(20):4059–4066, 2016.
- [165] J. Song, J. Li, X. Li, L. Xu, Y. Dong, and H. Zeng. Quantum dot light-emitting diodes based on inorganic perovskite cesium lead halides (cspb_x3). *Advanced materials (Deerfield Beach, Fla.)*, 27(44):7162–7167, 2015.
- [166] Y.-H. Kim, C. Wolf, Y.-T. Kim, H. Cho, W. Kwon, S. Do, A. Sadhanala, C. G. Park, S.-W. Rhee, S. H. Im, R. H. Friend, and T.-W. Lee. Highly efficient light-emitting diodes of colloidal metal-halide perovskite nanocrystals beyond quantum size. *ACS nano*, 11(7):6586–6593, 2017.
- [167] N. K. Kumawat, X.-K. Liu, D. Kabra, and F. Gao. Blue perovskite light-emitting diodes: progress, challenges and future directions. *Nanoscale*, 11(5):2109–2120, 2019.
- [168] B. Zhao, S. Bai, V. Kim, R. Lamboll, R. Shivanna, F. Auras, J. M. Richter, Le Yang, L. Dai, M. Alsari, X.-J. She, L. Liang, J. Zhang, S. Lilliu, P. Gao, H. J. Snaith, J. Wang, N. C. Greenham, R. H. Friend, and Di Dawei. High-efficiency perovskite-polymer bulk heterostructure light-emitting diodes. *Nature Photonics*, 12(12):783–789, 2018.
- [169] M. J. Jurow, T. Morgenstern, C. Eisler, J. Kang, E. Penzo, M. Q. Do, M. Engelmayr, W. T. Osowiecki, Y. Bekenstein, C. J. Tassone, L.-W. Wang, A. P. Alivisatos, W. Brütting, and Y. Liu. Manipulating the transition dipole moment of CsPbBr₃ perovskite nanocrystals for superior optical properties. *Nano letters*, 2019.
- [170] H. Huang, L. Polavarapu, J. A. Sichert, A. S. Sussha, A. S. Urban, and A. L. Rogach. Colloidal lead halide perovskite nanocrystals: synthesis, optical properties and applications. *NPG Asia Materials*, 8(11):e328, 2016.
- [171] J. Tilchin, D. N. Dirin, G. I. Maikov, A. Sashchiuk, M. V. Kovalenko, and E. Lifshitz. Hydrogen-like Wannier-Mott excitons in single crystal of methylammonium lead bromide perovskite. *ACS nano*, 10(6):6363–6371, 2016.
- [172] Y. Bekenstein, B. A. Koscher, S. W. Eaton, P. Yang, and A. P. Alivisatos. Highly luminescent colloidal nanoplates of perovskite cesium lead halide and their oriented assemblies. *Journal of the American Chemical Society*, 137(51):16008–16011, 2015.

-
- [173] E.-P. Yao, B. J. Bohn, Y. Tong, H. Huang, L. Polavarapu, and J. Feldmann. Exciton diffusion lengths and dissociation rates in CsPbBr₃ nanocrystal-fullerene composites: Layer-by-layer versus blend structures. *Advanced Optical Materials*, 501:1801776, 2019.
- [174] B. J. Bohn, Y. Tong, M. Gramlich, M. L. Lai, M. Döblinger, K. Wang, R. L. Z. Hoyer, P. Müller-Buschbaum, S. D. Stranks, A. S. Urban, L. Polavarapu, and J. Feldmann. Boosting tunable blue luminescence of halide perovskite nanoplatelets through postsynthetic surface trap repair. *Nano letters*, 18(8):5231–5238, 2018.
- [175] W. K. Bae, L. A. Padilha, Y.-S. Park, H. McDaniel, I. Robel, J. M. Pietryga, and V. I. Klimov. Controlled alloying of the core-shell interface in cdse/cds quantum dots for suppression of auger recombination. *ACS nano*, 7(4):3411–3419, 2013.
- [176] V. I. Klimov. *Nanocrystal quantum dots*. CRC Press, Boca Raton, 2nd ed. edition, 2010.
- [177] H. Huang, L. Polavarapu, J. A. Sichert, A. S. Susha, A. S. Urban, and A. L. Rogach. Colloidal lead halide perovskite nanocrystals: synthesis, optical properties and applications. *NPG Asia Materials*, 8(11):e328, 2016.
- [178] B. J. Bohn, T. Simon, M. Gramlich, A. F. Richter, L. Polavarapu, A. S. Urban, and J. Feldmann. Dephasing and quantum beating of excitons in methylammonium lead iodide perovskite nanoplatelets. *ACS Photonics*, 5(2):648–654, 2018.
- [179] K. Tanaka and T. Kondo. Bandgap and exciton binding energies in lead-iodide-based natural quantum-well crystals. *Science and Technology of Advanced Materials*, 4(6):599–604, 2003.
- [180] J. Li, L. Luo, H. Huang, C. Ma, Z. Ye, J. Zeng, and H. He. 2d behaviors of excitons in cesium lead halide perovskite nanoplatelets. *The journal of physical chemistry letters*, 8(6):1161–1168, 2017.
- [181] J. Shamsi, A. S. Urban, M. Imran, L. de Trizio, and L. Manna. Metal halide perovskite nanocrystals: Synthesis, post-synthesis modifications, and their optical properties. *Chemical reviews*, 2019.
- [182] Y. Onodera and Y. Toyozawa. Excitons in alkali halides. *Journal of the Physical Society of Japan*, 22(3):833–844, 1967.

- [183] Nirmal, Norris, Kuno, Bawendi, Efros, and Rosen. Observation of the "dark exciton" in cdse quantum dots. *Physical review letters*, 75(20):3728–3731, 1995.
- [184] J. Butkus, P. Vashishtha, K. Chen, J. K. Gallaher, S. K. K. Prasad, D. Z. Metin, G. Laufersky, N. Gaston, J. E. Halpert, and J. M. Hodgkiss. The evolution of quantum confinement in cspbbr 3 perovskite nanocrystals. *Chemistry of Materials*, 29(8):3644–3652, 2017.
- [185] G. Q. Zhang and A. Roosmalen. *More than Moore*. Springer US, Boston, MA, 2009.
- [186] G. Konstantatos and E. H. Sargent. *Colloidal quantum Dot optoelectronics and photovoltaics*. Cambridge University Press, Cambridge, [elektronische ressource] edition, 2013.
- [187] J. H. Davies. *The physics of low-dimensional semiconductors: An introduction / John H. Davies*. Cambridge University Press, Cambridge, 1998.
- [188] H. Haug and S. W. Koch. *Quantum theory of the optical and electronic properties of semiconductors*. World Scientific, Singapore, 3rd ed. edition, 1994.
- [189] S. Glutsch. *Excitons in Low-Dimensional Semiconductors: Theory Numerical Methods Applications*, volume 141 of *Springer Series in Solid-State Sciences*. Springer, Berlin and Heidelberg, 2004.
- [190] A. Salehi, S. Ho, Y. Chen, C. Peng, H. Yersin, and F. So. Highly efficient organic light-emitting diode using a low refractive index electron transport layer. *Advanced Optical Materials*, 5(11):1700197, 2017.
- [191] R. L. Z. Hoye, M.-L. Lai, M. Anaya, Y. Tong, K. Galkowski, T. Doherty, W. Li, T. N. Huq, S. Mackowski, L. Polavarapu, J. Feldmann, J. L. MacManus-Driscoll, R. H. Friend, A. S. Urban, and S. D. Stranks. Identifying and reducing interfacial losses to enhance color-pure electroluminescence in blue-emitting perovskite nanoplatelet light-emitting diodes. *ACS Energy Letters*, pages 1181–1188, 2019.

Part V. Appendix

Abbreviations

TDM : Transition dipole moment

PDM : Permanent dipole moment

OLED : Organic light-emitting diode

LED : Light-emitting diode

TVD : Thermal vapor deposition

OVPD : Organic vapor phase deposition

DFT : Density functional theory

TD-DFT : Time dependent density functional theory

EML : Emission layer

ETL : Electron transport layer

HTL : Hole transport layer

EBL : Electron blocking layer

HBL : Hole blocking layer

WGM : Waveguided mode

SPP : Surface plasmon polariton

ITO : Indium tin oxide

HOMO : Highest occupied molecular orbital

LUMO : Lowest unoccupied molecular orbital

EQE : External quantum efficiency

TADF : Thermally activated delayed fluorescence

TTA : Triplet-triplet annihilation

TPQ : Triplet-polaron quenching

ISC : Intersystem crossing

RISC : Reverse intersystem crossing

DOS : Density of states

ADPL : Angular dependent photoluminescence spectroscopy

BFP : Back focal plane

Molecules

CBP : 4,4'-Bis(N-carbazolyl)-1,1'-biphenyl

NPB : N,N'-Di(1-naphthyl)-N,N'-diphenyl-(1,1'-biphenyl)-4,4'-diamine

mCBP : 3,3'-Bis(carbazol-9-yl)biphenyl

mCP : 1,3-Bis(N-carbazolyl)benzene

Spiro₂-CBP : 2,7-Bis(carbazol-9-yl)-9,9-spirobifluorene

DPEPO : Bis[2-(diphenylphosphino)phenyl] ether oxide

PO₉ : 3,6-bis(diphenylphosphoryl)-9-phenylcarbazole

PMMA : Poly(methyl methacrylate)

PEDOT-PSS : Poly(3,4-ethylenedioxythiophene) : polystyrene sulfonate

poly-TPD : Poly(4-butylphenyldiphenylamine)

UGH-2 : 1,4-Bis(triphenylsilyl)benzene

BDASBi : 4,4'-bis[4-(diphenylamino)styryl]biphenyl

Coumarin6 : 3-(2-Benzothiazolyl)-N,N-diethylumbelliferylamine

DCM : 4-(Dicyanomethylene)-2-methyl-6-(4-dimethylaminostyryl)-4H-pyran

Ir(ppy)₂(acac) : Bis[2-(2-pyridinyl-N)phenyl-C](acetylacetonato)iridium(III)

Ir(mdq)₂(acac) : Bis(2-methyldibenzo[f,h]quinoxaline)(acetylacetonate)iridium(III)

Ir(piq)₂(acac) : Bis(1-phenylisoquinoline)(acetylacetonate)iridium(III)

Ir(bppo)₂(acac) : Bis(benzopyranopyridinone)(acetylacetonate)iridium(III)

Ir(bppo)₂(ppy) : Bis(benzopyranopyridinone)(2-(2-pyridinyl-N)phenyl-C)iridium(III)

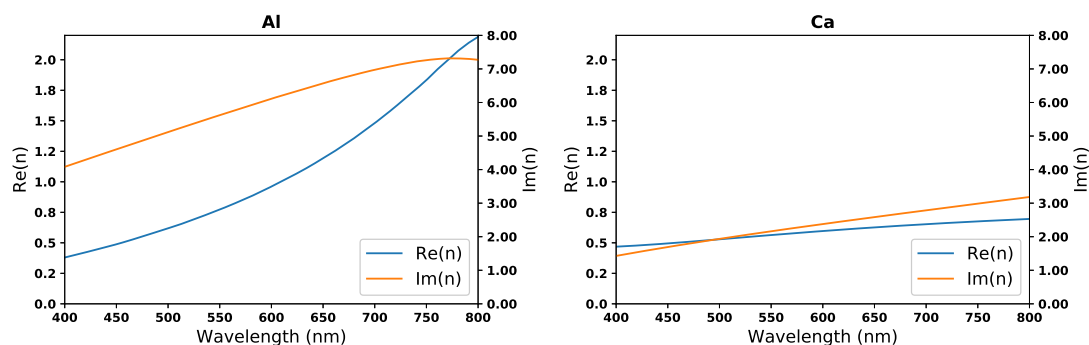
Ir(ppy)₂(bppo) : Bis(2-(2-pyridinyl-N)phenyl-C)(benzopyranopyridinon)iridium(III)

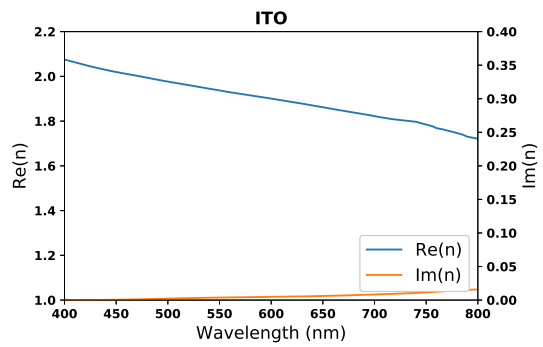
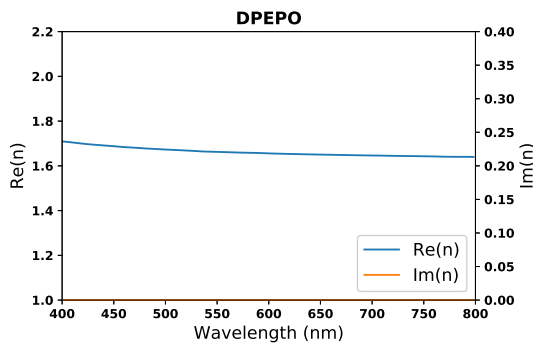
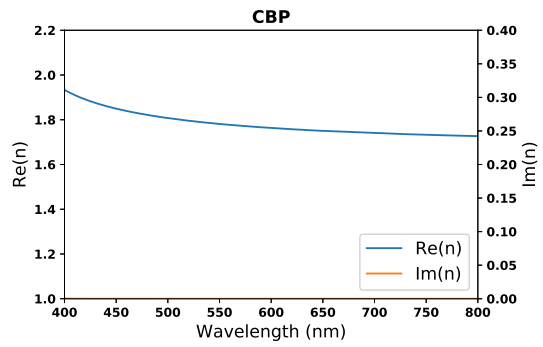
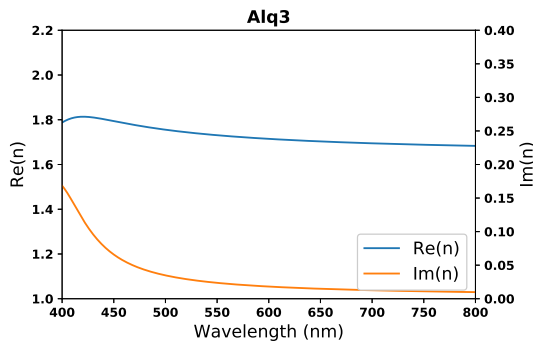
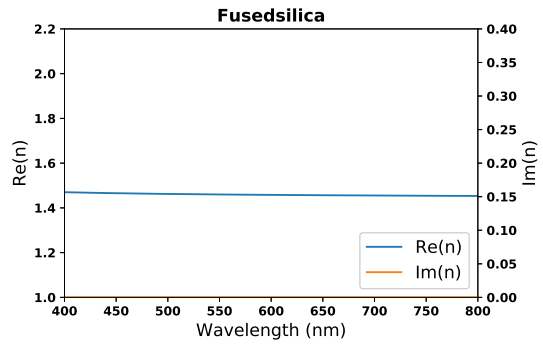
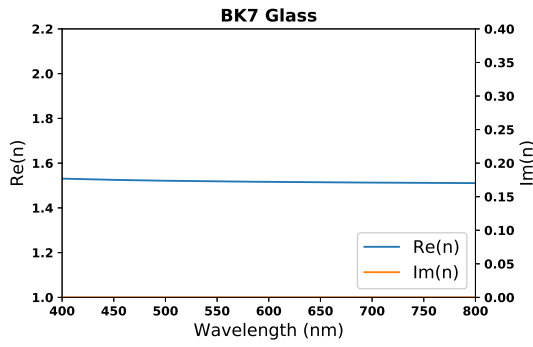
Ir(ppy)₃ : Tris[2-phenylpyridine]iridium(III)

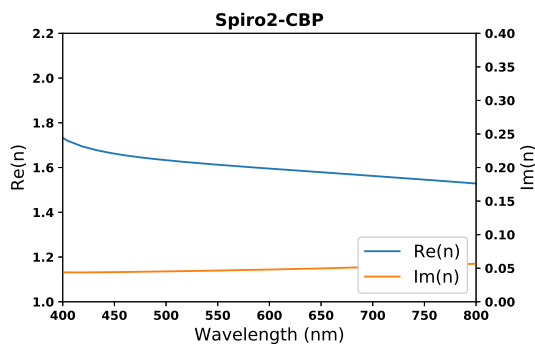
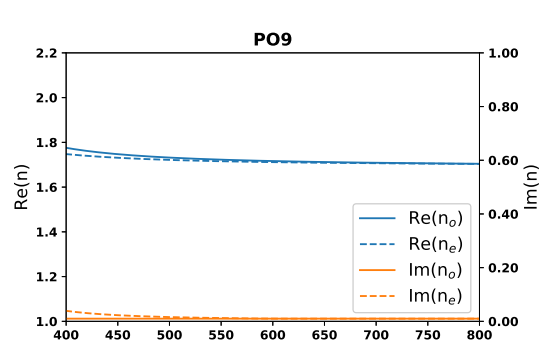
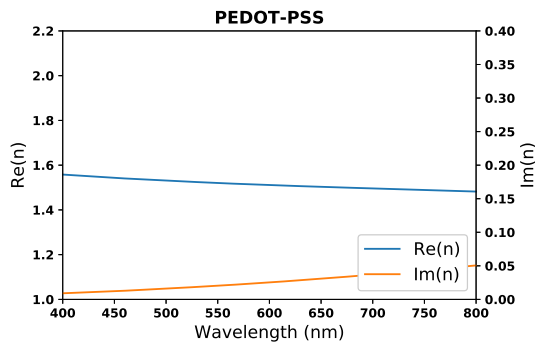
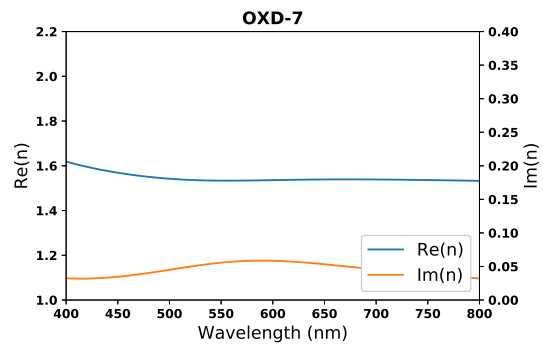
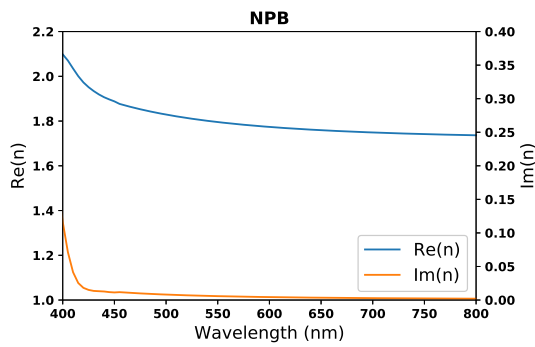
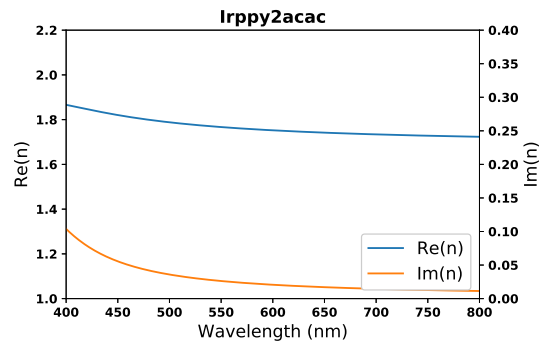
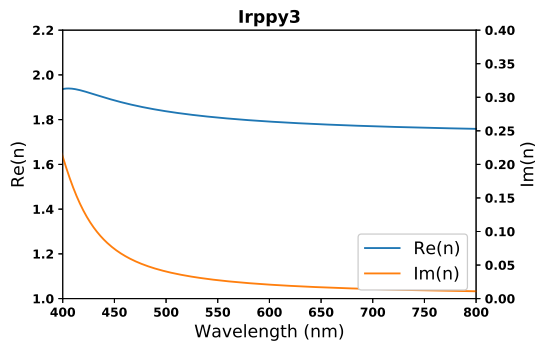
Ir(piq)₃ : Tris[1-phenylisoquinolino-C2,N]iridium(III)

Ir(chpy)₃ : Tris[(2-(1-cyclohexenyl)pyridine)] iridium(III)

Optical constants







Derivation of the alignment constant

The following paragraphs will describe the derivation of the relationship

$$\frac{p_{\parallel}^2}{p_{\perp}^2} \cdot n^4 = \text{const} \quad (10.7)$$

where p_{\parallel} and p_{\perp} denote the components of a TDM parallel or perpendicular to a substrate and n indicates the refractive index of the emissive film. The considerations as performed by the author were first published in [38].

Starting from a dipole model for a layered thin-film emissive device, the ratio of the power emitted into p-polarized, i.e. transverse magnetic (TM), modes by TDMs parallel to the film surface to TDMs perpendicular to the surface can be written as [15]:

$$\frac{P(p_{\parallel})}{P(p_{\perp})} = \frac{p_{\parallel}^2}{p_{\perp}^2} \cdot \frac{T_{\parallel p}^2 \cdot k_{z,\text{film}}^2}{k_{\parallel}^2 \cdot T_{\perp p}^2} \quad (10.8)$$

Therein the factors $T_{\parallel p}$ and $T_{\perp p}$ denote the transmission factors describing light propagation of p-polarized light in the microcavity surrounding the emissive film, k_{\parallel} is the component of the wavevector \vec{k} parallel to the film surface, which is constant over all involved media. The TDM is described by its components parallel (p_{\parallel}) and perpendicular (p_{\perp}) to the film surface. Finally, $k_{z,\text{film}}$ is the projection of the wavevector to the surface normal in the emitting medium.

The described system is modeled as a simple emissive film on top of a glass substrate covered with vacuum where refractive indexes are denoted as n_{sub} , n_{film} and n_{vac} . Using the Fresnel coefficients for an interface between two materials (e. g. $t_{\text{film}/\text{vac}}$ for the transmission from the emissive film to vacuum), the matrix transfer formalism yields the transmission factors as

$$T_{\parallel p} = \frac{t_{\text{film}/\text{sub}} \cdot (1 + r_{\text{film}/\text{vac}})}{1 - r_{\text{film}/\text{sub}} r_{\text{film}/\text{vac}}} \quad (10.9)$$

$$T_{\perp p} = \frac{t_{\text{film}/\text{sub}} \cdot (1 - r_{\text{film}/\text{vac}})}{1 - r_{\text{film}/\text{sub}} r_{\text{film}/\text{vac}}}$$

The resultant term then can be written as

$$\frac{P(p_{\parallel})}{P(p_{\perp})} = \frac{p_{\parallel}^2}{p_{\perp}^2} \cdot \frac{(1 + r_{\text{film}/\text{vac}})^2 \cdot k_{z,\text{film}}^2}{k_{\parallel}^2 \cdot (1 - r_{\text{film}/\text{vac}})^2} \quad (10.10)$$

This expression depends only on the reflection coefficient of the film-vacuum interface. Assuming this can be described as a single boundary, the corresponding Fresnel coefficient between two media, 1 and 2, can be calculated as:

$$r_{12} = \frac{n_1^2 \cdot k_{z,2} - n_2^2 \cdot k_{z,1}}{n_1^2 \cdot k_{z,2} + n_2^2 \cdot k_{z,1}} \quad (10.11)$$

Resulting in the following equation if $|\vec{k}| = \frac{2\pi}{\lambda}$ and $k_z = \sqrt{|\vec{k}|^2 - k_{\parallel}^2}$ is used,

$$\frac{P(p_{\parallel})}{P(p_{\perp})} = \frac{p_{\parallel}^2}{p_{\perp}^2} \cdot \frac{(4\pi^2 n_{\text{sub}}^2 - k_{\parallel}^2 \lambda^2)}{\lambda^2 n_{\text{sub}}^2 k_{\parallel}^2} n_{\text{film}}^4 \quad (10.12)$$

where λ describes the wavelength of the electromagnetic waves. For two different systems having the same angular radiation pattern and thus the the same power ratio $\frac{P(p_{\parallel})}{P(p_{\perp})}$ the following can be written:

$$\frac{P_1(p_{\parallel})}{P_1(p_{\perp})} = \frac{P_2(p_{\parallel})}{P_2(p_{\perp})} \quad (10.13)$$

$$\frac{p_{1,\parallel}^2}{p_{1,\perp}^2} \cdot \frac{(4\pi^2 n_{1,\text{sub}}^2 - k_{\parallel}^2 \lambda^2)}{\lambda^2 n_{1,\text{sub}}^2 k_{\parallel}^2} n_{1,\text{film}}^4 = \frac{p_{2,\parallel}^2}{p_{2,\perp}^2} \cdot \frac{(4\pi^2 n_{2,\text{sub}}^2 - k_{\parallel}^2 \lambda^2)}{\lambda^2 n_{2,\text{sub}}^2 k_{\parallel}^2} n_{2,\text{film}}^4 \quad (10.14)$$

If the refractive index of the substrate is the same for both materials, this can be simplified to.

$$\frac{p_{1,\parallel}^2}{p_{1,\perp}^2} \cdot n_{1,\text{film}}^4 = \frac{p_{2,\parallel}^2}{p_{2,\perp}^2} \cdot n_{2,\text{film}}^4 \quad (10.15)$$

Hence, the proposed condition has to be fulfilled:

$$\frac{p_{\parallel}^2}{p_{\perp}^2} \cdot n^4 = \text{const} \quad (10.16)$$

To verify the validity of this expression in more complicated systems, such as complete thin film LED stacks, different combinations of Θ and the refractive index were calculated for the emissive layer of the stack presented in chapter 5.4 were calculated. As depicted in fig. 10.21, the normalized radiation patterns match if the properties of the emissive layer yield the same value of ζ .

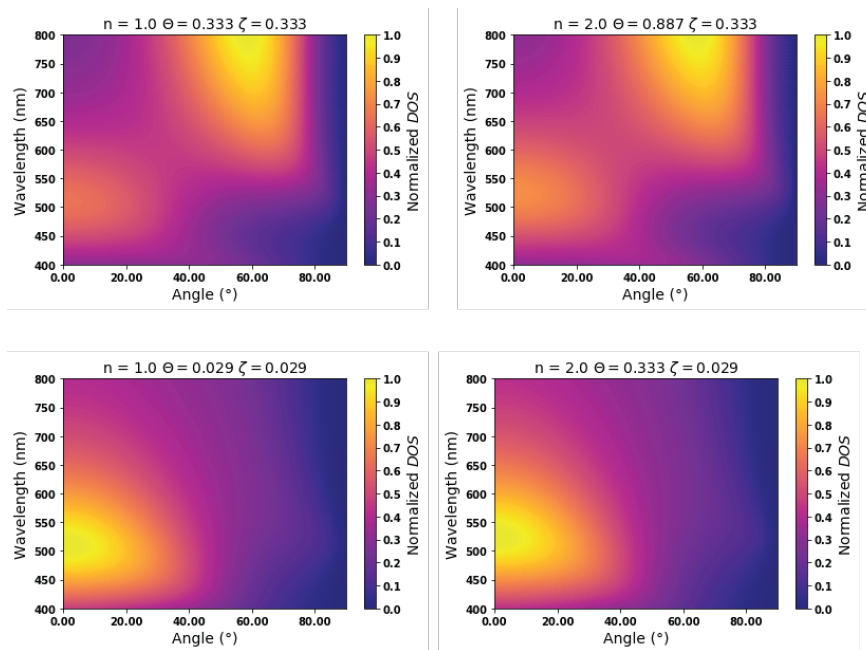


Figure 10.21.: Calculations of the stack presented in chapter 5.4 for different values of Θ and the refractive index of the thin emissive layer. The normalized radiation patterns match if the ζ value of two different systems is the same.

Involved researchers

- Chapter 2 is based on the author's master thesis which was supervised by Bert Scholz and Wolfgang Brütting.
- Chapter 4 originates from several publications the author was involved in [11, 34, 36–38, 169].
- Chapter 5 involves the optical simulations as implemented within the author's master thesis. Note that the considerations about the efficiency of thin film devices are based on [1].
- Chapter 6 : The software used for the computational chemistry throughout the thesis was the "Materials Science Suite" by Schrödinger Inc.. Note that different versions of this software were used throughout the work. Further, the computation of density functional theory and molecular dynamics was partially supported by Daniel Sylvinson M.R.. Optical simulations were performed based on the author's master thesis.
- Chapter 7 describes several basic experimental concepts. The angular resolved measurement setup was initially based on the layout used by Christian Mayr. Throughout the thesis, it was improved by the author and the students Philippe Linsmayr and Felix Höhnle, where the latter reworked the setup for fluorescence anisotropy measurements. Back focal plane imaging was performed by Carissa Eisler using the setup developed by herself and Adam Schwarzberg. Matthew Jurow and Mai Quynh Do provided perovskites used for the verification of the back focal plane imaging.
- Chapter 8 involves the work of Thomas Gimpel and Felix Höhnle. Where the former measured the preferential alignment of the polar molecules Coumarin6 and DCM in various host materials within his bachelor thesis. Felix Höhnle performed the fluorescence anisotropy measurements of Coumarin6. Hence a more detailed insight into the experimental setup and further results are given within his master thesis.
- Chapter 9 includes several publications as well as unpublished work. Properties of solution processed films containing Ir-complexes are published in [36, 37]. Samples prepared via OVPD were fabricated by Francisco Navarro, John Facendola and Matthew Jurow at the University of Southern California. Kristoffer Harms and Hans-Hermann Johannes provided the sky-blue homoleptic Ir-complexes based on the 1295 structure within the BMBF project "Interphase".

Chapter 10 describes the two publications [38, 169] which were co-authored by this thesis's author. The direct collaborators for this thesis were Matthew Jurow, Carissa Eisler and Erika Penzo as well as the undergraduate student Mai Quynh Do. This work was financially supported by the BaCaTec foundation within a travel grant to the Molecular Foundry at the Lawrence Berkeley National Laboratory. The considerations about the performance limit of perovskite LED devices were performed in collaboration with Carola Lampe and Prof. Alexander Urban.

Publications

Influence of molecular orientation on the coupling of surface plasmons to excitons in semitransparent inverted organic solar cells, M. Gruber, M. Mayr, **T. Lampe**, B.-C. Gallheber, B. J. Scholz and W. Brütting Appl. Phys. Lett. 106, 083303 (2015)

Understanding and predicting the orientation of heteroleptic phosphors in organic light-emitting materials, M. J. Jurow, C. Mayr, T. D. Schmidt, **T. Lampe**, P. I. Djurovich, W. Brütting and M. E. Thompson Nature Materials 15, 85–91 (2016)

Dependence of Phosphorescent Emitter Orientation on Deposition Technique in Doped Organic Films, **T. Lampe**, T. D. Schmidt, M. J. Jurow, P. I. Djurovich, M. E. Thompson, and W. Brütting Chem. Mater., 2016, 28 (3), pp 712–715

Tuning the Microcavity of Organic Light Emitting Diodes by Solution Processable Polymer–Nanoparticle Composite Layers, J. B. Preinfalk, F. R. Schackmar, **T. Lampe**, A. Egel, T. D. Schmidt, W. Brütting, G. Gomard, and U. Lemmer ACS Appl. Mater. Interfaces, 2016, 8 (4), pp 2666–2672

Mehr Licht durch orientierte Farbstoffmoleküle, T. D. Schmidt, **T. Lampe** and W. Brütting Nachrichten aus der Chemie 64 (5), 514-518 (2016)

Tunable Anisotropic Photon Emission from Self-Organized CsPbBr₃ Perovskite Nanocrystals, M. J. Jurow, **T. Lampe**, E. Penzo, J. Kang, M. A. Koc, T. Zechel, Z. Nett, M. Brady, L.-W. Wang, A. P. Alivisatos, S. Cabrini, W. Brütting, and Y. Liu Nano Lett., 2017, 17 (7), pp 4534–4540

Emitter Orientation as a Key Parameter in Organic Light-Emitting Diodes, T. D. Schmidt, **T. Lampe**, D. Sylvinson M. R., P. I. Djurovich, M. E. Thompson and W. Brütting Physical Review Applied 8, 037001 (2017)

Enabling electron conduction in anisotropic hole transport materials for superior optical properties in organic light emitting diodes, M. Schmid, **T. Morgenstern**, W. Brütting Organic Electronics 62, 216-219 (2018)

Correlating optical and electrical dipole moments to pinpoint phosphorescent dye alignment in organic light-emitting diodes, **T. Morgenstern**, M. Schmid, A. Hofmann, M. Bierling, L. Jäger, W. Brütting ACS Applied Materials and Interfaces 10, 37, 31541-31551 (2018)

Manipulating the Transition Dipole Moment of CsPbBr₃ Perovskite Nanocrystals for Superior Optical Properties, M. J. Jurow, **T. Morgenstern**, C. Eisler, J. Kang, E. Penzo, M. Do, M. Engelmayer, W. T. Osowiecki, Y. Bekenstein, C. Tassone, L.-W. Wang, A. P. Alivisatos, W. Brütting and Y. Liu, *Nano Lett.*, 2019, 19 (4), pp 2489–2496

Conference presentations

Dependence of phosphorescent emitter orientation on deposition technique, **T. Lampe**, T. D. Schmidt, and W. Brütting, DPG Frühjahrstagung 2016, Regensburg

Dependence of phosphorescent emitter orientation on deposition technique in doped organic films, **T. Lampe**, T. D. Schmidt and W. Brütting, SPIE Photonics West, 2016, San Diego

Optical simulations of birefringent organic semiconductor devices, **T. Lampe**, T. D. Schmidt, M. Gruber and W. Brütting, SIMOEP, 2016, Winterthur

Understanding the orientation of heteroleptic phosphors in organic light-emitting materials, **T. Lampe**, T. D. Schmidt, M. Jurow, P. Djurovich, M. Thompson and W. Brütting, SA Congress: Light, Energy and Environment, 2016, Leipzig

Orientation of Phosphorescent Dopants in Organic Vapor Phase Deposited Films, **T. Lampe**, J. Facendola, M. Jurow, F. F. Navarro, T. D. Schmidt, P. Djurovich, M. Thompson and W. Brütting DPG Frühjahrstagung, 2017, Dresden

Molecular alignment in organic guest-host systems, **T. Lampe**, P. Linsmayer and W. Brütting, 22nd International Krutyn Summer School, 2017, Krutyn

Preferential molecular alignment in organic thin films, **T. Lampe** and W. Brütting, Seminar talk at the Lawrence Berkeley National Laboratory, 2017, Berkeley

Controlling preferential alignment of heteroleptic phosphors in organic guest-host systems via film preparation parameters, **T. Lampe**, P. Linsmayer, T. D. Schmidt and W. Brütting, SPIE Photonics West, 2017, San Diego

Tunable Anisotropic Photon Emission from Self-Organized CsPbBr₃ Perovskite Nanocrystals, **T. Morgenstern**, M. Jurow, E. Penzo, J. Kang, M.

A. Koc, T. Zechel, Z. Nett, M. Brady, L.-W. Wang, P. Alivisatos, S. Cabrini, Y. Liu and W. Brütting, DPG Frühjahrstagung, 2018, Berlin

Correlating Optical and Electrical Dipole Characterization to Pinpoint Phosphorescent Dye Orientation, **T. Morgenstern**, M. Schmid, A. Hofmann, M. Bierling, L. Jäger and W. Brütting, MRS Spring Meeting, 2018, Phoenix

Manipulating the Transition Dipole Moment of CsPbBr₃ Perovskite Nanocrystals for Superior Optical Properties, **T. Morgenstern**, M. Jurow, C. Eisler, J. Kang, M. Engelmayer, P. Alivisatos, Y. Liu and W. Brütting, DPG Frühjahrstagung, 2019, Regensburg

Correlating Optical and Electrical Dipole Characterization to Pinpoint Phosphorescent Dye Orientation, **T. Morgenstern**, M. Schmid, A. Hofmann, M. Bierling, L. Jäger and W. Brütting, MRS Spring Meeting, 2019, Phoenix

Acknowledgements

During my work many people supported me whom I want to thank:

Prof. Wolfgang Brütting für seine Unterstützung während meines Bachelor- und Masterstudiums und für die Möglichkeit zu promovieren. Vielen Dank auch für die unzähligen Diskussionen und das aufgebrachte Vertrauen während meiner Promotion.

Prof. Hubert Krenner and **Prof. Kristaan Neyts** for the preparation of the second- and third report for this thesis.

Tobias D. Schmidt für seine Unterstützung zu Beginn meiner Promotion sowie die Ermutigung dieses lange Projekt überhaupt erst anzugehen.

Sebastian Wehrmeister für die unzähligen wissenschaftlichen und nicht wissenschaftlichen Diskussionen sowie die Ermutigung das Promotionsstudium zu beginnen.

Meinen Bürokollegen **Theresa Linderl** und **Eduard Meister** für die wunderbare Atmosphäre im Büroalltag.

Meinen Bachelor- und Masterstudenten **Philippe Linsmayer**, **Markus Schmid**, **Thomas Gimpel** und **Felix Höhnle**.

Allen anderen Kollegen der Organikgruppe **Thomas Zechel**, **Florian Graßl**, **Marc Gruber**, **Alexander Hofmann**, **Manuel Engelmayer**, **Tassilo Naujoks**, **Bilal Abbas Naqvi** und **Prakhar Sahay**.

Sowie dem restlichen **Lehrstuhl für Experimentalphysik IV**.

Bert Scholz für die Betreuung meiner Bachelor und Masterarbeit sowie die Zusammenarbeit zu Beginn meiner Promotion.

Matthew Jurow for his extensive support throughout my PhD work. Without you most of my scientific success would have never happened.

Erika Penzo for her support and the italian temperament.

The Mark E. Thompson Research Group at the University of Southern California. Especially **Mark E. Thompson** and **Peter Djurovich** for several fruitful discussions and **Daniel Sylvinson** for his support with DFT and MD calculations as well as the whole group for a wonderful time in Los Angeles.

Several people at the Lawrence Berkeley National Laboratory for their support during my research visit. In particular **Dr. Yi Liu** for supporting my work and **Mai Thi Quynh Do** for the synthesis of perovskite nanocrystals.

Carissa Eisler for several fruitful discussions about optical setups and simulations as well as the vast amount of snacks in her office.

Claudia Löflath und **Bettina Schestak** aus dem Sekretariat des Lehrstuhls EP4 für ihre Unterstützung in allen Fragen der Bürokratie.

Hans-Hermann Johannes und **Kristoffer Harms** von der Technischen Universität Braunschweig für die Synthese vieler Carbene-Komplexe sowie die vielen Diskussionen im Laufe des Projekts "Interphase".

Andre Walter für unzählige Diskussionen über Labview, Python und den sonstigen Arbeitsalltag.

Meiner Schwester **Carola Lampe** für wissenschaftliche Diskussionen rund um Perovskite sowie die eine oder andere Lehrstunde über Chemie

Prof. Alexander Urban Für die Bereitstellung von Perovskit Nanokristallen sowie wissenschaftlichen Austausch rund um Perovskit LEDs.

Sowie meiner Frau **Anja** und meinem noch ungeborenen Sohn dafür mich während der anstrengenden Zeit der Promotion ständig zu unterstützen.